Development of a fiber tracker for satellite-borne astroparticle physics experiments

Department of Mechanics, Mathematics and Management
AEROSPACE SCIENCE AND ENGINEERING
Ph.D. Program
SSD: FIS/01–EXPERIMENTAL PHYSICS

Final Dissertation

Development of a fiber tracker for satellite-borne astroparticle physics experiments

by
Panzarini Giuliana:

Supervisors:

Dr. Mario Nicola Mazziotta

Prof. Silvia Rainò

Coordinator of Ph.D. Program:
Prof. Marco Donato De Tullio

Course n°37, 01/11/2021-31/10/2024

Politecnico di Bari

Department of Mechanics, Mathematics and Management
AEROSPACE SCIENCE AND ENGINEERING
Ph.D. Program
SSD: FIS/01–EXPERIMENTAL PHYSICS

Final Dissertation

Development of a fiber tracker for satellite-borne astroparticle physics experiments

---

by
Giuliana Panzarini

Referees:

Dr. Adriano Di Giovanni

Prof. Francesco Arneodo

Supervisors:

Dr. Mario Nicola Maziotta

Prof. Silvia Rainò

Coordinator of Ph.D Program:
Prof. Marco Donato De Tullio

Course n°37, 01/11/2021-31/10/2024

Alla mia famiglia

Abstract

Cosmic rays are high-energy particles that originate from outer space and strike Earth's atmosphere. They are produced by extremely energetic phenomena in the Universe and represent a unique probe for understanding the physics behind the processes associated with their emission. Over the past decades significant breakthroughs have been achieved by means of different satellite-borne experiments. However, many phenomena remain only partially understood and new satellite-borne detectors need to be developed. The NUSES space mission is a future satellite experiment dedicated to the study of cosmic rays. This thesis focuses on the development and testing of a tracker detector based on the technology of scintillating fibers readout with SiPM for the Ziré experiment, one of the instruments onboard NUSES. At the beginning of this research activity a Geant4 simulation framework was developed to test the detector performance and optimize the tracker design in terms of fiber diameter and SiPM array pitch. Following simulation validation, a series of prototype modules were constructed and tested with high-energy particle beams at the CERN-PS. Based on the beam test data, the first prototype of Ziré, "Zirettino", was assembled for characterization studies. Finally, environmental testing of the structural model of the detector was conducted to test the capability of the tracker to withstand the vibrational stresses expected during launch. The vibration tests confirmed the robustness of the tracker, with no degradation in performance after the tests.

These results demonstrate that the fiber tracker designed is a promising solution for NUSES and other future space missions targeting cosmic radiation detection.

Contents

Introduction

Cosmic rays are high-energy particles produced by extremely energetic phenomena in the Universe that reach the Earth's atmosphere and represent a unique probe for exploring the properties of the astrophysical sources where they are accelerated. A number of experiments, both space-based and ground-based in past years have significantly advanced our understanding of high-energy astrophysical processes. However, many phenomena are still only partially understood and new detectors need to be developed for improving sensitivity and resolution, allowing the detection of fainter signals from distant sources.

The main goal of this work is the development of a scintillating fiber tracker detector for new generation satellite-borne experiments exploiting the technology of Silicon Photomultipliers (SiPM) for reading the light signals produced by the fibers. Scintillating fibers are suitable for satellite-borne detectors because of their light weight, flexibility and low cost. In addition, the linear arrays of SiPMs developed in recent years allow a reduction of the power consumption while keeping a high detector granularity. The fiber tracker studied in this work will be one of the sub-detectors of the Ziré experiment onboard the NUSES space mission. The NUSES space mission is a future satellite experiment for studying low-energy ($E < 300$ MeV) cosmic rays. It will also be a technological pathfinder for developing new methods to observe the cosmic radiation. It includes two instruments: Terzina, a prototype of a novel Cherenkov telescope concept, and Ziré, a detector aimed at monitoring low-energy cosmic ray fluxes.

The Ziré fiber tracker will consists of three X-Y modules, each one made up of two layers of scintillating fibers arranged orthogonally in two planes. A particle passing through the tracker will interact with the fiber material, depositing energy that produces light emission by means of the scintillation process. This light will be then collected at the two edges of the hit fiber by the SiPM array.

The main goal of my PhD project was to evaluate the performance of the tracker designed for Ziré in terms of detection efficiency, spatial resolution, and suitability for space applications.

In Chapter 1 the context of high-energy astrophysics is illustrated, introducing

the nature and origin of cosmic radiation and the main high-energy processes in the Universe. The main detection technologies used in cosmic radiation experiments are introduced, with a focus on scintillator and SiPM technologies. Then, a brief overview of some of the most relevant satellite experiments operated to date is provided, along with a summary of their main scientific results.

Chapter 2 introduces the NUSES space mission, with a detailed description of the Ziré experiment and of its fiber tracker.

Chapter 3 illustrates the design and development phase of the fiber tracker prototype. First, the working principle of scintillating fibers and of the tracker are explained in detail. Then, the results of simulations performed to study the fiber tracker performance in detecting low-energy electrons are presented. Finally, the phases of the construction of the first prototypes of the tracker are illustrated, with a focus on the front-end electronics developed for these prototypes.

Chapter 4 presents the results of the characterization tests carried out on the prototypes in two beam test campaigns performed at the CERN-PS in 2021 and 2022.

Chapter 5 describes the construction and testing phase of the first prototype of Ziré, named Zirettino. The results of a further beam test campaign performed at the CERN-PS in 2023 will be illustrated.

Finally, in Chapter 6 the results of the vibration tests performed on the structural model of the Ziré fiber tracker are discussed.

Chapter 1

Astroparticle physics

High-energy astrophysics is the branch of astronomy dedicated to exploring the most violent phenomena in our Universe. These phenomena are associated with the intense non-thermal emission of high-energy radiation and acceleration of particles in the proximity of cosmic objects characterized. Studying this radiation enables to study different cosmic sources such as Active Galactic Nuclei (AGN) and Quasars, Pulsars and Magnetars, Black holes (BHs), Neutron stars (NSe) and events like Supernova Explosions (SNe), Gamma-Ray Bursts (GRBs). The cosmic radiation consists of Cosmic rays (CRs) and Gamma rays (GRs).

CRs are high-energy charged particles, accelerated by intense magnetic fields and shock waves within sources such as Supernova remnants (SNRs), pulsars, and AGNs and traveling towards the Earth at nearly the speed of light. They are mainly composed of protons, with a smaller fraction of heavier nuclei and electrons.

GRs, the highest-energy form of electromagnetic radiation, are generated in the same energetic environments as cosmic rays through processes such as synchrotron radiation (SR), inverse Compton scattering (IC), and neutral pion decay.

The main goal of high-energies astrophysics is to study the cosmic radiation in order to understand the mechanisms governing their production, acceleration and propagation and studying the main properties of their sources.

Many experiments either space and ground-based, dedicated to the detection and study of radiation emitted from several astronomical objects have been designed and operated.

Section 1.1 of this chapter will provide a brief overview on the nature and origin of cosmic rays and gamma rays: in section 1.1.

Section 1.2 includes a brief summary of some of the most important high-energy processes in the Universe with a focus on the emission mechanism of cosmic and gamma radiation.

In section 1.3 the main techniques used to detect ionizing radiation will then be illustrated. Particular attention will be given to different radiation-matter interactions, which enable the development of various detectors used in high-energy astrophysics. The operating principles of the devices referenced throughout this work will be described in detail.

In section 1.4 the reasons that makes satellite-based experiments necessary will be outlined, and some of the main experiments conducted to date will be briefly presented.

1.1 Cosmic and Gamma rays

1.1.1 Cosmic rays

CRs are charged particles that travel throughout the Universe traversing the interstellar medium and continuously reaching the Earth from considerable distances. The energy spectrum of CRs is shown in figure 1.1. The spectrum extends from few GeV to beyond 10^{20} eV, with a flux that varies from few particles per cm^2 per second to about 1 particle per km^2 per century at energies above 10^{18} eV (Ultra-High-Energies (UHE)) [De Angelis and Pimenta, 2018]. In figure 1.1 are also shown the different contribution to the spectrum from the different components of CRs. The $\sim$ 98% of CR particles consists of protons and nuclei, of which $\sim$ 12% are α particles (i.e. Helium nuclei), 1% are heavier nuclei. The remaining 2% are electrons [Longair, 2011]. The electrons component of CRs in the Galaxy is responsible for the diffuse Galactic synchrotron radio emission [Di Bernardo et al., 2015].

At energies below 10^9 eV, the energy spectra of all CR species exhibit a pronounced drop. The flux of CRs at these energies is strongly correlated with the solar cycle: particles of galactic origin, entering the heliosphere, are subject to the turbulent solar wind and the interplanetary magnetic field (IMF). This strongly influences the propagation of low-energy CRs deflecting their trajectories and shielding the inner part of the solar system from a significant portion of these particles. This results in a substantial reduction in low-energies CRs flux at the Earth [De Angelis and Pimenta, 2018]. A larger solar activity results in larger disturbances in IMF. Consequently, the flux varies with the solar activity. This is the process known as "*solar modulation*" [Corti et al., 2016].

For energies above 10^9 eV the spectrum of primary CRs can be described with a power-law distribution:

$$\frac{dN}{dE} = KE^{-x} \tag{1.1}$$

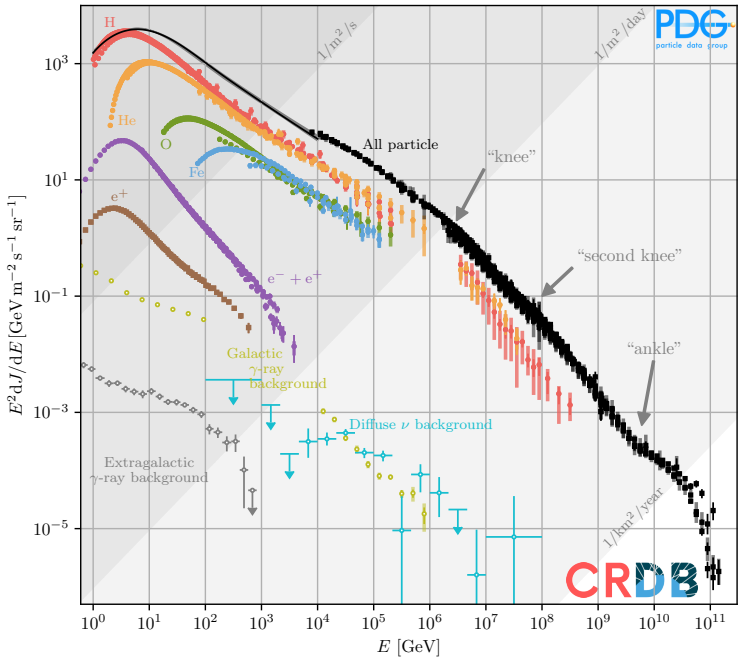

Figure 1.1: Spectrum of CRs from [Group et al., 2020].

with x varing in the range from 2.7 to 3.3 [De Angelis and Pimenta, 2018].

Figure 1.1 shows the spectrum obtained with data from a number of CR experiments. Three regions can be identified. The first region extends up to $\sim 10^{15}$ eV at the so-called "*knee*", where there is the first change in the index x from 2.7 to 3.1. CRs in this region are believed to be of a Galactic origin.

The spectrum of UHECRs is shown in figure 1.2. At energies of about 10^{18} eV there is the second transition point, the "*ankle*", where the spectral index changes from $\sim$ 3.1 to 2.7. At energies above 10^{19} eV the spectrum is strongly suppressed because of the interactions of CRs with the Cosmic microwave background radiation, a phenomenon known as the Greisen-Zatsepin-Kuzmin (GZK) mechanism (details in [Zatsepin and Kuzmin, 1966] and [Abbasi et al., 2008]).

Cosmic rays are detected through different methods depending on their energy range. For cosmic rays with energies between 30 MeV and 30 GeV (high-energy CRs) space-based observatories are employed. At higher energies ground-based observatories are required due to the reduced flux. When CRs with energies above 30 GeV (Very High Energy (VHE)) enter the atmosphere they produce extensive electromagnetic air showers (EAS). A EAS is the cascade production of a large number of secondary particles following the collision of a cosmic-ray particle with a nucleon. In case of CR protons the relevant process is:

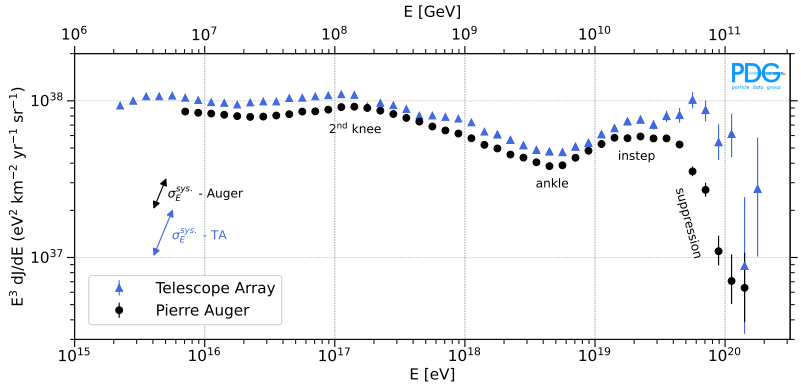

Figure 1.2: Spectrum of UHECRs from measurements of the all-particle CR flux from Telescope Array [Ivanov, 2019] (blue triangles) and the Pierre Auger Observatory [Aab et al., 2020] (black circles).

$$p + N \rightarrow \pi^{\pm}; \pi^0; K^{\pm}; K^0; p; n... \tag{1.2}$$

The short-lived hadrons rapidly decay producing a cascade of high-energy photons, electrons, positrons, muons and neutrinos that represent the penetrating component of the cascade. The secondary particles from this shower ultimately reach the ground. The lateral extension of these air showers can reach several hundred of meters on the ground and hence this secondary particles can be detected on the surface of the Earth by large air shower arrays [De Angelis and Pimenta, 2018].

The main interest in the study of CRs lies in understanding what the accelerators of these extremely energetic particles are and which processes govern their acceleration.

In order to accelerate particles to energy up to 10^{20} eV non-thermal emission processes are needed. The source of acceleration cannot be a static electric field, because the matter in astrophysical sources is in the state of a plasma. Hence, a proper accelerator is needed to allow particles to reach the relativistic energies observed in CRs spectra. A strong turbulent magnetic field is required, capable of generating a variable electric field fundamental for the acceleration mechanisms.

Several astrophysical objects have been identified as candidate sources of cosmic-ray acceleration. The Fermi experiment (see section 1.4.2) has confirmed that Supernova remnants in our galaxy are primary sources of CRs in the region below the knee [Ackermann et al., 2013]. It was proved that in SNRs, CR particles are accelerated via diffusive shocks. According to the classical model of the diffusive shock acceleration mechanism (described in detail in [Fermi, 1949] and [Bell, 1978]), particles repeatedly cross the shock wave front back and forth and gain energy each time. The Fermi acceleration mechanism predicts the observed power-law distribution for the energy

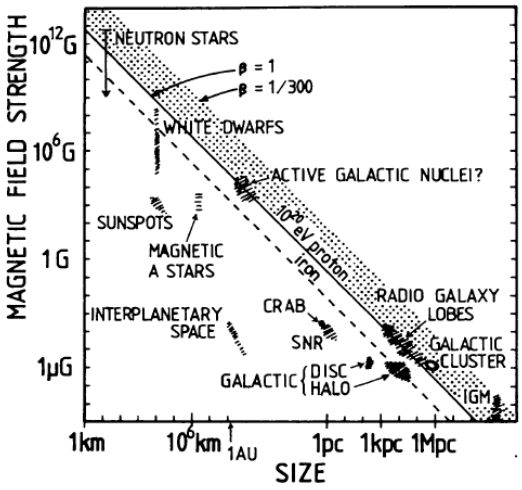

Figure 1.3: The Hillas plot rapresenting potential cosmic ray accelerator [Hillas, 1984].

spectra of relativistic charged particles.

The origin of CRs with higher energy is still a debated question. The condition for an object to confine and accelerate particles to a given energy E is known as Hillas criterion [Hillas, 1984] and is expressed by:

$$E \leq ZeBR \tag{1.3}$$

where Z is the charge of the particle to be accelerated, e is the electron charge, B is the strength of the magnetic field and R is the size of the acceleration region [Ptitsyna and Troitsky, 2010]. Figure 1.3 shows the Hillas plot, the graphical representation of this relation in a bi-dimensional plot where on the x-axis there is the size of the astrophysical sources and on the y-axis the strength of the magnetic field. CRs up to the "ankle" are believed to be accelerated in the powerful relativistic jets produced by Active galactic nuclei.

1.1.2 Gamma rays

Gamma rays are the most energetic part of the electromagnetic spectrum, with energies above 100 keV. Since photons at these energies are characterized by a small probability of interaction with matter, the Universe is nearly transparent to gamma rays, allowing them to reach Earth from cosmological distances, carrying information from their production sites and making them a powerful probe for the observation of astrophysical sources. In addition they are not deflected by the interstellar magnetic fields, and hence they can point directly to their sources [Longair, 2011]. On the other hand, the atmosphere is opaque to this radiation. Figure 1.4 shows the fraction

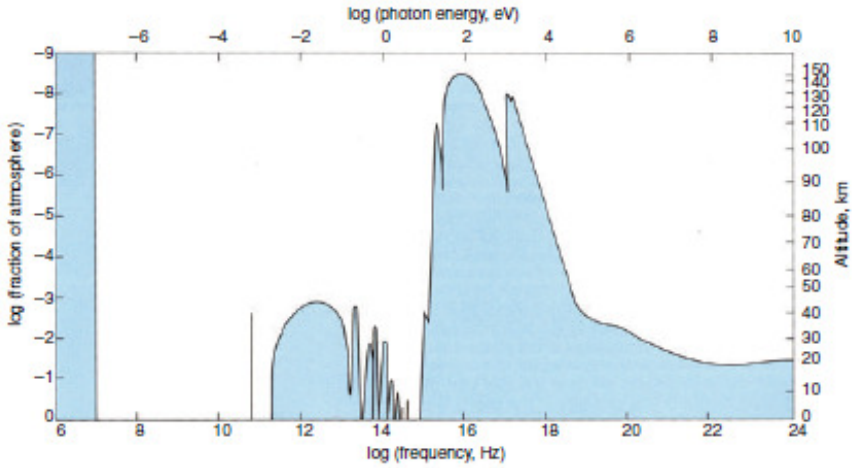

Figure 1.4: Transparency of the atmosphere as a function of the wavelength [Longair, 2011]

of atmospheric thickness that electromagnetic radiation can traverse without being absorbed as a function of the frequency (bottom axis) and the energy (upper axis) of the radiation. We see that gamma rays are not able to reach the ground and hence, space-based observatories are needed.

At energies above 10^{11} eV, photons are so energetic that they initiate electromagnetic cascades in the upper atmosphere and the Cherenkov radiation produced by the ultra-relativistic electrons and positrons in these showers can be detected at ground level by Cherenkov Telescopes arrays.

Figure 1.5 shows the gamma-ray sky at energies above 10 GeV, as observed by the Fermi LAT telescope. The bright band at the center of the image is the diffuse emission from the galactic plane, caused by the interaction of CR particles with the interstellar gas. Many discrete sources have been detected and are visible as bright spots. They are mostly AGN and pulsars. An additional contribution is the residual all-sky emission component, commonly called the isotropic diffuse gamma-ray background (IGRB) that accounts for unresolved extragalactic sources. Figure 1.6 shows the unified photon spectrum from [Ressell and Turner, 1990]. It collects experimental data in an energy range that spans ~ 30 energy decades. The first bump in the spectrum corresponds to the CMB while at higher energies it can be observed a power-law dependence of the flux as $E^{-2.4}$. A cutoff is observed at energies close to 1 TeV.

High-energy gamma rays are produced in the acceleration processes of charged particles, hence they are fundamental probes into cosmic accelerators. The capability of gamma rays to point their sources makes them a preferential tool not only for the

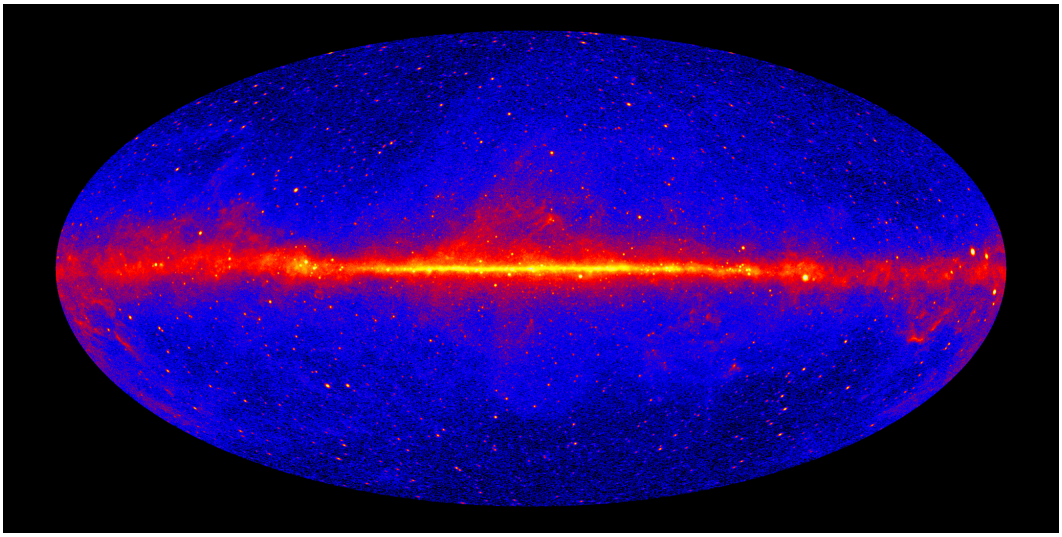

Figure 1.5: Gamma-ray sky in Galactic coordinates with the data of 12 years of observation of the Fermi Large Area Telescope with energies above 1 GeV. Credit: NASA/DOE/Fermi LAT Collaboration

observation of astrophysical sources but also for the study of acceleration processes in the non-thermal universe.

1.1.3 Gamma-ray production processes

Differently from charged particles, photons are not directly accelerated by electromagnetic field. Therefore, mechanisms for producing photons at very high energies are required. A number of different astrophysical processes results in gamma-ray emission. Mainly they are non-thermal processes involving high-energy particles interacting with electromagnetic fields.

Gamma-ray production processes are divided into leptonic and hadronic mechanism. Leptonic processes include electron-positron annihilation, bremsstrahlung and synchrotron radiation. The hadronic production consists in the gamma-ray emission from the decay of neutral pions produced by interactions between CR ions and the ambient medium.

Electron-positron annihilation

The annihilation of electrons with positrons results in the production of high energy photons which can collide with photons of the surrounding medium to produce particle–antiparticle pairs.

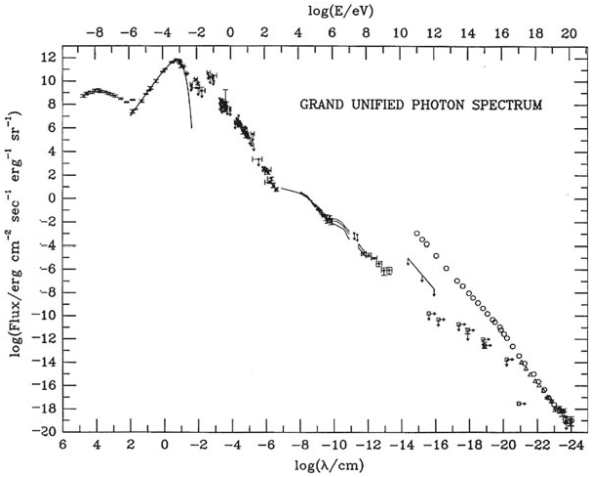

Figure 1.6: Spectrum of photons. From [Ressell and Turner, 1990]

Bremsstrahlung

Bremsstrahlung is the process in which a relativistic charged particle, typically an electron, is decelerated by the Coulomb fields of atomic nuclei, emitting gamma rays as it moves along its trajectory. The characteristic spectrum of bremsstrahlung is proportional to 1/E, where E is the energy of the emitted photon. The radiation length of the material X_0 is the characteristic amount of matter traversed, defined as the mean distance to be crossed in the material by the electron to reduce its energy of a quantity $1/e$. The radiation length X_0 is inversely proportional to the density of the material and atomic number.

This process is common in environments with high electron densities, such as supernova remnants and active galactic nuclei.

Synchrotron radiation

When a charged particle is bent into a circular orbit by a magnetic field, it radiates part of its energy as electromagnetic radiation, known as synchrotron radiation. Magnetic fields are present everywhere in astrophysical environments, where charged particles move in a helical motion around magnetic field lines. As they spiral, they emit synchrotron radiation, which can be used for tracing the distribution of high-energy particles and magnetic fields in these environments. This mechanism is responsible for the radio emissions observed in supernova remnants and extragalactic radio sources (see section 1.2). The energy loss rate for ultra-relativistic electrons due to synchrotron

radiation can be expressed as:

$$\frac{dE}{dt} = -\frac{e^4 B_\perp^2}{6\pi\epsilon_0 c m^2}\beta^2\gamma^2 \tag{1.4}$$

where e is the electron charge, $B_\perp$ is the component of the magnetic field perpendicular to the electron velocity, ϵ_0 is the permittivity of the free space, c is the speed of the light, $\beta = v/c$ an γ is the Lorentz factor and m is the electron mass [De Angelis and Pimenta, 2018].

The radiation spans over a wide range of the electromagnetic spectrum and, for very strong fields, it is produced in the gamma region.

This process dominates in environments with intense magnetic fields, such as the jets of AGN, Pulsar Wind Nebulae (PWNe), and other regions with high-energy electrons. In these environments, synchrotron radiation not only serves as a probe of particle acceleration but also indicates the strength and structure of magnetic fields, making it essential for understanding high-energy astrophysical phenomena.

Inverse Compton scattering

The Inverse Compton scattering is the process in which, relativistic electrons in cosmic rays up-scatter low-energy photons, such as stellar radiation or the cosmic microwave background (CMB), into the gamma-ray region of the electromagnetic spectrum. This process is crucial in environments with intense radiation fields, such as the vicinity of black holes, SNRs, and PWN, where energetic electrons and strong photon fields coexist.

Synchrotron Self-Compton

The self-synchrotron Compton (SSC) mechanism is a two-steps process in which a ultra-relativistic electron accelerated in a magnetic field generates synchrotron X-ray photons that in turn interact via Compton scattering with their own parent electron.

A useful approximate relation for the energy of the Comptonised photon is given by:

$$E_\gamma \simeq 6.5 \left(\frac{E_e}{\mathrm{TeV}}\right)^2 \left(\frac{\eta}{\mathrm{meV}}\right) \mathrm{GeV} \tag{1.5}$$

where E_γ is the energy of the scattered photon, E_e is the energy of the parent electron, and η is the energy of the seed photon [De Angelis and Pimenta, 2018]. This relation shows that low-energy photons can be boosted to GeV or even TeV energies, depending on the energy of the electron population. The SSC mechanism is crucial in modeling the

broadband emission from jets emitted by astrophysical objects and other high-energy environments. It requires environments where ultra-relativistic electrons are present, such as AGN or pulsar wind nebulae.

Hadronic interactions

Gamma-ray photons can also be the result of hadron decay processes. In particular, cosmic-ray protons can scatter particles of the interstellar gas producing neutral pions (π^0). These decay into pairs of gamma rays in times of the order of $\sim 10^{-16}$ s. This process is a significant source of gamma rays in high-density regions such as dense molecular clouds where such collisions are frequent.

1.2 High-energy processes in the Universe

1.2.1 Diffuse gamma-ray emission

The sky image shown in figure 1.5 is dominated by the emission of gamma-rays in the equatorial region. This is known as the Diffuse Galactic Emission (DGE), a continuum background signal produced in our Galaxy by interactions of CRs and Interstellar medium (ISM) and by IC scattering of interstellar soft photons from CR electrons.

The DGE also includes a fainter isotropic component of extragalactic origin, the isotropic gamma-ray background (IGRB) consisting of the sum of emissions from unresolved extragalactic sources and a residual Galactic foregrounds that are approximately isotropic [Ackermann et al., 2015].

Identifying the emission due to CR interactions with the ISM will enable the study of the CR distribution. This is an important physics goal of current experiments in order to better understand the origin and propagation of CRs.

1.2.2 Pulsars

Pulsars are rapidly-rotating neutron stars formed in the supernova explosion of massive star collapses characterized by strong magnetic, electric, and gravitational fields. During the parent star collapse, the angular momentum is conserved implying a very high rotation speed [Manchester and Taylor, 1977].

They were discovered as objects producing very stable periodic radio pulses with very short periods. This radio pulse is assumed to originate from beams of radio emission along the magnetic axis that is oriented at an angle with respect to the

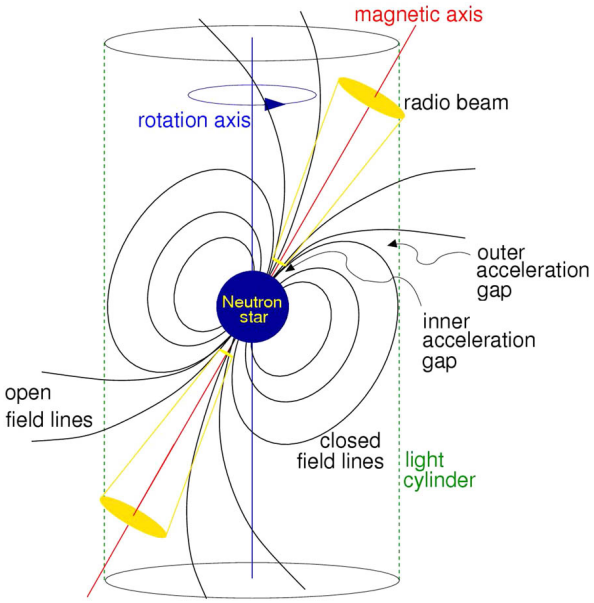

Figure 1.7: Sketch of the magnetic dipole model of a pulsar. The magnetic axis is inclined to the rotation axis. The beam of radiation at the magnetic poles gives rise to pulses as the star rotates due to the misalignment of the magnetic and spin axis [Lorimer and Kramer, 2004].

rotation axis as sketched in figure 1.7. The acceleration processes take place in a very complex magnetosphere. Near the surface of the neutron star, the magnetic field co-rotates with it at a high angular velocity Ω, generating an extremely strong electric potential along the magnetic poles. The induced electric field is so strong that the kinetic energies of charged particles in the outermost layers of the star surface exceed the work function of the surface material. This results in a fully conducting co-rotating plasma surrounding the NS called pulsar wind [Goldreich and Julian, 1969].

The magnetic field and charge distribution of the NS is sketched in figure 1.8 for the very simple case in which the magnetic dipole axis and the rotation axis are antiparallel [Ruderman and Sutherland, 1975].

A particle at a distance R from the rotation axis moves with a velocity $v = \Omega R$. The light cylinder is defined as the cylinder with radius equal to the maximum distance at which co-rotation is possible, i.e., the distance at which the rotation velocity equals the speed of light, $r_c = c/\Omega$. Inside the light cylinder field lines are almost those of a magnetic dipole, while field lines that cross the light cylinder are open. Particles tied to closed field lines co-rotate with the star and form the magnetosphere while particle tied to open lines can escape from the magnetosphere.

The polar cap is defined as the region delimited by field lines tangential to the light cylinder. This region is important for modeling the radio emission of the pulsar.

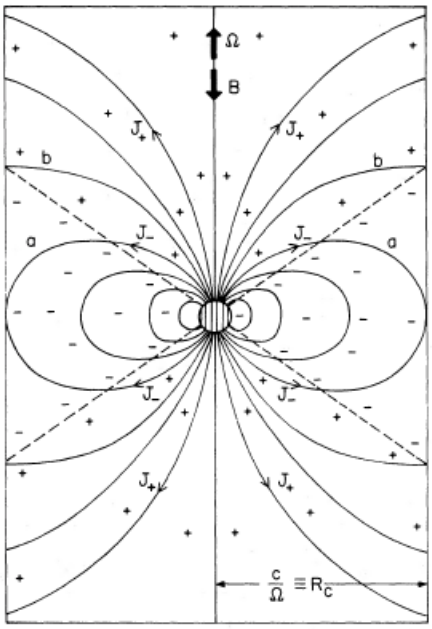

Figure 1.8: Sketch of the pulsar magnetosphere with antiparallel rotation and magnetic dipole axis. Line a is the last field line to close within the light cylinder [Ruderman and Sutherland, 1975].

Different theoretical models try to explain the emission of high-energy photons and particles in the magnetosphere of the NS. In figure 1.8 we see the presence of an inner and an outer acceleration gaps. These are the probable regions where charged particles are accelerated to very high energies and emit curvature radiation. These photons are enough energetic to produce an electron-positron pair in their interaction with the strong electromagnetic field close to the NS. These electrons and positrons emit high energy photons which produce more electron–positron pairs, creating a cascade effect. Pulsar light curves and emission spectra strongly depend on the emission region. Studying these curves can help in discriminating among the emission models.

The number of detected pulsars has grown with the 4th Source Catalog of the Fermi LAT [Smith et al., 2023] to more than 300. The spectra observed for these sources disfavors polar cap models [Abdo et al., 2010]. Various geometric models have been constructed to reproduce the observed behavior of light curves.

1.2.3 Supernovae and Supernova Remnants (SNRs)

At the end of the evolution of massive stars, a violent explosion defined as Supernova (SN) occurs. It consists of an extremely energetic explosion of the star with the ejection of its outer layer at high velocity, originating an expanding shell: the supernova remnant (SNR).

SNRs are believed to be primary sources of galactic cosmic rays. The shock wave originating in the Supernova explosion is a source of acceleration for charged particles up to hundreds of TeV or even PeV during the expansion in the interstellar medium. Gamma rays are then produced from the interaction of the accelerated protons, electrons and nuclei with the SNR environment.

Studies of SNRs offer insights into the ongoing processes of particle acceleration and the interactions of shock waves with the interstellar medium.

There are three types of SNRs: shell-type, pulsar wind nebulae (PWN), and composite, i.e. a shell-type SNR containing a PWN [De Angelis and Pimenta, 2018].

In shell SNRs the shock-wave from the SN explosion propagates outward, heating up and compressing the ISM producing a hot shell. The shell consists of the shock wave interacting with the ISM and is observable through the emission of electromagnetic radiation at different wavelengths.

When the collapse of the parent star in the SN explosion results in a Neutron Star (NS), the remnant consists of a rapidly rotating pulsar. A large part of the energy lost during the pulsar's slowdown is deposited into the wind of relativistic charged particles emitted by the NS. The interaction of the pulsar wind with the ISM surrounding the NS gives rise to a shock wave in which a large fraction of the initial magnetic energy of the wind is converted into particle energy. The processes involved are still poorly understood, but the Fermi mechanism and the magnetic re-connection are good candidates. The observation of these sources is a unique tool for understanding these acceleration phenomena. After the shock, the plasma mainly consists of electron-positron pairs that emit synchrotron radiation interacting with the nebula magnetic field and produce gamma rays throughout IC on low energy photons from CMB or local thermal emission [Mitchell and Gelfand, 2022].

1.2.4 Gamma ray Bursts (GRBs)

Gamma-ray bursts (GRBs) are the most energetic gamma-ray sources observed in the Universe. They are transient events consisting in a burst of gamma-ray photons, with a highly variable duration from fractions of a second to a few minutes. They are characterized by spectral emission and temporal profile significantly different between individual GRBs, which makes it difficult to categorize their morphologies [Fishman and Meegan, 1995].

They were accidentally discovered by the USA Vela satellites in 1967 and confirmed by many following space missions [Piran, 1999]. Because of the poor resolution of gamma-ray detectors used for tens of years since the first discovery, no GRB had ever

been associated to known counterparts, neither a possible host had ever been identified [Klebesadel et al., 1973]. First models adopted for GRBs assumed an isotropic emission from a galactic source. The extra-galactic origin would have implied an excessively large energy emission from a very small volume in the very reduced time.

From subsequent observations made with an increased sensitivity by the instrument BATSE, onboard the CGRO (Compton Gamma Ray Observatories) [Kniffen et al., 1991], an almost isotropic distribution of GRBs in the space was observed excluding almost all the possibilities of a Galactic origin that would produce a distribution concentrated over the galactic plane [Briggs et al., 1996].

BATSE data allowed also to classify GRBs in two classes, with short duration (< 2 s) and hard spectrum (SGRBs) and with long duration and soft spectrum (LGRBs) [Kouveliotou et al., 1993]. The separation between the two categories is not definite and there is some overlap, but this difference suggests two separate classes of progenitors.

Only in 1997 the Italian satellite Beppo-SAX (see [Boella et al., 1997]) allowed to precisely measure the coordinates of a burst, confirming that these bursts were generated in far galaxies. The localization followed the discovery of the afterglow [Costa et al., 1997].

There are two distinct phases in the emission: an initial burst of high energy photons, named prompt emission, and the afterglow, a long-lasting multi-wavelength emission that occurs after the first burst. The localization was hence made by means of a multi-waveband observation of the objects: after detecting a GRB, the satellite pointed its X-ray detector and collected a dissolving emission. Further observations with terrestrial telescopes identified a faint optical counterpart: a delayed dissolving emission of longer wavelength radiation constituting the afterglow. When the gamma ray emission disappeared, it was possible to collect optical images of the source and identify the very far galaxy that hosted the event [van Paradijs et al., 1997]. The LGRB was associated to a SN explosion, SN1998bw, with peak luminosities up to 10^{52} erg^{-1} [Galama et al., 1998].

Plausible model of GRBs proposed to associate them with SNe and NS mergers. A first model assume that the emission is produced by a collimated conical $e^+e^-\gamma$ fireball formed in the vicinity of a massive NS or black hole (BH) by neutrino-antineutrino annihilation [Rees and Meszaros, 1992]. An alternative model, the cannonball model, suggested, instead, that the emission is produced by jets of highly relativistic plasmoids of ordinary matter (cannonballs) launched from the core of the exploding SN or following mass accretion in compact binaries [Shaviv and Dar, 1995]. Both the hypothesies have been supported by the observation of a significant asymmetry in

the explosion of a supernova similar to the few ones clearly identified as counterparts of a gamma-ray burst from cosmological distance.

The afterglow is predicted by the fireball model to originate from the shock produced from the collision of the blast wave from the explosion with the surrounding interstellar medium. The resulting afterglows at progressively lower wavelengths (X-ray, optical, radio) is due to the expansion of shock wave slowing down and losing energy. X-ray afterglows have been observed for all GRBs, but only a half of GRBs also exhibit afterglows at optical and radio wavelengths.

Although SGRBs are always of extragalactic origin, they are less luminous than long GRBs. In addition, they appear less collimated or, in some cases, not collimated at all and less energetic than the long ones.

Progenitors of the short GRBs have not yet been identified, but it is believed that they may originate from the fusion of NS-NS or NS-BH in close binary systems. This is supported by recent observations of a GRB in the NS-NS merger associated to the gravitational wave signal GW1708171 [Abbott et al., 2016] [Goldstein et al., 2017].

Both classes of GRBs provide insights into the Universe's most extreme environments and processes. Furthermore, the afterglows serve as a source of information on the interaction between emission and acceleration processes involved in these events.

1.2.5 Active Galactic Nuclei (AGNs)

AGNs are among the most numerous gamma-ray sources observed to date. An AGN is a compact region at the center of a galaxy that is a strong emitter in a broad band of the electromagnetic spectrum. The emission has been observed in the radio, microwave, infrared, optical, ultra-violet, X-ray and gamma-ray wavebands [Padovani et al., 2017].

The current AGN unified model describes these objects as galaxies whose nucleus is a supermassive BH with a mass in the range of $10^4 - 10^{10}$ $M_\odot$ [Beckmann and Shrader, 2013]. Due to angular momentum conservation, the matter falling into the BH forms an accretion disk surrounding it. Friction heats the matter and changes its status into a plasma, and such moving charged material produces a strong magnetic field . The black hole spinning around its axis in this variable magnetic field generates a high potential difference between its equator and the poles, inducing an electric current which can transfer energy to the surrounding ionized gas. In this way bipolar jets of relativistic charged particles collimated along the spin axis are ejected from the nucleus. The charged particles in these jets moving in the magnetic field produce large amounts both of synchrotron radiation and of thermal radiation.

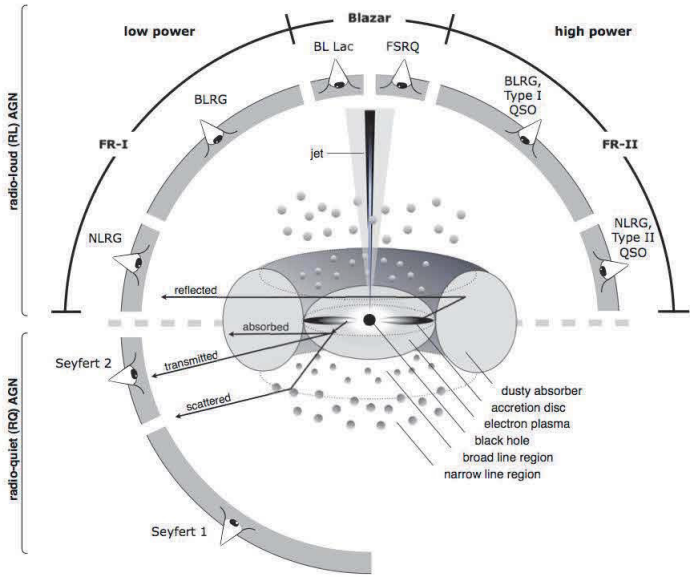

Figure 1.9: Sketch of the unified AGN model[Beckmann and Shrader, 2012].

AGNs are classified in radio-quiet and radio-loud depending on whether they are observed or not in radio. In figure 1.9 a scheme of the AGN unified model is illustrated [Beckmann and Shrader, 2012].

The radio-quiet AGNs are Seyfert galaxies, almost nearby objects with a modest luminosity. The emission spectra of these galaxies are characterized by strong optical emission lines. Historically they have been divided into types I and II. Differently from Seyfert II, Seyfert I galaxies show strong broad emission lines and a strong low-energy X-ray emission. In the current model Seyfert II are the obscured versions of the Seyfert I [Antonucci, 1993].

Radio-loud AGNs are quasars. They always show strong optical continuum emission, X-ray continuum emission, and broad and narrow optical emission lines but are characterized by a jet emission.

The unification scheme of AGN aims to explain the different characteristics observed in various types of AGN using two main parameters, the orientation of the AGN with respect to the line of sight, and the radio loudness. The first one determines the detectability of the central engine and the broad line region in the optical domain, the latter one indicates whether or not the AGN produces a significant jet [Beckmann and Shrader, 2013].

1.3 Detection technologies

Particle detectors are used to identify, measure position, momentum, and kinetic energy of particles. Depending on the interaction between the particles and the detector material, different types of detectors are required.

When radiation passes through the detector, it interacts with the material constituting the detector and deposits a fraction or all of its energy. If the material of the detector is *active*, meaning it responds to these interactions, it is possible to measure the energy deposited by the particle during the interaction or to count the rate of interaction events.

A *tracker* is a detector designed to measure the interaction point of particles as they cross the detector and to reconstruct the particle's path (or track) by measuring a series of discrete points where the particle interacted with the detector material. These points are known as hits. As the particle moves through the detector, it ionizes or excites the material, and the active components of the detector (e.g., silicon strips, scintillating fibers) produce an information on the interaction points. By mapping such hits, the detector reconstructs the path of the particle. If the tracker is placed in a magnetic field it can be capable of measuring the momentum of charged particles. In fact, by measuring the curvature of the track in the known magnetic field it is possible to obtain the momentum which is related to the radius of curvature since $v \propto RB_{\perp}$ [De Angelis and Pimenta, 2018].

Various tracker technologies have been developed each one with specific advantages depending on the requirements of the experiment. The latest systems are Silicon-based Trackers, consisting of Silicon strip or pixel devices that convert the information of the passage of ionizing radiation into a current pulse. They are characterized by an excellent spatial resolution (that can reach the order of few 10µm) that strictly depends on their segmentation (the pitch of pixels or strips), making them suitable for high-precision measurements [De Angelis and Pimenta, 2018]. Other systems include gaseous detectors (e.g. Drift Chamber) in which the signal is produced by drift ion pairs generated as a consequence of the gas ionization, scintillating detectors, in which the energy deposited by incident radiation results in the emission of optical photons that can be readout by a photosensor. In section 1.3.4 a brief review will address the operating principles and characteristics of scintillators.

Detectors that measure the energy of the particle are defined *calorimeters*. They are designed with dense absorbing materials in which particles deposit almost completely their energy thorough a series of interactions that result in an (ideally) contained electromagnetic (EM) or hadronic shower. They are generally categorized

into two types based on the type of particle interactions they are designed to measure: *Electromagnetic Calorimeter* and *Hadronic Calorimeters* [Knoll, 2010]. *Electromagnetic Calorimeters* are designed to measure the total energy of electrons and photons by total absorption. They can be "homogeneous", if the detector consists of a full active volume that completely absorbs the electromagnetic shower, or "sampling", consisting of an active medium which generates a signal and a passive medium which acts as an absorber. *Hadronic Calorimeters* are designed to measure the energy of hadronic showers initiated by inelastic strong interactions of highly-energetic charged or neutral hadrons with atomic nuclei. These interactions result in the production of secondary particles, which drive the development of the shower.

Some detectors combine tracking and calorimetry in a single system, allowing for simultaneous measurement of both the particle's trajectory and energy. This is especially useful in high-energy physics experiments, where precise energy and momentum measurements are needed for particle identification.

The choice of the proper technology depends on the experiment requirements. In particular, for space-based experiments, a number of constrains as the limited material budget and power consumption, and the critical working condition, such as extreme temperatures, intense vibrations and vacuum, the radiation damage, impose a number of restrictions on the allowed technology. Materials need to be lightweight, radiation-resistant, and capable of operating autonomously over long periods.

In this section the main radiation-material interaction processes will be briefly introduced, then I will summarize the main processes by which radiation interacts with matter, the technologies used for detectors in space-based experiments and the main experiments on-board satellite to date.

1.3.1 High-energy photon interactions

Gamma-ray detection is based on the interaction of the photon with the matter of the detector through three main processes, i.e. photoelectric absorption, Compton scattering and electron–positron pair production.

Figure 1.10 shows the total cross-section and partial cross-sections of photon-matter interaction as a function of energy in carbon and lead. The partial cross-sections correspond to the following processes: photoelectric effect ($\sigma_{p.e.}$), coherent scattering ($\sigma_{Rayleigh}$), Compton scattering ($\sigma_{Compton}$), pair production in the field of the nucleus (σ_{nuc}), pair production in the field of the electrons (κ_e), and the giant dipole resonance [1]($\sigma_{g.d.r.}$). For energy below 100 keV photoelectric effect is the leading process, in

[1]The giant dipole resonance is a collective excitation of atomic nuclei observed as a large, high-

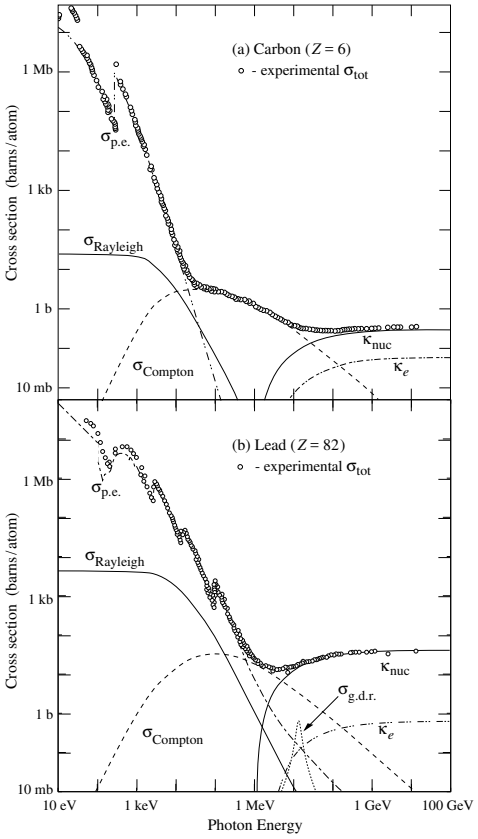

Figure 1.10: Photon total cross sections(circles) and partial cross-sections (lines) as a function of energy in carbon and lead [Navas et al., 2024].

the energy range between 100 keV and a few MeV Compton scattering becomes the dominant process, at higher energies electron-positron pair production dominates.

Photoelectric Absorption

Photoelectric absorption is the dominant process for photons with energies below the electron mass energy, $E_\gamma < m_e c^2$. When the photon energy is larger than the binding energy of the electron in the atomic shell of the detector material E_b, the photon is completely absorbed by the atom and a photo-electron is ejected from that shell with energy:

$$E_{PE} = E_\gamma - E_b$$

The most likely origin of the photo-electron emission is the K shell of the atom. The ejection of the electron from its parent shell creates a vacancy in that shell, which is filled by an electron from another shell, resulting in the emission of characteristic X-ray photon. The cross section of photoelectric absorption is proportional to Z^p with index p in the range between 4 and 5 depending on the photon energy. Therefore a gamma-ray detectors exploiting photoelectric effect should be made of high-Z materials [Knoll, 2010].

The photoelectric effect can be used for detecting photons below the MeV. The sensor will detect the photoelectron measuring its energy.

Compton scattering

The Compton scattering is the process in which a high-energy photon collides with an atomic electron, assumed to be at rest. The photon transfers a fraction of its energy and momentum to the electron. As a result of the interaction the photon is scattered at an angle θ with respect to the incident direction with a lower energy $E'_\gamma = h\nu'$:

$$E'_\gamma = \frac{E_\gamma}{1 + \frac{E_\gamma}{m_0 c^2}(1 - \cos\theta)}$$

where $E_\gamma = h\nu$ is the incident photon energy and $m_0 c^2$ is the rest mass of the electron [Knoll, 2010]. The differential cross section for Compton scattering is given by the Klein-Nishina formula:

$$\frac{d\sigma_C}{d\Omega} = \frac{r_e^2}{2}\left(\frac{E'_\gamma}{E_\gamma}\right)^2\left(\frac{E_\gamma}{E'_\gamma} + \frac{E'_\gamma}{E_\gamma} - \sin^2\theta\right) \tag{1.6}$$

energy peak in the cross sections of photo-nuclear reactions [Goldhaber and Teller, 1948].

where r_e is the classical electron radius [Klein and Nishina, 1929].

As in the case of the photoelectric effect, it is the ejected electron to be detected by an appropriate sensor.

Pair Production

For energies above than $2m_ec^2$, a pair production process can take place. It is a process of interaction of the photon with the nucleus of the atom that produces an electron-positron pair with the nucleus absorbing some of the energy or momentum that cannot be both conserved in vacuum.

Close to the threshold of the process, $2m_ec^2$, the probability for pair production is small but it rises sharply with energy and becomes the dominant effect for photon energies above few tens of MeV. All the photon energy exceeding the energy required to create the pair is equally shared in kinetic energy of the pair. The cross section grows reach an asymptotic value at some 100 MeV:

$$\sigma = \frac{7}{9}\frac{1}{n_a X_0} \tag{1.7}$$

with n_a the density of atomic nuclei per unit volume, and X_0 the radiation length [De Angelis and Pimenta, 2018].

1.3.2 Electronic energy loss by charged particles

Charged particles interact with the material of the detector mainly through Coulomb interaction. The interaction results in the transfer of a fraction of the energy of the charged particle to the atoms (molecules) of the medium, with the excitation or the ionization of the latter. As a consequence the charged particle is slowed down. When the particle passes through the detector, it interacts simultaneously and repeatedly with a large number of atoms, transferring only a small portion of its energy. Hence the effect is a continuous decrease of the particle energy. The differential energy loss of the charged particle within the material divided by the corresponding differential path length along the particle track is described by the Bethe formula:

$$\langle -\frac{dE}{dx} \rangle = K z^2 \frac{Z}{A}\frac{1}{\beta^2}\left[\frac{1}{2}\ln\frac{2m_ec^2\beta^2\gamma^2 W_{max}}{I^2} - \beta^2 - \frac{\delta(\beta\gamma)}{2}\right] \tag{1.8}$$

where $K = 4\pi N_A r_e m_e c^2$ with N_A Avogadro's number and r_e and m_e classical electron radius and electron mass respectively, ze is the charge of the incident particle, A and Z are the atomic mass and atomic number of the medium, I represents the mean

excitation energy of the detector and W_{max} is the maximum possible energy transfer to a recoil electron in a single collision [Navas et al., 2024]. It can be noticed that for non-relativistic particles the energy release is proportional to $\frac{1}{\beta^\alpha}$ where $\alpha \approx 1.7 - 1.5$ and to z^2 of the charged particle but also to Z of the detector material. For very high energies and for high density material the corrective term δ has to be included in the formula to justify the relativistic rise at high energy visible in figure 1.11. It represents the specific ionization energy loss for different charged particles in different material. It can be noticed that all the curves have a minimum corresponding to an energy deposit of about $2\,\mathrm{MeVcm^2g^{-1}}$. Particles with these energies are known as minimum ionizing particles (MIPs) [Knoll, 2010].

The probability distribution of energy loss by a charged particle in a thin layer of material is described by the Landau distribution [Landau, 1944]:

$$L(x) = \frac{1}{2\pi i} \int_{a-\infty}^{a+\infty} e^{s \log s + xs} ds \tag{1.9}$$

The distribution function for the energy deposit by 500 GeV pions crossing silicon of different thickness is shown in figure 1.12. The average energy loss, represented by the Bethe formula, is larger than the most probable energy loss and is independent on the the thickness of the material crossed. For very thick absorbers the distribution is less skewed but never approaches a Gaussian [Navas et al., 2024].

1.3.3 Electron interaction

The Bethe-Bloch formula is not adequate for describing the electron energy loss in the material. This is due to the fact that the mass of the impinging electron is the same as the mass of the orbital electron with which it interacts. Hence, in each collision, the interaction can produce a much larger deviation and a greater energy loss. In addition electrons can lose energy also because of radiative processes such as bremsstrahlung.

The total energy loss, hence is the sum of collisional and radiative losses:

$$\frac{dE}{dx} = \left(\frac{dE}{dx}\right)_c + \left(\frac{dE}{dx}\right)_r \tag{1.10}$$

where:

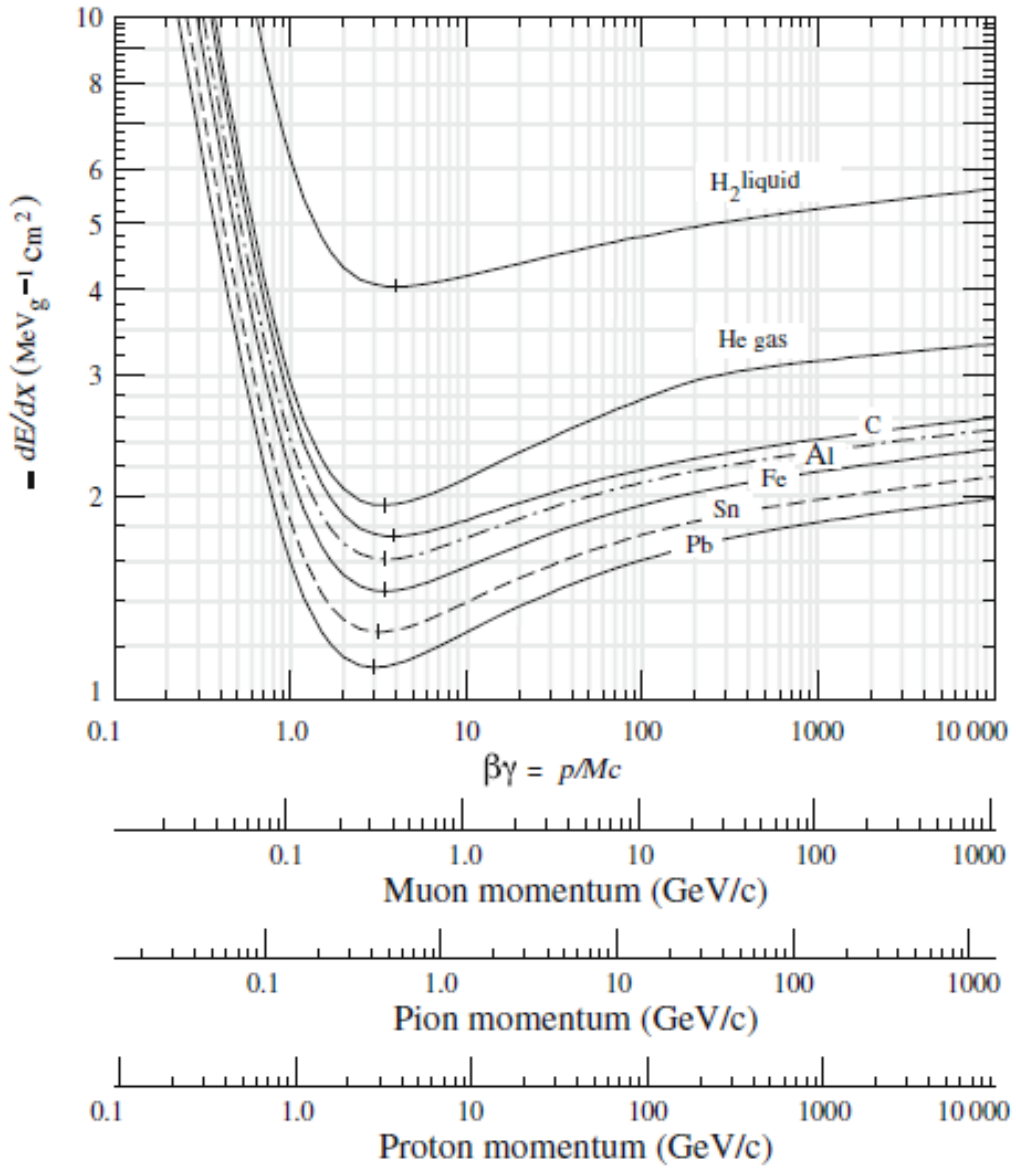

Figure 1.11: Specific ionization energy loss for muons, pions, and protons in different materials [Navas et al., 2024]

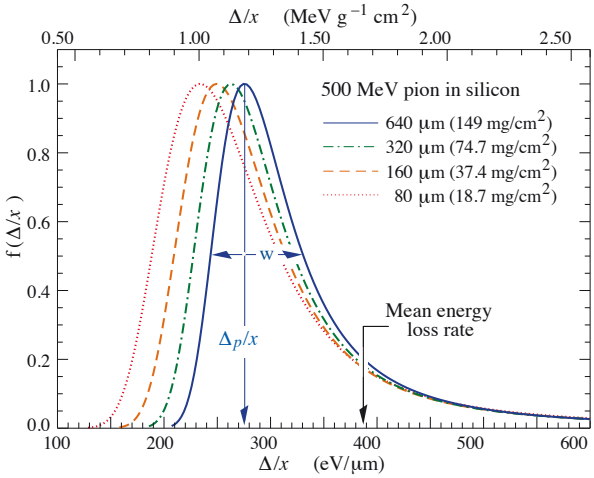

Figure 1.12: Distribution of the energy loss in silicon for 500 MeV pions, normalized to unity at the most probable value. W is the full width at half maximum [Navas et al., 2024]

$$-\left(\frac{dE}{dx}\right)_c = \frac{2\pi e^4 NZ}{m_e v^2}\left(\ln\frac{m_e v^2 E}{2I^2(1-\beta^2)} - \ln 2\left(2\sqrt{1-\beta^2} - 1 + \beta^2\right) + (1-\beta^2) + \frac{1}{8}\left(1-\sqrt{1-\beta^2}\right)^2\right)$$

$$-\left(\frac{dE}{dx}\right)_r = \frac{NEZ(Z+1)e^4\alpha}{m_e^2 c^4}\left(4\ln\frac{2E}{m_e c} - \frac{4}{3}\right) \tag{1.11}$$

with $\beta = \frac{v}{c}$ and α fine-structure constant [Knoll, 2010]. The factors E and Z^2 show that radiative losses are important for high electron energies and for absorber materials of large atomic number.

1.3.4 Scintillators

A scintillator is an absorbing material with the property to convert a fraction of the energy released by the ionizing radiation into light. When radiation passes through the scintillator, it interacts with the material through the processes described in the previous sections (1.3.1, 1.3.2, 1.3.3) transferring energy to the material. Only a small fraction of the deposited energy is converted into scintillation light. Scintillation efficiency is the ratio between the deposited energy and the energy emitted in the form of light. This is of the order of a few percent. The remaining energy is dissipated in the form of non-radiative processes known as quenching processes. The number of scintillating photons produced per MeV of energy deposited in the material is defined

light yield. An important requirement of scintillators is the transparency to their own emitted light [Navas et al., 2024].

Scintillators are among the cheapest detectors and are widely used in particle detection. In particular, they can be used in hodoscope configuration as tracking devices.

Scintillating materials are divided into two main groups: organic and inorganic. Inorganic scintillators are generally characterized by a larger light yield, of the order of 10^4 photons per MeV, compared to organics. Organics have very small signal formation times of few nanoseconds, and quite fast decay time from few to tens of nanoseconds. For this reasons they are detectors particularly well-suited for trigger applications. Inorganic scintillators instead are characterized by a higher density a larger atomic number with respect to organics and this make them suitable for applications requiring high conversion efficiency such as in gamma-ray detectors [Knoll, 2010].

The light produced by the scintillator needs to be converted in an electrical signal, by a proper photo-sensor coupled to the detector. Only a fraction of the produced light will directly reach the surface were the photo-sensor is located. The rest undergoes multiple reflections on the detector surfaces. The critical angle is defined as

$$\theta_c = \arcsin \frac{n_1}{n_0} \tag{1.12}$$

where n_0 and n_1 are the refractive indexes respectively of the detector material and the surrounding material [Knoll, 2010]. If the angle of incidence of the photon on the surface of the scintillator is larger than θ_c there is total internal reflection otherwise if the incidence angle is less than θ_c there is Fresnel reflection and partial transmission. It is important therefore to maximize the total internal reflection at all the surfaces with the exception of those coupled to the photo-detector where an opportune optical grease should be used to optically couple the scintillator with the photo-detector.

Organic scintillators

Organic scintillators are aromatic hydrocarbon compounds, where the scintillation processes are due to the specific molecular structure of energy levels. Figure 1.13 shows the $\pi - electron$ structure [Kolanoski and Wermes, 2020] where multiple singlet and triplet states are available for the excited configuration. The energy spacing between highly excited level is small, and hence molecules in these states are rapidly de-excited to the first excited singlet level, S_1 with non-radiative internal conversion. The S_1 level is approximately $3 - 4$ eV above the ground state and has a lifetime of few nanoseconds. Therefore, the result of energy deposition by ionizing radiation is a

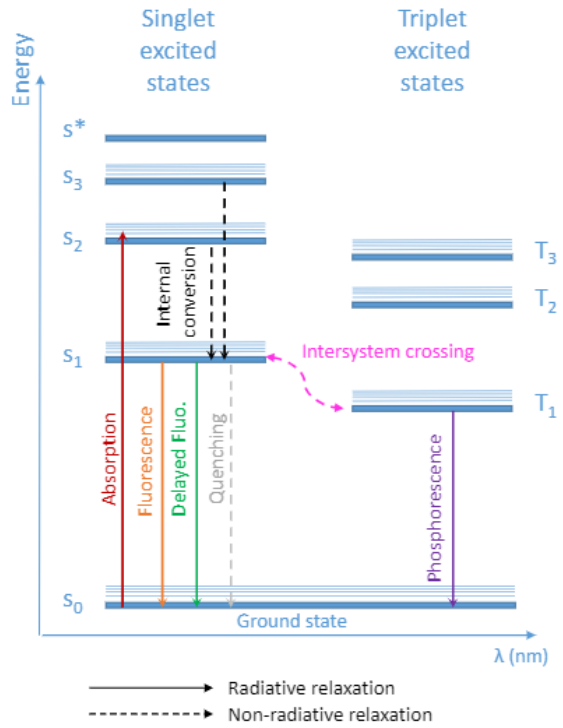

Figure 1.13: Schematic of scintillation mechanism in organic scintillator from [Kolanoski and Wermes, 2020]

number of excited molecules in the excited singlet level S_1 that promptly de-excite to the ground state S_0, emitting fluorescence light with a decay time of the order of nanoseconds. Phosphorescence emission occurs due to de-excitation involving triplet states. In this case, the decay time is of the order of few milliseconds and the wavelength is longer because the triplet state T_1 has a lower energy compared to S_1. Delayed fluorescence, on the other hand, is due to a fraction of molecules in the triplet state that are thermally re-excited to the singlet state S_1 and then de-excite to the ground level through fluorescence emission.

Organic scintillators are characterized by a good transparency to their scintillation emission. This is due to the Stokes shift between the optical absorption and the emission spectra due to the energy level structure. In organic scintillators the quenching consists of all the non-radiative de-excitation modes available in which energy is dissipated in the form of lattice vibrations.

Scintillation efficiency depends on the type and energy of the ionizing radiation. It can be derived from the Birks' formula for the energy emitted per unit path length as

a function of the specific energy loss:

$$\frac{dL}{dx} = \frac{S\frac{dE}{dx}}{1 + kB\frac{dE}{dx}} \tag{1.13}$$

In the previous, S is the scintillation efficiency and the term kB is a parameter related to the quenching effect known as Birks' constant [Birks, 1951]. Both S and kB are derived from experimental data. For MIPs the energy release is small hence the relation 1.13 reduces to:

$$\frac{dL}{dx} = S\frac{dE}{dx} \tag{1.14}$$

Therefore the light output is linearly related to the energy deposited. This is not true for slower particles with high ionization density.

Anthracene and Stilbene are the most widely used pure organic crystalline scintillators. However, since fluorescence in organic scintillators is related to the properties of the molecule, it is possible to dissolve an organic scintillator in an appropriate solvent, obtaining liquid scintillators. If the solvent can be polymerized, it is possible to create plastic scintillators. Liquid scintillators are widely used as detectors in large-scale applications; however, they are sensitive to the presence of water, oxygen or isopropyl alcohol in the solvent, because they reduce the light yield.

Plastic scintillators are of great interest because they are typically made from inexpensive materials that are more durable than crystals and can be easily shaped into a variety of different geometries and sizes. In plastic scintillators the energy is deposited into the polymer and is then transmitted to the luminescent molecules dissolved by means of a non-radiative transmission known as *Forster resonant energy transfer*. In this case, the emission spectrum coincides with that of the scintillator, while the absorption spectrum is primarily that of the solvent. Self-absorption is no longer negligible, so the solvent must be carefully chosen to maximize the separation between the emission and absorption spectra. Common plastic matrices consist of polystyrene (PS) or polyvinyltoluene (PVT) [Navas et al., 2024].

Plastic scintillators find widespread application in high-energy physics experiments. However, they must be handled with care, as the surface is particularly fragile and can develop microcracks which degrade transmission of light by total internal reflection. Moreover, they are susceptible to radiation damage [Kharzheev, 2019]. During irradiation, atomic bonds break, creating *radicals* which absorb light, reducing the light yield of the detector. This is a temporary damage since when the irradiation ends

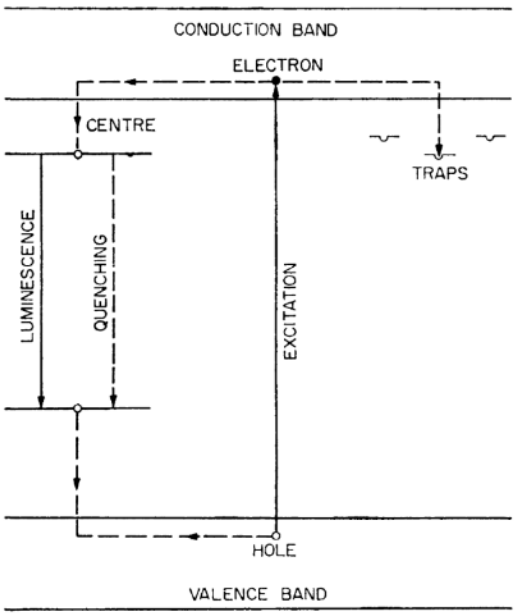

Figure 1.14: Simplified scheme of the mechanisms contributing to the production of scintillation light in inorganic crystals [Birks, 1964]

the bonds can reform.

Plastic scintillators can be fabricated into fibers with diameters of the order of a few hundred microns that find application in tracking detector allowing to reach very small spatial resolution.

Inorganic scintillators

Inorganic scintillators consist of crystalline materials, where the scintillation mechanism is due tho the energy band structure of the crystal lattice. Figure 1.14 shows the energy bands and the three steps of the scintillation mechanism in inorganic scintillators. Electrons in the valence band are bound at lattice sites while electrons in the conduction band are free to move throughout the crystal. The region between the valence and conduction bands is named *forbidden band* because electrons are not allowed to occupy energy levels in this band. The inclusion of a doping impurity properly chosen, the *activator*, creates allowed energy levels in the forbidden band at specific lattice sites, called *luminescent* or *recombination centers* [Knoll, 2010]. When ionizing radiation releases energy in the material, a large number of electrons are excited to the conduction band, leaving the same number of holes in the valence band. The hole and electron will migrate in the crystal until they reach a luminescent center. As the ionization energy of the dopant is lower than that of the lattice, a hole can ionize it. At the same time, an electron drifting in conduction band close to the

ionized luminescent center can neutralize it. The result is an activator site in an excited state that rapidly de-excite with the emission of luminescence radiation with a decay time from few tens to hundreds of nanoseconds. Lattice imperfections or impurities can introduce some allowed energy level below the conduction band, acting as "*traps*" from which the transition to the ground-state is forbidden. If the electron falls in these level, it needs additional energy, for example due to thermal excitation, to move back to the conduction band and neutralize an activator. This process generates the slow component of the emission, known as *afterglow*. A quenching process is also possible as radiationless transitions from some excited states to ground state are possible. As for organic scintillators, the emission spectra of inorganic scintillators are shifted to longer wavelenght preventing self-absorption, hence also inorganic scintillators are transparent to the luminescence emission.

The most common inorganic scintillators are Alkali Halides doped with metals, in particular NaI doped with Tl, and CsI doped with Tl or Na. These crystals exhibit a much larger scintillation yield compared to organic scintillators. The decay times can range from hundreds of nanoseconds to few milliseconds making the pulse produced by these detectors much slower if compared to organics [Knoll, 2010].

Fast inorganic scintillators are also employed. This term refers to a category of crystals, mainly rare earth halides and oxides, in which Cerium can be used as the activator. Common examples are rare earth oxyorthosilicates like YSO, GSO, LSO and LYSO. The decay time of Ce excited level is of about few tens of nanoseconds. Also these scintillators are characterized by high density and large Z resulting in a high conversion probability, and an excellent radiation hardness. The light yield is given by:

$$L = 10^6 \frac{SQ}{\beta E_g} \tag{1.15}$$

where E_g is the energy gap in eV, βE_g is the energy required to create an e-h pair, S is the efficiency of energy transfer to the luminescent center and Q is the efficiency of the luminescent center [Navas et al., 2024].

1.3.5 Photo-detectors

Photo-sensors are detectors converting an input light signal into a corresponding output electrical signal. In order to be coupled to scintillating detectors, photo-sensors must be sensitive to very low light intensities, down to a few photons. A photo-sensor absorbs the energy of an impinging photon and emits a photo-electron that undergoes a multiplication process in order to produce an amplified output signal.

The sensitivity of a photo-sensor can be expressed in terms of its *quantum efficiency*

(QE)

$$QE = \frac{n_{p.e}}{n_{ph}} \tag{1.16}$$

where n_{ph} is the number of incident photons and $n_{p.e}$ in the number of photo-electrons produced. Generally the QE is a function of the wavelength [Knoll, 2010]. The conventional approach has been to couple scintillators with photomultiplier tubes (PMTs). However, in recent decades, the development of solid-state photodetectors has led to significant advancements in the use of Silicon Photomultipliers (SiPMs) as alternatives to traditional PMTs.

Photomultiplier tubes

Photomultiplier tubes (PMTs) are photodetectors sensitive to light in the ultraviolet, visible, and near-infrared. A PMT consists of a photocatode, that converts the absorbed photon in a photo-electron by photoelectric effect, a large number of intermediate electrodes called dynodes, each with increasing positive voltage with respect to the previous one, which serve as electron multiplier, and an anode, that collects the electrons and produce the electrical output pulse. The system is sealed in a airtight glass enclosure. PMTs are characterized by a high sensitivity, a fast time response, a large multiplication factor. For a PMT the QE is characteristic of the photocatode material and generally is $\sim 20 - 30\%$ [Knoll, 2010].

Silicon Photomultipliers

Silicon Photomultipliers (SiPMs) are very compact solid-state photo-detectors for direct detection of light across the near-ultraviolet to near-infrared range. They are characterized by excellent sensitivity, high efficiency, significant gain, and robust stability against temperature and voltage fluctuations. Due to its high gain, a SiPM is well-suited for single-photon detection and photon counting applications. The SiPM technology is based on the PIN photodiode, a reverse biased p/n diode in which an impinging photon with energy larger than the band-gap and produces an electron-hole pair. Typical values of the band-gap are comparable with optical photon energies. The device produces an output electrical signal with an intensity proportional to the number of generated charge carriers, and therefore to the number of incident photons. In order to detect signals at intensities as low as a few photons, the photodiode is operated at a bias voltage just below the breakdown threshold (V_{bd}) of the order of few tens of V. This is known as *avalanche mode* and the device is named Avalanche Photo Diode (APD). This configuration ensures that the electron-hole pairs generated by individual photons are rapidly accelerated by the electric field, initiating an avalanche

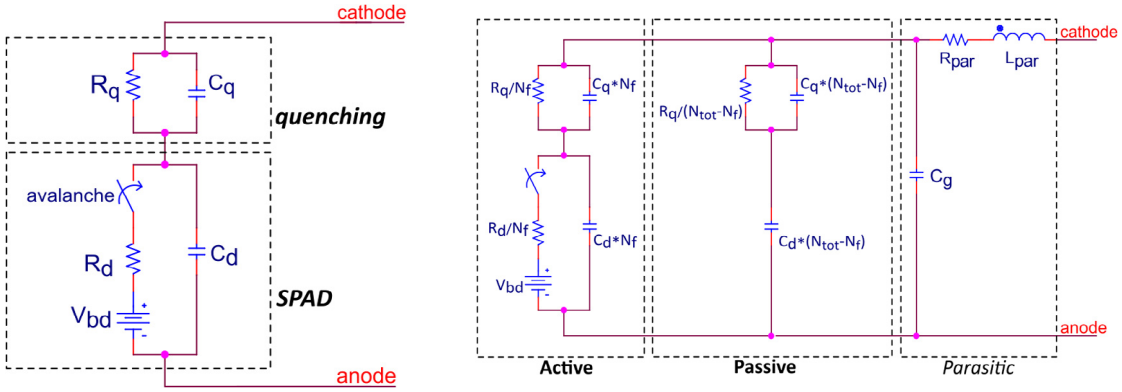

Figure 1.15: Left panel: equivalent electrical circuit of the SPAD with integrated quenching resistor. Right panel: Equivalent circuit of the SiPM, the passive part simulates the not triggered cells [Acerbi and Gundacker, 2019].

multiplication of charge carriers. The proportionality of the output signal with the number of incident photons is preserved. However, the gain of the APD is strongly influenced by temperature and operating voltage, making the detector highly sensitive to fluctuations in these parameters. When the operating point is set beyond the breakdown voltage V_{bd}, the APD operates in *Geiger Mode* (GM-APD). In this mode, the electric field across the junction is so high (in the order of few 10^5 V/cm) that a single charge carrier injected into the depletion layer triggers a self-sustaining avalanche multiplication. In order to interrupt the avalanche, the diode is connected in series with a quenching resistor with a resistance value of the order of few 100kΩ. In this configuration, the multiplication factor is so large that the proportionality between the charge generated by the incident radiation and the signal produced by the detector is lost. However, the high gain enables the detection of even single photons and hence the GM-APD is also named *Single Photon Avalanche Diode* (SPAD) [Knoll, 2010]. Left panel of figure 1.15 shows the equivalent circuit of a SPAD. R_q and C_q represent the quenching resistance and the relative parasitic capacitance; $C_d \sim 100$ pF is the junction capacitance and depends on the surface of the pixel and the thickness of the depletion region; R_d is the very small resistance provided by the silicon substrate ($R_d \ll R_q$) [Gundacker and Heering, 2020].

A SiPM consists of an array of a large number of SPADs connected in parallel. A schematic representation is shown in the right panel of figure 1.15. Each SPAD (or pixel) is a few tens of µm wide and hence the probability of repeatedly hitting the same SPAD is negligible for low intensity radiation, which ensures that each pixel is fired by a single photon, and hence proportionality between light intensity and electrical pulse amplitude is restored. In fact, because of junction saturation, each pixel produce a signal of fixed amplitude. The total output is the sum of

the signals from all the triggered pixels, so it is proportional to the number of photons detected. If the number of incident photon exceeds the number of pixels, the SiPM saturates and the proportionality is lost. The dynamic range is limited by the total number of pixels N_{pix} and the maximum number of detectable photons is $Npe = Npix * (1 - exp(-Nph * PDE/Npix))$ [Acerbi and Gundacker, 2019].

Usually SiPMs work at a *bias voltage* above the breakdown voltage, V_{bd}, of a quantity named overvoltage $V_{ov} \sim$ few V where V_{bd} is characteristic of the SiPM used and generally $V_{bd} < 80$ V . The gain is defined as the ratio between the pixel charge and the electron charge e

$$G = \frac{Q_{SPAD}}{e} \sim 10^5 - 10^6 \tag{1.17}$$

It is linear with the overvoltage i.e. $V_{ov} = V_{bias} - V_{bd}$, the surface of the pixel, and the thickness of the amplification region, which determines the capacitance $C = C_d + C_q$ since $Q_{SPAD} = CV_{ov}$. The output signal is a pulse with an extremely rapid rise time $\tau_{rise} = C_d R_d \sim 0.5$ ns corresponding to the rapid development of the avalanche, and a slower decay time $\tau_{decay} = C_d R_q \sim 30 - 100$ ns.

The Photo-detection efficiency (PDE) of the SiPM has three main contributions, the QE for e-h pair creation, the geometric efficiency or *fill factor* f_A and the triggering probability P, i.e. the probability that a photon initiates an avalanche.

$$PDE = QE \cdot f_A \cdot P \tag{1.18}$$

The PDE is a function of the wavelength of the incident photon and of the V_{ov}.

The primary source of noise in SiPM are dark counts. The dark count rate (DCR) is essentially due to carriers generated by thermal agitation in the sensitive region, known as dark events. The number of dark events is proportional to the bias voltage and to the temperature, approximately doubling every 10 °C. In SiPMs the typical DCR is of the order on $10 - 20$ MHz/cm^2, but arising from a single thermally generated carrier, dark counts are limited to single-photon signals and hence affect SiPM performance mainly for low photon detection. It is therefore fundamental to set a proper threshold on the output signal amplitude in order to discard all dark events. Further noise sources include afterpulsing (AP) and optical crosstalk (OC) and are known as *correlated noise*. The AP is a delayed pulse produced by carriers trapped by impurities within the material during the main avalanche that are succesively releasd and trigger a new avalanche following the tail of the primary event. The OC is due to photons created during the amplification process in a pixel that can reach a neighbor pixel, where they

initiate another avalanche.

SiPMs are characterized by high gain and high PDE, with excellent time resolution (see [Gundacker and Heering, 2020] and [Otte, 2016]). Therefore it is possible to use very low-noise front-end electronics consisting only of preamplifiers, comparators with programmable thresholds, and SiPM bias voltage control. Compared to traditional PMT, SiPMs are much more compact reducing the volume of the instrument. Moreover, at the same gain conditions, SiPMs require an operating voltages of some tens of volts, which is considerably lower than the several thousands of volts required for traditional PMT. These are fundamental requirements for any space-based application. Among the primary challenges associated with the use of SiPMs in space applications are their sensitivity to temperature and radiation. SiPM performance is strongly influenced by temperature variations, with extreme and fluctuating thermal conditions in space affecting critical parameters such as gain, dark count rate, and breakdown voltage. Additionally, SiPMs are prone to gradual degradation over time due to cumulative radiation damage which result in reduced efficiency and overall performance [Zheng et al., 2022].

1.4 Space-Based Observatories

In order to detect gamma rays and low-energy cosmic rays, measurements need to be performed above of the atmosphere of the Earth, which can absorb or scatter the radiation. Space-borne observatories are therefore needed. For very-high-energy cosmic rays, the flux of primary radiation is extremely low, the effective area of satellite-based experiments is insufficient due to the limitations imposed by the material budget of space technologies. In such cases, ground-based detectors are used. These exploit the interaction of CR particles and particles in shower produced by gamma rays, with the atmosphere, causing Cherenkov light emission.

The main interest in this work is on satellite-borne experiment. The typical requirements for these experiments are good energy resolution, good angular resolution.

The first dedicated gamma-ray astronomy mission was Explorer-XI launched in 1961. Over a period of 23 days, it observed 22 events from gamma rays of energy above 50 MeV isotropically distributed, implying some sort of uniform gamma-ray background, as expected from the interaction of cosmic rays with interstellar gas [Kraushaar et al., 1965]. In 1976 the Orbiting Solar Observatory 3 (OSO 3) satellite revealed that the gamma-ray distribution is highly anisotropic, with a more intense emission along the galactic equator and a region of increased intensity extending around the galactic center [Kraushaar et al., 1972]. The most important contribution

to gamma-ray astronomy in the 1960s came from the Vela satellites. They were aimed to the detection of gamma rays from nuclear tests on Earth and recorded flashes of gamma radiation from unknown cosmic sources that were associated to GRBs [Terrell et al., 1982]. In 10 years the Vela satellites observed 73 GRBs.

In the 1970s the Small Astronomy Satellite II (SAS-2) confirmed the diffuse gamma-ray background [Fichtel et al., 1977] and the COS-B ([Bonnardeau, 1977]) satellite produced the first detailed map of the sky at gamma-ray wavelengths and discovered about 25 discrete sources, including the pulsars in the Crab and Vela supernova remnants and the quasar 3C 273. However, the poor resolution of the instruments made impossible to associate most of such point sources with individual objects.

Spatial and temporal resolution of gamma-ray observations were improved with the Compton Gamma Ray Observatory (CGRO) launched in 1991 [Kniffen et al., 1991] and with the Fermi Gamma-ray Space Telescope lunched in 2008. These new observatories produced large amounts of data explaining a number of processes in the Universe.

1.4.1 The Compton Gamma-ray Observatory

The Compton Gamma-ray Observatory (CGRO) was the first gamma-ray observatory launched, in 1991, by NASA with the unique purpose of studying the sky in a broad energy band, from 30 keV to 30 GeV, with improved spectral and spatial resolution compared to all previous flown instruments [Kniffen et al., 1991].

It carried on-board four experiments which mapped the gamma-ray sky in complementary energy bands in order to study steady sources and transient phenomena: the Burst And Transient Source Experiment (BATSE); the Oriented Scintillation Spectrometer Experiment (OSSE); the Imaging Compton Telescope (COMPTEL); and the Energetic Gamma Ray Experiment Telescope (EGRET).

Figure 1.16 shows a sketch of the instruments and the respective energy ranges covered. BATSE was sensitive in the range [20 keV − 20 MeV], OSSE to energies between 50 keV and 10 MeV, COMPTEL was sensitive to photons in energy range [0.8 MeV − 30 MeV], and EGRET to energy from 20 MeV to 30 GeV.

BATSE

The primary purpose of BATSE was the detection and fast localization of GRBs. A near-real-time localization allowed to focus ground-based optical telescopes on the GRB, to detect a possible counterpart of the burst.

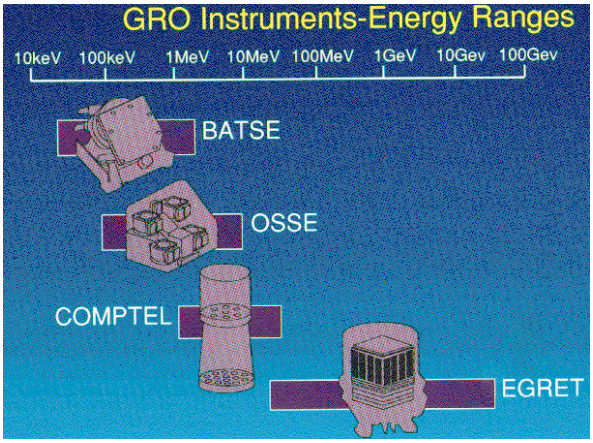

Figure 1.16: The energy regions covered by the four instruments on the CGRO from `http://heasarc.gsfc.nasa.gov/docs/cgro/epo/brochures/compton/bro5.html`.

BATSE consisted of eight detector modules arranged on the corners of the CGRO satellite in order to maximize the field of view of the instrument. Each module consisted of a Large-Area Detector (LAD) and a spectroscopy detector (SD). The LAD was a large flat disk of NaI(Tl) scintillator crystal with a diameter of ~ 50 cm and a thickness of ~ 1.27 cm coupled to a PMT. The detector design was optimized for directionality measurements. The SD detector consisted of a smaller scintillator, 12 cm in diameter and 7 cm thick, optimized to detect photons with good resolution in a broad energy band from 20 keV to 2 MeV.

During its nine-year mission BATSE detected 2704 GRBs with a rate of 0.8 GRBs per day. The map of GRBs detected by BATSE is shown in figure 1.17. From the data collected, BATSE observed an isotropic and homogeneous population of GRBs, proving their extragalactic origin. Furthermore BATSE data allowed the classification of GRBs in short and long ones.

OSSE

The main goal of OSSE was the study of localized sources in the energy range between 50 keV to 10 MeV. It was composed of four independent detectors operating as independent experiments. Each detector was a collimated scintillator consisting of a NaI(Tl) crystal 102 mm thick, optically coupled to a CsI crystal 76 mm thick, coupled to a PMT. A tungsten collimator, located directly above the NaI, defines the gamma-ray aperture of the detector. Both the scintillators and the tungsten collimator are enclosed in a NaI(Tl) annular shield for background rejection. This geometry allowed OSSE to reconstruct the images of individual sources. Generally the 4 detectors were operated in co-axial pairs; while one detector of a pair was observing the source, the

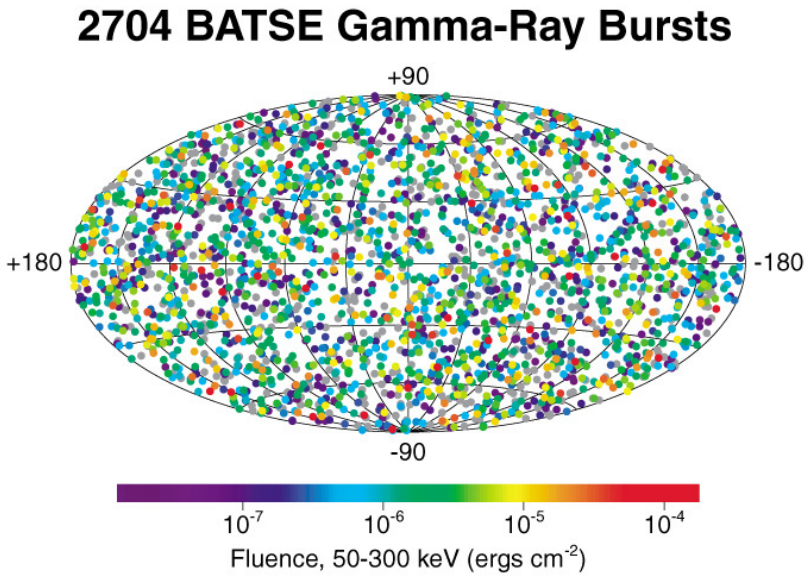

Figure 1.17: Locations of a total of 2704 Gamma-Ray Bursts recorded with BATSE during its nine-year mission. The burst locations are color-coded based on the fluence. Grey is used for bursts for which the fluence cannot be calculated due to incomplete data from `https://heasarc.gsfc.nasa.gov/docs/cgro/batse/`

other detector monitored the background allowing OSSE to detect fainter sources than those observable with BATSE.

During its observations period, OSSE detected many galactic sources including pulsars, neutron stars in binary systems, and black hole candidates. Many of these have been discovered as targets of opportunity following the detection of an outburst by BATSE. The sensitivity of the instrument to gamma-ray lines was exploited for mapping the diffuse galactic continuum emission, searching for evidence of a variable point source of 0.511 MeV line associated with the positron-electron annihilation. This is a very important signature of matter-antimatter annihilation and has been observed in the Galactic center region [Johnson et al., 1993].

COMPTEL

COMPTEL was the first imaging instrument covering the energy band from 0.8 MeV to 30 MeV. It consisted of two detector arrays. An upper detector, using liquid scintillator and a lower one using NaI crystals. Gamma rays were detected by two successive interactions. The incident photon, after interacting through Compton scattering in the liquid scintillator, underwent a second interaction in the downstream crystal scintillator. The locations of the interactions and energy losses in both detectors were measured for recostructing the incident photon direction that, for completely

absorbed photons, lies on the edge of a cone whose axis is the direction of the scattered photon. The sources were located from the intersection of circles generated by detected gamma rays [Schoenfelder et al., 1993].

During its operation period, COMPTEL has detected 63 gamma ray sources: 32 of these are steady sources, such as neutron stars and black hole candidates; the remaining 31 are GRBs. COMPTEL also succeeded in mapping the emission of the diffuse ^{26}Al detecting the 1.8 MeV gamma-ray line from its decay. COMPTEL showed a distribution clearly confined to the galactic plane. Source of ^{26}Al are assumed to be novae, supernovae or young massive stars. Since the galactic distribution of these potential sources is known, imaging of the line emission in the galaxy sets some constraints on the different source models.

EGRET

EGRET was the experiment on CGRO studying the highest gamma-ray energy window. It was sensitive to photons in the energy range from 20 MeV to 30 GeV and made detailed observations of high-energy processes associated with diffuse gamma-ray emission, GRBs, CRs, pulsars, and blazars. The main instrument were a tracker detector, a calorimeter and an anticoincidence system.

The tracker detector was a spark chamber, a gaseous detector in which the energy release produces a spark between the electrodes containing the gas. The tracker consisted of multiple chambers alternated to thin tantalum sheets. The high energy photon entering the telescope converted in the tantalum sheet in an electron-positronpair. If at least one particle of the pair was detected by the directional time-of-flight coincidence system as a downward moving particle, and if there was no signal in the anticoincidence scintillator, the spark chamber tracker recorded its track, providing a digital picture of the event. Then, the tracked particle entered the calorimeter producing an electromagnetic shower. The absorption of the shower provided a measure of the energy of the particles and therefore of the incident gamma ray.

EGRET revised catalogue lists 170 sources with no counterpart at lower energy. About 130 of them remain unidentified. Candidate counterparts included pulsars and their wind nebulae, supernova remnants, massive stars, X-ray binaries, microquasars, blazars, radiogalaxies, and galaxy clusters. In addition EGRET performed detailed studies of diffuse gamma-ray emission.

Figure 1.18 shows a map of the sky above 100 MeV in Galactic coordinates, as seen by EGRET. The horizontal bright line across the equatorial plane is the Milky Way with his center at the center of the map. The diffuse galactic emission is the dominant

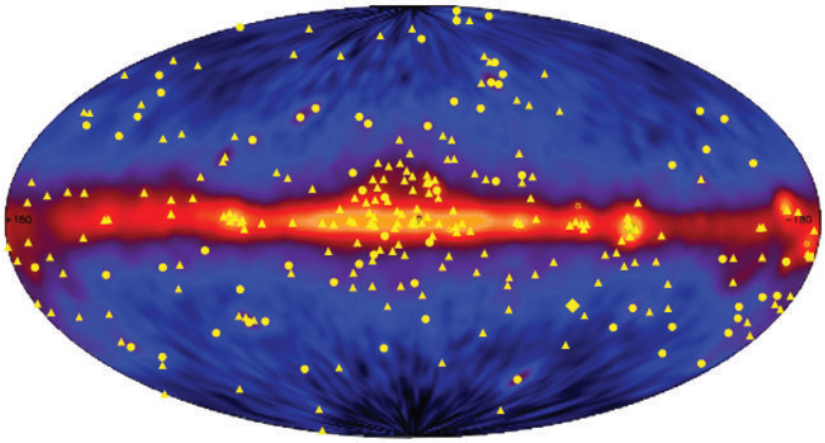

Figure 1.18: The EGRET all-sky map shows an image of the sky at gamma-ray energies above 100 MeV in Galactic coordinates. The diffuse emission, which appears brightest along the Galactic plane, is primarily due to cosmic-ray interactions with the interstellar medium. The yellow symbols show the distribution of discrete sources detected in the all-sky survey: circles are active galactic nuclei; stars are pulsars; squares are solar flares; the diamond is the Large Magellanic Cloud; and the triangles are unidentified sources[Longair, 2011].

source. Individual gamma-ray sources appear as excesses above the modeled diffuse emission.

One of the most important results of EGRET was the observation of the diffuse gamma component in Large Magellanic Cloud (LMC) and the absence of any similar component in the Small Magellanic Cloud (SMC). This established that the sources of CRs that produce the diffuse gamma component are local and therefore, if the galaxy mass is low, CR interactions with the galactic matter should not be observed. This was a confirmation of the fact that the CR production takes place inside the galaxies.

EGRET discovered 6 new pulsars candidates. Figure 1.19 shows their light curves in five energy bands: radio, optical, soft X-ray (<1 keV), hard X-ray/soft gamma ray (10 keV - 1 MeV), and hard gamma ray (above 100 MeV). The Vela, Geminga and Crab pulsars are clearly visible as bright knots of emission in the Galactic plane in the right portion of the image in figure 1.18. From the light curves studies it was observed that they are very different in the various wavelengths, implying that the emission mechanism is energy-dependent. However all light curves exhibit a double-peak in the hard γ-ray region. This observation suggested the emission models of polar cap and slot gap for particle acceleration and interactions [Thompson, 2008].

Most of the sources detected along the Galactic plane remained unidentified suggesting that the spatial resolution was not sufficient to make unique associations. Using several statistical techniques, various authors found indications of associations of

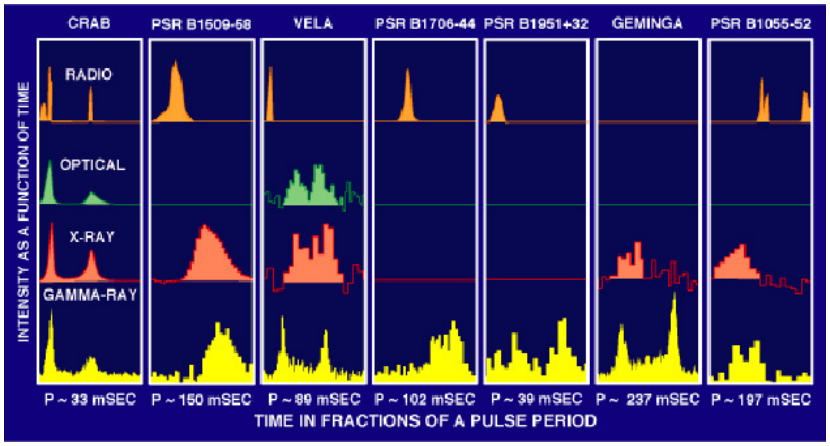

Figure 1.19: Light curves of seven gamma-ray pulsars in five energy bands. Each panel shows one full rotation of the neutron star.

EGRET sources with star forming regions or groups of hot and massive stars, supernova remnants, or pulsar wind nebulae [Thompson, 2008].

EGRET observations of extragalactic sources showed a huge variability of these sources. EGRET detected numerous bright, well-localized sources positionally consistent with prominent blazars. Numerous highly-variable blazars were also detected providing useful insights into jets and other AGN features.

1.4.2 The Fermi Gamma-ray Telescope

The Fermi Gamma-ray Space Telescope, formerly called the Gamma-ray Large Area Space Telescope (GLAST), is an astro-particle space mission for studying gamma rays in the energy range from 10 keV to beyond 300 GeV, launched on June 11, 2008 with a NASA Delta II rocket. The orbit is at 565 km altitude and 25.6° inclination, with a period of about 90 minutes [Thompson and Wilson-Hodge, 2022]. On board the satellite there are two main instruments: the Large Area Telescope (LAT), and the Gamma-Ray Burst Monitor (GBM).

The main scientific objectives of the LAT are the identification of gamma-ray sources and studying origins of diffuse Galactic emission, understanding the particle acceleration mechanisms at the sources, detecting and understanding the high-energy emission of gamma-ray burst and transient sources. The GBM can detect gamma-ray bursts from 150 keV to 30 MeV across the whole of the sky not occluded by the Earth.

The Large Area Telescope

The LAT is a pair conversion telescope sensitive to photon in the energy range from 20 MeV to beyond 300 GeV. The overall dimensions of the LAT are $1.8 \times 1.8 \times 0.72$ m^3.

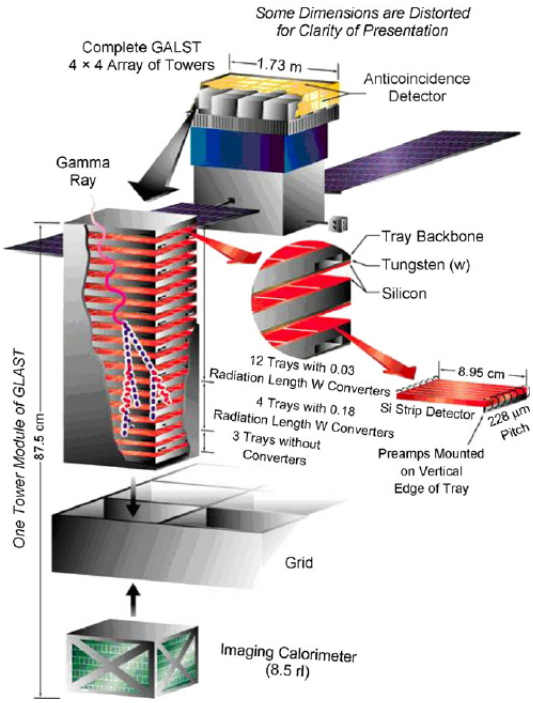

Figure 1.20: Sketch of the LAT sub-detectors [Baldini et al., 2005].

The field of view is 2.4 sr covering about 20% of the sky at any time. The whole sky is observed every two orbits (corresponding to about 3 hours). The LAT is characterized by an angular resolution of 0.1 at 10 GeV, a relative energy resolution decreasing between 10% at 100 MeV and 5% at 1 GeV, increasing again to 10% at 30 GeV and an effective area of about 1 m^2.

It consists of a 4 × 4 array of identical towers arranged in a low-mass alluminium frame and surrounded by a segmented anticoincidence detector (ACD), needed to discriminate gamma rays from charged cosmic rays. Each tower has a cross section of 37×37 cm^2 and an height of 66 cm, and is equipped with a precision tracker/converter (TKR), and a calorimeter (CAL). When an incident gamma-ray undergoes pair-conversion in a converter layer, the TKR tracks the electron and positron. Then the calorimeter measures the energy of the electromagnetic shower that develops from the charged particle. Figure 1.20 shows a sketch of the LAT instrument.

The TKR consists of 16 converter planes of tungsten in which gamma rays are expected to convert into e^+ e^- pairs, interleaved with 18 xy-tracking planes, consisting of two layers (x and y) of single-sided silicon strip detectors (SSDs) with 228 µm strip pitch, that record the passage of charged particles allowing the reconstruction of their directions. The two lower tracking planes are not equipped with converter foils, thus allowing to accurately measure the entry point of electrons and positrons in the calorimeter [Atwood et al., 2009].

The calorimeter is composed by 16 identical modules of 96 CsI(Tl) crystals of $2.7 \times 2 \times 32.6$ cm^3, hodoscopically arranged in 8 layers of 12 crystals each. The total vertical depth of the calorimeter is 8.6 radiation lengths (for a total instrument depth of 10.1 radiation lengths). The readout is done by PIN photodiodes, mounted on both sides of each crystal, measuring the scintillation light produced. The difference between the light detected at the two ends allows the determination of the position of the interaction along the longitudinal direction of each crystal. Each crystal provides three spatial coordinates for the charged particle: the position of the crystal in the array provides two coordinates and the third is provided by the light-yield asymmetry. The position resolution achieved by the ratio of light seen at each end of a crystal scales with the deposited energy and ranges from a few mm for low energy depositions (10 MeV) to a fraction of a mm for large energy depositions (>1 GeV)[Atwood et al., 2009].

The ACD allows the discrimination of photons from the charged cosmic-ray background. It consists of 89 plastic scintillator tiles: 25 tiles are on the top and 16 tiles cover each of the 4 lateral sides of the instrument, providing a spatial information that can be correlated with the signals from tracker and the calorimeter modules. Scintillation light from each tile is recorded by wavelength shifting fibers embedded in the scintillator and connected at both ends to 2 PMTs.

The Gamma-Ray Burst Monitor

The GBM is an instrument designed for the studies of spectra and time profiles of transient sources. It is sensitive to photons in the energy range from 8 keV up to 30 MeV.

It consists of 4 groups of 3 NaI(Tl) cylindrical scintillator crystals with a diameter of 12.7 cm and a height of 1.27 cm positioned at the 4 corners of the spacecraft, and 2 cylindrical BGO scintillator crystals, placed on opposite sides of the LAT, providing nearly full sky coverage [Bissaldi et al., 2009].

Scintillators are directly coupled to PMTs for the light collection. The energy resolution is 12% FWHM at 511 keV. The NaI detectors are sensitive in the lower end of the energy range, from a few keV up to 1 MeV, where bursts typically emit the most energy, and provide burst triggers and locations. The BGO scintillators cover the energy range form 150 keV up to 30 MeV [Atwood et al., 2009]. Figure 1.21 shows the position of the 14 scintillator detectors on the Fermi spacecraft. The GBM is capable to reconstruct the direction of a transient by the comparison of the count rates of different detectors.

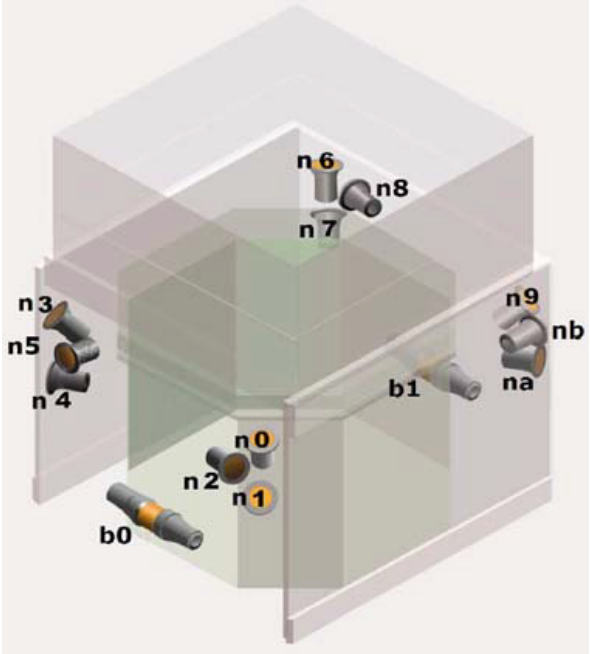

Figure 1.21: The placement of the 14 GBM detectors on the Fermi spacecraft: the 12 NaI detectors are indicated with label from n0 to nb while two BGOs with b0 and b1 [Bissaldi et al., 2009].

Results

Fermi has now been operational for 16 years. With the data collected during this time, it has produced a series of important scientific discoveries. These are collected in the Fermi general or specific catalogs that provide localization, energy spectrum and temporal variability of each source.

Figure 1.5 shows the sky observed by Fermi at energies between 1 and 100 GeV, in Galactic coordinates. The color scale is logarithmic, from dark blue to yellow. The diffuse Galactic emission corresponds to the horizontal central band. The isolated red and yellow spots correspond to the individual sources listed in the catalog.

The LAT observation of diffuse gamma-ray emission shows an isotropic distribution and a linear relationship with the atomic gas column densities in agreement with the prediction from the commonly used CR propagation models. This confirm the hypothesis on the basic production processes for interstellar Galactic emission [Abdo et al., 2009].

Fermi has been the first telescope able to unambiguously identify gamma-rays from SNRs with full sky coverage and to discriminate between possible emission mechanisms. It identified more than 40 SNRs emitting in the gamma-ray energy band.

Pulsars, pulsar wind nebulae (PWNe), and binaries have all been identified as gamma ray sources spatially coincident with known Galactic SNRs [Acero et al., 2016].

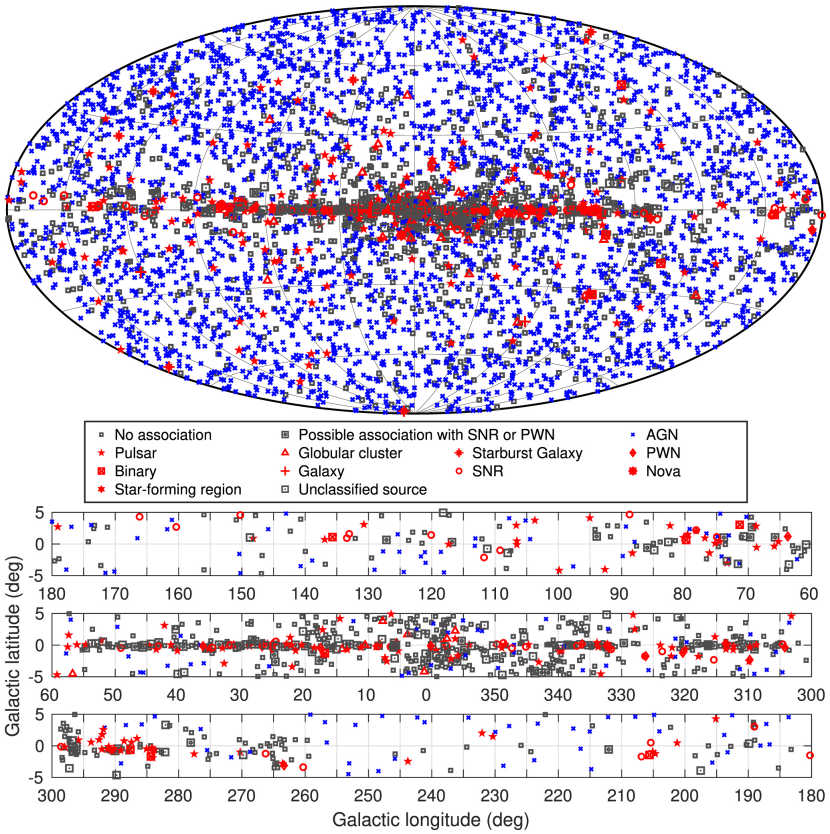

Figure 1.22: In the top panel a full sky map showing the sources detected by the LAT. Pulsar are plotted with a red star, SNR with a red circle, AGNs are plotted with blue cross. Unassociated sources and sources associated to counterparts of unknown nature are plotted in black. In the three bottom panel a zoom on thee Galactic plane is split into three longitude bands [Abdollahi et al., 2020]

The LAT also detected gamma rays produced from the interactions of the shock waves of the expansion of the remnants with the gas cloud.

The last published general catalog is the 4FGL [Abdollahi et al., 2020] updated in three successive release DR-2 [Ballet et al., 2020], DR-3 [] and DR-4 [Ballet et al., 2024]. All the sources collected in this catalog are shown in the sky map in figure 1.22 with a zoom on the Galactic plane reported in the three panels on the bottom of the figure. It contains the results of about 14 years of observation, including about 7194 gamma-ray sources including binary system, pulsars, supernova remnants, blazars.

The largest class of galactic gamma-ray sources is the class of pulsars including 135 young pulsars, 120 millisecond pulsars, and 37 associations to non-LAT pulsars. These are collected in the 3^{th} Pulsar Catalog [Smith et al., 2023] The Fermi LAT has brought the number of discovered pulsars from the 7 detected from the CGRO to more than 300 [Abdollahi et al., 2022].

The high photon statistics of the Fermi LAT allowed detailed study of light curves and emission spectra. All of the spectra can be fitted by power laws with exponential cutoffs and led to exclude emission models like polar-cap suggesting a gamma ray emission far from the star surface as supported by the outer-gap model [Caraveo, 2010].

The LAT data also allowed the discovery of millisecond pulsars, which have a rotational period less than about 10 milliseconds. The leading theory for the origin of these objects is that they are old, rapidly rotating neutron stars that have been accelerated from the mass loss of a companion star in a close binary system [Tauris and van den Heuvel, 2003].

The largest class of extra-galactic sources is that of Blazars that includes 2251 identified or associated with BLLs or FSRQ active galaxies and 1492 with unclassified blazars. These blazars are all presented in the 4^{th} AGN Catalog [Ajello et al., 2022].

Chapter 2

The FTK for the Ziré experiment onboard the NUSES space mission

2.1 The NUSES space mission

The NUSES (Neutrinos and Seismic Electromagnetic Signals) space mission is a future mission for the study of the cosmic radiation. The main scientific goals of the mission are detecting UHE CRs, monitoring the fluxes in CR of electrons in the energy range $[2 - 200]$ MeV and protons in the energy range $[30 - 350]$ MeV, detecting low-energy photons ($[0.1 - 50]$ MeV), looking for possible correlation of variation of cosmic-ray fluxes with seismic activity due to Magnetosphere-Ionosphere-Lithosphere Coupling (MILC). It will also be a technological pathfinder for developing and validating new observation methods and technologies for future space-borne detectors.

The project was proposed by the Gran Sasso Science Institute (GSSI) and is carried out in close cooperation with the Italian National Institute of Nuclear Physics (INFN) and several international Universities. The proposal has been approved by the Italian Space Agency (ASI) as a new space mission.

An industrial partnership with Thales Alenia Space Italy (TAS-I) was established for the development of the platform and the final integration of the satellite. Figure 2.1 shows a scheme of the structure of the NIMBUS platform (New Italian Micro BUS), designed by TAS-I. It is based on a new satellite bus concept specifically developed for Low Earth Orbit (LEO) micro satellites which foresees a Multi-Function Modular Frame approach consisting in the integration of the needed number and type of standard trays. One tray is allocated for the payload and is customizable to meet the specific requirements of each mission. Additional trays essential for the platform are largely standardized and can support a wide range of applications. These include the Electric

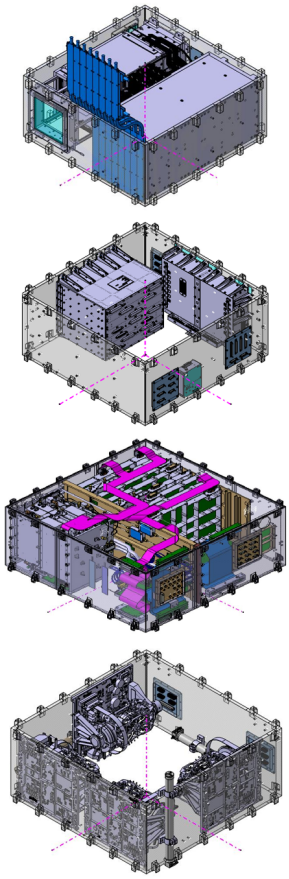

Figure 2.1: Scheme of the NIMBUS platform. From the top to the bottom the payload tray, the EPS tray, the DHC tray and the AOCS tray.

Power Systems (EPS) tray, the Data Handling Control (DHC) and the tray dedicated to Altitude and Orbit Control System (AOCS).

NUSES will be a ballistic mission with no propulsion for orbital elevation corrections. It will operate at an altitude of 550 km with a high inclination of approximately 97.6°, orbiting in a Sun-Synchronous and dusk-dawn mode along the day/night boundary line with a lifetime of 3 years. The orbit has been tailored around the requirement of optimal detection of the Cherenkov light from the dark side.

The satellite will host two scientific payloads named Terzina and Ziré. Figure 2.2 shows a general scheme of the NUSES satellite design [Aloisio et al., 2023b], illustrating the position of the two payloads. The Terzina field of view will be pointed to the dark side of the Earth's limb.

Terzina is a detector dedicated to test and validate a new concept of space-based Cherenkov telescope designed for the detection of light emitted by extensive air showers (EAS) induced by Ultra-High-Energy Cosmic Rays (UHECRs) or Earth skimming neutrinos in the dark side of the Earth's limb [Aloisio et al., 2023a].

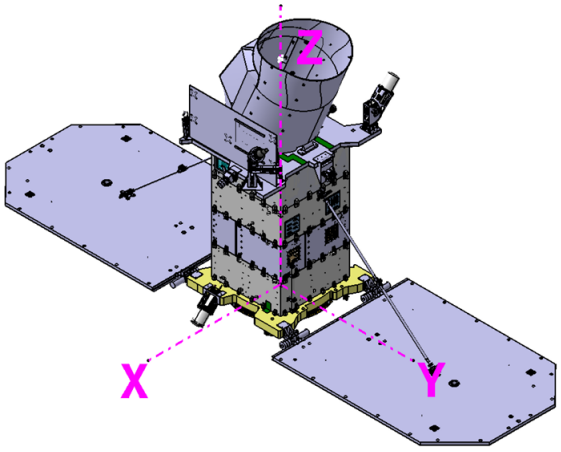

Figure 2.2: General scheme of the NUSES satellite design.

Ziré is an experiment dedicated to the measurement of the fluxes and spectra of cosmic rays with energies up to hundreds MeV investigating possible correlations with phenomena occurring in the magnetosphere and ionosphere with natural Earth phenomena, e.g. earthquakes or volcanic eruptions, as described by the MILC (Magnetospheric-Ionospheric-Lithospheric Coupling) model [Piersanti et al., 2020]. It will also detect gamma rays with energy below few tens of MeV, to study both transient events and steady sources. Ziré will include the Low Energy Module (LEM), a spectrometer for electrons in the [0.1˘7]MeV energy range and protons in the [3˘50]MeV energy range.

Among the primary objectives of NUSES is the validation of SiPM technology as a viable alternative to traditional PMTs in satellite applications. In fact, their compactness, low power consumption and low cost make SiPMs the ideal devices for space applications; however, their suitability for use in space still needs to be tested. All detectors readout onboard NUSES will be based on SiPMs.

2.2 The Ziré experiment

The main task of Ziré experiment is to measure the features of the CR spectrum in the energy region from few MeV up to a few hundreds MeV. As illustrated in section 1.1.1 the portion of CRs spectrum below 1 GeV is strongly influenced by Solar activity. The Sun has a period long 11 years in which his activity increases from a minimum, it reaches a maximum and decreases again. At the same time also the magnetic field inside the Heliosphere has a cyclic variation of about 22 years. This results in continuously variable spectra for various particle species. There are different

theoretical models that try to predict low-energy CR fluxes in specific period of time. These models for protons and helium nuclei have been validated from experiments (for example see [Bartocci et al., 2020]) but at present there are not direct measurements of electrons in the MeV energy range. Ziré will perform measurement on cosmic particles below 1 GeV allowing to understand the mechanisms regulating their transportation in the heliosphere. This will be important to study the interplanetary magnetic field and its interactions with the Earth magnetosphere.

In addition, the study of the energy spectrum of low-energy galactic CRs, allows the monitoring of space weather. In fact, during periods of high solar activity, events like solar flares and Coronal Mass Ejections can cause high-intensity emission of Solar Energetic Particles (SEPs), with energies from a few tens of keV to a few GeV. These particles, accelerated and transported by the heliosphere, can reach the Earth and cause space weather phenomena, such as geomagnetic storms, which could damage orbiting objects.

In addition, there are particles of Solar and galactic origin, trapped in the Earth's magnetosphere. These form two distinct zones named Van Allen radiation belts, the inner radiation belt and the outer radiation belt. The inner belt consists of electrons with energies up to 10 MeV and protons with energies reaching 700 MeV, confined within a region spanning 1.1 to 2 Earth radii. The outer belt, on the other hand, primarily contains electrons with energies below 10 MeV, trapped in a region extending from about 4 to 9–10 Earth radii. One of the main objectives of the experiment is to study the fluxes ofparticles trapped in these belts in order to identify any possible anomalies in the fluxes of low-energy electrons, protons and light nuclei.

Different experiments, in the last years, have detected many anomalies, statistically correlated to geophysical phenomena, such as anomalous bursts of charged particles precipitating from the lower boundary of the Van Allen belts
[Sgrigna et al., 2005]. These correlation could be theoretically described by the MILC model that hypothesize the emission of atmospheric acoustic gravity waves that develop around the epicenter of the seismic event and perturb the atmosphere producing disturbs in the ionosphere. This could locally modify the magnetic field in the Van Allen belts causing a variation in the flux of charged particles trapped in the belts [Piersanti et al., 2020]. One of the main objectives of Ziré is to verify the possible coincidence of these anomalies with seismic events.

Additionally Ziré will be capable of detecting low-energy gamma rays from 0.1 MeV up to few tens of MeV, to study both transient phenomena and steady sources.

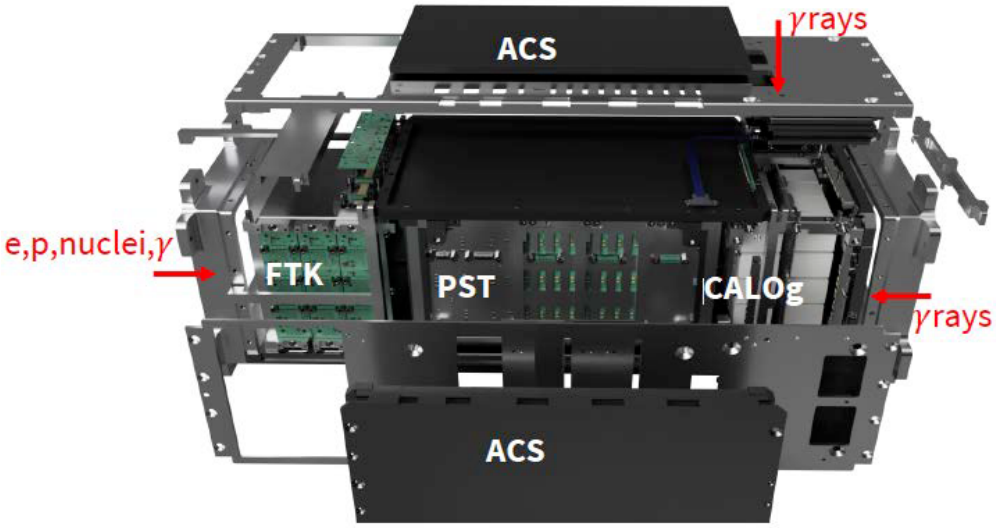

Figure 2.3: Exploded view of the Ziré instrument (the LEM detector is not shown) illustrating the final detector design. Charged particles will enter from the FTK side while gamma rays will mainly enter from the side of the CALOg.

2.2.1 The Ziré design

In figure 2.3 a model of the Ziré experiment is shown. It consists of several sub-detectors that will be used to perform spectral measurements. Referring to figure 2.3, the detectors from left to right are: a scintillating Fiber TracKer (FTK), a Plastic Scintillator Tower (PST), a Gamma calorimeter (CALOg) and an AntiCoincidence System (ACS).

The FTK is composed of three X-Y modules with a sensitive area of 9.6×9.6 cm^2, with a 2.5 cm spacing between the modules. The FTK has the task of reconstruct the tracks of charged particles. Each module consists of two orthogonal planes. Each plane is made of two layers of scintillating fibers with a diameter of 750 µm, arranged in a staggered double array layout. The total on-axis thickness of each module is about 1.4 mm to reduce the multiple Coulomb scattering inside the module and to reduce the charged particle energy loss. Figure 2.4 shows a photo of a X-Y module of the FTK [Mazziotta and Pillera, 2023].

The PST is a stack of 32 layers, each composed by three plastic scintillator bars of 4×12 cm^2 cross section, arranged in a hodoscopic configuration. Each scintillator bar is read out at both ends by a pair of SiPMs positioned at the center of each side. The first two X-Y layers with thicker bars are readout by 4 SiPMs per side for redundancy. The purpose of the PST is to enable the instrument to perform particle identification. The first six layers of the PST, namely those closer to the FTK, are 1 cm thick, while the other 26 layers are 0.5 cm thick. On one side, the SiPM pair has a 1×1mm^2

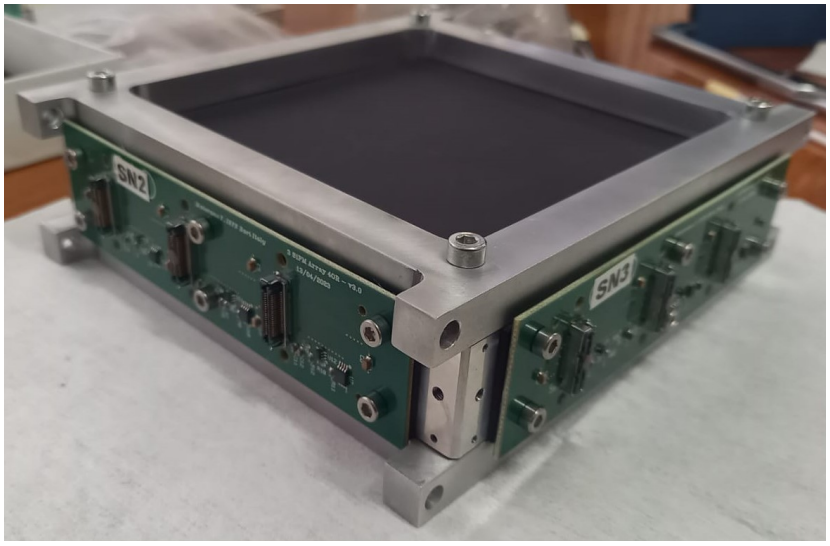

Figure 2.4: Photo of one module of FTK.

cross-section to enable detection of signals consisting of few photoelectrons. On the other side, two $3 \times 3\text{mm}^2$ SiPM are used to ensure a large dynamic range. In figure 2.5 a CAD scheme of the PST is shown. The left panel shows the scintillating bars with the indicated SiPM positions, while the right panel displays the mechanical structure housing the printed wiring board (PWB) on which are soldered the SiPMs and the cables used to route signals to the front-end boards. The total weight of the PST is of around 5.3 kg. Figure 2.6 shows a photo of the realization phase of the PST for the structural model. In the left panel, a few wrapped scintillating bars are shown.

The CALOg is a calorimeter consisting of 32 optically independent LYSO crystals arranged in two layers, each consisting of a 4×4 matrix of crystal cubes of $2.5 \times 2.5 \times 3\ \text{cm}^3$. Each cube is readout at one side by a combination of 7 SiPMs. The left panel of figure 2.7 shows the schematic view of the PWB hosting the groups of SiPMs for all the crystals of one layer. Each group consists of a central SiPM with a cross-section of $6 \times 6\ \text{mm}^2$, two SiPMs $3 \times 3\ \text{mm}^2$ on the two opposite side of the central SiPM and two SiPMs $1 \times 1\ \text{mm}^2$ on a third side. The total instrument estimated weight is of around 6 kg. The CALOg is used for incoming charged particles energy measurements and for the detection of gamma rays in the energy range $0.1\ \text{MeV} - 50\ \text{MeV}$. Figure 2.8 shows the components of the calorimeter. In the left panel of the figure a cubic scintillating crystal is shown; in the central panel is shown the matrix where the cubes are placed; in the right panel is shown the support structure of the detector.

The ACS is made of 9 plastic scintillator tiles, each 0.5 cm thick. Figure 2.9 shows the CAD renderings illustrating the structure of the ACS . In the left panel the complete instrument is rapresented. We can see that the nine tiles form two subsystems: the

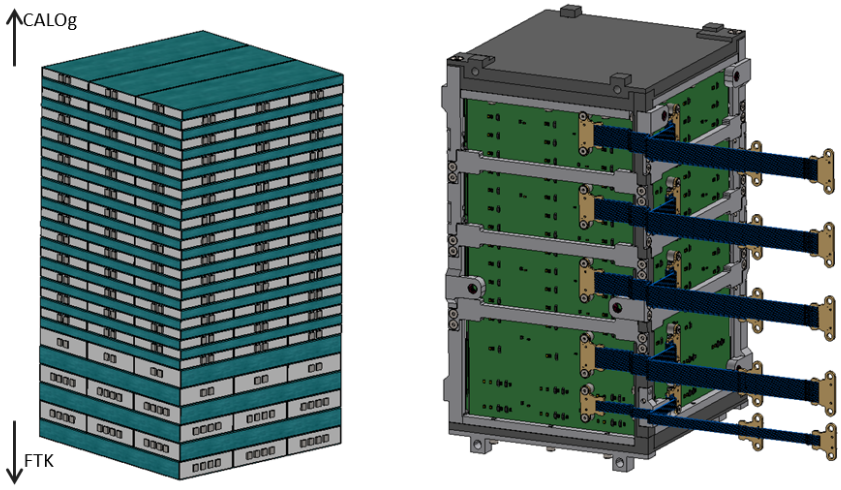

Figure 2.5: CAD scheme of the PST subdetector. Left: scintillator bars in hodoscopic configuration, the square on the bars rapresent the SiPM positions. Right: CAD of the mechanical structure hosting the PWBs designed for the SiPMs.

Figure 2.6: Photo of the realization of the structural model of the PST. In the flight model Aluminum foil will replace black vinyl tape.

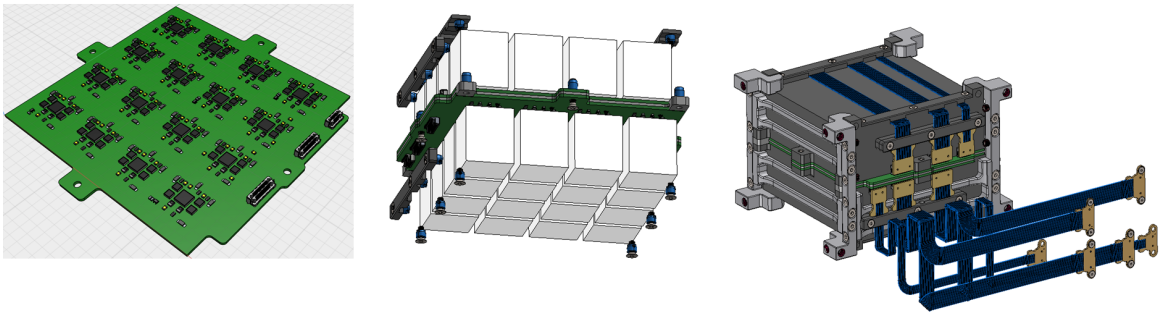

Figure 2.7: CAD schemes of the CALOg. Left panel: PWB hosting the groups of 7 SiPMs required for a single crystal readout. Central panel: scheme of the two layer of 4×4 scintillating crystals. Two PWBs are positioned between the two layers. Right panel: representation of the final instrument including the mechanical structure and the cables.

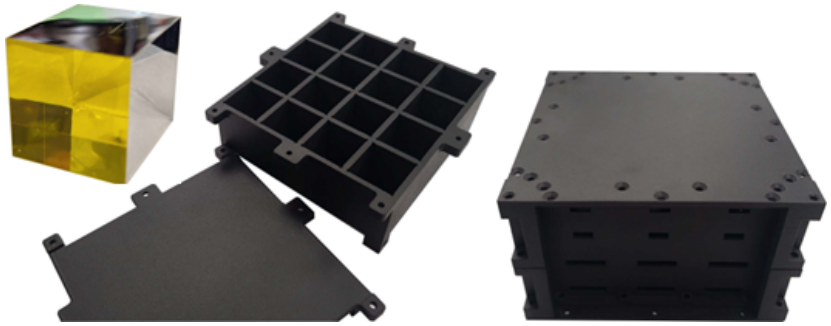

Figure 2.8: Left panel: a scintillating crystal for the $4 \times 4 \times 2$ matrix shown in the central panel. Right panel: the CALOg mechanical structure.

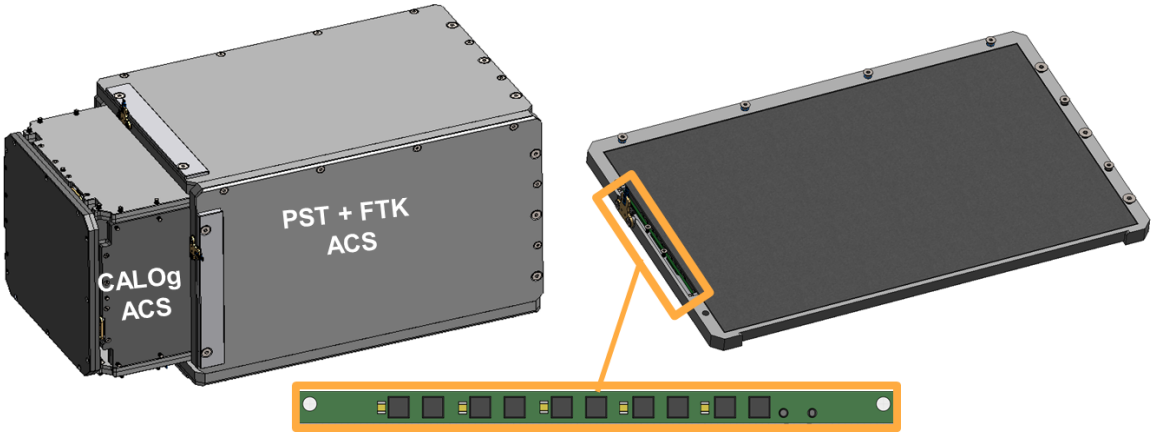

Figure 2.9: CAD schemes of the ACS. At the left: complete detector scheme including a larger ACS of the PST and FTK and a smaller ACS for the CALOg. At the right: A single wrapped tile of plastic scintillator in the mechanical structure made of WINDFORM XT 2.0. At the bottom: a detailed view of the PWB with the SiPMs.

first surrounds the PST and FTK on all four sides, while the second shields the four sides and the front face of the calorimeter. In the right panel a detail of a single tile is shown. It consists of a plastic scintillator tile placed within a WINDFORM XT 2.0[1] support structure. At the bottom of the figure is reported an incept view on the PWB hosting the SiPMs used for the readout of each tile. The ACS provides a veto system for side entering or not fully contained incoming charged particles. The final instrument will be 50 cm long with a square cross-section of 21.5 cm side.

The weight of the whole instrument will be of about 22kg.

Finally, the LEM is a compact particle spectrometer with dimensions of $10 \times 10 \times 10$ cm^3, designed to be integrated into the outer structure of the NUSES bus. Its main task is to measure energy and direction of low energy electrons (down to few hundreds keV) and protons with energies between 3 and 50 MeV in order to study possible MILC

[1] https://www.windform.com/sls-materials/windform-xt-2-0/

signatures [Nicolaidis et al., 2023].

The Electronic Unit (EU) consists of different custom design electronic boards with a total of more than 1000 readout channels. Each subsystem has its own dedicated set of acquisition boards, named DAQ-units, each managed by a main board shared across all subsystems, referred to as the concentrator. The concentrator is responsible for coordinating data acquisition across subsystems, boards configuration, data processing and communication with the satellite. Each DAQ unit (except the one dedicated to the LEM) includes several Citiroc 1A front-end ASICs from Weeroc[2], each with 32 input channels, and an FPGA to manage acquisition within the unit and communicate with the concentrator (the DAQ-unit board is described in detail in section 5.1).

Four DAQ units are allocated for FTK readout, each equipped with six ASICs, resulting in 192 channels per board and a total of 1152 channels. Two DAQ units, each with three ASICs, are used for the PST front-end. A single DAQ unit, equipped with four ASICs, handles the CALOg and ACS front-ends. An additional DAQ unit is included for redundancy. The LEM front-end is managed by a dedicated board.

Figure 2.10 shows a scheme of the positioning of the Ziré instrument inside the satellite tray. It is placed next to the EU.

The line of sight of the whole instrument point always towards the celestial horizon, with CRs entering from the window at the top of the FTK. In in figure 2.10 can be noticed a second window placed at the side of the CALOg, a third window is placed on the back of the tray at the bottom of the CALOg. This window allow to use this sub-detector also for independent measurements of incoming gamma rays.

The FTK, PST, and CALOg subdetectors will offer various trigger options, such as the MIP, High Energy (HE), and Low Energy (LE) triggers for detecting protons, electrons, and gamma rays. These triggers will be configured remotely from the ground by adjusting parameters like the number of layers with signal and the energy thresholds. feature of the mission is the The key feature of the mission is the possibility to implement a full SiPM-based readout for all subdetectors, replacing the traditional Photomultiplier Tubes (PMTs) commonly used in space experiments. The innovative integration of SiPMs in both the Zirè and Terzina experiments aboard the NUSES satellite represents a key advancement for this mission. SiPM technology is the optimal solution for space-based experiment due to its compact size, low power consumption, and high detection efficiency. Moreover both Hamamatsu and FTK SiPM technologies will be tested in the same space mission.

[2] https://www.weeroc.com/read_out_chips/citiroc-1a/

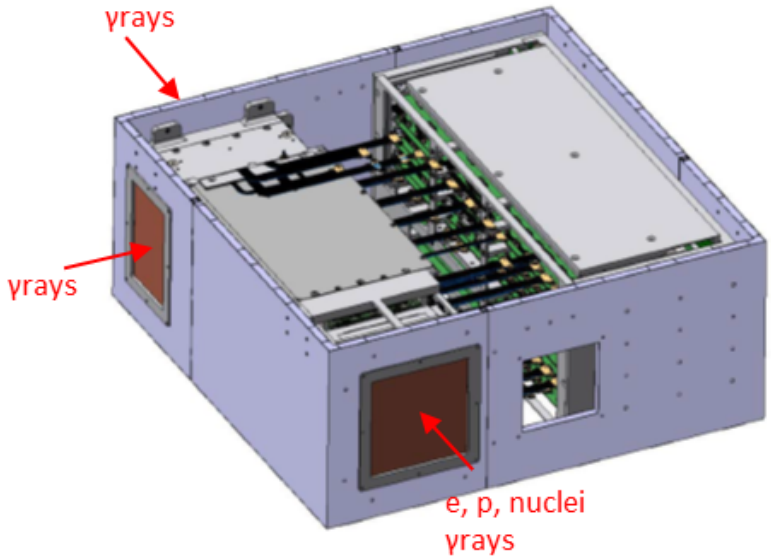

Figure 2.10: CAD view of the satellite tray dedicated to the Zirè payload and the EU. The Zirè instrument is in the left of the tray. Two windows on the satellite are visible. These allow the entrance of charged particles and gamma rays. Another window is placed on the other side of the tray, to allow gamma rays to enter the calorimeter from the back.

2.2.2 Simulation studies

Preliminary Monte Carlo simulations of incoming electrons and protons have been performed with the Geant4 toolkit [Agostinelli et al., 2003] in order to evaluate the expected performance of Ziré and optimize its design. Figure 2.11 shows an example of two simulated events. The figure shows the display of a 50 MeV proton and of a 20 MeV electron.

A preliminary estimation of the detector acceptance has been obtained requiring the trigger condition consisting in an energy deposit greater than 0.1 MeV and 0.3 MeV in the FTK and in the first PST layer (PST0) respectively, together with a full event containment request for the simulated events. Preliminary results for the acceptance are shown in figure 2.12. It can be observed that the acceptance reaches a peak of about 200 cm^2 sr for 10 MeV electrons and 100 MeV protons and decreases with energy due to the full event containment request.

CR particles have been simulated in the energy range from 0.1 MeV up to 10 GeV to evaluate the particle identification capability of the instrument. The sum of the energy deposition in FTK and PST0, Δ_0, from the Bethe formula:

$$\Delta_0 \propto \frac{z^2}{\beta^2} \tag{2.1}$$

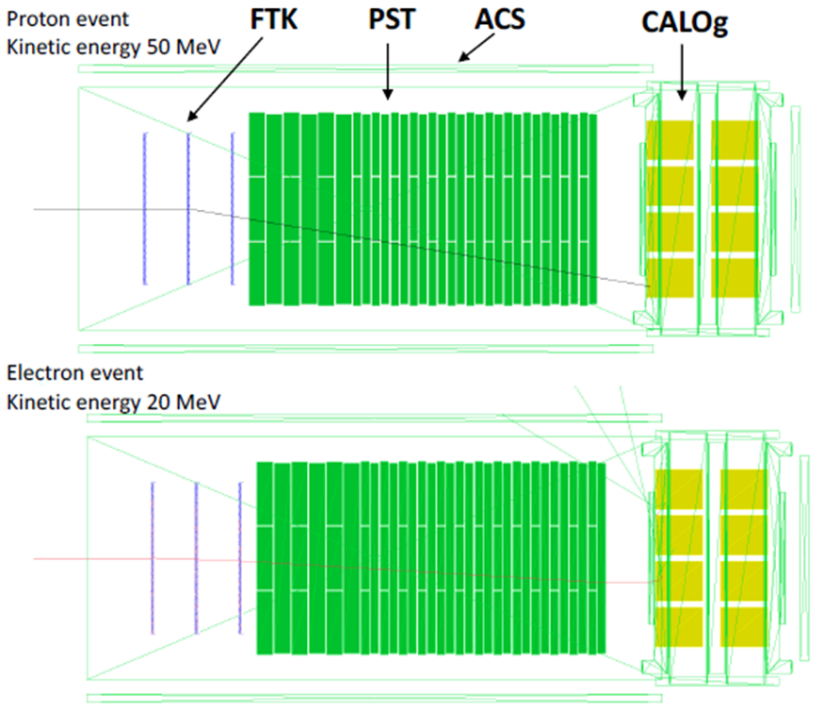

Figure 2.11: Display of two simulated events. The top panel shows a proton with a kinetic energy of 50 MeV. The bottom panel shows an electron with a kinetic energy of 20 MeV [De Mitri and Fernandez Alonso, 2023]

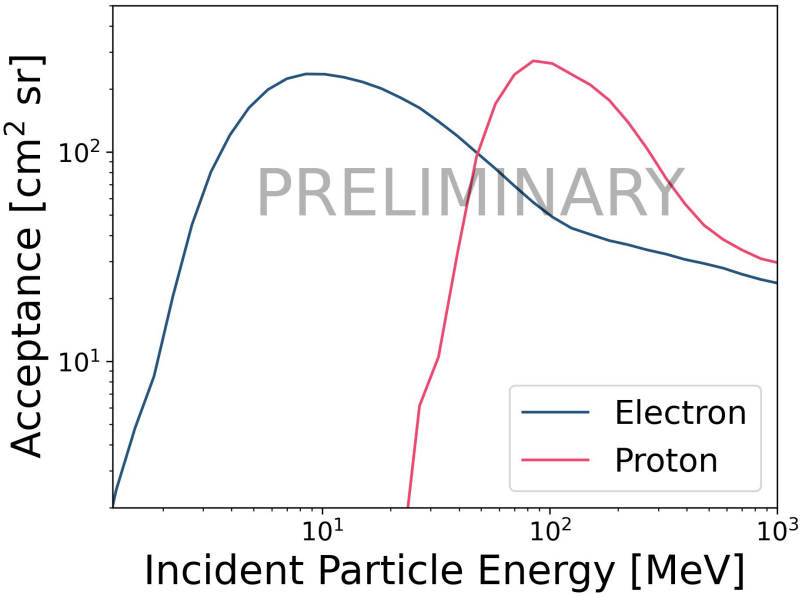

Figure 2.12: Preliminary estimate of the acceptance for protons and electrons (energy deposit > 0.1 MeV and > 0.3 MeV in the FTK and first PST layer (PST0) respectively and full containment required).

Since for fully contained non-relativistic nuclei the energy deposited in the whole instrument $E_{dep} \simeq E_k \propto \beta^2$ it follows that:

$$\Delta_0 \propto \frac{z^2}{E_{dep}} \tag{2.2}$$

The relationship between the energy deposited in the FTK and PST0 is hence linear in $1/E_{dep}$ and exhibits a quadratic dependence on the charge of the non-relativistic ion. This dependency allows for identifying ions with different charges.

The figure 2.13 shows the simulation results for electrons, protons, and helium nuclei with energies ranging from 0.1 MeV to 10 GeV. The plot presents the energy Δ_0 as a function of $1/E_{dep}$ for events that satisfy the full containment condition, and with an energy release exceeding 0.1 MeV in the FTK and 0.3 MeV in the PST. We can see different families of events corresponding to different ions aligned along distinct curves in the plot. This enables particle identification using the instrument, as particles with different charges and energies deposit energy in characteristic ways that result in separable patterns. The diffuse component within the electron family is due to relativistic electrons, for which Δ_0 remains approximately constant as E_{dep} varies. This effect arises because, for relativistic electrons, the energy deposition pattern stabilizes, reducing the dependency of Δ_0 on E_{dep}. The events located along the line correspond to those with the minimum energy required to traverse all three FTK modules and deposit the threshold energy of 0.3 MeV in the PST0. Ions with lower energies are unable to meet the data selection criteria applied.

2.3 The Ziré Fiber TracKer

Figure 2.14 shows the CAD view of the FTK sub-detector. As illustrated in section 2.2.1 it consists of three modules each one made of two orthogonal planes, composed of two staggered layers 9.6 $\times$ 9.6 cm^2 of round scintillating fibers Kuraray SCSF-78MJ2[3] with a diameter of 750 µm.

The fibers have a polystyrene core with a refractive index n = 1.59. A fluorescent dye is dissolved in the polystyrene matrix. The core is surrounded by a double cladding structure. The inner cladding is made of polymethylmethacrylate (PMMA) (n = 1.49), while the outer cladding is made of a fluorinated polymer (n = 1.42). The double cladding allows to enhance the trapping efficiency, which is of about 5.4%, assuming that light propagates in the fiber via total internal reflections. In section 3.1 the light

[3] `http://kuraraypsf.jp/psf/`

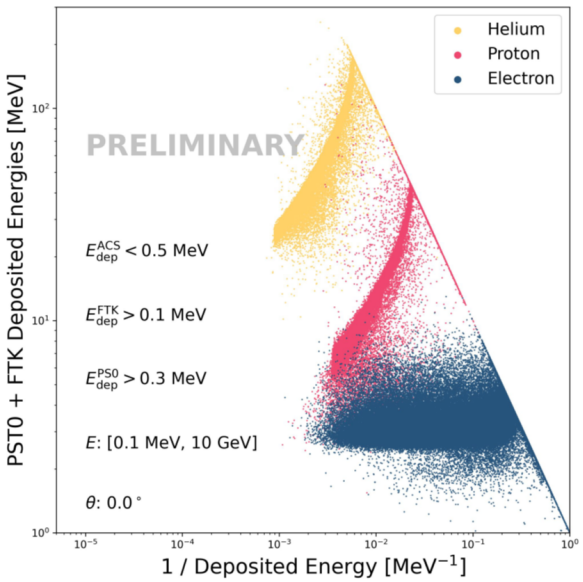

Figure 2.13: Particle Identification from the correlation between the energy deposit inside the FTK+PST0 and the inverse of the total energy deposition in the whole detector.

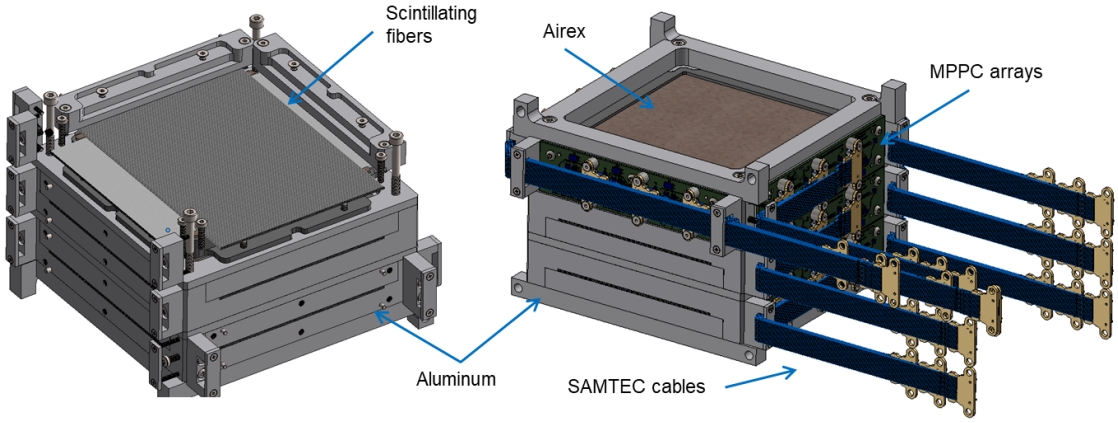

Figure 2.14: CAD view of the 3-modules Ziré FTK.

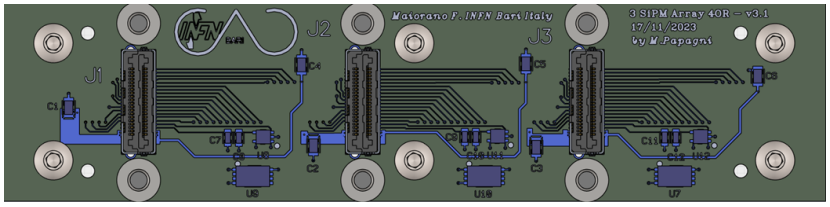

Figure 2.15: CAD rapresentation of the PWB designed for the three SiPM arrays that will readout each side of the Ziré FTK. On one side of the PWB are soldered the three SiPM arrays, on the other the three LSHM-120 Samtec connectors.

propagation in scintillating fibers is thoroughly illustrated. The edge of each plane is readout by three 128 channels SiPM arrays Hamamatsu S13552 [4] developed for the LHCb SciFi tracker [Joram et al., 2015]. The SiPM array consists of two 64-channels arrays with a gap in between of 0.22 mm. The individual pixels have a cross section of 57.5 µm $\times$ 62.5 µm. Pixels are are arranged in strips of 4 $\times$ 26 pixels, resulting in a channel area of 0.23 mm $\times$ 1.62 mm with a pitch between adjacent channels of 0.25 mm.

The three SiPM arrays are soldered on one side of a PWB as illustrated in figure 2.15. The PWB is designed for ORing groups of 4 adjacent SiPM strips (*OR4* configuration) routed to a 32-channels LSHM-120 Samtec connector assembled on the other side of the PWB. The *OR4* results in an effective strip pitch of 1 mm and allows a reduction of the number of electronic channels. The 32 analog SiPM signals readout by each connector are then routed to the distant FEB using high-speed 50 Ω multi-channel HLCD SAMTEC cables[5]. The PWBs of the FTK are also equipped with temperature sensors in order to monitor the SiPM conditions.

The primary task of the FTK, in addition to measuring the impact point, the trajectory, and the deposited energy in the three layers by the incoming particles, is to provide a fast trigger signal for the other subdetectors. Hence the module closest to the PST (the last crossed by the impinging particle) is readout at both the ends of each plane to enable a trigger logic that requires coincidence of the signals from the same fiber (or group of adjacent fibers) from both sides. This approach enhances the precision of the event detection and allows for more reliable signal identification by ensuring that only events with coincident signals on the same fibers are processed. The other two modules are read out from only one side in order to limit the number of readout channels, optimizing the system's complexity and resource usage.

[4]Hamamatsu Photonics S13552 MPPC array, `https://www.hamamatsu.com/eu/en/product/optical-sensors/mppc/mppc_mppc-array/S13552.html`

[5]High Speed Hermaphroditic Cable, HLCD-20 0.50 mm Pitch, Samtec: `https://www.samtec.com/products/hlcd`

The SiPM readout is performed with the CITIROC1A ASIC. This component was designed by Omega-Weeroc[6] with a declared Technology Readiness Level (TRL) 7 of 8, indicating that the technology has been tested and flight qualified.

The FTK readout system will consist of four FEBs, each one hosting six front-end ASICs, an analog to digital converter (ADC) and a Field Programmable Gate Array (FPGA) for local central processing unit (CPU) processing. All boards are connected to a motherboard (concentrator) equipped with a FPGA for DAQ system management.

A mechanical aluminum support structure has been designed to provide robust support while maintaining a lightweight design, essential for satellite applications. Additionally, Airex foam is used on both sides of the fibers to ensure robustness and structural integrity for the tracker modules.

[6] https://www.weeroc.com/products/sipm-read-out/citiroc-1a

Chapter 3

The Fiber TracKer prototype design and realization

The aim of this work is the development of a new tracker detector for space-based experiments based on scintillating fibers readout by SiPMs. An important constraint for space-based experiments is the maximum weight of the payload together with the maximum power consumption allowed. In current detectors, trackers rely on well-established technologies, such as single-sided silicon micro-strip detectors (SSDs). Orienting the strips of each layer perpendicularly to those of the adjacent layers or the use of Double-sided silicon detectors (DSSDs) as in experiment such as AMS-02 ([Bourquin, 2005]) allows the reconstruction of the 3 track coordinates in each plane. However for these detector the electronic noise increases with the capacitance of the silicon strip, which is proportional to the strip length [Group et al., 2020].

The proposed tracker design consists of multiple planes of scintillating fibers in hodoscopic arrangement in order to allow 3D track reconstruction readout by SiPM arrays. This chapter will introduce the design that has been developed with a focus on the properties of scintillating fibers. The results of the simulation studies conducted to determine the detector performance will then be described, followed by an overview of the prototype construction phase.

3.1 Scintillating fibers

As discussed in Section 1.3, plastic scintillators provide significant versatility in detector design and fabrication, allowing for a wide range of shapes and sizes. Specifically, scintillating fibers can be obtained by extruding plastic scintillators into thin fibers. These fibers can have different cross-sectional geometries, with the most

common being circular, typically with diameters ranging from a few hundred microns to a few millimeters. A critical design consideration is the trade-off between fiber diameter and detector performance. A smaller diameter enhances the spatial resolution achievable by the final detector, which is essential for accurately determining the position of ionizing events. However this choice reduces the scintillation light yield, since the volume of scintillating material is reduced. A reduced light yield implies a lower number of photoelectrons produced by the incident particle, which is directly proportional to the signal amplitude generated by the photodetector. If this signal is comparable to noise levels, the discrimination of the signal from the background may no longer be possible, resulting in a decreased signal-to-noise ratio.

The interesting feature of the scintillating fibers is that they serve a dual function: they act as scintillator converting the ionization energy deposited by charged particles into optical photons and simultaneously as a light pipe that transports these photons to the photo-detectors placed at the fiber ends. This dual role simplifies the detector design and enhances its efficiency, as the same material serves two critical functions.

Scintillating fibers consist of a thin scintillating core, surrounded by one or two layer of cladding material with typical thickness of few percents of the fiber diameter and a slightly smaller refractive index. Generally, polystyrene is used as polymer for the core thanks to its relatively high refractive index $n_{core} = 1.59$. However, it has a poor scintillation light yield, and therefore organic fluorescent dyes (referred to as "*activators*") are added to the polymer matrix in order to improve the scintillation efficiency. The dye is properly selected in order to have a high efficiency ($> 95\%$) [Lecoq, 2020]. A secondary dye is frequently added to inhibit self-absorption of the emitted light. It acts as a wavelength shifter, absorbing the light emitted for fluorescence by the activator dye and re-emitting it at longer wavelengths where both the dye and polystirene are transparent. This process reduces light loss and improves the overall photon yield. Typically, the scintillation yield is approximately 8000 or more photons per MeV of deposited energy.

The transport of scintillation light to the photodetector within the scintillating fiber primarily occurs through total internal reflection at the core-cladding interface. Common cladding materials are polymethylmethyacrylate (PMMA, $n_{cladding} = 1.49$) and fluorinated polymethacrylate (FP, $n = 1.42$) [Joram et al., 2015].

Figure 3.1 shows the schematic of light transmission in the fiber. When a particle traverses the fiber, it deposits energy along its track, which is absorbed and isotropically re-emitted as scintillation light. The scintillation light divides into *meridional rays* and *skew rays*. Meridional rays are those light rays emitted close to the axis of the fiber. They travel within the fiber core and pass through the center of the fiber with

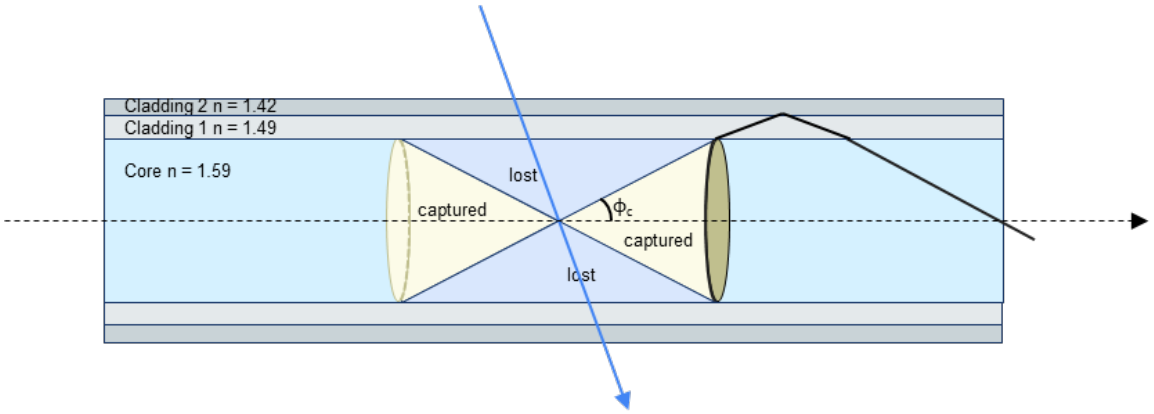

Figure 3.1: Propagation of meridional rays in a scintillating fiber with two cladding layers. Photons emitted with directions lying in the yellow cone are transmitted through the fiber, while photons emitted at other directions are lost.

a geometric path which lies in a plane that contains the axis of the fiber. On the other hand, skew rays are rays originated near to the outer rim of the core and travel within the fiber without following a path aligned with the axis of the fiber that, unlike meridional rays, they do not intersect.

Meridional rays will be guided to the photo-sensor at the end of the fiber, provided that they strike the core-cladding interface at an angle greater than the critical angle required for total internal reflection. This condition defines an acceptance cone within which the light is confined. Light outside this cone strikes the interface at an angle smaller than the critical angle, resulting in partial reflection and partial transmission, with the transmitted portion potentially escaping the fiber. Referring to the scheme in figure 3.1, the critical angle is

$$\theta_c = \arcsin \frac{n_{cladding}}{n_{core}} \tag{3.1}$$

with $n_{cladding}$ and n_{core} the refractive index of cladding and core respectively. Hence, the angle subtended by the cone is

$$\phi_c = \frac{\pi}{2} - \theta_c \tag{3.2}$$

With typical values of $n_{cladding} \simeq 1.49$ and $n_{core} \simeq 1.59$, $\theta_c \simeq 69.6°$ and $\phi_c \simeq 20.4°$. The fractional solid angle subtended by the cone in given by:

$$F = \frac{\Omega}{4\pi} = \frac{1}{4\pi}\int_0^{\phi_c} d\Omega = \\ = \frac{1}{4\pi}\int_0^{\phi_c} 2\pi \sin\phi d\phi = \frac{1}{2}(1-\cos\phi_c) = \frac{1}{2}(1-\sin\theta_c) = \frac{1}{2}(1-\frac{n_{cladding}}{n_{core}}) \simeq 0.03 \tag{3.3}$$

and hence only a $\sim 3\%$ of total generated light is trapped within the fiber.

For single cladding fiber at the interface cladding-air a fraction of escaped light is trapped into the cladding and by total internal reflection is transmitted to the photosensor. However, since this interface has inferior optical quality, this fraction is small. The use of a double cladding with decreasing refractive index enable to recapture part of the escaped light and the fraction of trapped photons can rise up to $\sim 5\%$. This value correspond to meridional rays only. However light can also propagate via *helical paths*, where the skew rays spiral along the fiber. While these helical rays can potentially contribute to the detected signal, their longer path lengths and increased number of reflections result in greater attenuation. Given that the typical fiber attenuation length Λ are in the range $3 \div 5$ m, helical rays generally give a negligible contribution compared to meridional rays. The attenuation length depends on the wavelength λ and increases for larger λ. The light intensity as a function of the distance from the point of scintillation can be approximated as:

$$I(x,\lambda) = I_0 e^{-\frac{x}{\Lambda(\lambda)}} \tag{3.4}$$

This relationship highlights the exponential decay of light intensity due to absorption and scattering processes within the fiber material. The careful selection of materials and the use of wavelength-shifting dyes are crucial for optimizing the attenuation length and maximizing the detection efficiency.

In conclusion, the use of scintillating fibers in detector systems offers a unique combination of high spatial resolution, efficient light transport, and flexibility in detector design. Fibers are particularly well-suited for applications where minimal material budget, high radiation tolerance and compact design are critical, such as in space-based or large-scale high-energy physics experiments.

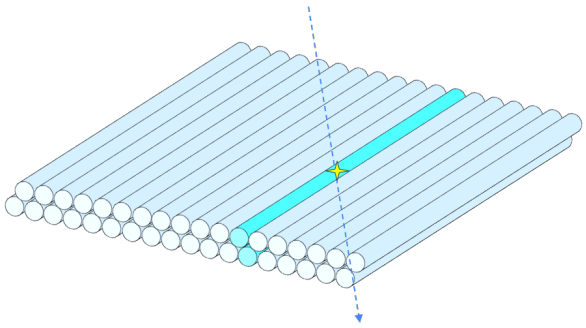

Figure 3.2: Sketch of a single ribbon obtained with a staggered double-layer arrangement of scintillating fibers. The particle will cross at least two fibers in the upper and lower ribbon, releasing energy in both and hence increasing the number of photons produced in one hit.

3.2 The Fiber Tracker Concept

The main task of a tracker is to detect impinging particles with high efficiency and reconstruct their tracks with good spatial resolution. In general, a tracker is a highly segmented detector designed to determine the precise location within the device where the energy was released by ionizing radiation. The higher the granularity of the detector, the greater the precision in determining the position. The ability to shape fibers with arbitrarily small diameters makes them ideal candidates for constructing trackers. As a first approximation, the spatial resolution of a fiber is given by $\frac{d}{\sqrt{12}}$ where d is the diameter. Hence, very small diameters can ensure accurate spatial resolution. However, they also result in a reduced light yield, making it difficult to discriminate the signal from noise, thereby compromising the detection efficiency.

The trade-off between spatial resolution and efficiency is crucial to optimize the detector's performance. In this context, the choice of the scintillating fiber diameter plays a key role. In this work, fibers with both 500 µm and 750 µm in diameter were tested in order to experimentally assess this trade-off. The simulations and tests performed aim to examine the effect of the fiber diameter on the particle trajectory reconstruction capability and on the amount of light collected by the SiPMs with the goal of optimizing the detector design based on the experiment requirements.

In order to enhance the light signal, staggered multi-layer arrangements can be employed as shown in figure 3.2. In this configuration, the centers of the fibers in the two layers are arranged along the x-axis at a distance equal to their radius R, as shown in the figure 3.3. By applying the Pythagorean theorem, the distance between the fiber centers along the y-axis is:

$$H = \sqrt{(2R)^2 - R^2} = R\sqrt{3} \tag{3.5}$$

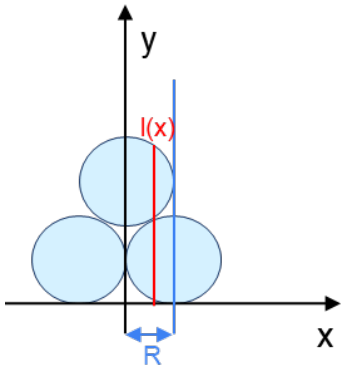

Figure 3.3: Positioning of the fibers in the two layers. The thickness traversed by a vertically incident particle at a distance x from the fiber center is indicated by the red segment l(x).

Indicating with l(x) the material thickness traversed by a vertically passing particle at a distance x from the fiber center, it can be written as the sum of contributions from the two layers:

$$l(x) = (l_1(x) + l_2(x)) \tag{3.6}$$

where $l_1(x)$ the path length in the upper layer and $l_2(x)$ in the second layer. $l_1(x)$ represents the track length for a vertically incident particle in the single-layer configuration. This length is distributed between a minimum $l_{1min} = 0$ (when the particle passes between two fibers) and a maximum $l_{1max} = 2R$ (when the particle passes through the center of the fiber). Considering a particle incident at a distance x from the center of the fiber, the expression for $l_1(x)$ is given by:

$$l_1(x) = 2\sqrt{R^2 - x^2} \tag{3.7}$$

with $x \in [0, R]$. Assuming a constant particle distribution in dx, i.e., $\frac{dN}{dx} = constant$, the average thickness of the material crossed in this configuration can be evaluated as follows:

$$\langle l_1 \rangle = \frac{\int_0^R \frac{dN}{dx} l_1(x) dx}{\int_0^R \frac{dN}{dx} dx} = \frac{1}{2R} \int_0^R 2\sqrt{R^2 - x^2} dx = \frac{\pi}{2} R \tag{3.8}$$

The expression for $l_2(x)$ is given by:

$$l_2(x) = 2\sqrt{R^2 - (R - x)^2} \tag{3.9}$$

with $x \in [0, R]$. The complete expression for the thickness of material crossed by a

vertical incident particle is:

$$l(x) = 2\sqrt{R^2 - x^2} + 2\sqrt{R^2 - (R - x)^2} \tag{3.10}$$

In this configuration, the traversed thickness varies from a minimum $l_{min} = 2R$ (when the particle passes through the center of the fiber in one of the two layers and hence between the two fibers of the other layer) to a maximum that can be determined by differentiating the expression for $l(x)$ with respect to x:

$$\frac{dl(x)}{dx} = 0 \Rightarrow x = \frac{R}{2} \Rightarrow l_{max} = 2\sqrt{3}R \tag{3.11}$$

With similar considerations to those previously mentioned, the average value can be evaluated as:

$$\langle l \rangle = \frac{\int_0^R \frac{dN}{dx} l(x)dx}{\int_0^R \frac{dN}{dx}dx} = \frac{\int_0^R \frac{dN}{dx} l_1(x)dx}{\int_0^R \frac{dN}{dx}dx} + \frac{\int_0^R \frac{dN}{dx} l_2(x)dx}{\int_0^R \frac{dN}{dx}dx} = \pi R \tag{3.12}$$

Therefore, the track length is, on average, greater, and thus the energy released will be higher, producing a detectable light signal. If the photosensor used to readout the plane is capable of reading both the fibers in the two layers on the same channel, this arrangement does not increase the total number of readout channels.

By alternating multiple planes in which fibers are arranged perpendicularly to those in the adjacent plane, 3D positional information can be reconstructed. Figure 3.4 shows a sketch of two planes of a fiber tracker. This is an established concept that has been applied in a number of past and present experiments.

If the fiber length is much smaller than the attenuation length Λ_{att}, the mean number of photons produced in a single scintillating fiber can be expressed as

$$\mu_{ph} = \int_{\Delta x} \frac{dE}{dx} dx \; Y \; \epsilon_{scint.} \tag{3.13}$$

where Δx is the thickness of the material traversed, $\frac{dE}{dx}$ is the energy loss per unit path-length, Y is the fiber light yield ans ϵ is the fiber trapping efficiency. Typical values for fiber trapping efficiency are $\epsilon_{scint.} \sim 5.4\%$. The nominal fiber light yield is in the range $Y \sim 7000 \div 10000$ photons per MeV. For Minimum Ionizing Particles (MIPs) the energy release in the plastic thickness corresponding to the fiber diameter of 500 μm is $\Delta E \approx 0.15$ MeV. The estimated number of photons is $\mu_{ph} \approx 43$ photons while for a fiber diameter of 750 μm $\mu_{ph} \approx 65$ photons.

A photosensor with high QE and gain, sensitive to single-photon signals is needed

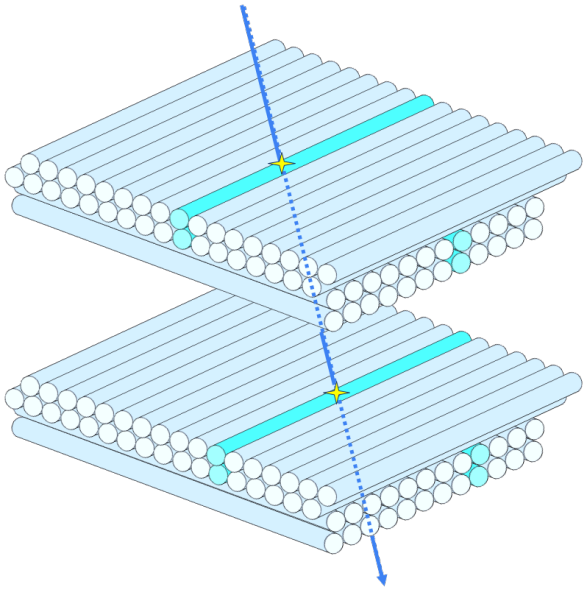

Figure 3.4: Sketch of two fiber tracker plane for track reconstruction.

to convert this faint light signal into an electric pulse of sufficient amplitude. SiPMs are well suited photo-detectors for this application. Assuming a PDE of $\sim 40\%$, it is expected to detect respectively ~ 17 and ~ 26 photoelectrons (p.e.) per MIP for the fibers of 500 µm and 750 µm diameters.

In recent years, the SiPM technology has undergone significant advancements, with the use of scintillators coupled to SiPMs rather than traditional PMTs becoming increasingly prevalent. The development of SiPM linear arrays makes fiber tracker readout with SiPMs a promising option.

A fiber tracker offers numerous advantages compared to other tracking technologies. Plastic scintillator fibers are notably lightweight and contribute to keep a reduced material budget. Additionally, obtaining X-Y position information in the way described above requires a significantly lower number of electronic channels compared to those typically needed for pixel-based trackers. Furthermore, fibers are easy to assemble, even in more complex geometries beyond the simple planar configuration.

All these features make the fiber tracker particularly well-suited for space-based applications proven its compatibility to space environment. In addition, the capability to implement a tracker composed solely of active layers, without the inclusion of passive converter planes, can be exploited for enhanced Compton electron tracking in the upcoming generation of sub-GeV photon telescopes. However, since plastic scintillators are built from materials with low atomic number, their Compton scattering and pair production cross-sections are lower compared to denser materials. Consequently, a greater number of tracking planes is required. On the other hand, the radiation length

of a plastic scintillator ($\approx$ 40 cm) is larger than that of heavier material and hence the multiple scattering angle of charged particles for a given detector thickness is reduced. This trade-off between material properties and tracking precision must be carefully balanced in the design of fiber trackers for specific applications.

3.3 FTK Modeling and Simulations

3.3.1 Modeling

The FTK will be a multiple module detector. The single module consists of two orthogonal planes, named "*view planes*", of cylindrical scintillating fibers. The fibers in each view are arranged in two staggered ribbons, disposed in a close-packed configuration and readout by a linear array of SiPMs with strip pitch comparable to the fiber radius. In this configuration if the SiPM strip pitch is equal to the fiber radius each fiber is readout by two adjacent SiPM strips. The coupling is illustrated in figure 3.6. Due to the staggered arrangement, the signal from a particle passing through the plane at normal incidence, is spread over at least three adjacent strips. The number of fired strips increases with the incidence angle. Hence, a signal from at least three strips is expected. Since the central strip is associated with the two halves of the two adjacent active fibers, while the lateral strips are associated with only one half each, the signal from the central strip is expected to have a larger amplitude. The impact position can be determined by the centre-of-gravity of the signals from the fired strips. This allows to enhance the position resolution.

For a precise position resolution, the noise contribution due to SiPM dark counts must be mitigated. This can be achieved selecting a proper threshold on the signal.

The dark signals typically correspond to signals of 1-2 photoelectrons. In contrast, the expected signal for a particle interaction is on the order of approximately a few tens of photoelectrons. Therefore, setting a threshold of three photoelectrons can be a good trade off: it effectively filters out noise while minimizing the risk of discarding physics events. "*Fired*" strips will then be grouped, forming *clusters* of adjacent strips.

3.3.2 Simulation

A simulation of the detector performance was implemented using the GEANT4 package [Agostinelli et al., 2003]. In this section, an introduction and overview of the GEANT4 toolkit is given, along with a description of the aforementioned simulation. GEANT4 version 10 was used for this work.

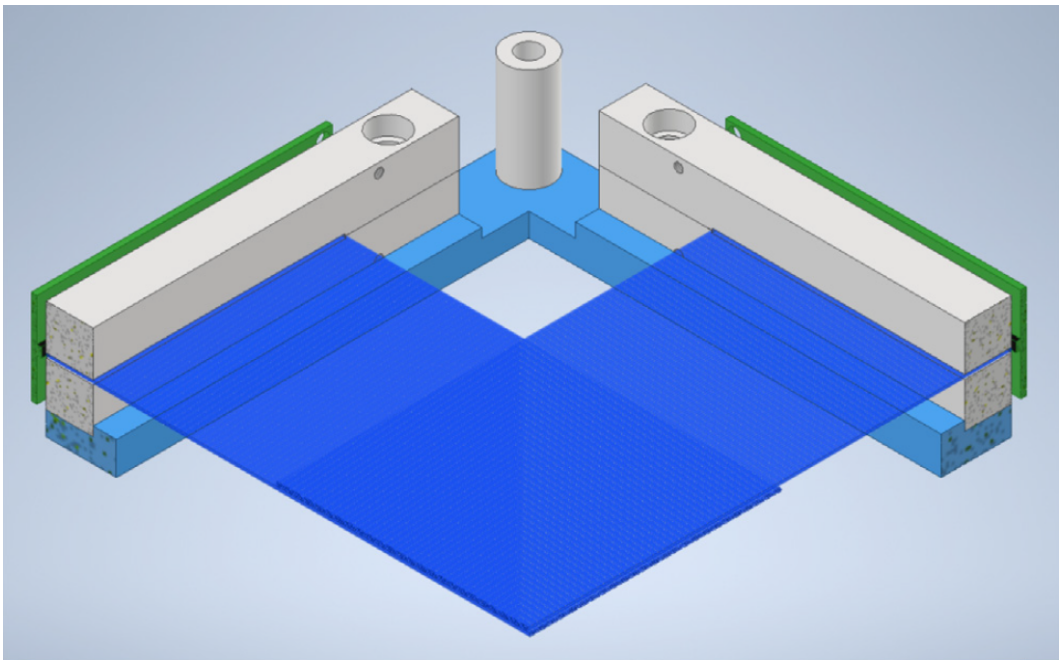

Figure 3.5: Cross sectional view of a X-Y plane of fibers in the detector prototype.

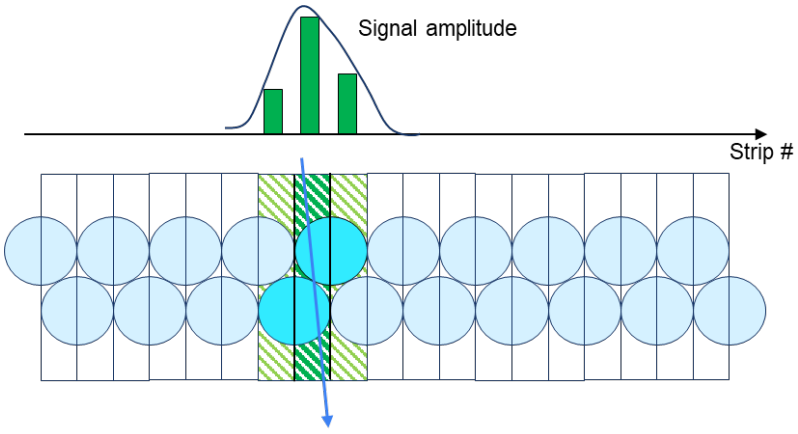

Figure 3.6: Scketch of the fiber-SiPM coupling. Each sensor collect the light from two halves of the two adjacent fibers in the ribbon. A particle crossing the plane will hit at least 2 fibers and hence at least 3 strips will be fired. The coordinate is determined by the charge centroid on the activated strips.

The GEANT4 toolkit

GEANT4 is an object-oriented toolkit written in C++ designed to simulate the interaction of particles with matter. With this toolkit it is possible to handle all the aspects of the simulation from basic system properties such as the detector geometry, the materials, the physics processes involved, the fundamental particles, the primary particles generation, to the management of tracking, sensitive detectors, the collection of relevant information and the storage of events and tracks. The software is based on an extensive set of physical models for managing particle-matter interactions, based on Monte Carlo simulation methods collected in a large number of libraries continuously refined and expanded.

Tracker Geometry

The geometry implemented with the simulation software consists of three tracker modules, each one with a surface area of 10 $\times$ 10 cm^2, kept at a distance of 2.5 cm apart. A scheme of the geometry is shown in figure 3.7. Both the size of the module and the number of modules, as well as the distance between them, are customizable. Each module is composed of two views (X and Y). Each view consists of two staggered ribbons of polystyrene fibers. The number of fibers in each layer depends on their diameter, which is a customizable parameter in the simulation. In the present work, fibers with diameters of 500 µm and 750 µm were chosen.

The simulation

Due to the complexity of the system, simulating the scintillation processes along with the corresponding optical photons would have resulted in excessive computational costs. For this reason, the simulation was limited to the energy deposition within the material of the fibers. In addition, for this reason, it was not necessary to simulate the physical volume of the SiPMs; the fired strips of the SiPM arrays were reconstructed in the analysis phase based on the information on the hit fibers. For each event, the information on the hit fibers in each plane and the total charge deposited in each of them was recorded in a ROOT file[1].

The simulated dataset consists of both electrons and photons at normal incidence with a logarithmic energy distribution in the range between 0.1 MeV and 5 GeV. Particles are uniformly emitted by a square region of 2 mm side placed at 2 mm from the center of layer 2.

[1]ROOT: Data analysis framework: `https://root.cern/`

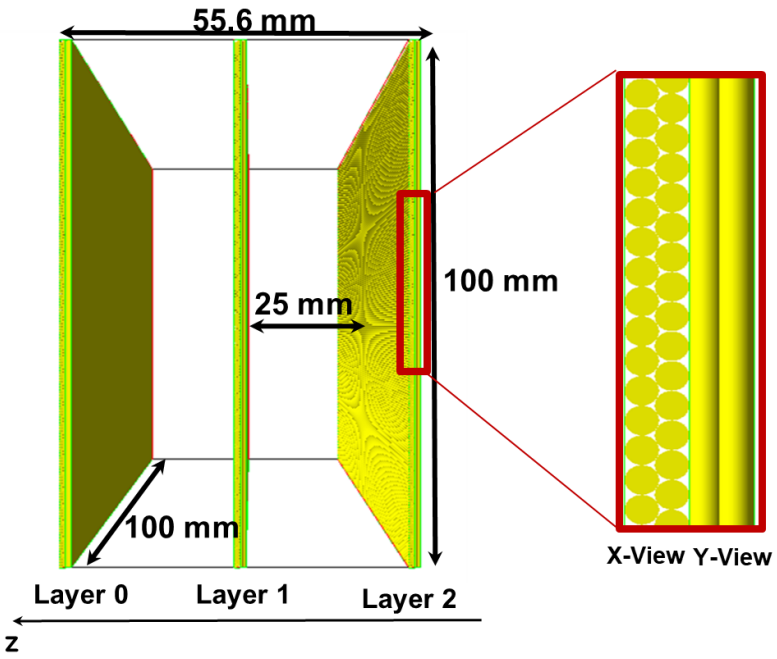

Figure 3.7: Sketch of the geometry implemented in the simulation. It consists of three tracker layers each made of two crossed plane of scintillating fibers in a double ribbon staggered configuration. Each module has an active area of 10×10 cm^2 and is placed at a distance of 2.5 cm from the adjacent plane. Simulated particles originate from a square region with a 2 mm side, located 2 cm from the center of the layer 2 and with momentum directed in the positive z-axis direction.

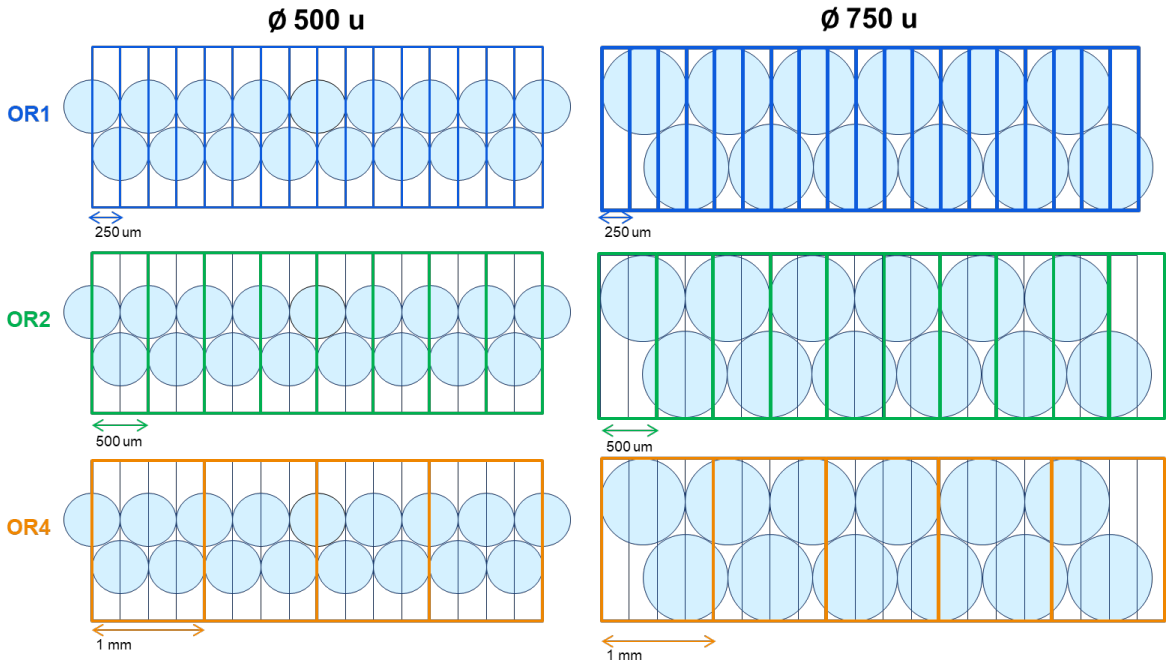

Figure 3.8: Sketch of different simulated configuration. Left: the three configurations for fibers with 500 µm diameter with strip pitch 250 µm (top), 500 µm (center) and 1 mm (bottom). Right: the same configurations for fibers with a diameter of 750 µm. Different configuration will also be tested with detector prototypes (see section 3.4). Different readout pitches will be obtained OR-ing adjacent channels OR-ing of two channels will produce the 500 µm pitch ("OR2") and OR-ing four channels produce the 1 mm pitch ("OR4").

To estimate the mean number of photons collected at the end of the fiber from the total energy deposited in each fiber, the following relation is used:

$$\mu_{ph} = \Delta E \times \mathrm{Y} \times \epsilon \tag{3.14}$$

where ΔE is the energy deposited in the fiber, $Y = 8000$ photons/keV is the fiber light yield assumed, $\epsilon = 5.4\%$ is the trapping efficiency of the fiber. Assuming that the SiPM PDE corresponds to the nominal value $PDE = 40\%$, the number of photoelectrons collected by the SiPM strip from the fiber $N_{p.e.}$ can be extracted from a Poisson distribution with mean value:

$$\mu_{p.e.} = \mu_{ph} \times \mathrm{PDE} = \Delta E \times \mathrm{Y} \times \epsilon \times \mathrm{PDE} \tag{3.15}$$

Strips with at least 3 photoelectrons are considered "fired". Adjacent hit strips are grouped into a cluster. Each view plane provides the position of the cluster in that view, calculated as the charge centroid. For details on the clustering see section 3.5.4.

The primary interest lies in evaluating the capability of the detector to track charged particles as their energy varies, and subsequently, in assessing how this performance is influenced by the choice of some parameters, such as the fiber diameter and the pitch of the SiPM array. For this reason the six configurations represented in figure 3.8 were tested.

Figure 3.9 shows the distribution of the total number of photoelectrons in each plane as a function of the primary electron energy. Referring to the geometry illustrated in the figure 3.7, the top panels correspond to the two Y-view (left) and X-view (right) planes of layer 2, central panels are referred to the layer 1, while the bottom panels refers to layer 0. From the top to the bottom, the planes are ordered along the direction of the incident particle. In the first figure (top left), we can observe a distinct family of events for energies below ~ 0.5 MeV, where the number of photoelectrons increases with energy and reaches a peak. These events are associated with electrons that do not have enough energy to reach the second plane (X-view) and are completely absorbed in the first (Y-view) plane. At higher energies, a plateau is reached, corresponding to through-passing electrons, which release the same amount of energy in the plane, independently from their energy. For these events, the average number of photoelectrons is around 25. In the subsequent layers, the family of absorbed electrons shifts to higher energies. By the last plane, electrons are passing through if their energy exceeds approximately 1.5 MeV.

Figure 3.10 reports the same plots for fibers with a diameter of 750 µm. A similar behavior to that discussed for the 500 µm fibers is observed, but in this configuration the plateau is reached in the first fiber layer at around 1 MeV, and it stabilizes at approximately 36 photoelectrons since the thickness of the material traversed is larger. This results in a higher yield from the plane, thereby increasing the signal-to-noise ratio.

In figure 3.11 the distribution of photoelectron number in the clusters of the Y-view of layer 2 is reported for different fiber radius and SiPM strip pitch. Only events in which the primary electron has a kinetic energy above 2 MeV were selected to take into account only the contribution of passing through electrons. The distributions are fitted with a Landau distribution folded with a gaussian. The light yield can be estimated with the most probable value of the best fit curve. The larger thickness of material traversed in the case of fiber with a diameter of 750 µm the higher the mean number of photoelectron. Similar results are observed in the other layers.

In figure 3.12 are reported the cluster size distributions on the Y-View of layer 2 for primary electrons with kinetic energies above 2 MeV for different the six different configurations. For the configuration with a fiber diameter of 500 µm and a pitch of

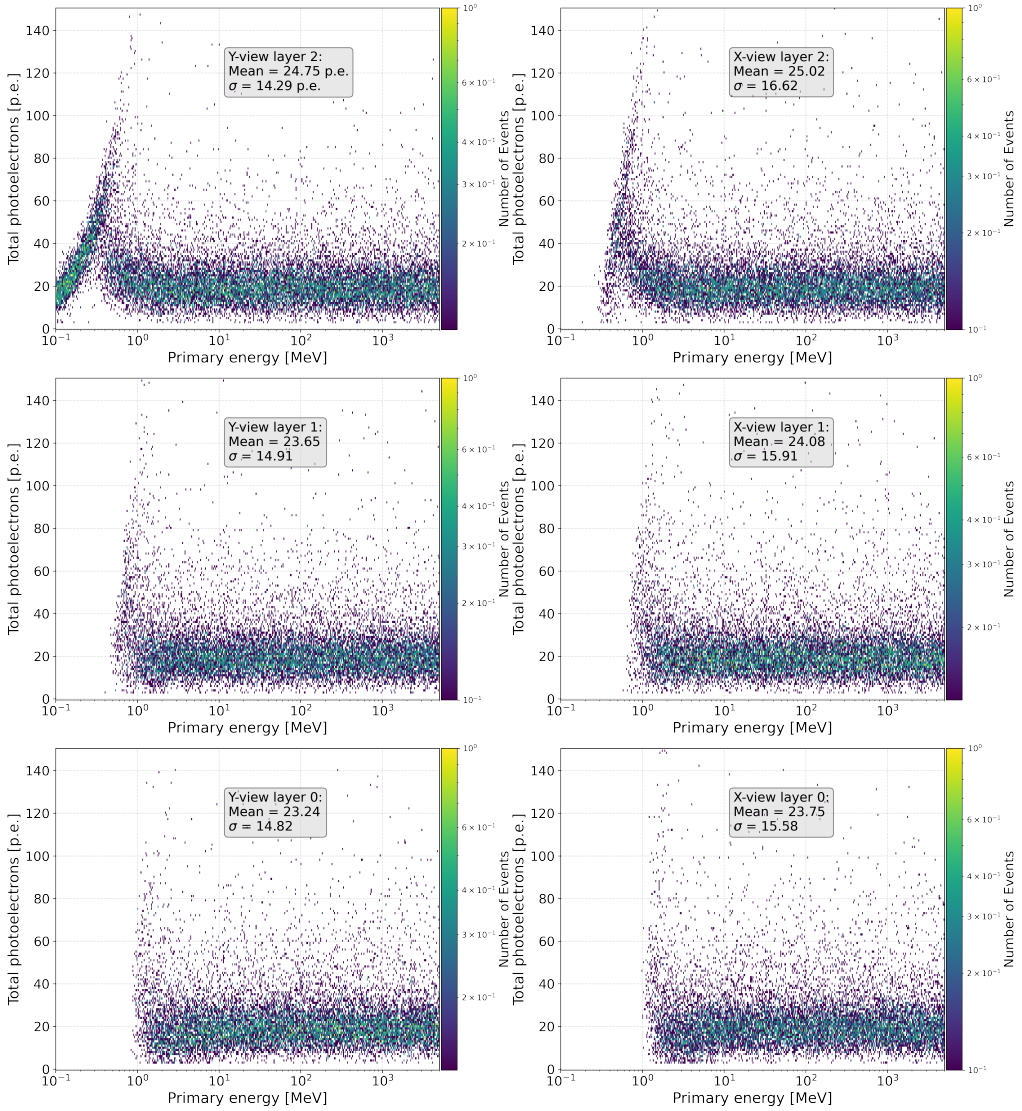

Figure 3.9: Distributions of the total number of photoelectron collected in each view plane for fibers with 500 µm diameter. Top panels: Layer 2 Y-view (left) and X-view (right). Central panels: Layer 1 Y-view (left) and X-view (right). Bottom panels: Layer 0 Y-view (left) and X-view (right).

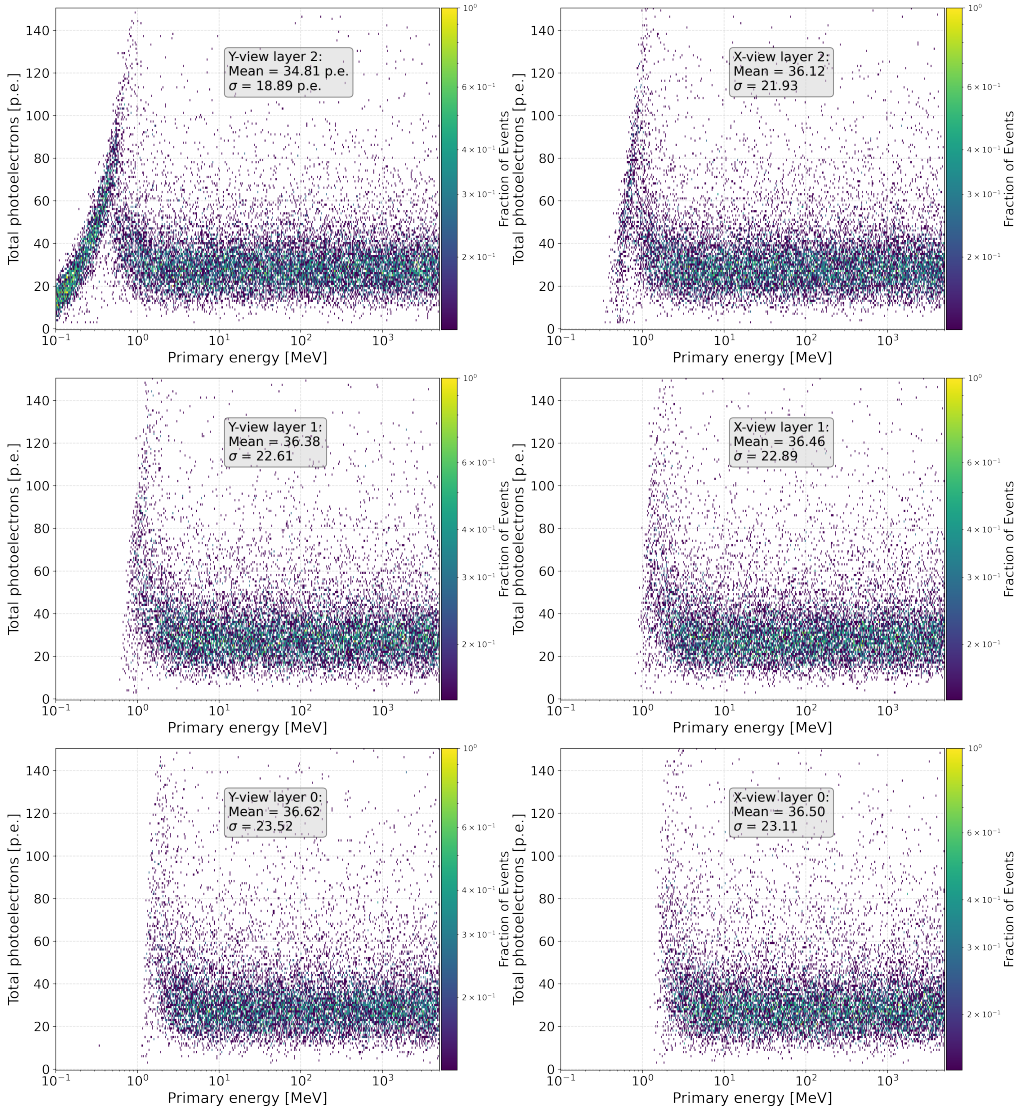

Figure 3.10: Distributions of the total number of photoelectron collected in each view plane for fibers with 750 µm diameter. Top panels: Layer 2 Y-view (left) and X-view (right). Central panels: Layer 1 Y-view (left) and X-view (right). Bottom panels: Layer 0 Y-view (left) and X-view (right).

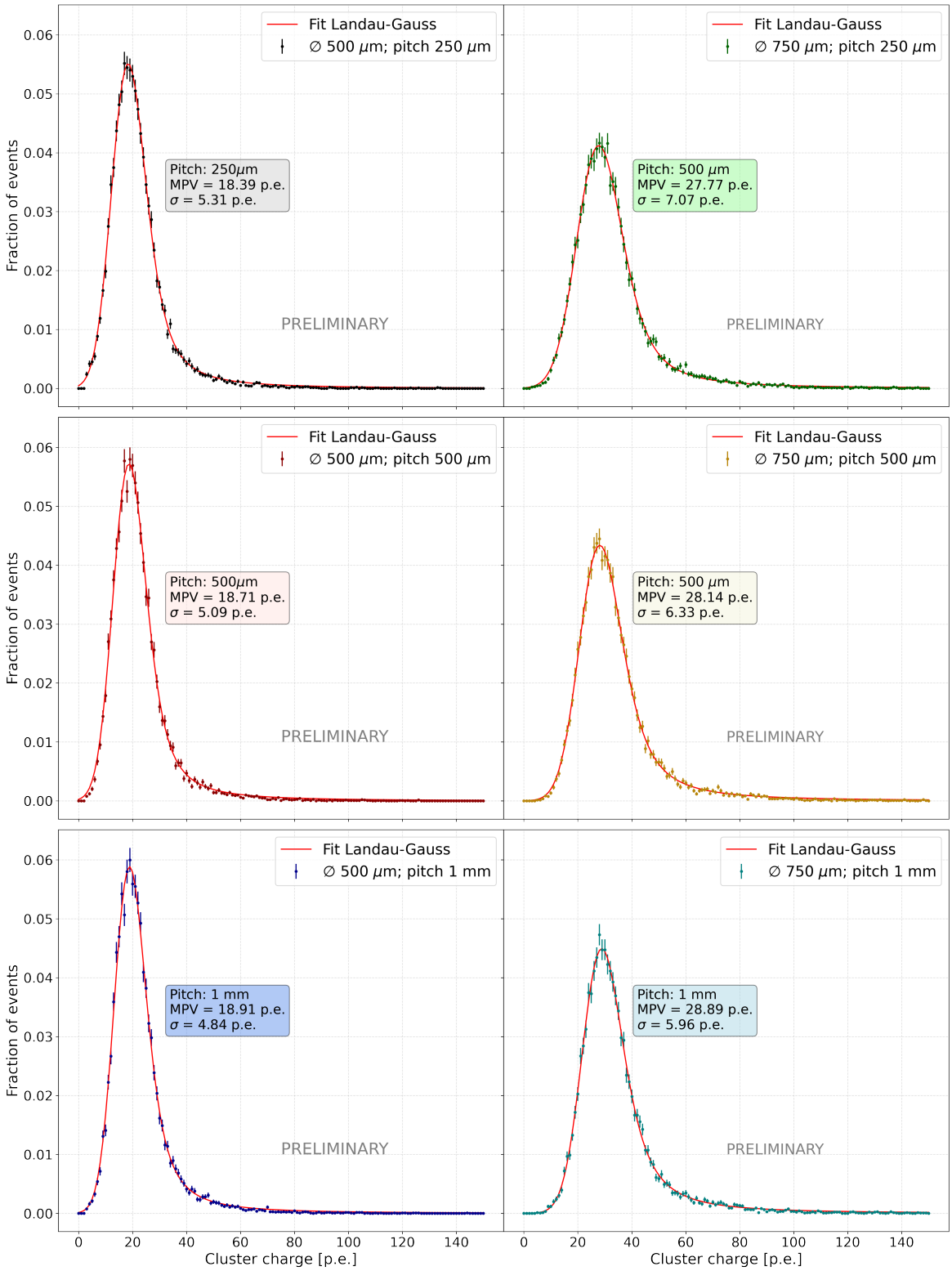

Figure 3.11: Charge distributions in clusters for incident electrons with kinetic energy above 2 MeV, for various configurations of fiber diameter and SiPM strip pitch.

250 µm (top left panel), referring to the plateau events as predicted by the model, most clusters consist of 3 strips, with a significant presence of 2-strip clusters. In the second configuration, where the number of channels is halved by doubling the pitch from 250 µm to 500 µm (left center panel), the cluster size decreases to an average of 2 strips. This happens because each strip is coupled to one complete fiber and the two halves of the adjacent fibers in the upper ribbon, hence the charge sharing is reduced to only two strips. Further increasing the pitch to 1 mm (bottom left panel) results in an equal distribution of cluster size between 1 and 2 strips. In this configuration, 4 adjacent strips are grouped into a single strip, which in some cases covers both illuminated fibers, while in others, it does not and hence two strips are fired. These considerations may be useful for implementing a trigger logic that requires the coincidence of a certain number of adjacent strips. For the three configurations with a fiber diameter of 750 µm we see that for the 250 µm pitch (top right panel), the cluster size ranges from 3 to 5 strips. This occurs because a single fiber is typically read by 3 strips. However, this configuration is not of practical interest because the number of strips (and therefore the number of required readout channels) per fiber is too high, offering no practical advantages. The right-center panel shows the results for the configuration with a 750 µm fiber diameter and a 500 µm pitch. Here, each fiber is read on average by 2 strips, and hence 2-strip and 3-strip clusters are the most common. Finally, the configuration with a 750 µm fiber diameter and a 1 mm pitch (bottom right panel) has a dominant cluster size of 2 strips as in the case of fibers with 500 µm diameter and 500 µm pitch.

The trigger efficiency for the different configurations was also estimated, defined as the probability of registering a charge of at least 3 photoelectrons in each view for at least two out of three modules. The plot in figure 3.13 summarizes the results of the efficiency as a function of the incident particle energy for the six configurations. Hence fibers with 500 µm would be sensitive to lower-energies electrons, with a drawback of being characterized by a lower light yield. It can be seen that the system shows a high efficiency, larger than 90% for electrons with energies above approximately 1.5 MeV. The threshold energy is slightly higher for configurations with a fiber diameter of 750 µm, as these fibers are capable of stopping electrons with higher energies compared to those with a diameter of 500 µm. However, no significant differences are found among different configurations in the plateau region.

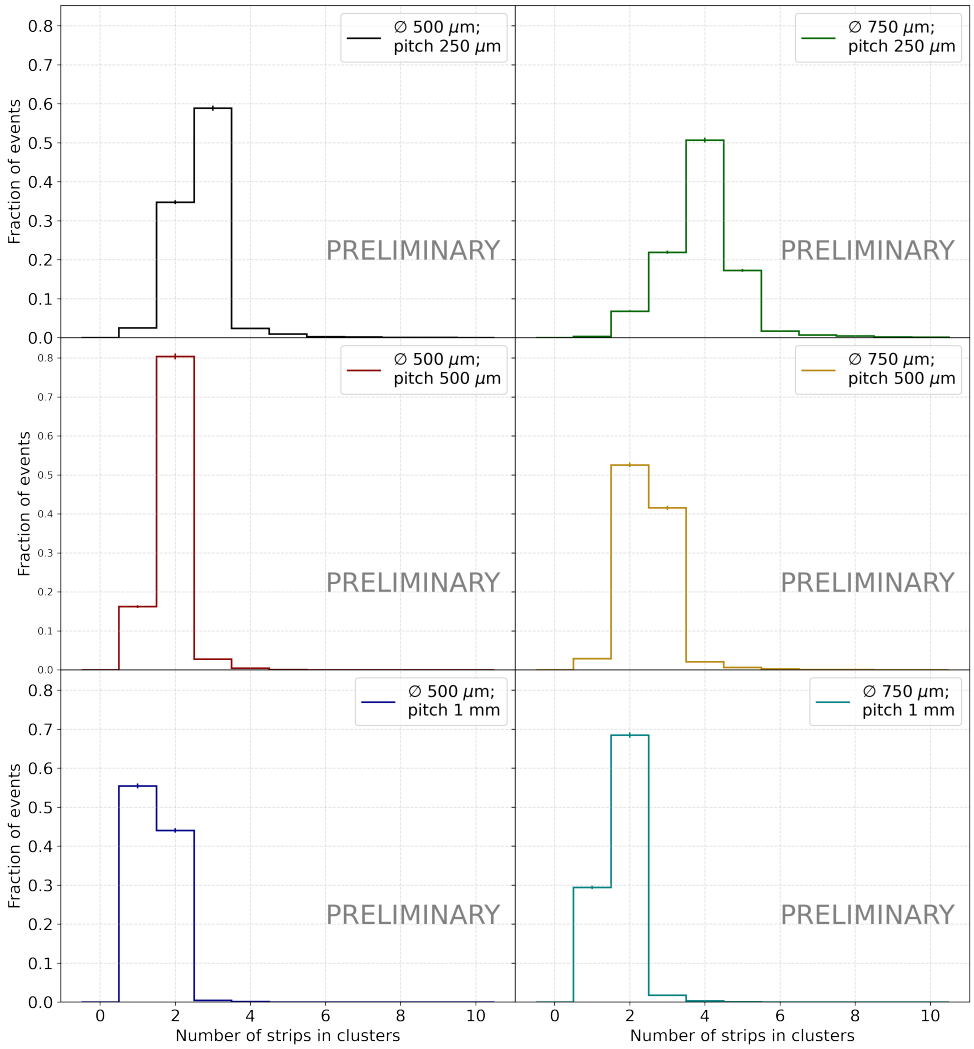

Figure 3.12: Cluster size distributions in clusters of the Y-view plane of layer 2 for incident electrons with kinetic energy above 2 MeV. Results are shown for various configurations of fiber diameter and SiPM strip pitch.

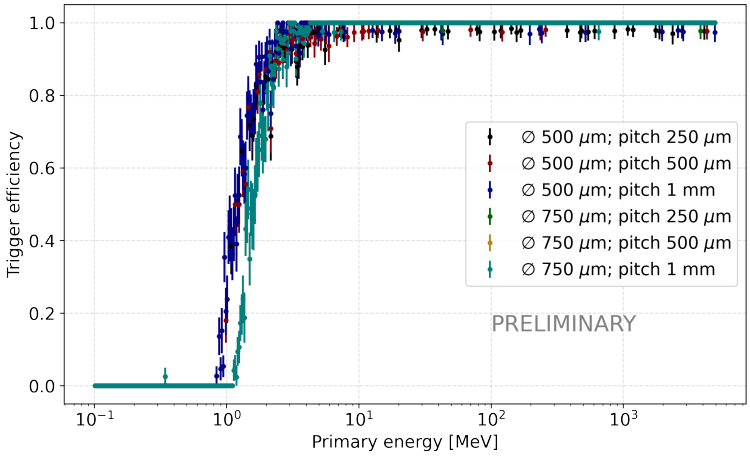

Figure 3.13: Trigger efficiency as a function of the electron kinetic energy for different configurations.

Position reconstruction

In order to evaluate the spatial resolution of the detector, the track of each particle is reconstructed from the information of the clustering position. The particle position in each view is given by the charge centroid of the cluster. An event selection was performed considering only events with at least one cluster per view in at least two layers. The best fit track in both the X-Z and Y-Z planes is evaluated. They are described respectively with the two equations

$$\begin{aligned} x &= m_x z + q_x \\ y &= m_y z + q_y \end{aligned} \tag{3.16}$$

with m_x and m_y and q_x and q_y the slope and the intercepts of the track best fit in the X-Z and Y-Z planes respectively.

These can be used to reconstruct the position x_{rec} and y_{rec} on each module. The residuals on each plane are then calculated as the distance between the calculated position and the reconstructed position:

$$\begin{aligned} r_x &= x_{clu} - x_{reco} \\ r_y &= y_{clu} - y_{reco} \end{aligned} \tag{3.17}$$

The expected distribution of the residuals is a Gaussian centered at zero with the σ corresponding to the spatial resolution of the tracker.

Figures 3.14, 3.15 and 3.16 show the distribution of residuals of the Y-view plane

	Resolution [µm]	
Strip pitch [µm]	250	500
Layer2 Y-view	62 ± 1	67 ± 1
Layer2 X-view	62 ± 1	67 ± 1
Layer1 Y-view	81 ± 4	81± 4
Layer1 X-view	81 ± 4	81 ± 5
Layer0 Y-view	81 ± 5	89 ± 5
Layer0 X-view	85 ± 5	89 ± 5

Table 3.1: Summary of the resolution values estimated from the fit of the residual distributions for fibers with 500 µm diameter. The resolutions and errors are estimated from the fit with the pseudo-experiment method.

respectively of the first, second and third tracker module. The results for the six configurations are summarized in tables 3.1 and 3.2.

In figure 3.14 the distribution of the residuals for the first module traversed by the particle are shown. The distribution is Gaussian, centered around zero for each of the configurations under examination. The best spatial resolution is achieved in the configuration with fibers of 500 µm diameters coupled to a SiPM array with a strip pitch of 250 µm (top left panel), and it is also reduced compared to the nominal value $\frac{pitch}{\sqrt{12}} \simeq 72$ µm, thanks to charge sharing between adjacent strips. The resolution is slightly higher but still smaller than the nominal value for the configuration with the pitch of 500µm (bottom left panel). In contrast, for fibers with a diameter of 750 µm, the resolution is unchanged between configurations with pitches of 250 and 500 µm. When the pitch is increased to 1 mm (bottom right panel) with 750 µm diameter fibers, the resolution slightly increase, since the larger pitch is compensated by charge sharing between adjacent strips. On the contrary, for fibers with a diameter of 500 µm, in the configuration with a strip pitch of 1 mm, the charge sharing is negligible causing a worsening in the resolution. Similar considerations apply to the X-view plane of the same layer.

In figure 3.15 the distributions for layer 1 are shown. In these distribution tails begin to appear. These are caused by charged particles undergoing multiple Coulomb scattering with the nucleus of atoms of the material as they pass through the tracker planes. This can result in significant deviations from the expected trajectory, increasing the residuals and generating tails in the data. Consequently, the distribution becomes the sum of two gaussians with different width. In this case, the resolution can be estimated from the Full Width at Half Maximum (FWHM) of the best fit curve and noting that for a Gaussian function, $FWHM = 2\sigma\sqrt{2\ln 2}$. The errors on the FWHM values are estimated with the pseudo-experiment method.

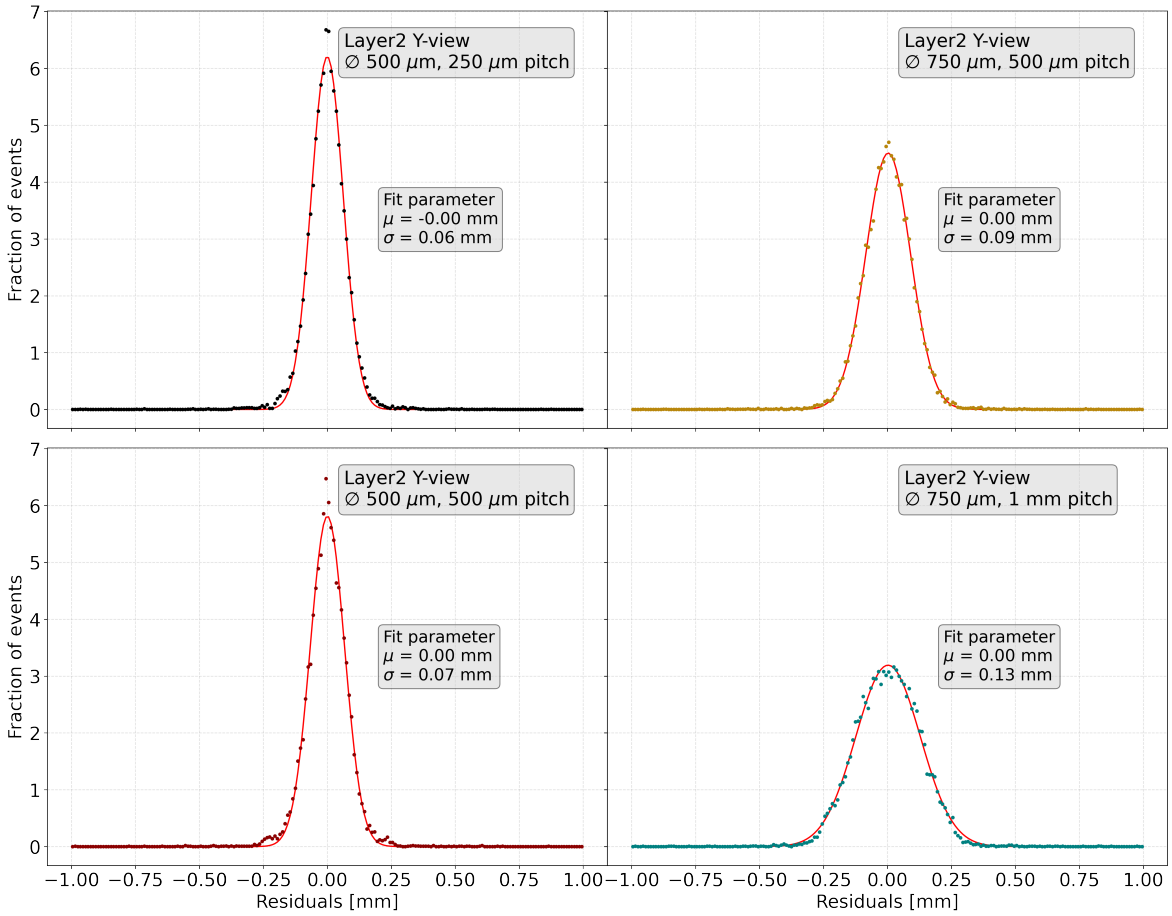

Figure 3.14: Distributions of residuals in the Y-view plane of layer 2. Top left: configuration with 500 µm diameter fibers and 250 µm SiPM strip pitch. Bottom left: configuration with 500 µm diameter fibers and 500 µm SiPM strip pitch. Top right: configuration with 750 µm diameter fibers and 500 µm SiPM strip pitch. Bottom left: configuration with 750 µm diameter fibers and 1 mm SiPM strip pitch.

	Resolution [µm]	
Strip pitch [µm]	500	1000
Layer2 Y-view	88 ± 1	126 ± 1
Layer2 X-view	88 ± 1	127 ± 1
Layer1 Y-view	102 ± 6	144 ± 8
Layer1 X-view	115 ± 6	157 ± 8
Layer0 Y-view	106 ± 6	153 ± 9
Layer0 X-view	115 ± 7	157 ± 9

Table 3.2: Summary of the resolution values estimated from residual distribution for fibers with 750 µm diameter. The resolutions and errors are estimated from the fit with the pseudo-experiment method.

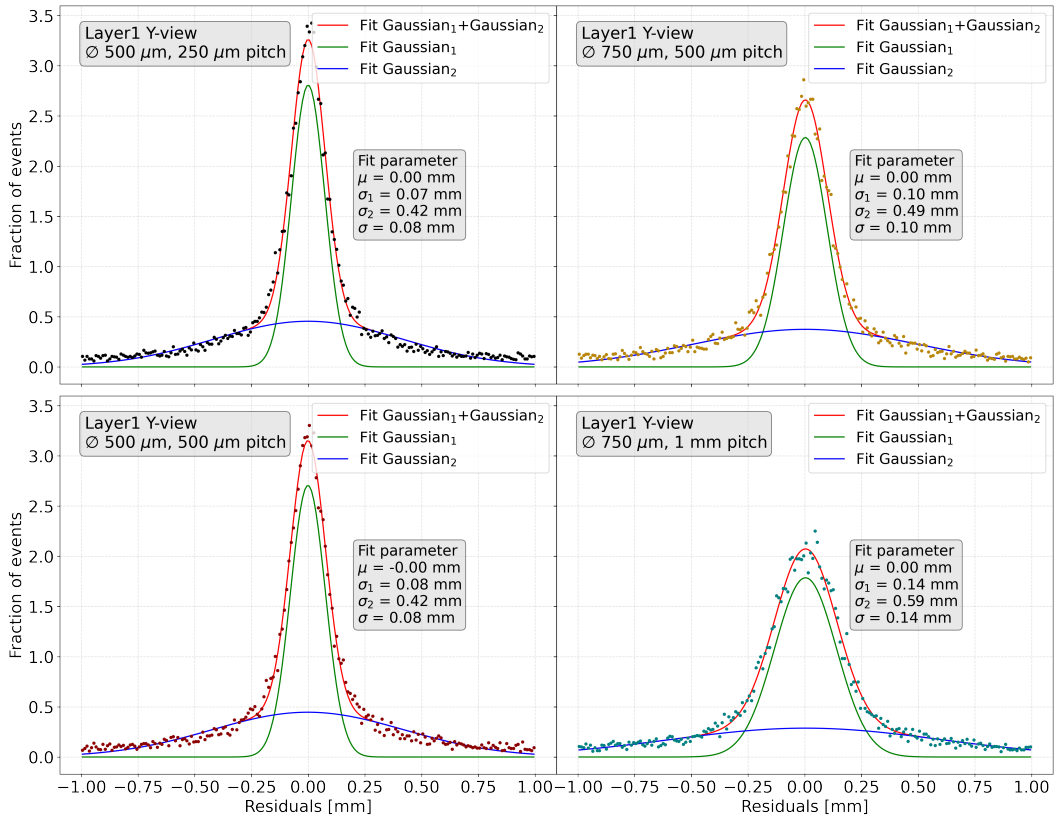

Figure 3.15: Distributions of residuals in the Y-view plane of layer 1. Top left: configuration with 500 µm diameter fibers and 250 µm SiPM strip pitch. Bottom left: configuration with 500 µm diameter fibers and 500 µm SiPM strip pitch. Top right: configuration with 750 µm diameter fibers and 500 µm SiPM strip pitch. Bottom left: configuration with 750 µm diameter fibers and 1 mm SiPM strip pitch.

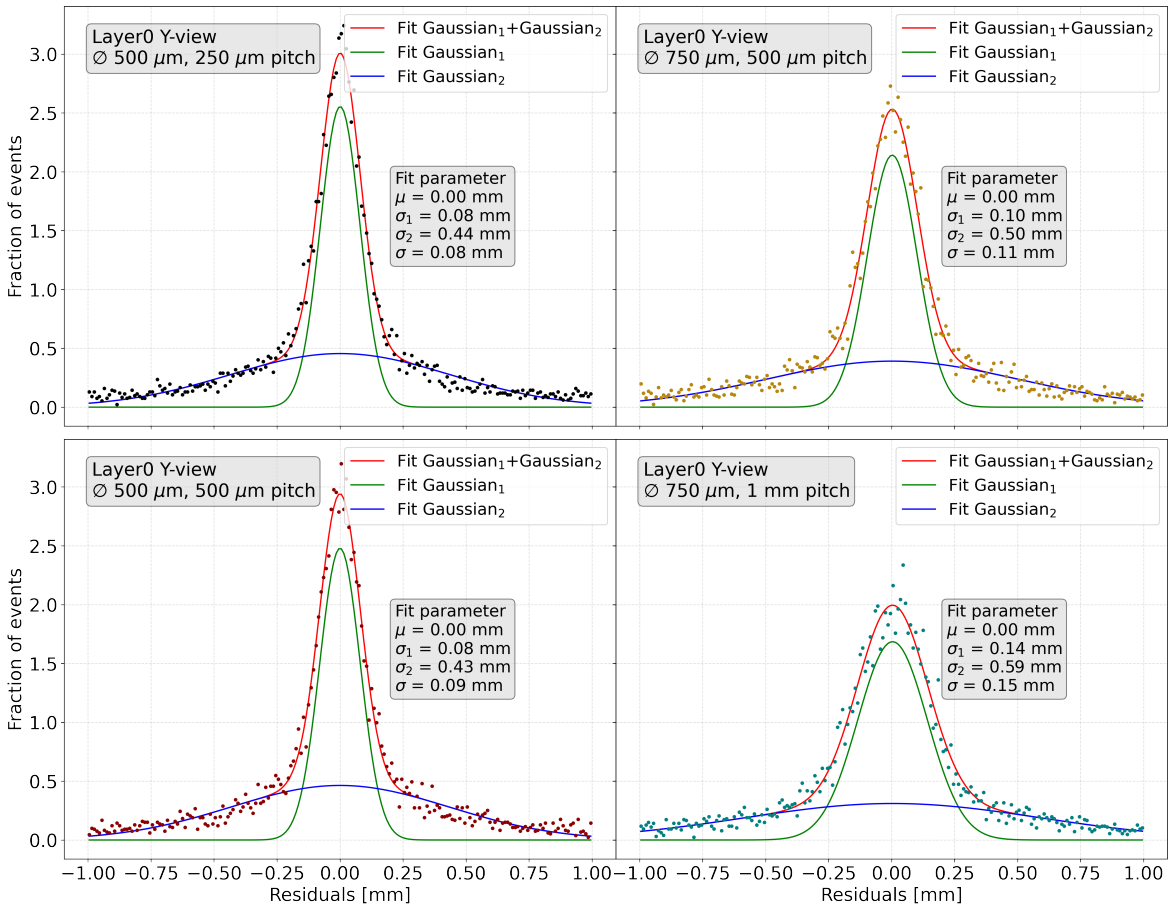

Figure 3.16: Distributions of residuals in the Y-view plane of layer 0. Top left: configuration with 500 µm diameter fibers and 250 µm SiPM strip pitch. Bottom left: configuration with 500 µm diameter fibers and 500 µm SiPM strip pitch. Top right: configuration with 750 µm diameter fibers and 500 µm SiPM strip pitch. Bottom left: configuration with 750 µm diameter fibers and 1 mm SiPM strip pitch.

Finally, the equation of the line in space can be written in parametric form, with parameter t using 3.16 as:

$$\vec{r}(t) = \begin{pmatrix} x \\ y \\ -t \end{pmatrix} = \begin{pmatrix} m_x \cdot t + q_x \\ m_y \cdot t + q_y \\ -t \end{pmatrix} = \begin{pmatrix} m_x \\ m_y \\ -1 \end{pmatrix} \cdot t + \begin{pmatrix} q_x \\ q_y \\ 0 \end{pmatrix} = \vec{v} \cdot t + \vec{r_0} \tag{3.18}$$

Then, denoting the unit vectors along the Cartesian axes as $\hat{i}$, $\hat{j}$ and $\hat{k}$, the direction cosines are:

$$\begin{cases} c_x = \frac{\langle \vec{v}, \hat{i} \rangle}{\|vecv\|} \\ c_y = \frac{\langle \vec{v}, \hat{j} \rangle}{\|vecv\|} \\ c_z = \frac{\langle \vec{v}, \hat{k} \rangle}{\|vecv\|} \end{cases} \tag{3.19}$$

Therefore, combining the two previous equations, we have:

$$\begin{cases} c_x = \frac{m_x}{\sqrt{m_x^2 + m_y^2 + 1}} \\ c_y = \frac{m_y}{\sqrt{m_x^2 + m_y^2 + 1}} \\ c_z = \frac{-1}{\sqrt{m_x^2 + m_y^2 + 1}} \end{cases} \tag{3.20}$$

Therefore, if the Monte Carlo track is $\vec{r}_{MC}$ with the direction cosines directly stored in the simulation output, the angular separation θ between the Monte Carlo track and the reconstructed track tracks can be evaluated as:

$$\theta = \arccos \langle \vec{r}, \vec{r}_{MC} \rangle = c_x \cdot c_{x_{MC}} + c_y \cdot c_{y_{MC}} + c_z \cdot c_{z_{MC}} \tag{3.21}$$

Figure 3.17 shows the distribution of the angle θ indicating the angular resolution of the tracker.

In figure 3.18 is reported the angular resolution as a function of the primary energy. The 50%, 68% and 90% quantiles are evaluated in each energy bin, these are used to study respectively the 50%, 68% and 90% containment angles. The curves are reported in the plot. The red curve shows the theoretical limit that takes into account the intrinsic resolution of the instrument and the mean deflection due to the multiple Coulomb scattering in the material of the fiber tracker layers. The contribution of the intrinsic resolution can be expressed as:

$$d\theta_{res} = \frac{pitch}{\sqrt{12}} \frac{1}{d} \tag{3.22}$$

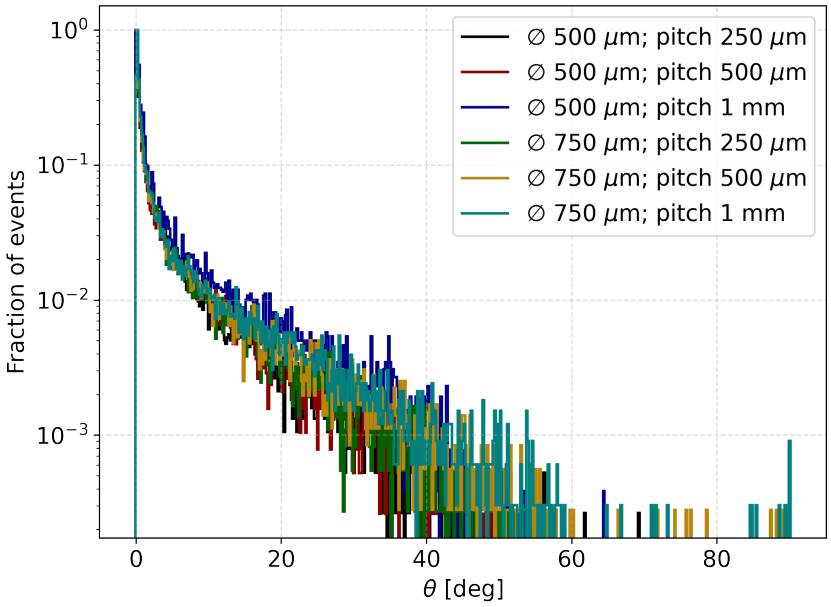

Figure 3.17: Distribution of the angle θ between the Monte Carlo track and the reconstructed track.

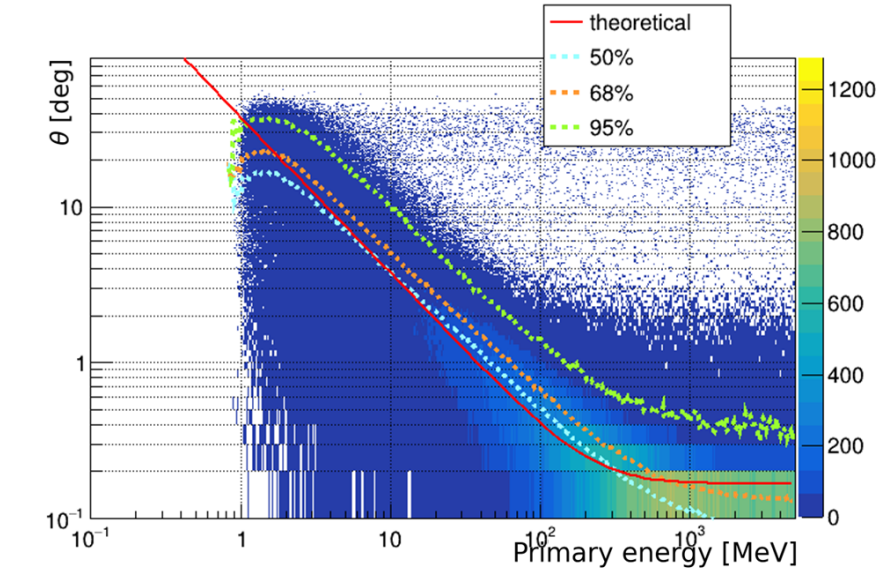

Figure 3.18: Distribution of the angular separation θ between the Monte Carlo track and the reconstructed track as a function of the energy. The containment at 50%, 68% and 95% are also reported. The theoretical line in red shows the limit due to multiple Compton scattering and to the resolution of the instrument.

with d the separation between the tracker modules.

The mean multiple Coulomb scattering deflection can be expressed as:

$$d\theta_{MCS} \simeq \frac{13.6 \text{ MeV}}{\beta pc} Z \sqrt{\frac{X}{X_0}} \tag{3.23}$$

where p, βc, and Z are the momentum, velocity, and charge number of the incident particle, and $\frac{X}{X_0}$ is the thickness of the scattering medium in radiation lengths [Navas et al., 2024]. For relativistic electrons $\beta \sim 1$ and $pc \sim E$ and hence the relation 3.3.2 give the dependence of the minimum deflection from the energy. The two contributions can be added in quadrature, yielding the theoretical value of the average deflection in the tracker. The angular separation at 68% containment for $E > 100$ MeV is $\theta_{68} < 0.7°$ and $\theta_{68} < 0.1°$ for $E > 1$ GeV, respectively.

Similar results have been obtained for simulation with protons. In conclusion, these simulation studies have demonstrated how the performance of the detector is influenced by the diameter of the chosen fibers and the pitch of the sensors used for light collection at the fiber ends. The studies indicate that the best results are achieved with strip pitches comparable to the fiber radius. However, using a pitch approximately equal to the fiber diameter allows for effective charge sharing, thereby maintaining high performance while halving the number of electronic channels required for system readout. At the same time, although thinner fibers provide better resolution, the charge collected with thicker fibers is greater, facilitating better signal discrimination from noise and ensuring higher efficiency with limited contamination from false events.

3.4 The prototype

In order to evaluate and validate the performance of the proposed tracker, I have been involved in the development of multiple prototype modules over recent years. This effort led to the construction of a final tracker prototype composed of three modules each consisting of two orthogonal layer. One module has been realized using fibers with a diameter of 500 µm and two using fibers with a diameter of 750 µm. In this preliminary prototypes the active region of each module is of about 3.2×3.2 cm^2.

3.4.1 Scintillating fibers

The first prototype was assembled with Saint-Gobain BCF-12 circular fibers with a diameter of 500 µm . Following preliminary tests for evaluating the light yield of these fibers (see section 4.1.1) for the final three tracker modules, multi-clad blue

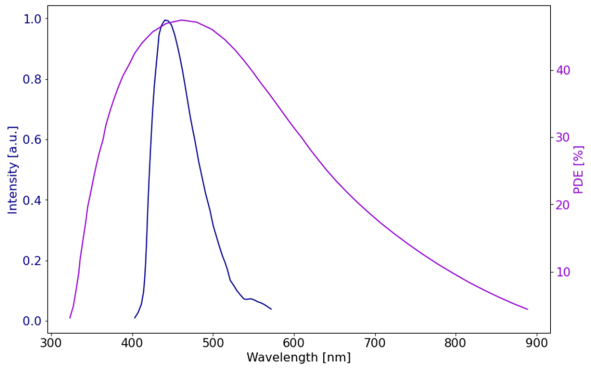

Figure 3.19: PDE of HPK S13552 SiPM array and nominal emission spectrum of Kuraray SCSF78-MJ scintillating fibers. The PDE is measured at $V_{op} = V_{BD} + 3.5V$. The maximum PDE reaches 47% at the peak sensitivity wavelength $\lambda_p = 450$ nm, which is matched with the peak emission wavelength of the scintillating fiber.

emitting fibers with circular cross-section from Kuraray were selected, specifically, the SCSF78-MJ. These fibers include a polystyrene core with a primary dye of p-terphenyl (PT) and a waveshifter component of tetraphenyl-butadiene (TPB). The two cladding layers have a thickness of about 4% of the fiber radius. The inner cladding is made of PMMA and the outer cladding is made of a fluorinated polymer (FP). The refractive index of the material is decreasing from the core to the outer cladding, $n_{core} = 1.59$, $n_{cladding1} = 1.49$, $n_{cladding2} = 1.42$.

To compare the performance of tracker modules with different fiber diameter, as in simulations, different modules were assembled using fibers with 500 µm and 750 µm diameters.

Figure 3.19 shows in blue the nominal emission spectrum. It extends from $\sim$ 440 nm to 500 nm with the peak emission at 425 nm. The mean number of photoelectrons observed by a SiPM at the end of a fiber per mm of scintillating fiber traversed by a charged particle is between 15 and 20. Typical attenuation lengths for these fibers are in the order of few hundreds of cm and hence within the requirement of the detector.

3.4.2 Silicon Photomultiplier

As highlighted in section 3.2, scintillating fibers produce a limited number of photons in response to particle energy deposition. Consequently, to ensure a high tracking efficiency, the photodetector coupled to the fibers must meet several requirements. These include achieving a high PDE within the wavelength range corresponding to emission spectrum of the fibers, and the capability to implement a high channel density system, while minimizing power consumption and keeping low production costs. As previously mentioned, SiPMs offer the optimal solution for these

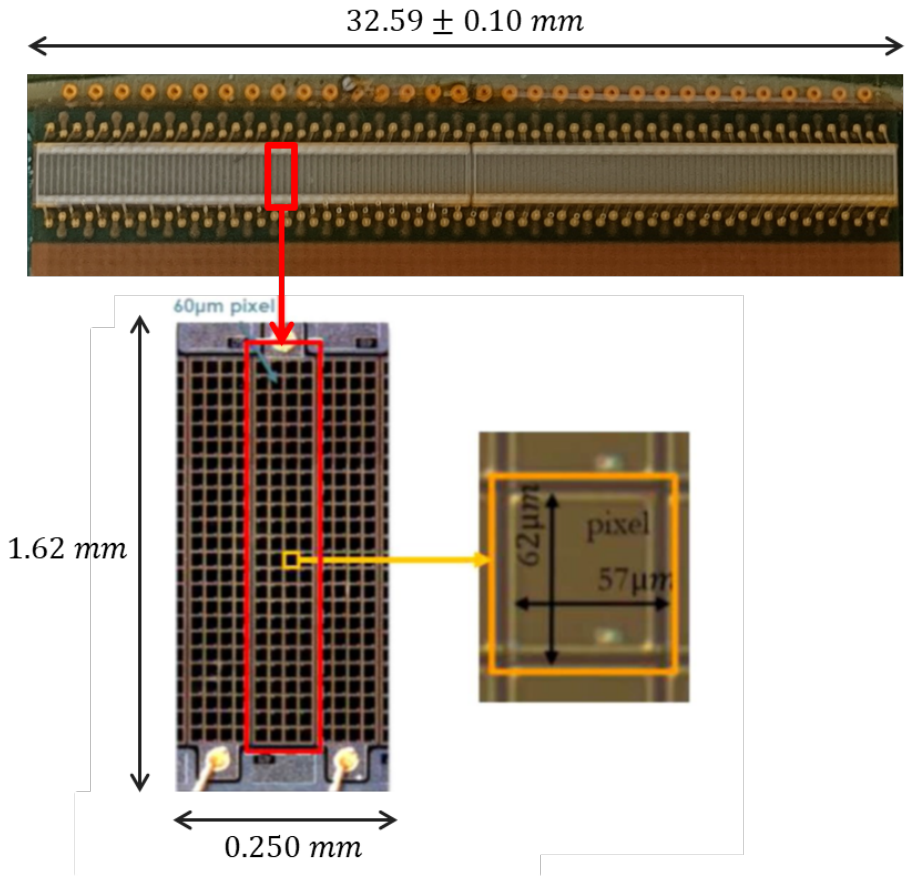

Figure 3.20: Inset view of the Hamamatsu 128-channel SiPM linear arrays S13552 and a zoom on the single strip structure in order to show the pixels disposition [Gruber, 2020].

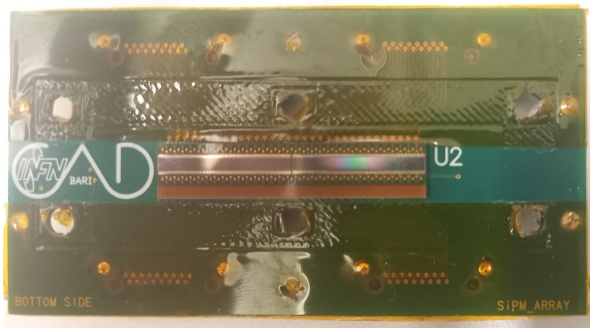

Figure 3.21: Photo of the PWB designed for the SiPM array.

requirements.

In particular for the LHCb SciFi tracker, Hamamatsu developed the S13552 custom 128-channel SiPM linear arrays[2] [Joram et al., 2015]. It consists of two 64-channels arrays mounted on a common printed circuit board (PCB) with a separation of 0.22 mm. Each channel, or strip, has an area of 0.23×1.62 mm^2 consisting of 4×26 pixels with size 57.5×62.5 µm^2. The resulting strip pitch is 250 µm. The pixel size was maximized to increase the QE, as larger pixels enhance the geometrical fill factor (FF). For these SiPMs, the FF is approximately 78%. However, the increased pixel size introduces saturation effects on the strips. In order to reduce optical cross-talk, isolation trenches are implemented between pixels. An epoxy protection layer 105 µm thick covers the optical window.

Figure 3.19 shows a comparison between the SiPM PDE and the scintillating fiber emission spectrum. As can be seen the wavelength ranges are in perfect alignment, ensuring optimal photon detection efficiency.

Figure 3.20 shows close-up view of the SiPM array, highlighting its structure. The SiPM array is bonded on one side of a dedicated printed wiring board (PWB) designed to route all the 128 channels to four LSHM-120 Samtec multi-channel connectors located on the other side of the PWB (see figure 3.21). The routing is configured to alternate connections between adjacent strips and connectors, as depicted in figure 3.22. This design facilitates the generation of electronic signal coincidence at a hardware level.

The bias voltage is supplied to the SiPMs through separate lines at each connector.

To study the possibility of reducing the number of electronic channels, which is crucial for space applications, two different PWB interfaces (OR-masks) were designed, allowing to perform parallel readout of multiple adjacent strips. Specifically two different types of interface were built, the OR-ing 2 adjiacent channels ("*OR2*) and

[2]Hamamatsu Photonics S13552 MPPC array, `https://www.hamamatsu.com/eu/en/product/optical-sensors/mppc/mppc_mppc-array/S13552.html`

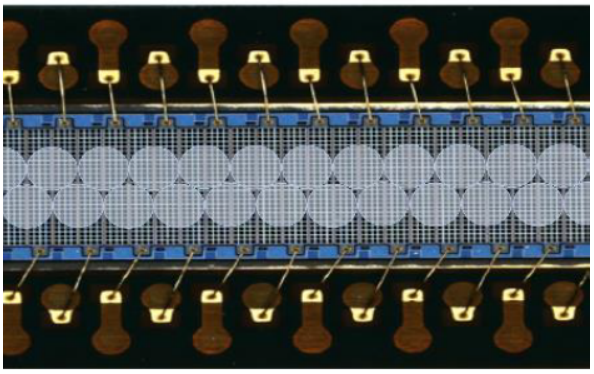

Figure 3.22: Wiring scheme for the connection of the adjacent strips to alternate connectors. This configuration allows to share the information relative to a single fibre on different ASICs.

the OR-ing 4 adjacent channels ("*OR4*"). Figure 3.8 shows the different configuration tested. The left panel reports the configurations for fiber with 500 µm diameter in the three different configurations: no mask in the top panel, OR2 in the central panel and OR4 in the bottom panel. The right panel reports the same configurations with fiber of 750 µm diameter.

The interface masks are designed with four LSHM-120 Samtec connectors on one side (aligned with those on the SiPM array PWB) and either two or one LSHM-120 Samtec connectors on the opposite side. Figure 3.23 shows the CAD view of the OR interface PWBs.

The standard configuration, with no mask interface, will be referred to as "*OR1*". In the OR1 configuration, fibers are read out by 128 channels requiring 4 connectors (250 µm pitch). When the OR2 mask is applied, the number of channels is reduced to 64 (2 connectors), and increasing the readout pitch to 500 µm. With the OR4 setup, the channels are further reduced to 32, allowing the use of a single connector (readout pitch 1 mm).

A larger readout pitch reduces the number of electronic channels but simultaneously decreases the spatial resolution of the tracker. Therefore, it is essential to find a trade-off between these two aspects to optimize both the resolution and the number of required electronic channels.

3.4.3 Module

Each module of the prototype was realized according to the model described in the section 3.2. The module has a square cross-section with a side of $\sim$ 3.2 cm in the X-Y plane. This dimension correspond to the width of the SiPM array. The minimum

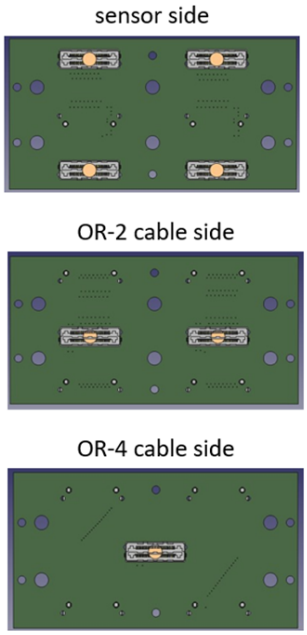

Figure 3.23: CAD views of the OR interface PWBs. The first shows the side to be connected to the sensor PWB, the other two show the cable side of the OR-2 and OR-4, respectively requiring 2 and 1 cables respectively.

separation between two adjacent modules is dictated by the dimension of the SiPM PWB. Each module consists of 2 planes, one for the X-view and one for the Y-view. The single view consists of a fiber ladder with a length of about 12 cm and a width of about 3.2 cm, consisting of two staggered ribbons of fibers.

3.4.4 Prototype assembly

Ribbon assembly

In order to achieve a good spatial resolution, the fiber mats in the different planes must be assembled with precision. Defects in the positioning of the fibers will affect the position reconstruction accuracy.

A jig was manufactured with a specific design to keep the fibers in place in the staggered configuration and control their tension. Two end-caps, where the fibers have to be glued, are fixed to the jig.

The fibers were cut into sections of approximately 14 cm length to extend a few centimeters beyond the end-caps. Each ribbon was assembled by aligning the fibers side by side in contact within the jig. The photo in the left panel of figure 3.24 shows this step of the assembly procedure. The photo in the right panel provides a detailed view of the fibers aligned within the jig. A thin layer of epoxy glue (EPO-TEK 301)

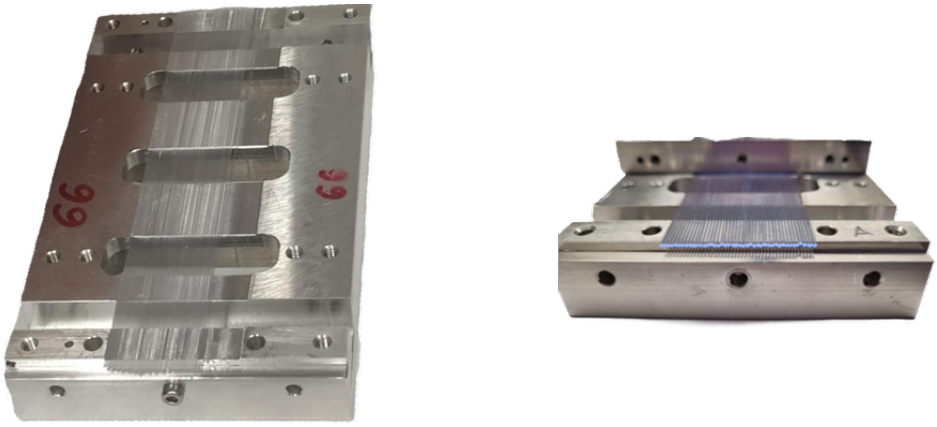

Figure 3.24: Assembly of a FTK ribbon. Left: the fibers are aligned in the dedicated jig forming a ribbon. Right: detailed view of the precise alignment of the fibers within the cavity specifically designed in the jig to fit the correct number of fibers.

was carefully applied to the end-cap before positioning the fibers, ensuring precise alignment and secure fixation of the fibers in their designated positions. The epoxy has a pot-life of eight hours which provides sufficient working time for positioning all the fibers of the ribbon. To ensure a precise alignment of the two ribbons they differ by one fiber. After the realization of the two ribbons it is necessary to wait for the epoxy cure-time before proceeding with the assembly of the ladder for the single view.

Ladder assembly

The view ladder is built by accurately aligning and stacking the two preassembled fiber ribbons in their own jig (left panel of 3.25). The right panel shows the complete ladder after the jig removal. A precise diamond milling of the ends of the fiber mats and of the end-caps is done to provide a smooth contact surface with the SiPM arrays. Following the described procedure, two ladders were assembled.

Module assembly

The two ladders were subsequently mounted on a dedicated aluminium support structure, oriented orthogonally to each other to form an X-Y module. The jigs were removed at the end of the process, when each plane is fixed on the frame as illustrated in figure 3.26. During the three year of my PHD three fiber tracker modules were built, one with fibers with a diameter of 500 µm and 2 with diameter of 750 µm. In figure 3.27 a photo of the three layer telescope obtained by stacking the three modules is shown.

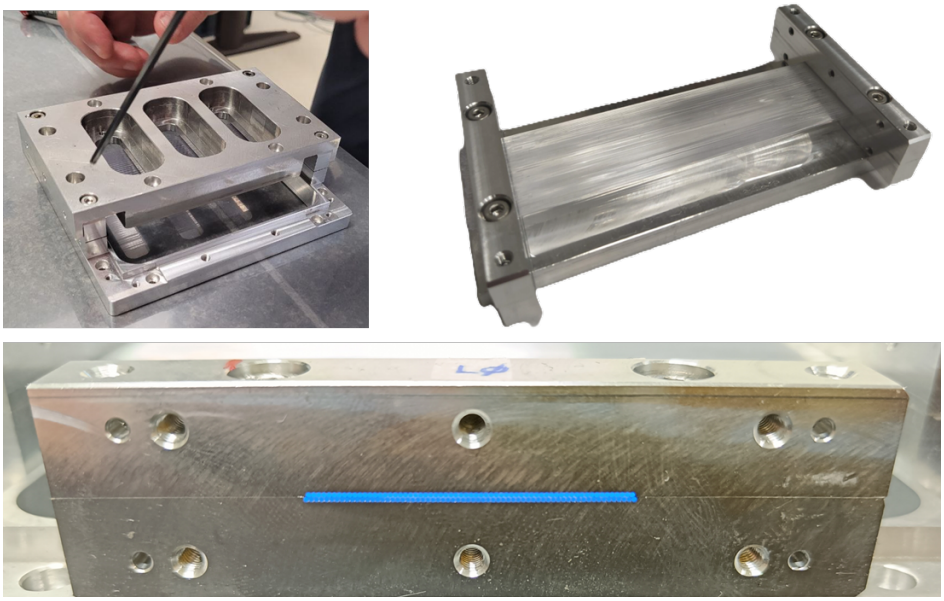

Figure 3.25: Top panels: procedure of assembling two ribbons to form a view plane. Left: the two fiber ribbons are accurately aligned by means of their own jig in an aluminum frame structure. Right: the completed two-ribbon plane. The end-caps keep fibers in position and ensure the correct tension to be applied. Bottom panel: detail of the final fiber positioning in the ladder.

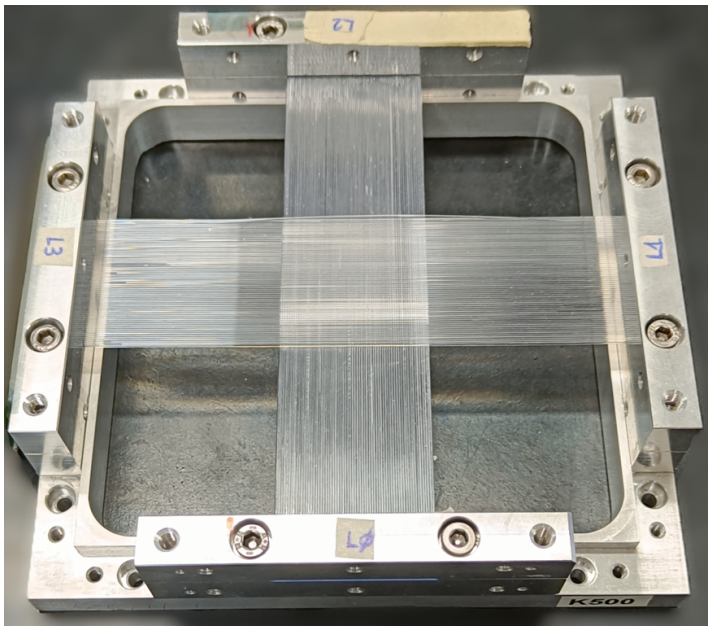

Figure 3.26: The X-Y module of the fiber tracker prototype.

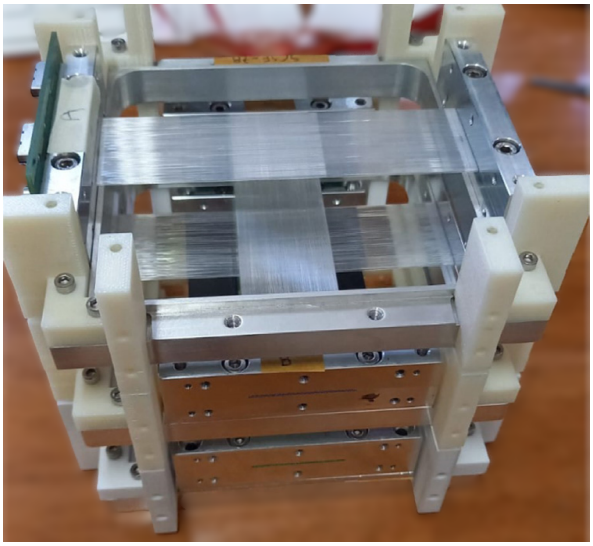

Figure 3.27: Three X-Y modules of the fiber tracker protorype.

3.5 Front-end electronics

The readout system includes a custom front-end board (FEB) specifically developed for prototype evaluation.

The FEB hosts four Petiroc 2A ASICs, a CAEN A7585D SiPM voltage module and a Kintex-7 FPGA mounted on a Mercury+ KX2 module. The FPGA si responsible for managing the trigger settings, configuring the ASIC parameters and handling the data acquisition (DAQ). Each Petiroc 2A ASIC can readout 32 channels, hence enabling the FEB to handle a total of 128 channels, sufficient to fully interface with a Hamamatsu S13552 SiPM array. The Petiroc 2A ASIC was used because it provides a fast trigger line for each channel, and additionally, internal ADC (Analog to Digital Converter) modules allow for the digitization of charge and time information within the ASIC itself, ensuring reduced power consumption. The FEB is characterized by high operation flexibility, allowing it to be used in a variety of applications.

3.5.1 Petiroc 2A ASIC

The Petiroc 2A is a 32-channel front-end ASIC specifically designed by Omega-Weeroc for SiPM readout, optimized for precise and accurate energy and timing measurement. This chip was selected for its ability to integrate a high-speed, low-jitter trigger mechanism with precise charge and time measurements. It provides individual trigger line outputs for each input channel, and includes onboard ADCs for digitization of both charge and time signals.

Figure 3.28 shows the block diagram of the ASIC. Each channel at the input of

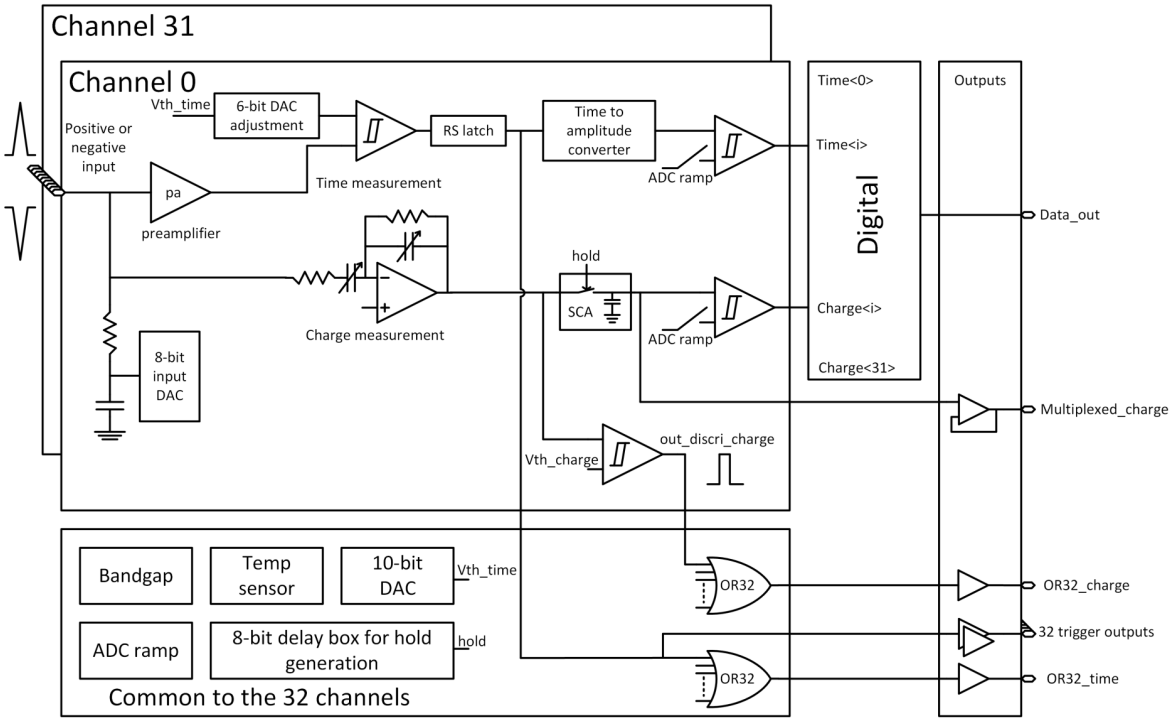

Figure 3.28: Petiroc 2A ASIC block scheme.

the ASIC features an 8-bit input digital-to-analog-converter (DAC) that allows for trimming the high voltage applied to each SiPM within a 1V range. This feature allows to adjust the detector gain non-uniformity when using the chip coupled with SiPM arrays. The input DACs is controlled through proper Slow Control registers.

The input signal is DC coupled and is divided into two distinct paths: a fast trigger line for precise timing measurements and a charge measurement line.

The fast trigger line consists of an inverting preamplifier with a 1 GHz bandwidth and a nominal fixed gain of 40, followed by a fast discriminator. The threshold of the discriminator can be adjusted using a programmable common 10-bit DAC followed by an individual 6-bit DAC for each channel. The output can vary in the range $[0.89, 1.89]$ V with the global threshold from 0 to 1023 DAC units while the 6-bit local threshold can trim the value around the global threshold in a range of about 100 mV with $\sim$ 1.5 mV/DACunit. The effective threshold value for each channel vth_{time} can be expressed as:

$$vth_{time} = 0.89 \text{ V} + (th_{global} * 0.92 \text{ mV}) - (th_{fine} * 1.5 \text{ mV}) \tag{3.24}$$

where th_{global} is the 10-bit DAC value and th_{fine} is the 6-bit local threshold DAC value.

The diagram in figure 3.29 summarizes the steps of the readout process. When one

of the 32 preamplifier signals exceeds the time discriminator threshold, the trigger output generated is sent to a Time to Amplitude Converter (TAC) that allows precise time of arrival (TOA) measurement. The TAC fine ramp is triggered by the discriminator and stopped by the leading edge of the TDC reference 40 MHz clock, within 25 ns. The information on the start clock pulse is stored as *CoarseTime* by a 9-bit ADC. The final analog level of the TAC ramp is then digitized over 10-bits by a Wilkinson ADC as *FineTime* value. The time information can be reconstructed from the relation:

$$t = P_{ck40} \times (CoarseTime + 1) - FineTime \tag{3.25}$$

where $P_{ck40} = 25$ ns is the period of the TDC reference clock running at 40 MHz.

In parallel, the same signal is routed to the charge line. The charge measurement path includes a programmable shaper connected to a switched capacitor array (SCA). The SCA captures the peak amplitude of the shaper output, proportional to the input charge, and holds it for a configurable duration before digitizing it via a 10-bit Wilkinson ADC. The hold can be delayed between 25 ns and 100 ns with a 8-bit register. Parallel to the SCA, the shaper output is also routed to a charge discriminator with a threshold set by a common 10-bit DAC. It provides a second-level trigger information to filter events above a certain energy threshold and reject noise.

Referring to diagram in figure 3.29, the signal is shaped by the CR-RC shaper, that holds the amplitude in the SCA at the time defined by the hold delay. If a start conversion from the FPGA is sent to the ASIC the digital conversion of ADC (charge) and TDC (time) information starts. The conversion time is of 12.8 µs.

While many ASIC parameters are adjustable via dedicated register configurations, key settings such as the preamplifier gain and trigger level range critical for optimizing SiPM readout are not directly programmable. However, small adjustments can be made by varying the voltage on specific pins. A precise operating point was determined to ensure optimal performance of the Petiroc 2A in conjunction with the HPK S13552 SiPMs. In particular the gain was reduced to 20 by placing a 120 kΩ resistor between the vref_time_pad (pin 71 of the ASIC) and ground. This also shifts the pre-amplifier baseline from $\sim$ 1.15 V to $\sim$ 1.75 V increasing the dynamics for the discriminator of $\sim$ 600 mV. In this configuration the Time threshold (vth_{time}) DAC Code 0 correspond to about 1.473 V while DAC Code 1023 2.41 V (details in [Pillera et al., 2023])

The Petiroc 2A operates in different configuration modes. It can be used in *full analog mode* without any internal clocking, supporting both photon counting and triggered charge measurement with outputs available either as triggers or multiplexed analog signals, or in *full digital mode* providing fully digitized output data using internal

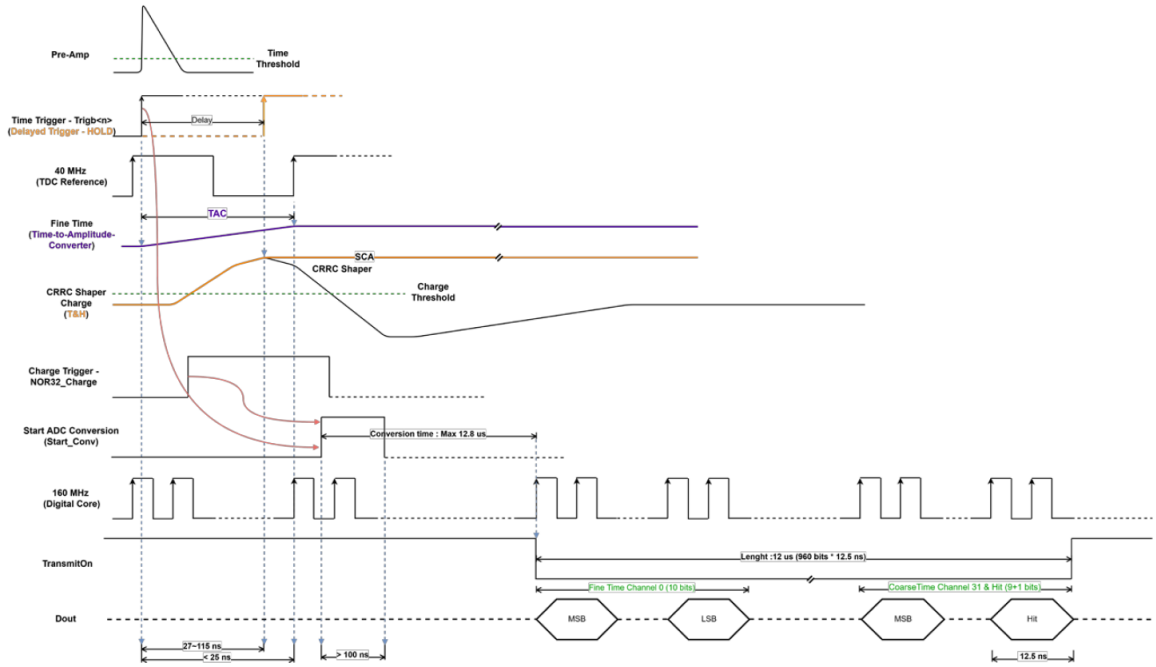

Figure 3.29: Timing diagram of Petiroc 2A readout sequences.

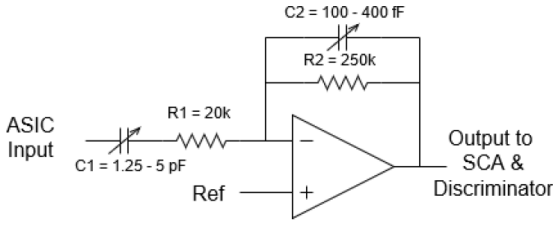

Figure 3.30: Petiroc 2A CR-RC shaper for charge measurement.

ADC and TDC. In photon counting mode, it is possible to set a first level threshold below one photoelectron.

In full analog mode, the digital part of the ASIC is deactivated and an internal multiplexer sequentially outputs the charge and the hit value is from all the 32 channels. In full digital mode, the ASIC provides both the time and charge data for all channels. The operation rate is in this case limited to 40 kHz due to analog-to-digital conversion (12.8 µs maximum) and serial data outing (12 µs).

Figure 3.30 shows the diagram of the CR-RC shaper for charge measurements. The capacitors C_1 and C_2 can be programmed through the slow control registers of ASIC in order to set the proper value of time constants $\tau_1 = R_1C_1$ and $\tau_2 = R_2C_2$. There are 4 different values allowed for both the constants: 25, 50, 75, and 100 ns for a total of 16 different combination. The output of the shaper is sent to a Switched Capacitor Array (SCA) along with a Track & Hold stage. Figure 3.31 illustrates the track &

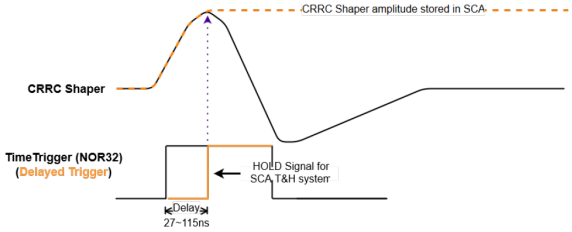

Figure 3.31: Example of shaper output signal and formation of the corresponding delayed time trigger.

hold mechanism. The hold signal is generated internally from a delayed NOR32_time (Time Trigger) discriminator output. The delay can be programmed with an 8-bit DAC in the range from 27 ns to 115 ns with $\sim$ 0.34 ns/$DACu$. Once selected the appropriate delay around the shaper peaking time, the peak of the shaper amplitude signal will be stored in the SCA and ready to digital conversion. The conversion can start only if the input signal amplitude exceeds the threshold of the time discriminator.

When configured, the PETIROC2A operates in free running mode, supplying the digital discriminator signals to the FPGA. Channel triggers can be latched, allowing the ASIC to reset and be ready for a new acquisitions. The ASIC includes a probe register for debugging and monitoring internal test points. It is possible to select to output either analog or digital signals. Only one analog and one digital signal can be probed at the same time. The analog probe can be configured to output the preamplifier signal or the discriminator threshold, including the 6-bit trimming. The digital probe can be used to output the shaper signal.

3.5.2 The Petiroc-FEB

Figure 3.32 shows a picture of the Petiroc-FEB. The board was designed, developed and assembled by the Electronics Service of the INFN unit of Bari. During the development of the fiber tracker prototype, I have contributed to the development of the data acquisition software and in the testing and optimizing this board. As anticipated, the board is equipped with four Petiroc ASICs, with a total of 128 readout channels. A first version of this board (V1) was used to perform the ASIC characterization measurements. A second version of the board (V2) was developed afterwards, and four units were produced, with the capability of 512 readout channels in total. The board and DAQ infrastructure is based on the previously developed MOdular System for Acquisition, Interface and Control (MOSAIC) [De Robertis et al., 2018]. The FPGA handles the ASICs and trigger configurations as well as the DAQ.

There are 6 Nuclear Instrumentation Modules (NIM) input and output lines

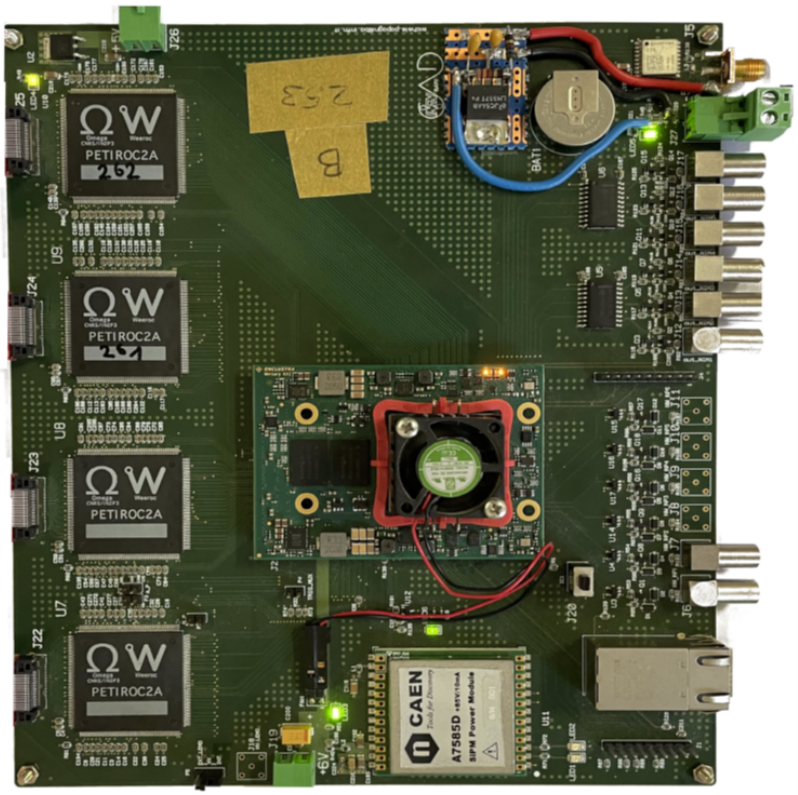

Figure 3.32: Picture of the PETIROC-FEB V2.

for external trigger operation and synchronous multiboard operation. The FEB is connected to a host with TCP/IP network interface. A Global Positioning System (GPS) is also present on board for possible uses requiring absolute timing information. Four LSHM-120 Samtec multi-channel connectors are used to route 32 SiPMs signals to each ASIC. For all applications discussed in this thesis, high speed HLCD 50 Ω multi-channels Samtec cables are used to connect the FEB to the PWBs where the sensors are mounted. The bias voltage is supplied to the SiPMs on a separate line on the same connector. The bias is provided onboard by the A7585D module, but it is also possible to provide external bias through a LEMO connector excluding the internal bias line with a jumper. The board is powered by a +6 V line for the FPGA and the A7585D module, a +5 V line for the ASICs and a -5 V line for the NIM I/O section.

The 128 trigger lines provided by the four ASICs are routed to the FPGA. The FPGA is responsible for implementing the trigger logic among different trigger configurations.

All the channels operate in free-running mode, if the amplitude of a channel signal exceeds the discriminator threshold the trigger produced by the ASIC is sent to the FPGA. Depending on the trigger logic adopted the FPGA can send a start ADC conversion signal and a reset signal to all the ASICs.

The relevant configurations for the applications discussed in this work are the following:

- *periodic trigger*: the board takes data at a rate of 1 kHz;
- *single channel trigger*: the board takes data from all channels if the signal amplitude of a single channel exceeds the discriminator threshold;
- *coincidence of any two consecutive channels*: the board takes data from all channels if the signals from two adjacent channels exceed the respective discriminator thresholds;
- *external trigger*: the board acquires data only if an external validation arrives in the hold window after a discriminator trigger (*External*) or always (*ExternForce*);
- *disable*: disable the trigger capability of the board.

The periodic trigger is used for randomly sampling the baseline, for pedestal measurements. The single channel trigger or *single mode* allows triggering on dark counts in the SiPMs, to perform quick charge calibration measurements. The coincidence of any two consecutive channels or "*adjacent mode*", was specifically

developed for the FTK in OR1 configuration. The trigger requires a threshold-crossing signal from two adjacent channels, which are read out by two consecutive ASICs. As discussed above, the passage of an ionizing particle is expected to fire at least three neighboring strips, yielding signals with multiple photoelectrons on at least two adjacent channels. This mode aims to mitigate false triggers caused by dark noise while keeping an efficiency above 95%.

For all trigger modes except for disable and external trigger, when a channel signal exceeds the discriminator threshold, the FPGA waits for a coincidence with the multiplicity required by the trigger logic within a time window defined by the user through the triggerDelay register to decide whether to take the event. If the condition is met within the time window, the FPGA sends the start ADC conversion signal after a delay set by the chargeDelay register. Otherwise, it sends a reset to all channels. After the reset, that terminates after approximately 100 ns, the board is ready for a new acquisition.

When the boards operate in external trigger, after a trigger produced from a channel signal exceeding the threshold, the FPGA waits for an external trigger for the time specified by the triggerDelay. Again, if the condition is met in this time window, the start ADC conversion and reset signal are sent by the FPGA to all ASICs after a time interval specified by the chargeDelay register. If an external signal arrives and no channel produces a trigger output, with extern trigger there is no conversion, while with externForce, the conversion stars without delay and hence the reset is sent after 100 ns

The FEB provides the possibility to operate in standalone mode or in multiboard mode, with one board working as *master* and the others as *slaves* (*master-slave* mode). The master-slave is a synchronized operation mode where the master board operate with one of the trigger modalities described above, except for the "disable", and propagates the clock signal through a NIM output to the slave boards. The trigger capability must be disabled on the board configured to operate as a slave. At each trigger, the master board sends in the clock line the information of the 32-bit event counter ID by modulating the width of 32 clock pulses. Using this system a slave board is synchronized with the master using a single line.

The version V2 of the PETIROC-FEB includes some improvements in the board design, the most significant being the addition of the GPS and dedicated pads for the resistors discussed in Sec. 5.2.1. Another feature of the board is the possibility to readout one-wire temperature sensors, which can be placed close to the SiPMs. A total of four boards have been assembled and used during these years.

3.5.3 The DAQ software

The DAQ software of each board is based on a custom C++ code (*host-sw*). The *host-sw* requires a text file named *configuration file* containing all the board and ASIC settings. The configuration file is organized in several subsections. The header of the file contains the IP address of the FEB (ADDRESS), and the ROLE of the FEB indicating if the FEB operates as master (*master*), slave (*slave*) or in standalone (*alone*) mode. A first section, named TRIGGER, contains the trigger settings: the trigger logic expressed as an integer code from 0 to 15 (the *mode*), the *triggerDelay* register value, i.e. the width of the time window during which the FPGA waits for the trigger condition to occur following a signal from a channel exceeding the discriminator threshold or the time window during which the FPGA waits for the validation after an external trigger signal, and the the *chargeDelay* register value, i.e. the width of the time window after which the FPGA sends the start ADC conversion to the ASICs. Both the triggerDelay and chargeDelay values are expressed in integer units of 25 ns. Then four sections follow, one for each chip, specifying all the ASICs parameters. Values for registers common to all the 32 channel of the ASIC are defined as *global*, while parameters characteristic of each channel are defined as *local*. For each ASIC there are two different subsections, one for local parameters, divided in 32 subsections, one for each channel, and one for global parameters. Each ASIC section is identified by a string PETIROC i with i from 0 to 3. Each channel subsection is identified by the string CHANNEL j with j from 0 to 31. The global parameter subsection is indicated as GLOBAL Below is a list of the most relevant local parameters:

- inputDAC: 8-bit DAC to set the bias voltage trimming from 1 to 2 V;
- cmdInputDAC: bit to enable/disable the the bias voltage trimming (0 = disabled);
- mask_discri_time: bit to mask the time discriminator of the channel (0 = no mask);
- ThDAC: 6-bit DAC value for time threshold trimming;
- mask_discri_charge: bit to mask the charge discriminator (0 = no mask);

Here follows a list of notable global parameters:

- Vth_time: 10-bit DAC to set the ASIC time discriminator threshold;
- DAC_delay: 8-bit DAC to set the time trigger delay;

- Cf: 4-bit DAC to set the value of the feedback capacitor in the CRRC shaper;

Once the configuration file is specified, the host software provides a set of options to interact with the board:

- *chip_init*: updates the values in all the registers with the values in the configuration file indicated;
- *setHV* value: sets the SiPM high voltage (HV) to the specified value in volts (value = OFF turns off the SiPMs);
- *pedestals*: starts a pedestal run by setting the trigger mode to periodic;
- *daq* duration: starts an acquisition run of the duration specified in seconds;
- *set_analog_probe* channel: enable to use the probe to test the preamplifier output signal;
- *set_analog_mux*channel: enable to use the probe to test the shaper output signal;

To facilitate the DAQ operations and the use of the *host-sw* throughout the project, I contributed to the development of an interface (interface-sw) implemented in Python. By means of simple Python-scripting the interface-sw allows to operate also in master-slave mode.

The initial phase of the acquisition procedure involves configuring the FEBs by specifying their respective IP addresses, defining the acquisition mode either standalone or multiboard, and assigning the role of each FEB designated as either alone, master, or slave. The high voltage settings for the SiPMs connected to each ASIC must be provided. Following this, all required parameters are input to generate the configuration file, using dedicated configuration functions. Once the configuration file is generated, the acquisition process can be initiated. Specialized functions, developed specifically for this process, perform the initialization of all ASICs with the generated configuration file, set the appropriate HV levels for the SiPMs. Finally a dedicated function launch the data acquisition process for the time window selected by the user.

In standalone acquisition mode, data acquisition is initiated concurrently across all selected FEBs. In master-slave mode, the acquisition process begins on the slave boards first. After a programmable delay of few seconds, the acquisition on the master board is subsequently started. The acquisition process on each board operates independently. At the end of the selected acquisition time (t_{daq}), each process must be halted. A dedicated function is responsible for terminating all processes. In standalone mode all

the process are killed simultaneously, while in master-slave mode the master process is stopped before the slave ones. Finally SiPM HVs are turned OFF and the interface acquisition program terminates.

The DAQ process produces a binary file for each board containing data from all the ASICs. The interface-sw produce also an additional file for each board containing the copy of the configuration file in json format. Both the files are named with a timestamp containing information on date and time of the acquisition start. A pedestal acquisition is done biasing the SiPMs with a voltage below the breakdown and providing a 1 kHz periodic trigger to the ASICs to sample the baseline. In each pedestal run, 10000 triggers are collected per ASIC.

A gain calibration run is performed in single trigger mode, without any light source. In this way the triggers can be issued by dark counts of the SiPMs, and in a few tens of s a significant number of dark events can be taken, with spectra extending up to 5-6 p.e., that can be used for gain calibrations.

3.5.4 Data processing

Petiroc data output

The four Petiroc ASICs on the FEB, operating in full digital mode, produce a serial output containig time and charge measurements for all the 32 channels, as shown in the diagram in figure 3.33. The rate is limited to 40 kEvent/s due to analogue to digital conversion time, which takes a maximum of 12.8 µs, and the serial data output speed of (12 µs).

Each data packet consists of 960 bits. The first $32 \times (9 + 1)$ bits contain two pieces of information for each channel: the hit data and the coarse time. The hit is a 1-bit value that indicates whether the signal in the corresponding channel has exceeded the discriminator threshold. The remaining 9 bits encode the CoarseTime information. This is followed by $32 \times (10 + 10)$ bits, where the $(10 + 10)$ bits for each channel represent the 10-bit ADC charges and the 10-bit *FineTimes* respectively.

The data from the ASICs are routed to the FPGA, which elaborates the packets from the four ASICs adding the information on the ASIC identifier, the tag for the event and a flag indicating whether the packet was correctly written.

The final data structure consists of a 2-byte boolean for the *Flag*, 1-byte unsigned integer for the ASIC identifier (*asicID*), 32 2-byte unsigned integers for the ADC charges *ADCcharges*, 32 2-byte unsigned integers for the fine time (*FineTime*), 32 2-byte unsigned integers for the coarse time (*CoarseTime*), 32 2-byte booleans for the *hit* information, and 4-byte unsigned integer containing the tag of the event (*tagID*).

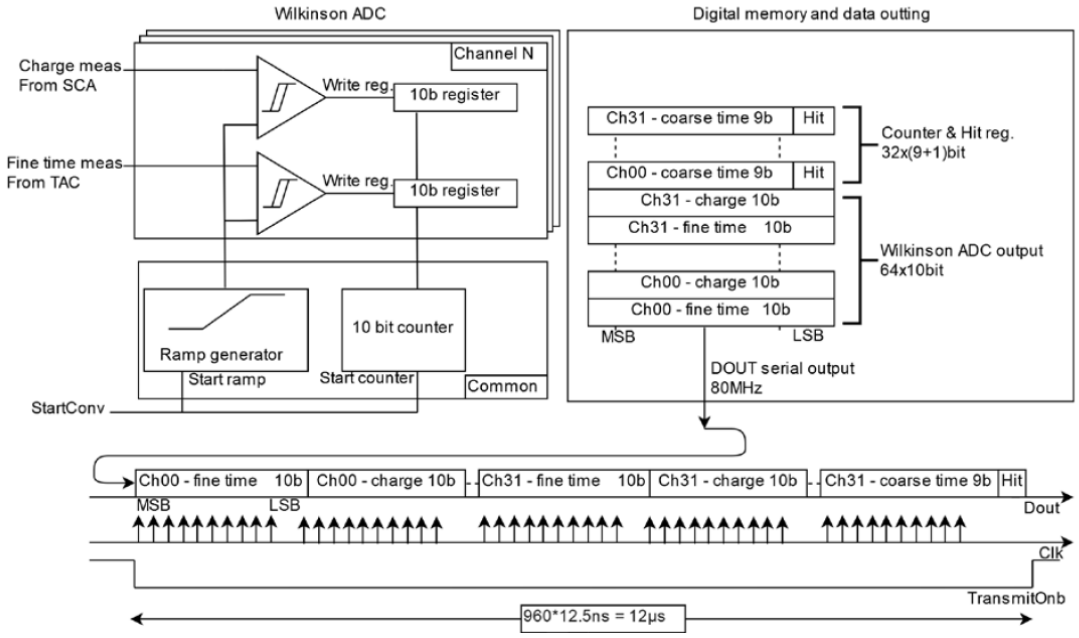

Figure 3.33: Digital readout of Petiroc 2A

The FEB records all the data in a binary file, writing four data packets per event. These raw data are subsequently processed and analyzed off-line using python scripts. The first step of the processing involves discarding corrupted or incomplete events and stacking the data related to each individual event across the four ASICs.

Pedestal subtraction

As discussed in section 1.3.5 the key feature of SiPMs is the proportionality between the charge produced during the avalanche and the number of photon detected. The charge can be expressed in term of the amplitude of the output signal according to the relation:

$$Q = \int_0^T i(t)dt = \int_0^T \frac{V(t)}{R}dt \tag{3.26}$$

where i(t) is the current signal generated by the detector, V(t) the voltage measured on the load resistance R and T is the pulse duration. Because of the high sensitivity, the elevated gain and the response linearity of SiPMs, it is possible to discriminate signals differing of a single p.e.. In fact, the charge distribution exhibits few peaks at a fixed distance corresponding to different number of photons. Each peak has a Gaussian shape centered at the most probable value of charge. The variance is due to the SiPM noise and to the gain fluctuation of individual pixels. Each peak can be fitted with a

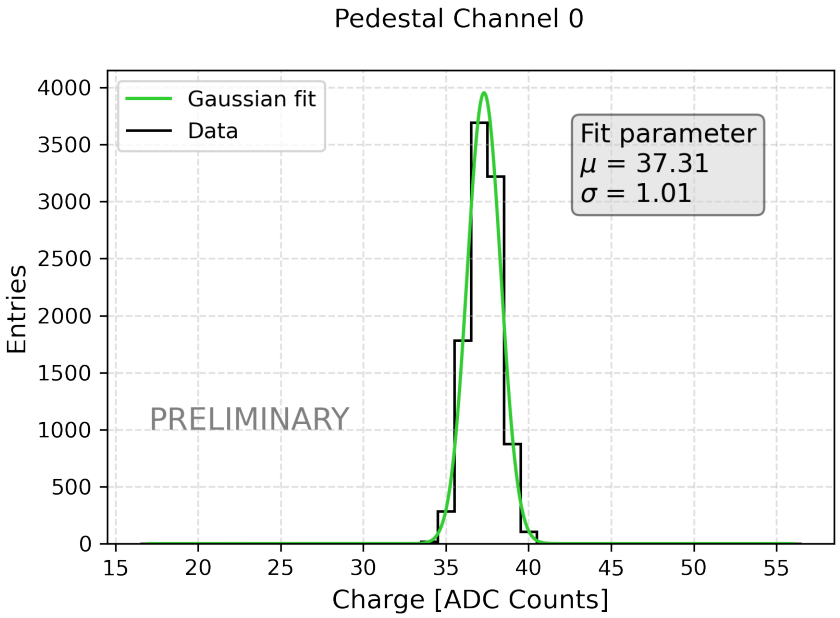

Figure 3.34: Pedestal charge distribution in ADC counts of channel 0 of FEB 252. The green line represents the Gaussian fit curve.

Gaussian function:

$$f_i(x) = a_i e^{-\frac{(x-\mu_i)^2}{2\sigma_i^2}} \tag{3.27}$$

where μ_i is the mean value of the Gaussian fitting the i-th peak and σ_i is its variance.

In order to properly calibrate the charge in ADC channels to the corresponding number of P.E., it is necessary to first subtract the pedestal. The pedestal provides a measurement of the electronic noise in the readout system, present even in the absence of a physical signal. This noise can originate from various sources, such as thermal noise in the sensors, electronic fluctuations in the circuits, or ambient background noise. The pedestal is measured by performing a specific pedestal run consisting in sampling the charge value of the signal randomly using a periodic trigger internally generated by the board. Originating from a combination of random noise processes, the charge distribution of the pedestal follows a Gaussian distribution centered around the overall noise mean value. Figure 3.34 is reported the distribution of ADC counts corresponding to the charge of the pedestal of the channel 0 of ASIC 0 of board 252. The mean value of the pedestal is extracted from the Gaussian fit curve while the standard deviation represents the overall noise level of the channel. These two values are characteristic of the ASICs and the SiPM and hence vary from channel to channel. Therefore they are estimated for each channel of each ASIC. Figure 3.35 shows a summary of all the pedestal fits for board 252. It can be seen that, despite fluctuations in the pedestal values across different channels, the channels within the same ASIC exhibit relatively

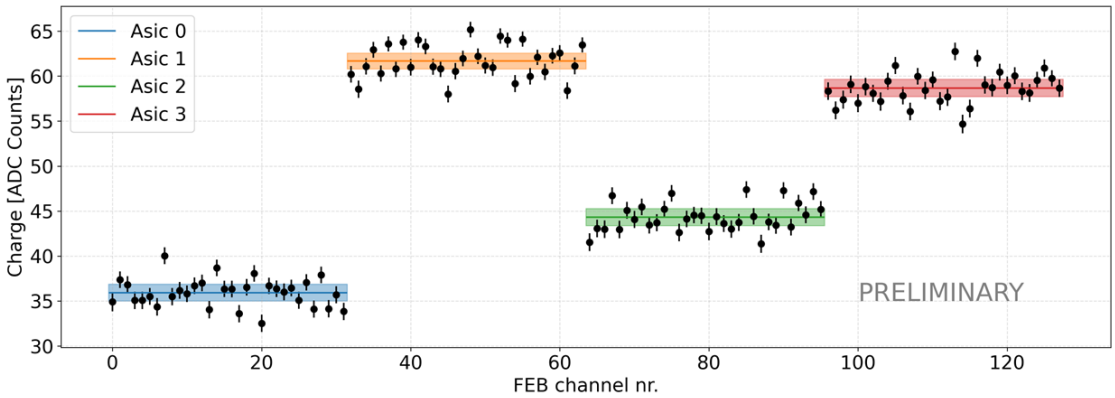

Figure 3.35: Summary of the pedestal fits for all channels on board 252. The points represents the mean value, μ, of the Gaussian fit for the pedestal charge distributions, while the error bars indicate the standard deviation,σ, derived from the same fits. The colored bars depict the average pedestal value for each ASIC, with the corresponding intervals spanning half of one standard deviation.

close pedestal values, with a slight spread around the mean value. However, more significant differences are found between different ASICs. In order to estimate the charge in ADC units in each channel the respective pedestals mean value is subtracted to all the measurements.

Charge calibration

After pedestal subtraction, the charge distributions start from zero and exhibit multiple equally spaced peaks. The distance between consecutive peaks represents the conversion factor between ADC counts and the number of photoelectrons, referred to as the gain. Unlike the pedestal, the gain is fixed for the electronic channel and varies only the component due to intrinsic property of the SiPM and is expected to exhibit minimal variation across the SiPMs within the same array. To simplify the calibration process, the 32 channels of each ASIC have been combined, resulting in a single aggregate distribution, as shown in the figure 3.36 that reports the charge distribution for the ASIC 0 of board 252. After individuating and locating all the peaks above a minimum threshold, each peak was fitted with a Gaussian and the fit parameters were extracted and used to evaluate the gain. In figure 3.37 the position of the peaks from the mean values, μ_i of the Gaussian fits with the respective errors from the σ_i, are reported as a function of the number of p.e. associated to the peaks. The slope of the best linear fit curve passing through the pedestal can be interpreted as the total gain of the system consisting of the SiPM and the front-end.

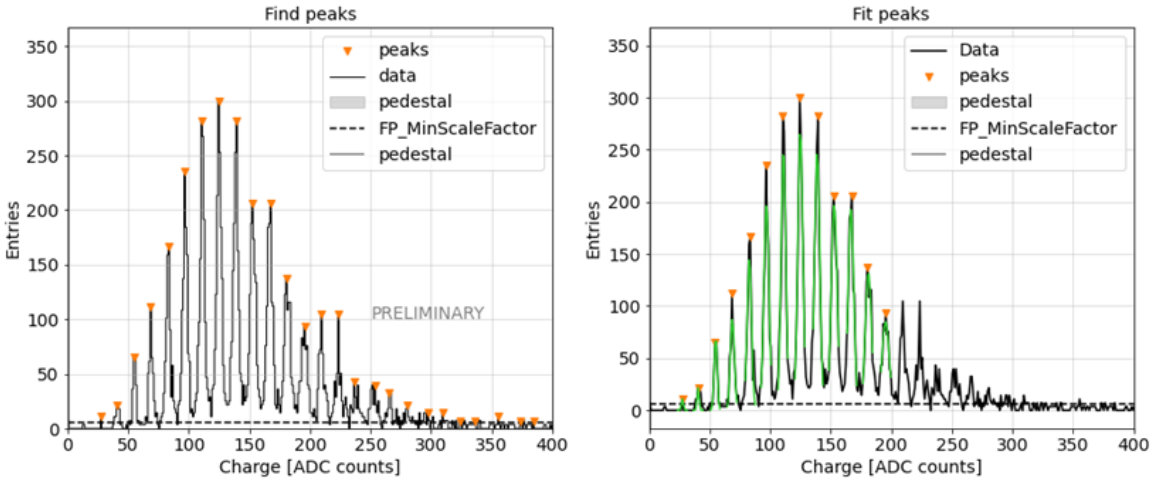

Figure 3.36: ADC charge distribution for the ASIC 0 of board 252 obtained by merging the charge on all the channels of the ASIC after subtracting the pedestal channel by channel. Each peak corresponds to a specific number of P.E. In the right panel each peak was fitted with a Gaussian (green curves). Fit parameters were extracted for each peak.

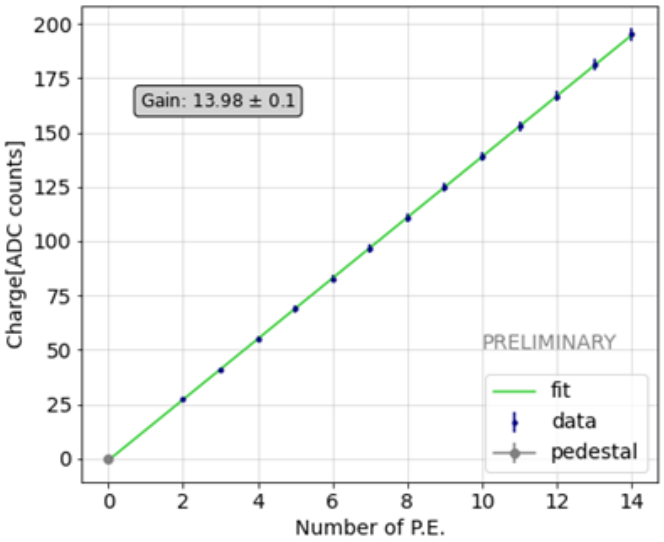

Figure 3.37: Charge in ADC counts as a function of the number of photo-electrons (P.E.). The data are fitted with a straight line passing through the pedestal (gray point at the origin), whose slope represents the gain in ADC counts per photoelectron.

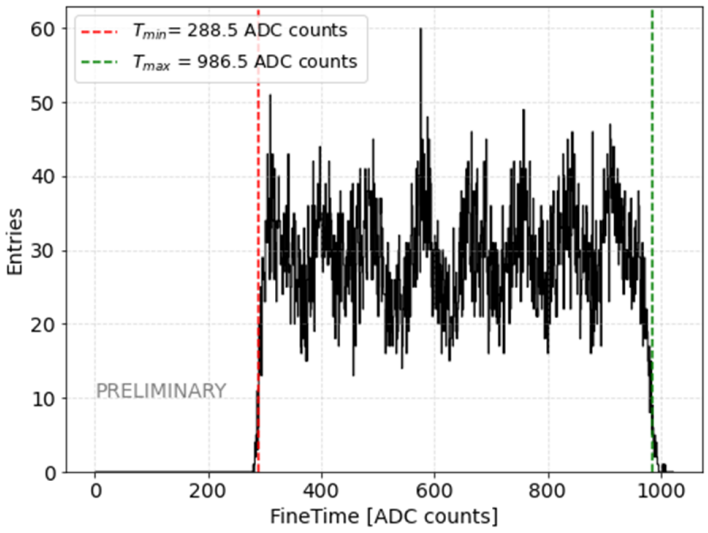

Figure 3.38: *FineTime* distribution of ASIC 0 of FEB 252. The dashed lines correspond to the T_{min} and T_{max} identified requiring $N(FineTime) = 0.1 \times N_{max}$.

Time calibration

As discussed in section 3.5.1 the absolute timing is given from relation 3.25. The plot in figure 3.38 shows the distribution of the *FineTime* measured with the ASIC 0 of FEB 252. This distribution is common on all the ASICs for all the FEBs. It can be seen that the dynamics is reduced with respect to the all aviable TDC values between $T_{min} \sim 288$ ADC counts and $T_{max} \sim 986$ ADC counts where T_{min} and T_{max} are defined as the edges of the interval in which the number of counts $N(FineTime) > 0.1\ N_{max}$, indicating with N_{max} the maximum number of events in the distribution. Therefore equation 3.25 becomes:

$$t = \frac{P_{ck40}}{(T_{max} - T_{min})} \times (CoarseTime + 1) - FineTime \tag{3.28}$$

This relation is use to calibrate the absolute times of events.

At the end of the whole calibration process, a new data structure is obtained containing the information on charge in p.e. units, time in ns, hits and trigger tag. The hits contain the information on the fired strips.

Clustering

At this stage, cluster signals are identified. A cluster is defined as any group of adjacent strips with a signal at least 3σ above the pedestal. The cluster charge is

determined by summing the charges in the strips that form the cluster, while the cluster position is defined as the charge centroid of the strips:

$$Q_i = \sum_{j \in clu_i} q_j \tag{3.29}$$

$$x_i = \frac{1}{Q_i} \sum_{j \in clu_i} q_j x_j \tag{3.30}$$

$$\sigma_i = \frac{pitch}{\sqrt{12}} \sqrt{\frac{\sum_{j \in clu_i} q_j^2}{Q_i^2}} \tag{3.31}$$

where q_j and x_i are respectively the charge and the position of the j-th strip and the sum is performed only on strips in the i-th cluster. In the previous relation $\frac{pitch}{\sqrt{12}}$ is the uncertainty on the position of each strip and the uncertainty on the charge of the j-th strip is assumed negligible compared with the uncertainty on the position. If this condition is not met, the inclusion of this term would increase the error on the cluster position, thereby improving the chi-squared value in the fit for the track direction 5.3.1.

Chapter 4

Prototype characterization

In this chapter, the tests performed on the prototype modules will be described. Specifically, the initial tests were conducted to compare the performance of fibers produced by different manufacturers. Subsequently, performance was analyzed based on variations in the SiPM array pitch and fiber diameters to reproduce the simulated configurations. The results of these tests indicate that using larger-diameter fibers readout by SiPMs with a wider pitch provides a good compromise between maintaining a limited number of readout channels and achieving good detector performance.

4.1 Module performance

4.1.1 Test beam 2021

Set up

The first module of the fiber tracker prototype was built in 2021 using Saint-Gobain BCF-12 round fibers with a diameter of 500 µm. In October of the same year, the module was tested with a 10 GeV/c pion beam at the T9 PS facility at the CERN (Conseil Européen pour la Recherche Nucléaire). Preliminary results of this test were described in [Mazziotta et al., 2022]. In this first beam test campaign only one FEB was available, which allowed for the readout of 128 channels. These were used to read a portion of the X-Y module, as shown in the bottom-left panel of figure 4.1. Two ASICs were used to read one half of the strips in the X-view (32 ASIC channels for the odd SiPM strips and 32 channels for the even strips, for a total of 64 channels) and another two for the Y-view. In this way we could study the performance of the quadrant highlighted in orange in the figure, corresponding to an active area of 1.6×1.6 cm^2. The module was positioned on the beam-line so that the center of the quadrant was

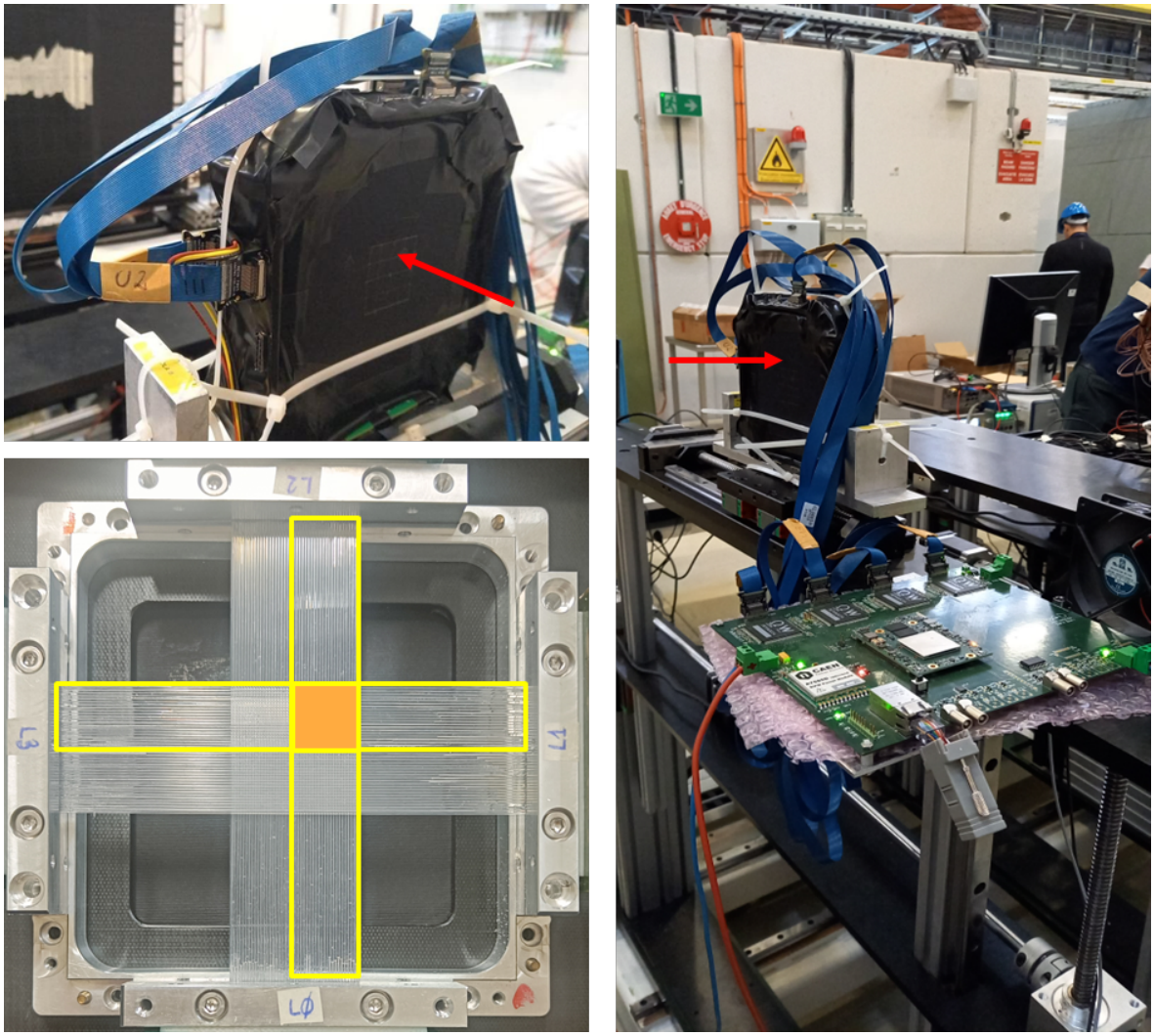

Figure 4.1: Beam Test Photo, 2021: Top-left panel: Close-up of the tracker module as mounted on the beamline. The module is wrapped in black cardstock and tape to shield the photodetectors from external light. The module's active region is sketched on the surface of the black wrap. Bottom-left panel: Detailed view of the tracker module. Fibers connected to photodetectors in each view are highlighted in yellow. The module was aligned with the beam so that it would be impacted in the region of interest, marked in orange. Right panel: Photo of the module on the beamline. At the bottom, the FEB used to read out signals from all four sides of a single quadrant is visible.

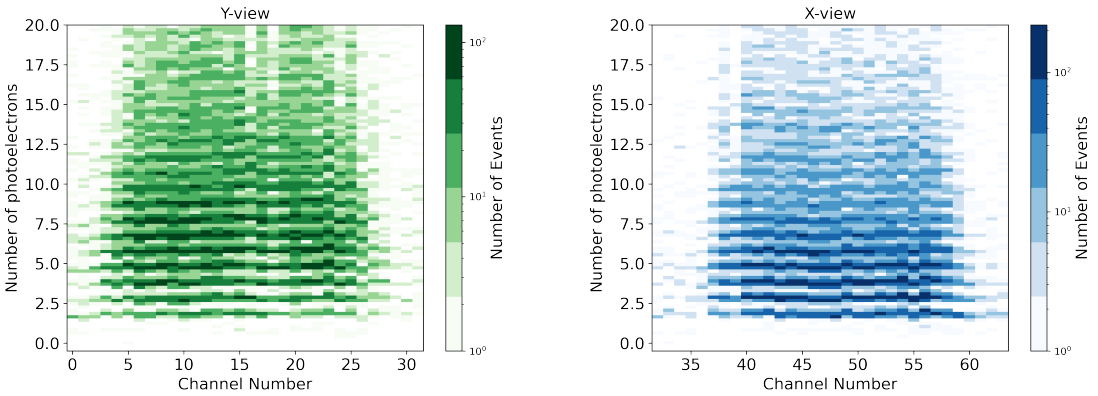

Figure 4.2: Hit map of the Y-view (left panel) and X-view (right panel) strips showing the distribution of the number of detected photoelectrons in each channel. The SiPMs have been biased with $V_{OV} = 4.5$ V.

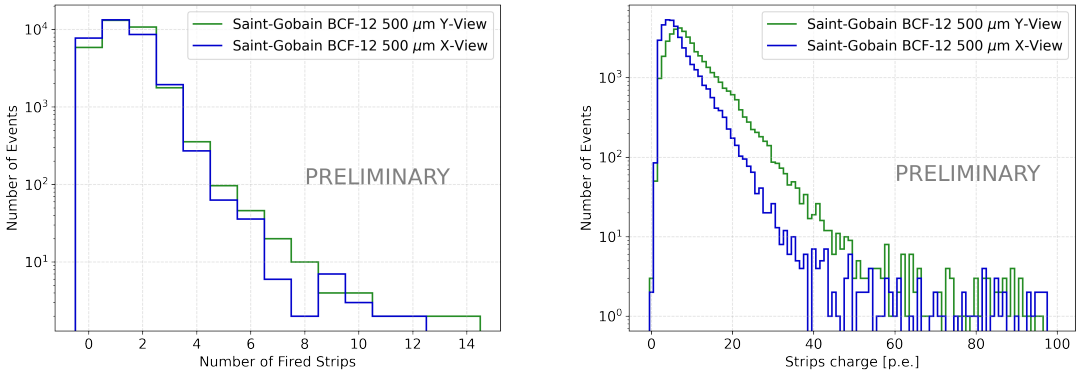

Figure 4.3: Left panel: Distribution of the number of hit in each event for the two views. Right panel: distribution of the number of photoelectrons detected per strip in each event.

hit by the beam.

Measurements were performed with an external trigger provided by a telescope of two plastic scintillator bars ("*finger*") each 0.5 mm thick with an active area of 10×1 cm^2, placed orthogonally to each other in order to select a 1×1 cm^2 region, followed by two square tiles of 10×10 cm^2 cross section. A coincidence among signals from both fingers and the first tile was required. The second tile had a hole in its center with a diameter of 2 cm and was used as a veto to discard events with showers accompanying the primary particle. The trigger logic was implemented using a CAEN DT5495 logic unit[1]. The DAQ was controlled by a Raspberry Pi 4.

[1] `https://www.caen.it/products/dt5495/`

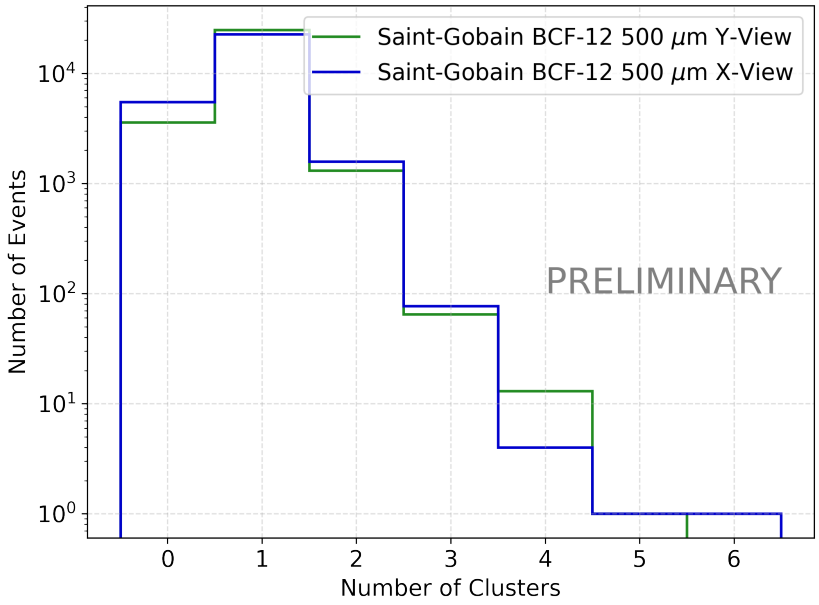

Figure 4.4: Distribution of the number of cluster in the two view planes. The zeros are due to events that triggered only one of the two planes.

Results

Data were processed as described in section 3.5.4. Figure 4.2 shows the 2D hit map of detected photoelectrons in each channel for a stack of different runs in the same configuration with a bias voltage on SiPMs $V_{OV} = 4.5$ V. The left panel shows the results for the Y-view plane, while the right panel those for the X-view. The small channel-to-channel fluctuations on the photoelectrons are due to the fact that calibration is performed by averaging all the ASIC channels. Figure 4.3 displays the distributions of the fired strips in the two views (left panel) and the distribution of the number of photoelectrons detected in each strip (right panel). The mean number of fired strips is about 2, with an average charge of 10 p.e. per strip.

Further insights can be gained from the distributions related to clusters of adjacent strips. Figure 4.4 shows the distribution of the number of reconstructed clusters in each event of the same runs used for the previous plots. In most events there is only one cluster per view plane. In addition, by analyzing the cluster size distribution shown in Figure 4.5, which represents the number of strips forming a cluster, we see that the majority of clusters consist of either one or two strips.

Figure 4.6 shows the distributions of p.e. in the clusters for triggered events in the X-view plane (in blue) and in the Y-view plane (in green). It is apparent that

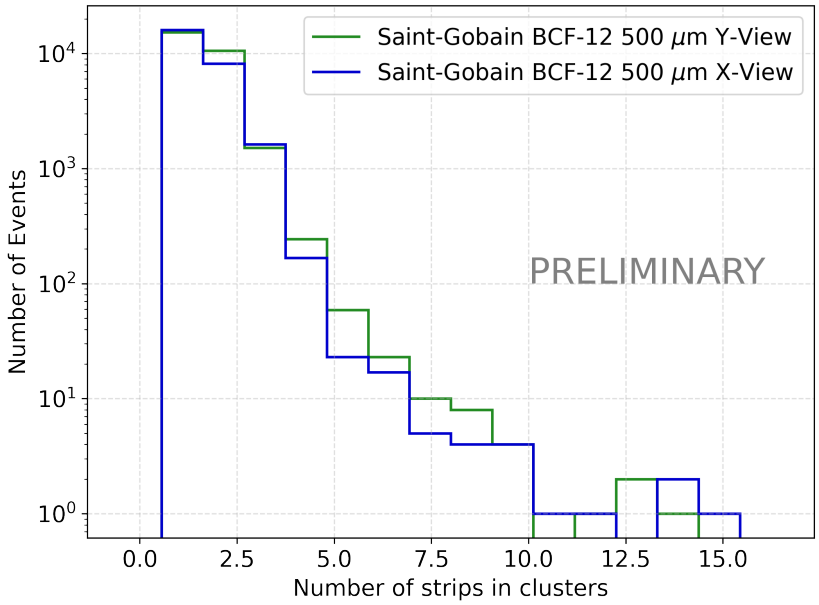

Figure 4.5: Distribution of the cluster size in the two view planes. The cluster size is defined as the number adjacent strips in a cluster.

the reconstructed clusters in the Y view exhibit a larger charge compared to those in the X view. This difference could infer manufacturing defects within the module, such as misalignment of the scintillating fibers, or small shifts in the positioning of the photodetectors. In addition, both the distributions exhibit a structure consisting of a peak followed by a shoulder, which indicates the presence of two distinct populations of events. To investigate the origin of such populations, the distribution of the cluster charge is studied as a function of the cluster size. Figure 4.7 shows the distributions of p.e. within clusters of increasing size. The left panel refers to the Y-view. Right panel shows the results for the X-view. In both views the charge distribution for clusters of size 1 is the most populated, with a Most Probable Value (MPV) of about 10 photoelectrons (p.e.). Conversely, the distributions for cluster consisting of two strips are less populated and shifted towards higher charge values $\sim$ 20 p.e. From geometric considerations and simulation studies (see Chapter 3.3) for fibers of 500µm diameter readout by SiPMs with a 250µm pitch, we expect clusters with sizes between 2 and 3 strips and a charge yield of approximately 25 p.e. The prevalence of single-strip clusters with a charge of about 10 p.e. may be attributed to gain non-uniformities across individual channels and suboptimal threshold settings for each channel.

In figure 4.8 the charge distributions of clusters larger than 2 strips are fitted with a Landau distribution folded with a gaussian distribution in order to extract the Most

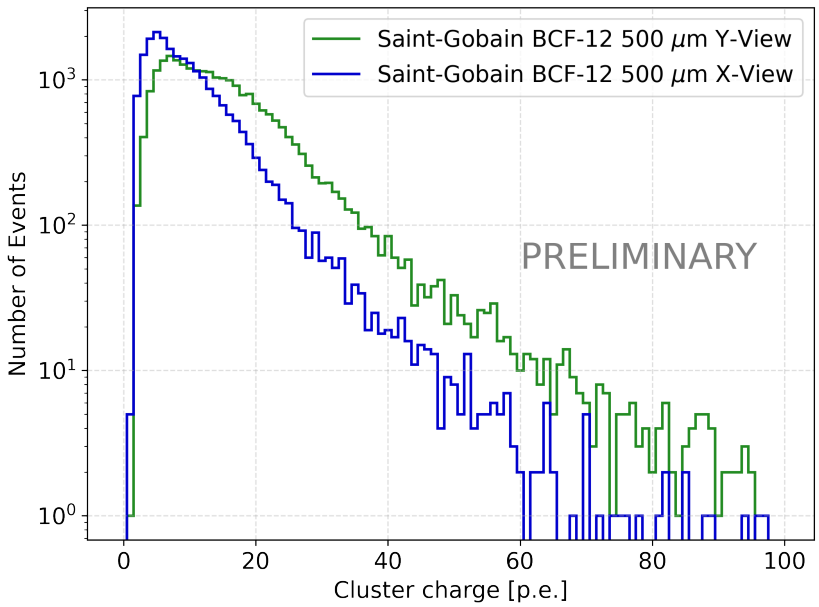

Figure 4.6: Distribution of the photoelectrons in the clusters in the two view planes.

Probable Value (MPV). This is indicative of the yield of p.e. from each plane. As previously observed, a noticeable discrepancy in yield is observed between the X and Y planes. Specifically, the MPV of the photoelectrons distribution for the Y-view is around 15 p.e. per particle, while for the X-view, the MPV is approximately 10 p.e. This may be related to some differences in the two plane assembly. In addition, both planes exhibit significantly lower yields compared to the values predicted by Monte Carlo simulations. A lower light yield from the BCF-12 fibers compared to the nominal value was also reported by [Bravar et al., 2020].

4.1.2 Test beam 2022

Set up

Due to the inefficiencies observed in the X-view plane compared to the Y-view plane during the 2021 Test Beam, as well as the overall yield lower than expected, a new XY module equipped with Saint-Gobain BCF-12 500 µm fibers was built at the beginning of 2022. Additionally, in the first half of the year, the first plane of a new module using Kuraray SCF78-MJ 500 µm diameter fibers was built. Both these modules were tested together in August 2022 during a new test beam campaign with 15 GeV/c pions at the T9 beamline of the CERN PS. During the same year, three new Petiroc FEBs were assembled, thus enabling the readout of a total of 512 channels.

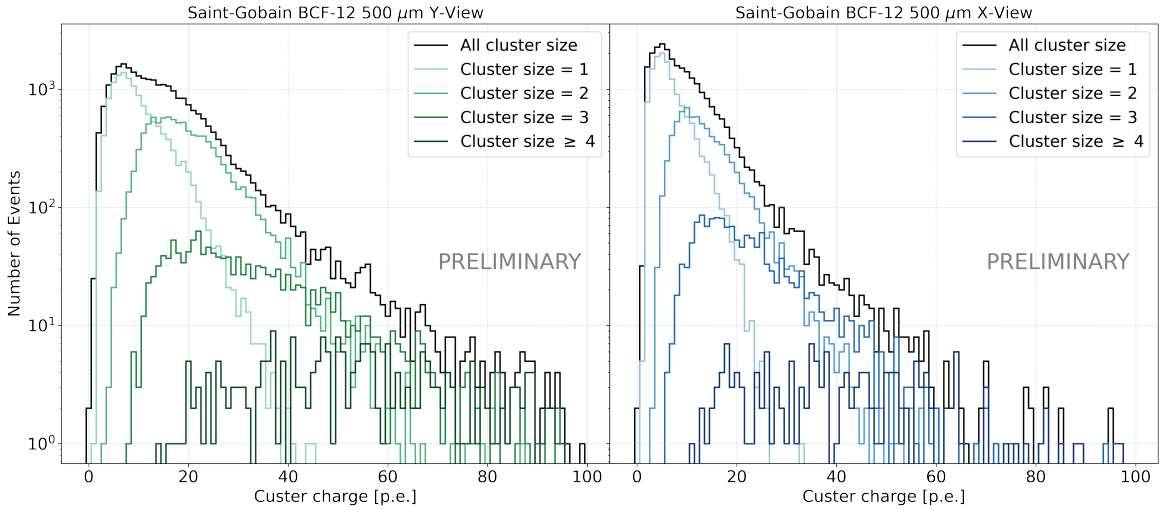

Figure 4.7: Distribution of the photoelectrons in clusters with different size in both views. The overall distribution is superimposed to the other distributions (in black).

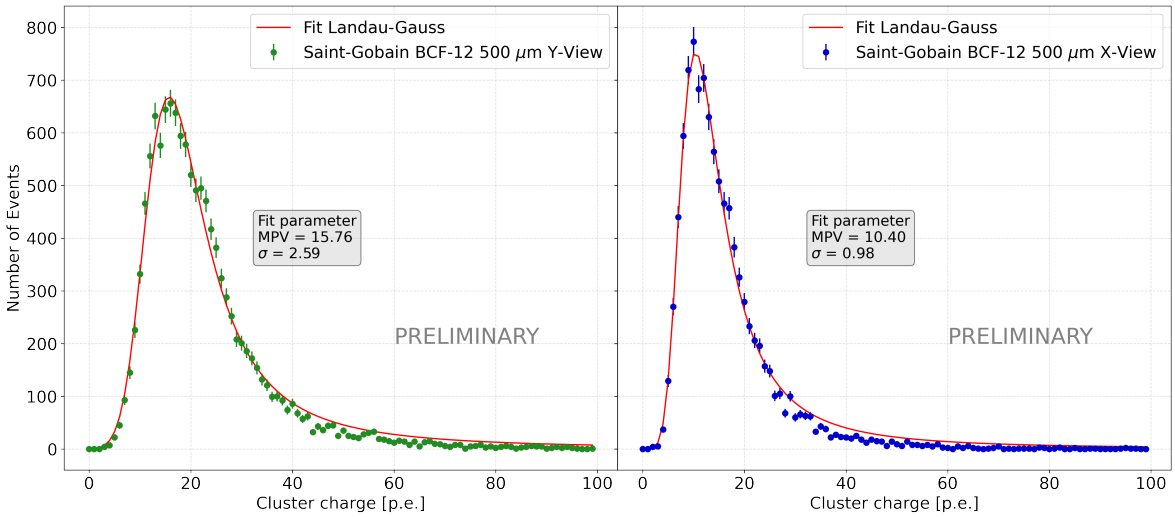

Figure 4.8: Cluster charge distribution in photoelectron units (p.e.) for the two views selecting only clusters composed of at least 2 strips. The distribution are fitted with a Landau distribution folded with a gaussian. The MPVs represent the p.e. yield from each plane.

The two modules of the detector are shown in detail in the top-right panel of figure 4.9. The first module consists only of the Y-view plane, equipped with Kuraray SCF78-MJ 500 µm diameter fibers (K500),while the second module consists of the new X-Y module made with Saint-Gobain BCF-12 500 µm diameter fibers (SG500). A third module, including an imaging calorimeter made of a LYSO scintillating crystal coupled with two planes of WLS fibers, is also visible. However, tests involving this module will not be discussed in this work.

The prototype, consisting of the three modules, was positioned on the beam-line using a dedicated support frame. This structure includes a bracket mounted on two stages that allows precise alignment and positioning of the prototype in the X and Y directions along the beam-line. This setup is shown in the bottom-left panel of figure 4.9. The right panel shows the full beam-line, with the beam direction (z axis) indicated by the red arrow. The four FEBs are visible in the bottom-left corner of the photo, while the same telescope used for triggering in the 2021 beam test is visible in the top-right corner, highlighted by the light blue box.

Results

As in the previous analysis, runs taken in the same configuration were merged and analyzed after calibration and clustering. Specifically, Figure 4.10 shows the distributions of the number of photoelectrons in clusters with size of at least two strips, fitted with a Langaus distribution defined as a Landau distribution folded with a gaussian. It is evident that the best-fit curve for the Kuraray fibers exhibits a MPV much closer to the nominal value, indicating that these fibers provide a higher yield than the SG500 fibers.

By reading the Kuraray fiber plane from both ends using the interface PWB with the OR2 mask it was possible to test whether this configuration could keep the performance while halving the number of readout channels for each plane by half. This test was performed with a beam of negative pions with 15 GeV/c momentum. For the readout of the 2-ORed side 2 ASICs from one FEB are required. The plane without the mask (OR1) was fully readout using all 4 ASICs from another FEB. Figure 4.11 shows a comparison of the cluster size distributions between the two configurations, OR1 and OR2. As expected, the number of events with a cluster size greater than 2 is significantly reduced in the OR2 configuration, since the two active fibers are readout by no more than 2 strips. Most clusters in the OR2 configuration consist of either 1 or 2 strips. The single-strip clusters are due to the inefficiency of the second strip: the second strip in the cluster readout a smaller portion of the hit fibers compared to

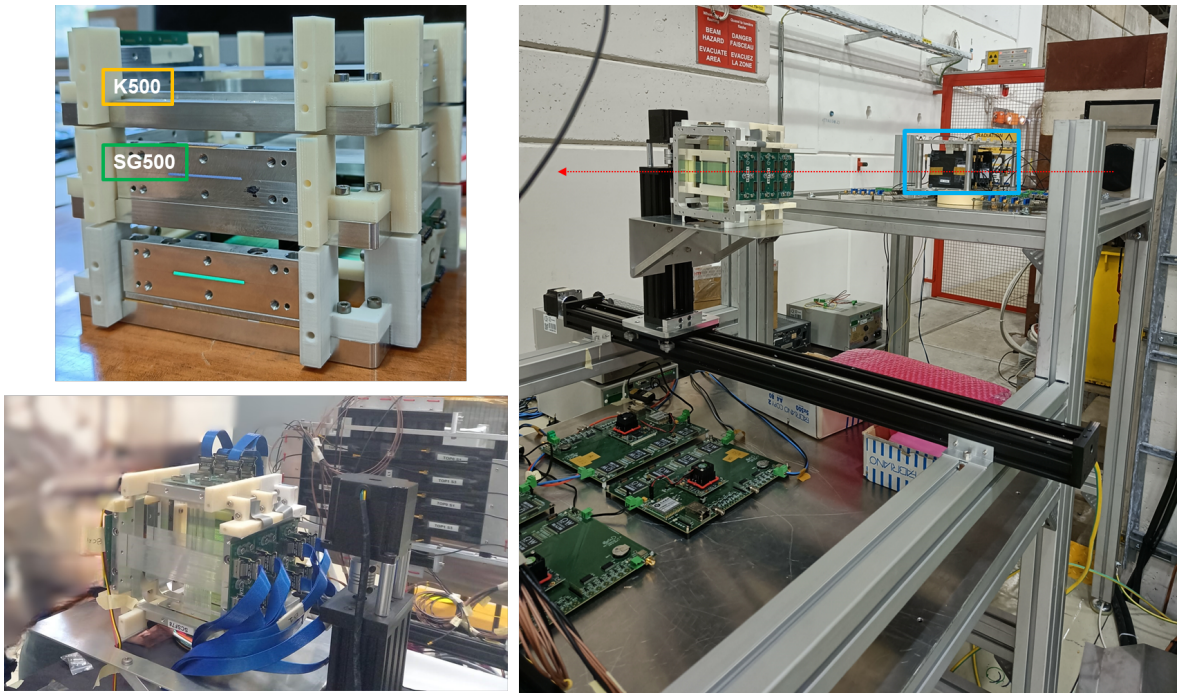

Figure 4.9: Photos of the beam test setup of 2022. Top left panel: detail of the prototype. The first module consists of the single plane made of Kuraray SCF78-MJ fibers with diameter of 500 µm, the second module consists of the X-Y module made with SG BCF-12 fibers with 500 µm diameter, the third module consists of a calorimeter and it is not described in this work. Bottom left panel: detail of the prototype on the beamline. Right panel: setup on the beamline. The telescope used for the external trigger is highlighted by the light blue box, followed by the prototype positioned on the movable stage. The FEBs can be seen at the bottom, and the red arrow indicates the beam direction.

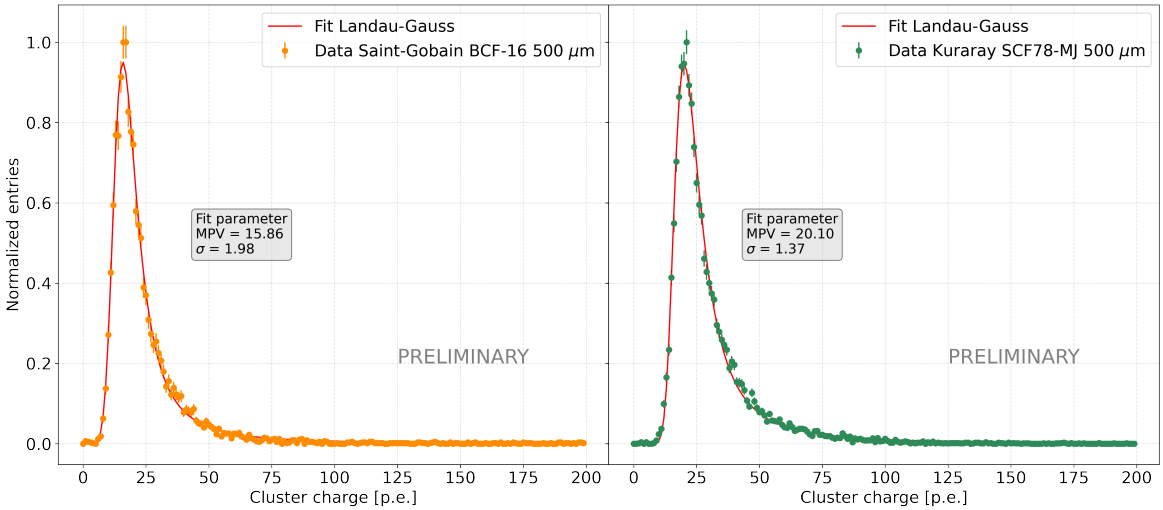

Figure 4.10: Cluster charge distribution in photoelectron units (p.e.) for the two Y-view planes corresponding to the two different fiber manufacturers Saint Gobain and Kuraray. For the plot clusters with at least two strips in the cluster are selected. The distributions are fitted with a Langaus distribution. The MPV provides an indication of the light yield from the plane.

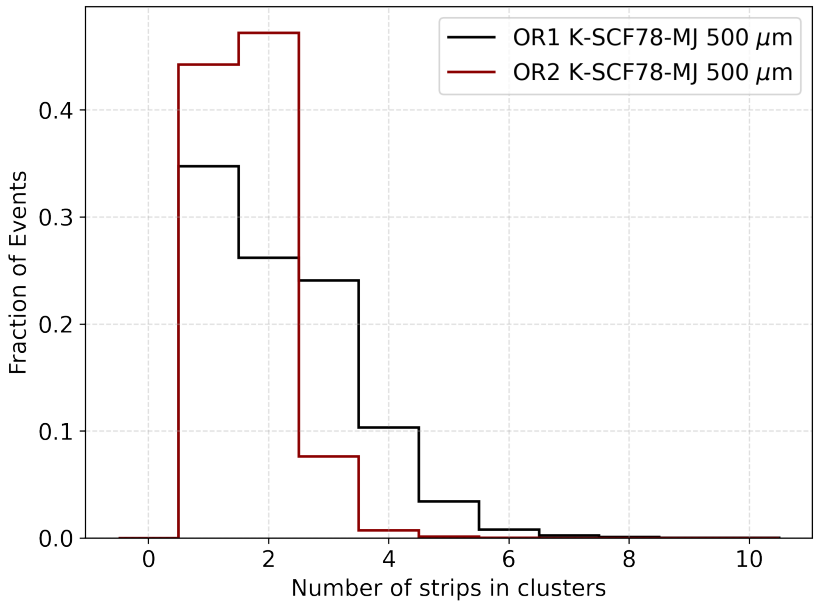

Figure 4.11: Distributions of the number of strips in the cluster for the two configurations with Kuraray fibers with 500 µm diameter: in black results for the configuration OR1 corresponding to a strip pitch of 250 µm; in red results for the configuration OR2 corresponding to a strip pitch of 500 µm.

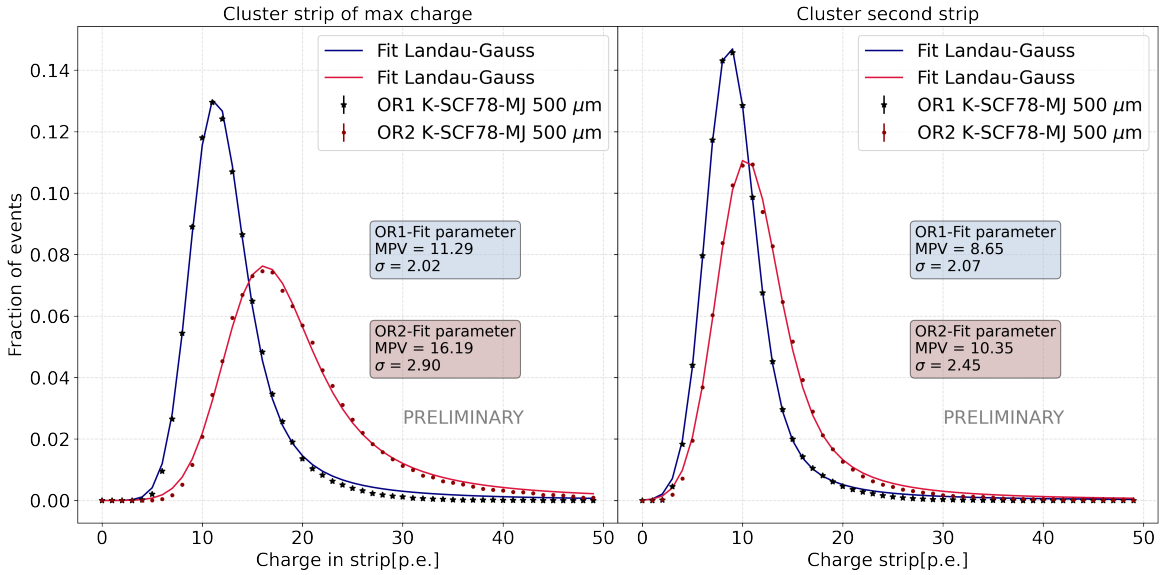

Figure 4.12: Photoelectron Distributions in the cluster strips. Left panel shows the distributions for the strip with maximum charge. Right panel displays those for the second strip. A cut on clusters with size ≥ 2 was applied to the events. Data for the OR1 configuration are shown in black, and those for the OR2 configuration in red. The distributions are fitted with a Langaus distribution.

the other strip in the cluster (i.e. the strip with the maximum charge), and therefore collects a considerably smaller fraction of light causing a possible inefficiency.

Figure 4.12 shows the distribution of p.e. counts in the strip with the highest charge in the cluster (left panel), in the second strip (central panel) and in the least energetic strip (right panel). This is shown for clusters with more than two strips for the OR1 configuration and for cluster with more than one strip for OR2 configuration. As expected, the number of photoelectrons in the strip with the maximum charge of the cluster is significantly higher for the OR2 configuration with respect to OR1. The charge in the second strip is similar for both configurations, as in both cases the second strip reads only half of the fiber.

Figure 4.13 shows the charge distributions in strips for the OR1 (black) and OR2 (red) configurations. The OR2 configuration features a larger number of photoelectrons actually collected by OR-ed strips. It can also be observed that the distribution for this configuration exhibits a peak at the rightmost end, which corresponds to ADC saturation due to signal exceeding the maximum measurable range of the ADC.

Figure 4.14 shows the distributions of the cluster charge in the OR1 (black) and OR2 (red) configurations. The plot shows that the total number of photoelectrons in the cluster does not change significantly when using the OR2 mask. Additionally, the presence of the second population of clusters at lower charge is slightly reduced in

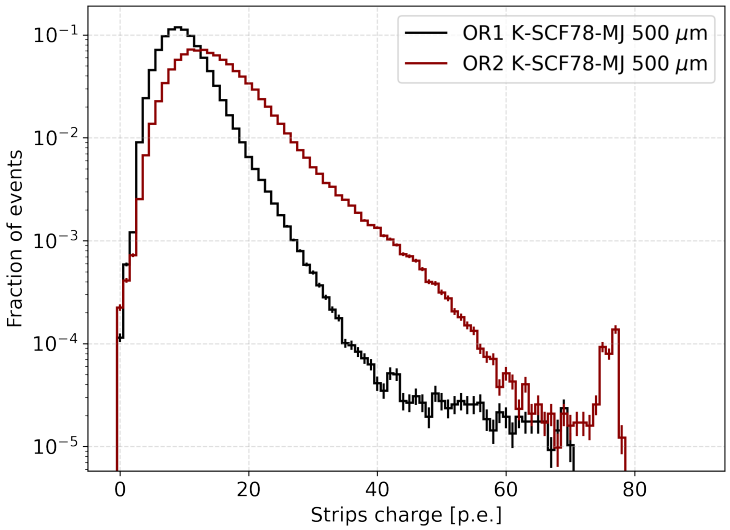

Figure 4.13: Distribution of the number of p.e. in strips for the 500µm diameter fibers in the two configurations OR1 (in black) and OR2 (in red).

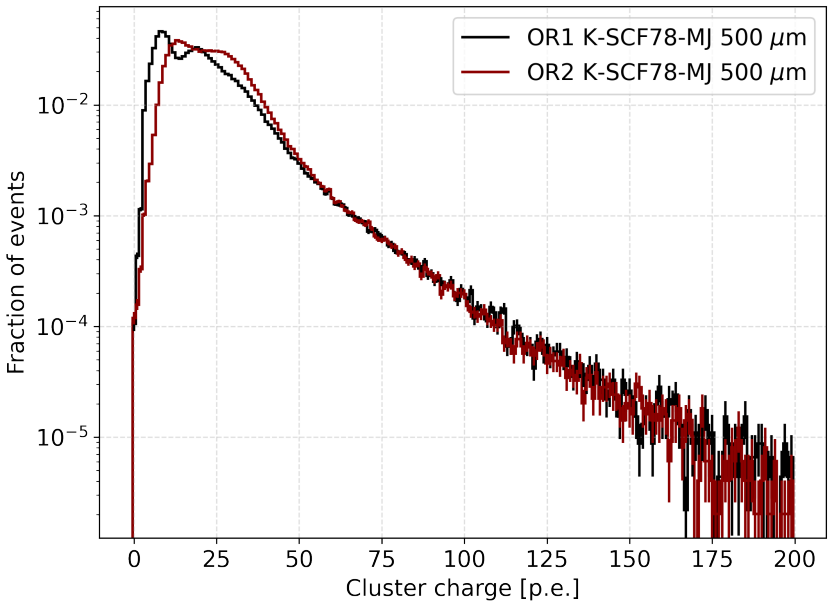

Figure 4.14: Distributions of photoelectrons in clusters. In black results for the OR1 configuration while in red results for the configuration with OR2 mask.

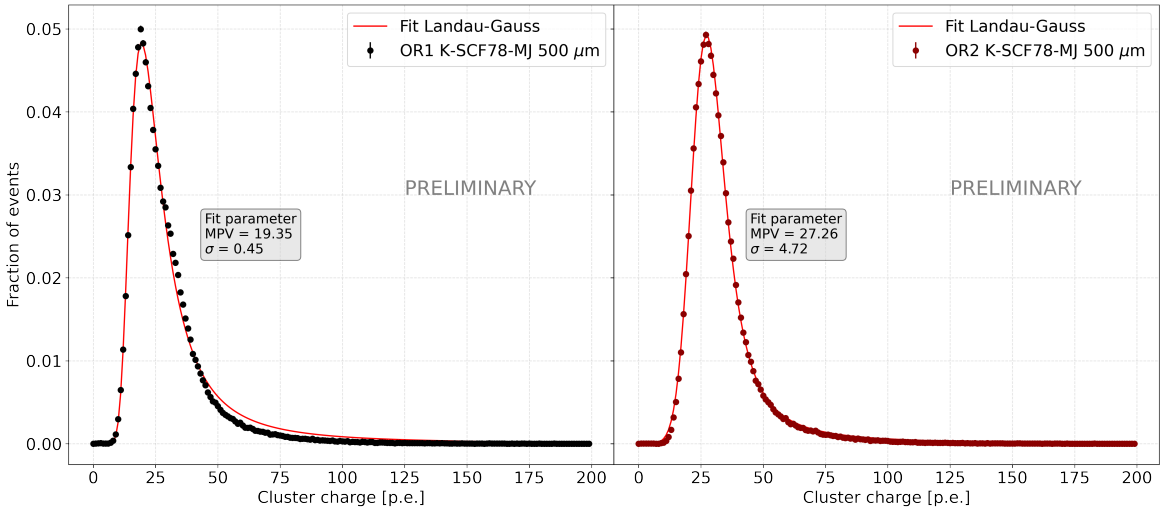

Figure 4.15: Cluster charge distribution for the two configurations OR1 (left panel) and OR2 (right panel) with fibers of 500µm diameter. The distributions are fitted with a Langaus distribution. The MPV for the OR2 configuration is slightly higher and comparable with nominal value.

the OR2 configuration, although it does not disappear entirely. This may be due to fluctuations in the gain of individual channels, which can lead to an underestimation of the cluster charge, as well as to dead strips that further contribute to this underestimation.

Figure 4.15 shows the distribution of charge in clusters consisting of at least one strip. Left panel shows the distribution for the OR1 configuration, while right panel shows the results for the OR2 configuration. The distributions are fitted with a Langaus distribution. We see that the MPV is slightly higher in the OR2 configuration, and remains close to the nominal value.

Figure 4.16 shows the distributions of the position reconstructed from the cluster charge centroid for the two configurations OR1 (in black) and OR2 (in red). The position is evaluated assuming the origin of the axis at the center of the plane. It can be concluded that the position reconstruction is not affected by the OR-ing of adjacent channel.

During the same test beam, a third X-Y module was assembled with Kuraray SCF78-MJ fibers with a diameter of 750 µm. In the OR1 configuration, each fiber is readout by at least three adjacent strips, resulting in a large number of readout channel required. From simulation results it was observed that this configuration does not provide a significant improvement in spatial resolution or efficiency with respect to the OR2 configuration.

The advantage of using fibers with a larger diameter lies in the increased material

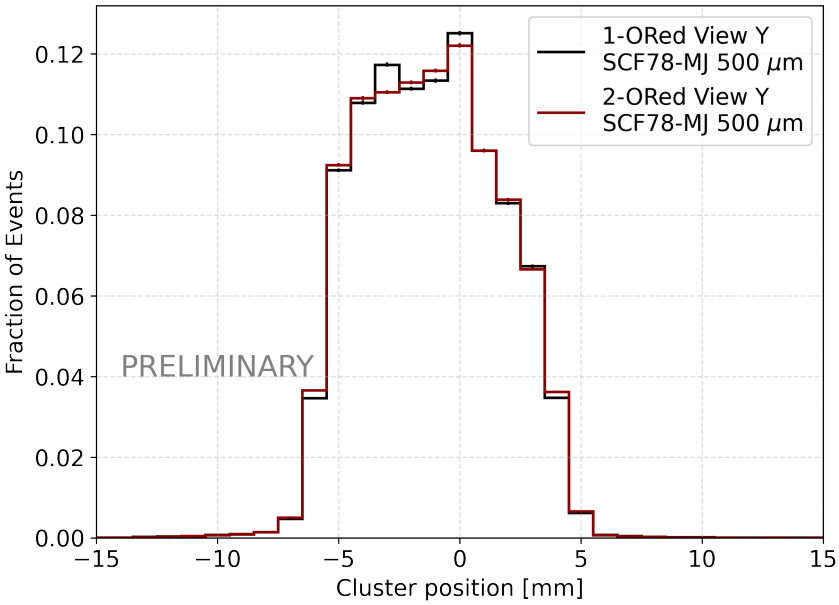

Figure 4.16: Distributions of cluster position for the two configurations OR1 (black) and OR2 (red).

thickness, which results in a higher number of photoelectrons produced, leading to an improvement in detection efficiency. However, oversizing the fiber diameter would negatively impact the spatial resolution of the tracker due to the reduced segmentation and increased scattering for low-energy particles. For this reason, fibers with a diameter larger than 750 µm were not considered.

The performance of this new module was evaluated during the same test beam by comparing, in the same runs, measurements taken from the Y-view plane of the 750 µm module (K750) in OR2 configuration with those from the Y-view plane of the 500 µm Kuraray module (K500), which was also in the OR2 configuration.

Two FEBs were used, one for each of the two planes. Two ASICs of each FEB were required for the readout of the complete OR2 side. Additionally, the other sides of both the K500 and K750 planes were readout using four adjacent strips in a OR4 configuration, thus allowing to compare all possible configurations.

In figure 4.17 the cluster size distributions are presented. The top panel shows the data for the OR2 configuration, while the bottom panel displays the data for the OR4 configuration. As expected, the use of larger diameter fibers results in larger cluster sizes. Moreover, it can be observed that for the K500 plane, there are no significant differences in the cluster size distribution using the OR2 or OR4 mask. In contrast, as expected, for K750 plane, the OR4 configuration significantly suppresses the occurrence

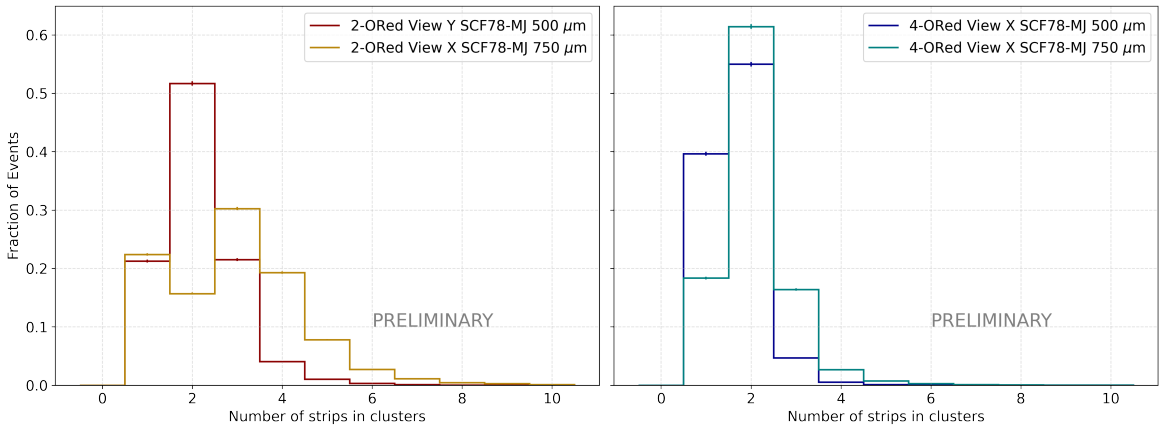

Figure 4.17: Distributions of the number the cluster for the two configurations OR2 (left panel) and OR4 (right panel). In each plot the comparison between fiber with 500 µm and 750 µm diameter are shown.

of clusters larger than three strips, favoring clusters of size 1 and 2 instead.

In Figure 4.18 the photoelectron distributions in clusters are shown for both the OR2 (top panel) and OR4 (bottom panel) configurations for the two planes, K500 (left panels) and K750 (right panels). The data are fitted with a Langaus distribution. We see that the yield for the K750 plane is almost twice that of the K500 plane. On the other hand, the yield is only slightly affected by OR-ing 2 or 4 channels.

Figure 4.19 shows the cluster position distributions for the OR2 (left panel) and OR4 (right panel) configurations. Each plot shows the comparison of the results for both the 500 µm diameter and 750 µm diameter fibers. The position of the beam is correctly reproduced in the configuration with the larger diameter fibers and the OR-ing of a larger number of channels.

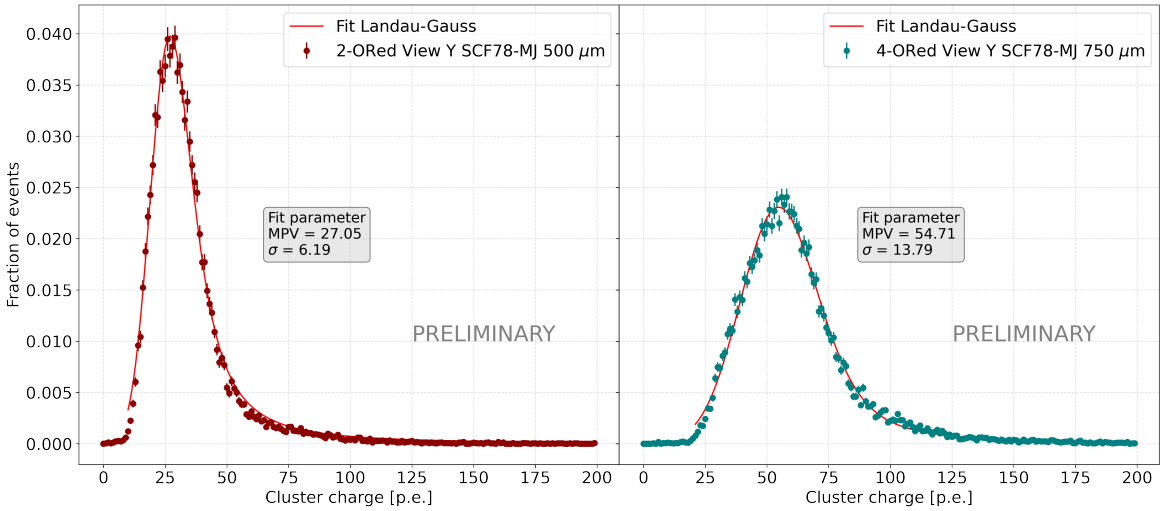

Figure 4.18: Cluster charge distribution for the two configurations tested. Left panel: fibers of 500µm diameter in OR2 configuration. Right panel: fibers of 750µm diameter in OR4 configuration. The distributions are fitted with a Langaus distribution. The MPV of 750µm diameter fibers is higher due to increased thickness of material traversed.

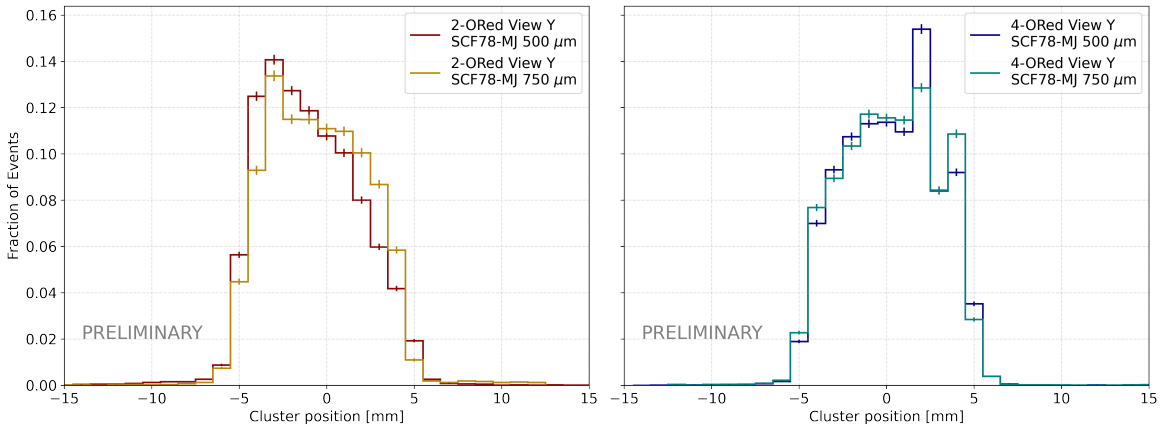

Figure 4.19: Distributions of cluster positions for the two configurations OR2 (left panel) and OR4 (right panel). In each plot the comparison between fiber with 500µm and 750µm diameter are shown.

Chapter 5

A Ziré prototype: Zirettino

In the spring of 2023, the first full prototype of the Ziré payload (see section2.2), named *Zirettino*, was designed and built. The prototype integrates all subsystems on a small scale and consists of a single X-Y module of the scintillating fiber tracker (FTK), read out from all four sides, 8 layers of plastic scintillator tiles (PST) in hodoscopic configuration, and 8 scintillating crystal cubes for a single layer of the calorimeter (CALOg) (4 LYSO crystals and 4 Gadolinium Aluminium Gallium Garnet (GAGG) crystals to compare the performances of the two different materials). Additionally, plastic scintillators are positioned on all four sides of the instrument and on the bottom side to form the anti-coincidence system (ACS). The design and construction of the prototype mechanical structure were entrusted to Sophia High Tech. The prototype was developed with the aim of validating the performance of the detector and accurately determining the optimal operating parameters and final configuration of the instrument [Panzarini et al., 2024]. In particular, the INFN was responsible for the assembling and testing of the FTK.

5.1 The readout electronics

The readout system for Zirettino was developed by Nuclear Instruments and designed according to the specifications of the flight model electronics. It consists of two evaluation boards CITIROC-FEBs, each one hosting two DAQ units. The Zirettino DAQ unit is equipped with four Citiroc 1A ASICs, an ADC and an FPGA for handling the trigger settings of the single board, configuring the ASIC parameters and handling the data acquisition. The CITIROC-FEB controls the acquisition of the two DAQ units. One DAQ unit is dedicated to the readout of the PST, the CALOg and the ACS. Three units are required for reading-out all the FTK channels.

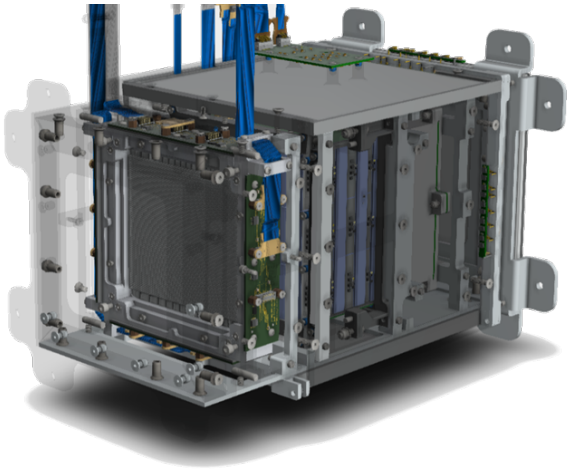

Figure 5.1: Schematic view of Zirettino prototype.

5.1.1 Citiroc 1A ASIC

The Citiroc 1A is a 32-channel analog chip designed for positive-signal SiPMs readout. Figure 5.2 shows the block diagram of the ASIC.

Each input channel is equipped with an 8-bit input DAC, that allows for trimming the bias voltage applied to each SiPM in a dynamic range of 4.5 V to equalize the gain on all the input channels. The input signal features two parallel AC coupled lines for charge measurements, one for the Low Gain (LG) and one for the High Gain (HG). The voltage gain is programmable with a 6-bit register. The dual gain readout allows the increase of the dynamic range of the ASIC. Each charge line consists of a voltage preamplifier, followed by a CR-RC shaper with adjustable peaking time in the range $12.5 - 87.5$ ns.

A trigger line can be connected to one of the two HG or LG charge lines. This consists of a fast shaper followed by two discriminators with programmable thresholds with a 10-bit global register and a 4-bit local register. One is used for the hit register of each channel and provides a trigger for the chip OR-ing all the 32 channels of the ASIC. The other provides a trigger time flag. Since the ASIC does not have auto-trigger capability, the trigger signals must be sent to a front-end system capable of determining, through a trigger logic, whether to convert the measurement or not.

The chip can operate in analog charge integration mode by integrating the shaper output, or in photon counting mode using the 32 trigger output lines.

The Citiroc 1A ASIC can operate in two different modes for charge measurements: track and hold or peak detector. The operation in peak detector mode is illustrated in figure 5.3: before the trigger signal (trig), the peak detector is in a tracking state. When a falling edge on the trig signal occurs, the peak detector switches to the peak

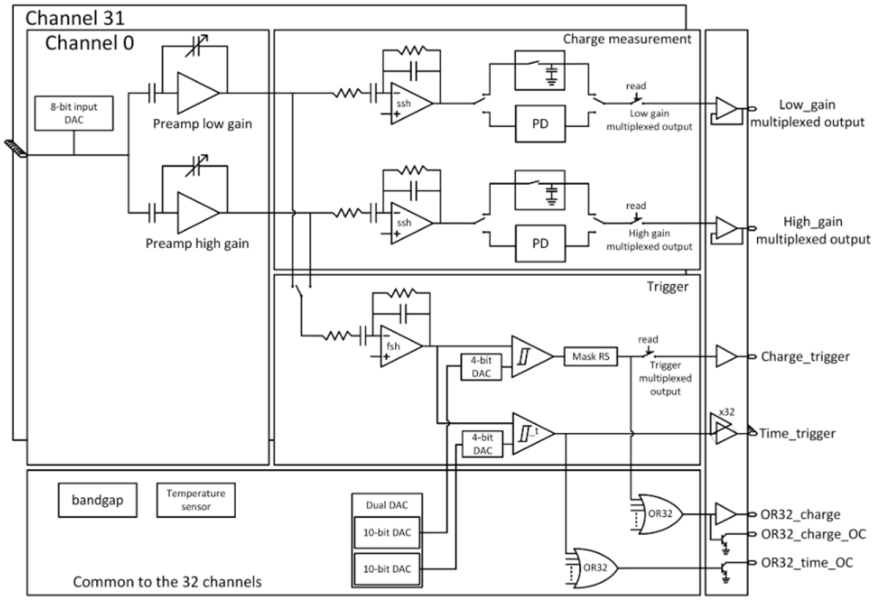

Figure 5.2: Citiroc 1A ASIC block scheme.

sensing state measuring the peak values of the signal from the slow shaper until a rising edge is detected on the hold (Hold_hg or Hold_lg) signal. At this point, the peak detector enters the hold status and retains the peak value until a falling edge is observed on the hold signal. Withe this transition the status of the peak detector switches again to track mode.

The track and hold operation is schematized in figure 5.4. A hold_hg (or hold_lg) signal controls the measurement: when this hold signal is "low" the chip is in track status and detect the amplitude of the shaper signal. When there is a transition of the hold signal to high the chip is in hold mode. The HG and LG charge measurements are read in serial using a multiplexed output.

5.1.2 The CITIROC1A-FEB

The CITIROC1A-FEB designed for testing the Zirettino prototype consists of a concentrator board hosting a central FPGA and connected to a mezzanine board which is equipped with two DAQ-units. Each DAQ-unit hosts 4 Citiroc 1A ASICs, four SHM-120 Samtec connectors and an FPGA for controlling the DAQ of the individual unit. Additionally, the board includes a number of NIM I/O channels for the input and output of logical signals such as trigger and validation.

For the readout of the whole Zirettino, two FEBs are required, along with two concentrators and four DAQ units. The concentrators can operate in synchronous

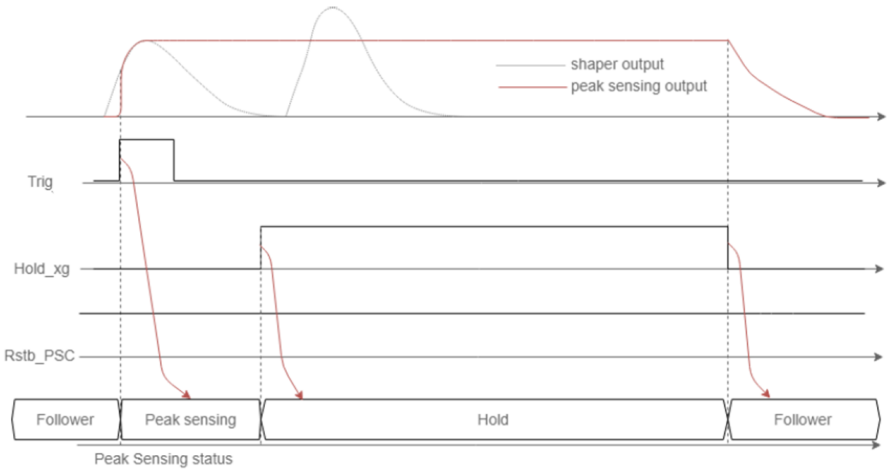

Figure 5.3: Scheme of the peak detector operation.

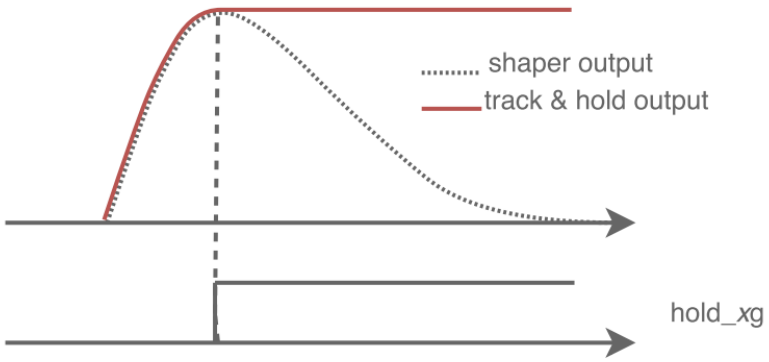

Figure 5.4: Track and hold working mode.

mode, in a master-slave configuration. On the master concentrator, one of the DAQ units is dedicated to reading-out the PST, CALOg, and ADC, while the other is responsible for reading-out the central SiPM arrays located on the four sides of the FTK plane, and thus reads the central quadrant of the FTK plane. The two DAQ-units on the slave concentrator, are dedicated to the readout of the remaining sectors of the FTK.

The master board is configured to send a trigger signal to the slave concentrator. An external validation signal allows the board to synchronize with the PETIROC-FEB, and the event tag is assigned through a modulated clock, similarly to the process described for the PETIROC-FEB.

Different logic conditions have been implemented including the FTK, the PST, and the CALOg. In particular, the FTK can provide a trigger to the other subsystem by requiring the coincidence of a signal on the same strip on both the right and left sides in both the X and Y views of the central section of the tracker. In order to take into account possible misalignments between the left and right sides of the same view the left-right coincidence request is implemented between pairs of adjacent strips.

5.1.3 The DAQ software

The DAQ software was developed in collaboration with National Instruments and results in an executable application that allows the user to configure the ASICs and perform measurements.

To configure both DAQ-units on a FEB, the acquisition software needs the IP address of the concentrator and a configuration file containing all the parameters of both the concentrators and the ASICs. In this file, the information about the trigger logic must also be included. The concentrator allows measurements to be taken in both internal and external trigger modes. Additionally, a periodic trigger is available for pedestal measurements. In internal trigger mode, the concentrator can implement various logic configurations based on triggers generated by the individual DAQ units. It can also discard the acquisition of events that are not validated by an external validation signal. All of these options need to be specified in the configuration file. After the FEBs have been configured, it is possible to start an acquisition using a different option in the acquisition software. This requires specifying the duration of the acquisition run.

I have worked on the development of a python interface software to manage acquisition processes through simple python scripts. It was possible to adapt a significant portion of the functions already written for the PETIROC-FEB software,

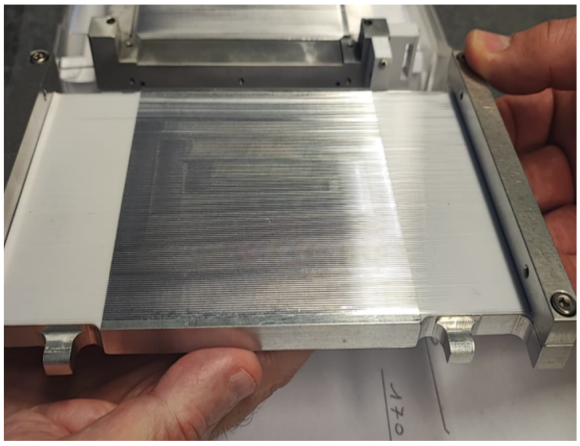

Figure 5.5: Fibers positioned in the ribbon jig.

thereby achieving the same functionalities described in section 3.5.3.

5.2 The Zirettino FTK

The FTK of Zirettino was developed based on the tests performed on the prototype described in Chapter 4. Kuraray SCF78-MJ fibers were chosen due to their higher light yield compared to Saint-Gobain BCF-12. Additionally, it was observed that using 750 µm diameter fibers in the OR4 configuration does not degrade the performance of the detector. Therefore, to reduce the number of electronic channels, thus meeting the power budget requirements of the NIMBUS platform hosting Ziré, the module was designed using this configuration.

The assembly procedure followed for the FTK module is similar to the one illustrated in section 3.4.4. The FTK module features an area of $\sim 10 \times 10$ cm^2 and consists of two planes of fibers placed along the X view and Y view respectively. Each view consists of two ribbons arranged in a staggered configuration. The two ribbons differ of 1 fiber, with 131 fibers in the bottom ribbon and 130 fibers in the top one. The 1-meter long fibers are cut in sections of 17 cm and placed in a jig specifically designed. The end plates of the jig allow to fix the fiber in position as shown in figure 5.5. The glue is deposited directly on a frame where the jig can be fixed for the glue curing time. The two ribbons are built in the same way and then assembled together forming the first view. After repeating the procedure for the other view a complete module is obtained.

The scintillation light is readout with the S13552 SiPM array by Hamamatsu. Each side is readout by three SiPM arrays mounted on a PWB specifically designed for OR-ing the groups of four adjacent strips. Three LSHM-120 Samtec connectors are

Figure 5.6: FTK module assembled for the Zirettino prototype.

assembled on the other side of the PWB allowing to read out the whole side with a total of $32 \times 3 = 96$ channels. The whole FTK is readout by 12 SiPM arrays for a total of 384 readout channels.

5.3 Tracking capability

To verify its performance, Zirettino underwent a series of beam test campaigns from late 2023 to early 2024. During these beam tests, the tracker plane prototypes described in the previous chapter were also placed along the beamline and were operated as ancillary tracker units. Specifically, the K500 module was positioned at the front of the beampipe, followed by Zirettino, with two K750 planes placed upstream.

5.3.1 Tracking algorithm

The main interest of these tests is to determine the spatial resolution that the prototype can achieve. In order to evaluate the spatial resolution, the trajectory of the

particle needs to be reconstructed. This is done using the following tracking algorithm for the external tracker planes.

The chosen reference frame is a right-handed coordinate system, with the positive z-axis oriented along the beam direction. The vertical fiber planes provide position information along the x-axis, while the horizontal fiber planes give the y-coordinate. After identifying all clusters in each event, it is assumed that the coordinate of the passing particle along the axis corresponding to the view plane is the center of gravity of the cluster charge. The z coordinate is measured from the center of the plane to the first tracker plane. Only events with at least one cluster in both the X and Y views in at least two out of three external tracker planes are selected. Therefore, for these events, we have a set of positions in the Y view and another in the X view for each of the fired tracker modules. In each event the projections of the track in the X-Z and Y-Z planes are reconstructed by fitting all possible combinations of these points with a straight line and selecting the one that minimizes the chi-squared value. The two curves are described by the equations:

$$\begin{aligned} x &= m_x z + q_x \\ y &= m_y z + q_y \end{aligned} \tag{5.1}$$

with m_x and m_y and q_x and q_y the slopes and the intercepts of the track best fit in the X-Z and Y-Z planes respectively. These can be used to reconstruct the positions x_{rec} and y_{rec} of the track in each module. The residuals on each plane are then calculated as the distance between the calculated position and the reconstructed position:

$$\begin{aligned} r_x &= x_{clu} - x_{reco} \\ r_y &= y_{clu} - y_{reco} \end{aligned} \tag{5.2}$$

The expected distribution of the residuals is a gaussian centered at zero with σ corresponding to the spatial resolution of the tracker. However, the three modules measure the position of the particle in a local coordinate system. In order to obtain the global coordinates it is necessary to perform a translation of a quantity $x_0; i$ and $y_0; i$ in the two view respectively on each module in order to align the three modules.

The alignment is obtained by means of an iterative procedure that corrects the position of each module with respect to the others at each iteration until systematic deviations are minimized. An initial gaussian fit of the residual distributions identifies the systematic offsets $x_{0;i}$ and $y_{0;i}$ on each module of the external tracker as the mean of the best fit curve. To perform the alignment, this offsets are subtracted from the cluster position evaluated from the charge centroid in each module. The new positions

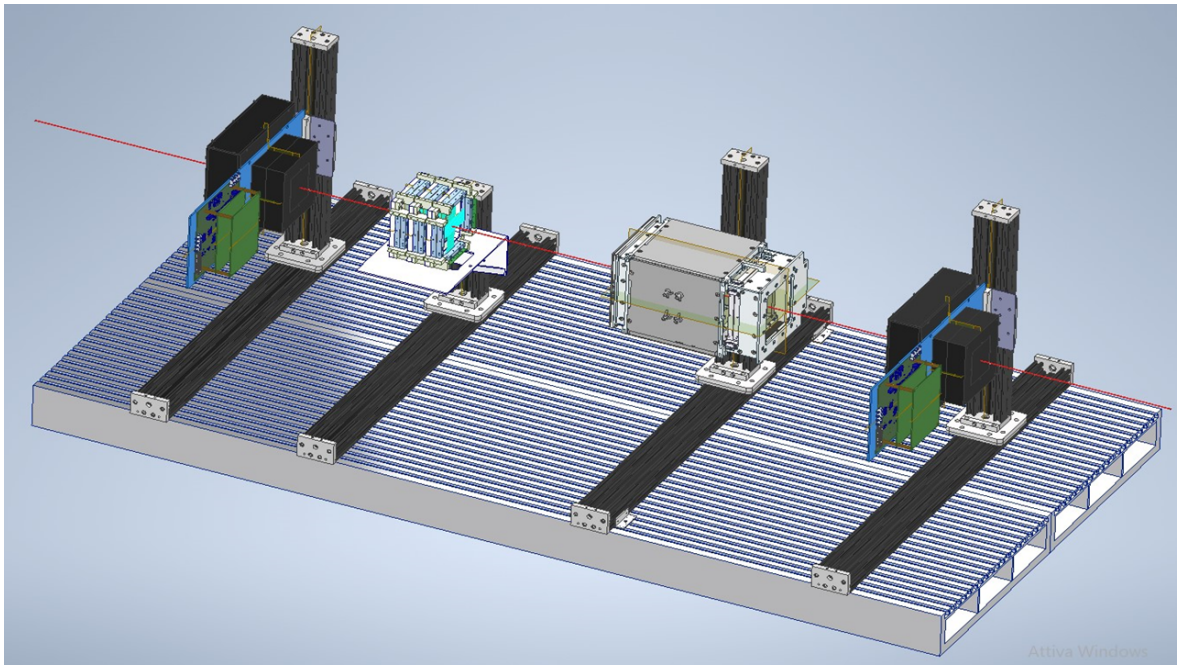

Figure 5.7: CAD scheme of the detectors along beam line in the Zirettino test beam campaigns.

are used to re-evaluate the tracks using the same algorithm defined above, leading to the determination of updated fit parameters m_{x_1}, m_{y_1}, q_{x_1} and q_{y_1}. With these new parameters, the reconstructed position on each module is recalculated, and the new residuals, are obtained. From the distribution of the new residuals the new offsets are evaluated as the mean value of the best-fit gaussian distribution. A second iteration of the previous alignment procedure is applied. At the end of the alignment procedure, the distribution of the residuals become a perfect gaussian centered at zero, ensuring accurate alignment across all modules. The width of the distribution decreases at each iteration. The sigma of each distribution represents the spatial resolution of the corresponding plane.

Using the tracking parameters after two iterations, m_{x_2}, m_{y_2}, q_{x_2} and q_{y_2} the impact point on the Zirettino tracker plane can be determined. The distribution of the residuals can be fitted with a gaussian function, where the mean value represents the offset to be subtracted from the cluster positions on the zirettino module. By iterating this procedure twice, the alignment of the Zirettino module with the other external tracker modules is achieved.

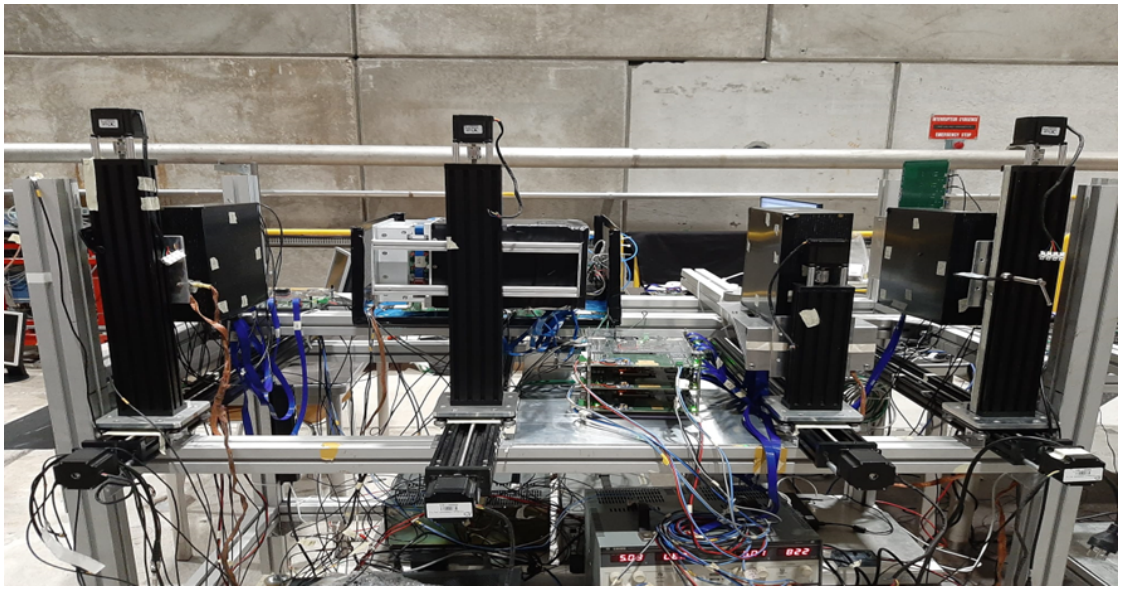

Figure 5.8: Setup of the test beam at the CERN PS T10 line in September 2023. Zirettino is positioned on the second stage at the center of the setup with the FTK facing the beam. Three external tracker are positioned on the other three stage enclosed in three black boxes to prevent external light from reaching the photodetectors. Two telescope of plastic scintillators are positioned at the ends of the beamline to provide an external trigger signal.

5.3.2 The beam test at the PS-T10

The first beam test was performed at the T10 line at the CERN PS facility in September 2023. Figure 5.7 shows the CAD scheme of the setup implemented in this beam test. In the scheme the beam direction is from right to left and is the direction of the z-axis of the right-handed coordinate system chosen for the analysis.

The various detectors are positioned on the beam using mechanical stages that allow precise positioning in the x and y directions. The detectors are mounted on specially shaped aluminum brackets designed to avoid obstruction of the active areas. Upstream and downstream on the beamline, on the same brackets holding the tracking planes, boxes containing the scintillator telescopes for the external trigger are placed. Each telescope consists of two thin plastic scintillator bars ("fingers") arranged orthogonally followed by two square scintillator tiles, the second of which featuring a central hole to serve as a veto. As in the previous beam tests, the trigger logic can be implemented by selecting an arbitrary number of scintillators in the two telescopes. The tracking planes, as shown in the figure, are placed inside boxes made of DELRIN POM-C[1] to isolate the modules from external light while keeping a low material budget along the beamline. The first support holds the box containing the K500 module. The next

[1] https://hmpsrl.it/categoria-prodotto/plastica/delrin-pom-c/

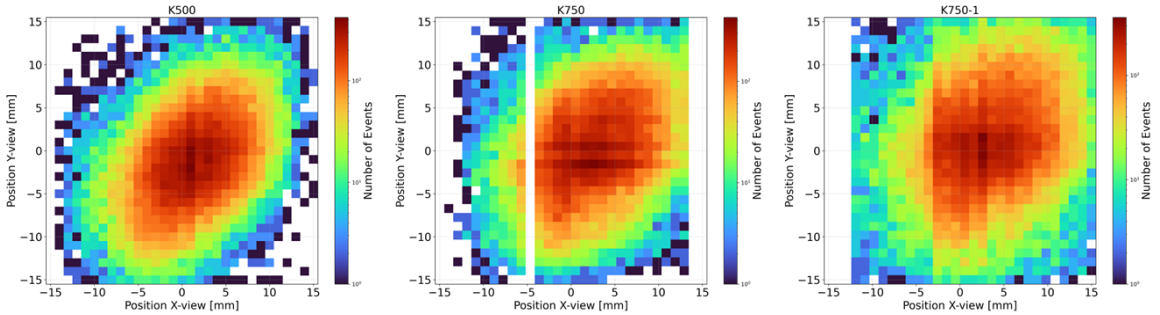

Figure 5.9: Cluster positions in the X and Y views after two alignments for the three external tracker modules K500 (left panel), K750 (central panel) and K750_1 (right panel). The beam position is clearly visible at the center of the detector active region. It can be observed the broadening of the beam across the three successive modules.

stage supports the Zirettino prototype with the FTK positioned in front of the beam pipe. Finally there are two additional external tracking planes, designated as K750 and K750-1.

The first module K500 is readout only on two sides, one in the X-view and one in the Y-view. The FTK of Zirettino and the module K750 are readout on all the 4 sides. The last tracker module K750-1 is readout only by the same two sides as the K500. The data acquisition for the modules occurs synchronously: the K500 tracker is connected to a FEB, which acts as the master for both the other PETIROC-FEBs and the two CITIROC-FEBs. The acquisition is triggered externally by the signals produced by the two telescopes. This trigger is sent to the master FEB, which then transmits a trigger signal to the other PETIROC and CITIROC FEB boards in the chain, along with a clock signal modulated to provide the slave boards with the acquisition event tag.

The data from both Zirettino and the external tracker are processed as described in section 3.5.4.

The cluster positions are then reconstructed. Figure 5.9 shows the distribution of the cluster positions in the X-view and Y-view for each external tracker module on the beamline. The beam position is clearly reconstructed. The white band in the central figure is due to a dead strip in a SiPM array. Figure 5.10 shows the same distribution for the Zirettino FTK. We see that the events are concentrated in the central region of the plane, corresponding to the shadow of the external tracker. This is due to the external trigger configuration that requires a hit in the external tracker and, as a result, it selects tracks within the central $30 \times 30\text{mm}^2$ quadrant.

After selecting only events where at least one cluster is present in the X-view of at least two external tracker modules, and similarly for the Y-view, the particle tracks were

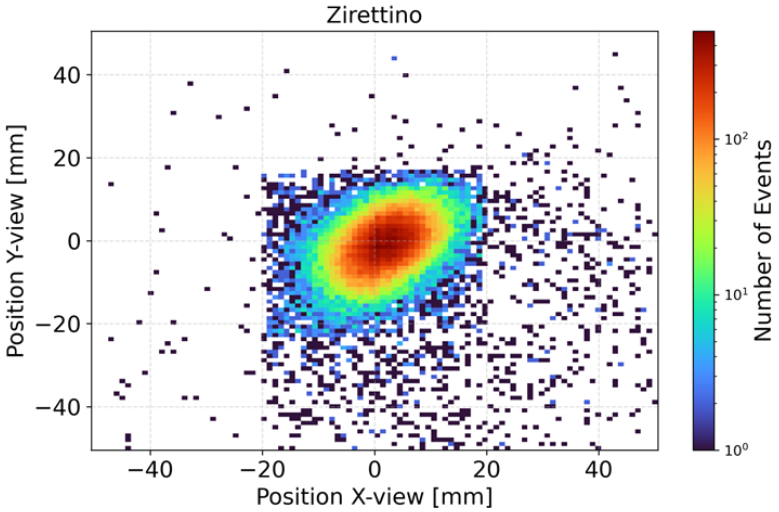

Figure 5.10: Cluster positions in the X and Y views after two alignments for Zirettino tracker module

determined and the impact positions on each module were reconstructed. The resulting residual distributions are shown in Figure 5.11. We can see that before alignment, the residual distributions do not have null mean and exhibit large spreads.

After subtracting the mean value, determined from the Gaussian fit of the residual distribution, from the cluster position and iterating the procedure twice, the resulting distributions are shown in Figure 5.12. The distributions are perfectly peaked at zero but they are no Gaussian, instead, slight tails can be observed caused by multiple Coulomb scattering of charged particles with the atoms of the material on the beamline. The best fit curve is the sum of two Gaussian distributions with the same mean value but different sigma and amplitude. In this case, the resolution is determined by a combination of the widths of both the gaussians and was evaluated from the FWHM of the best fit function. Figure 5.12 shows the residual distribution fitted with the sum of two gaussians (red curve). The two gaussians are also reported in the plot. The errors on the FWHM values are estimated with the pseudo-experiment method.

The spatial resolution becomes poorer in the downstream modules, as the thickness of the material traversed by the beam particle increases. The best value is (159 ± 7) µm in the first plane, and it increases up to (294 ± 13) µm in the last plane. Table 5.1 summarizes the results on the three external tracker modules.

The tracks calculated using the external tracker planes were used to evaluate the impact point on the Zirettino tracker module as well. The residual distribution after the alignment procedure is shown in Figure 5.12. It can be observed that the spatial resolution found is of about $\sim (346 \pm 5)$ µm. With a strip pitch of 1 mm, the expected spatial resolution is

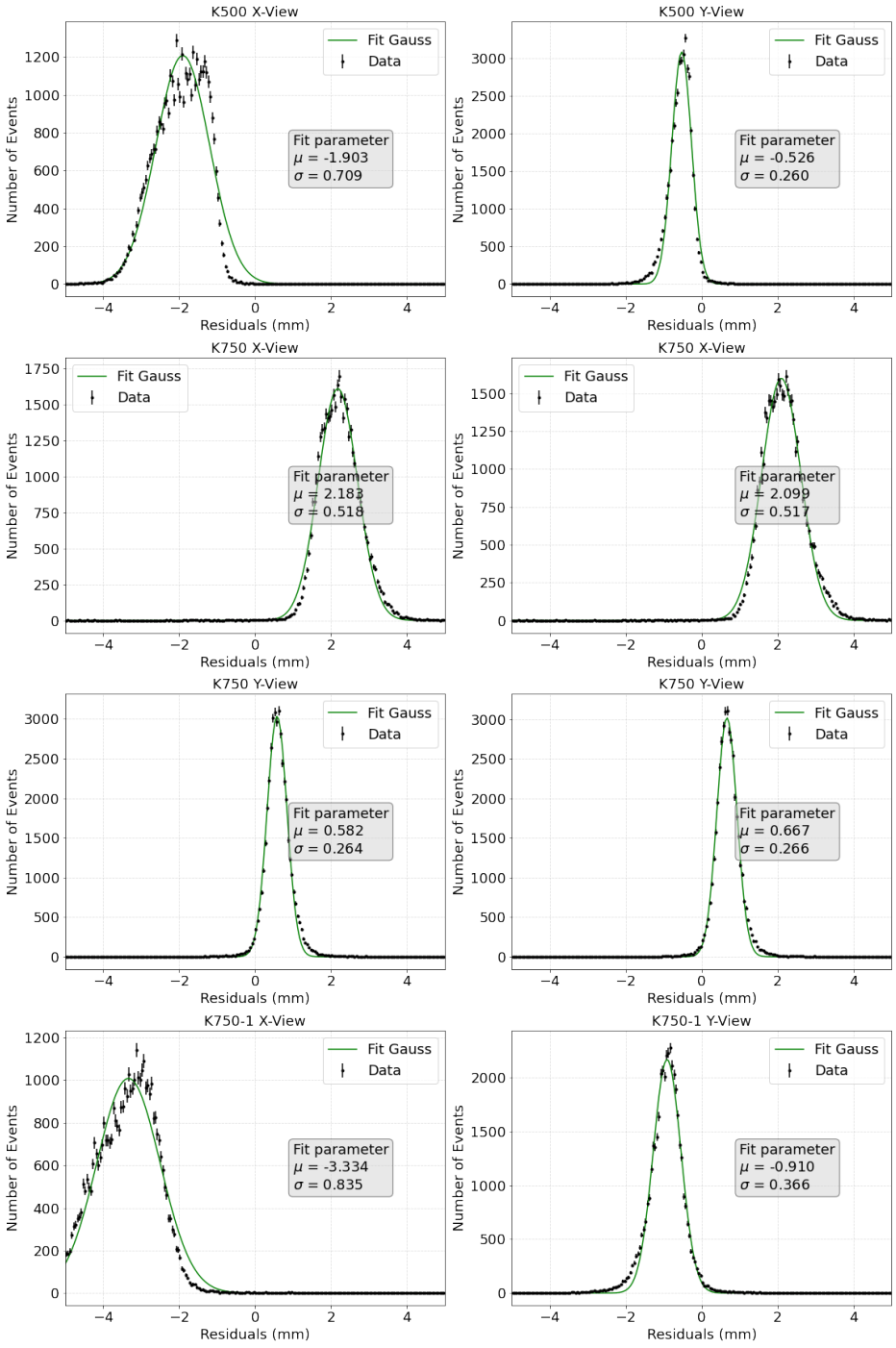

Figure 5.11: Residual distributions for the external tracker module before the alignment procedure. In left panels are the distributions for X-view planes, in right panel that referred to the Y-view. Top panels shows data for the first external tracker K500. The second and third row are for the K750 module readout by all the four sides. The bottom panels shows the data for the last module K750_1. The distributions are fitted with a gaussian to determine the offsets for each plane.

	Resolution [µm]
K500 X-view	159 ± 7
K500 Y-view	164 ± 10
K750 X-view	243 ± 10
K750 X-view	226 ± 10
K750 Y-view	209 ± 10
K750 Y-view	221 ± 16
K750_1 X-view	294 ± 13
K750_1 Y-view	277 ± 13

Table 5.1: Summary of the resolution values estimated from the residual distributions. The resolutions and the errors are estimated from the fit with the pseudo-experiment method.

$$R \simeq \frac{pitch}{\sqrt{12}} = 289 \text{ µm} \tag{5.3}$$

The values obtained are consistent with expectations. The slightly higher value is due to multiple Coulomb scattering that particles undergo as they pass through the various material layers separating the tracker modules. Additionally, the track was reconstructed from the external tracker modules, which have a resolution comparable to that of the module under examination.

Figure 5.14 shows the reconstructed positions compared with the cluster positions. The three plots in the top panels show the results for the three external tracker modules, the bottom panel shows the data for the FTK of Zirettino. Despite a slight spread in the innermost planes a good correlation is found.

To verify the dependence of the spatial resolution on the cluster charge, we studied the residual distribution compared to the cluster charge. This is shown in Figure 5.15. The three panels at the top shows the results for the three external tracker. The bottom panel shows data from the Zirettino FTK. We see that for the first external tracker, the events causing a larger spread in the residuals predominantly correspond to clusters with a charge below approximately 40 p.e.. In contrast, for the subsequent modules, this correlation is less significant, and the amplitude of the residual distribution becomes nearly independent of the cluster charge.

Plots in Figure 5.15 show the correlation between the residuals and the charge in the clusters, the top panel for the three external tracker modules and the bottom panel for the Zirettino FTK. Low energy clusters mainly contribute to the spread of the residuals.

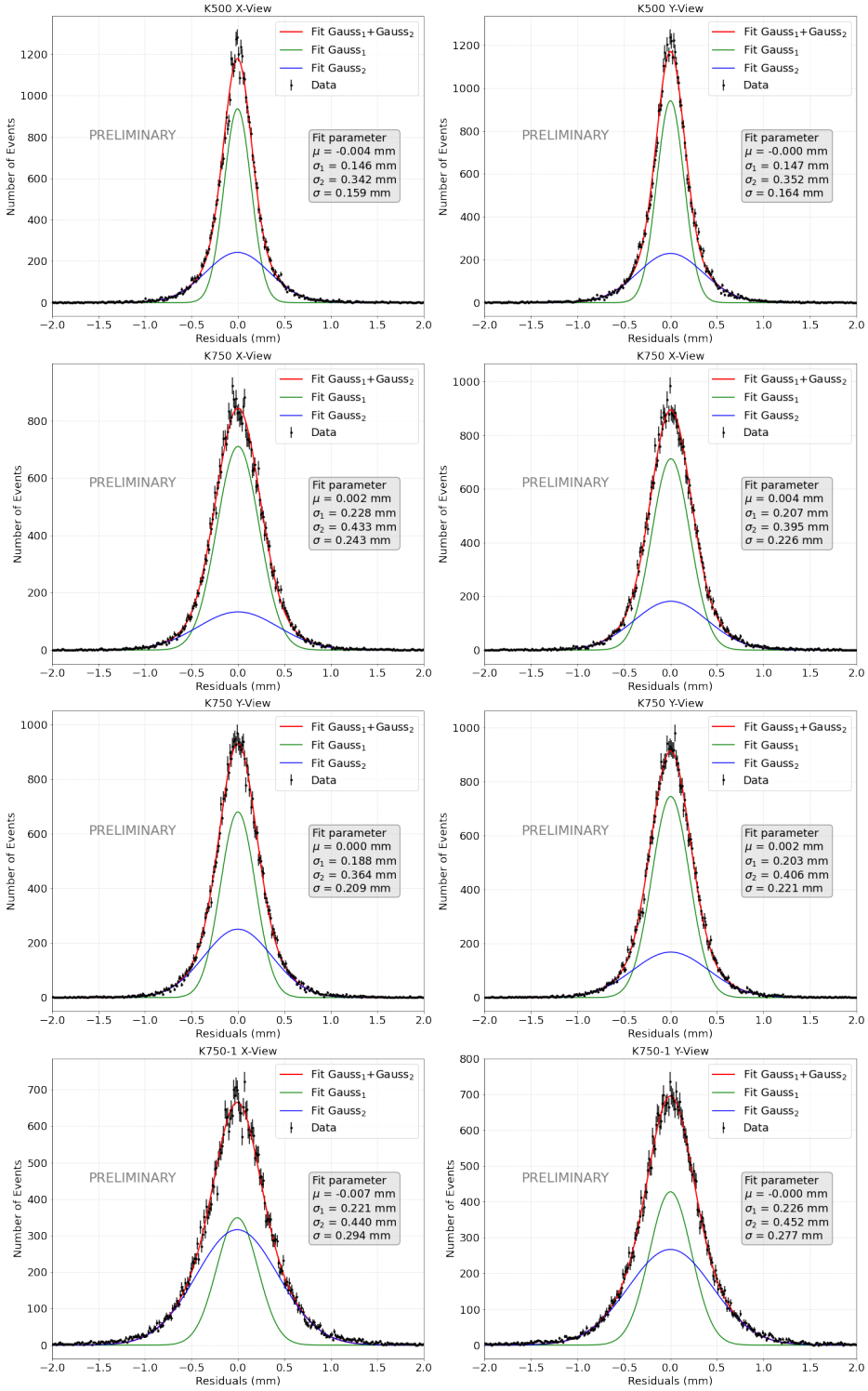

Figure 5.12: Residual distributions for the external tracker modules after the alignment procedure. In left panels are the distributions for X-view planes, in right panel that referred to the Y-view. Top panels shows data for the first external tracker K500. The second and third row are for the K750 module readout by all the four sides. The bottom panels shows the data for the last module K750_1. The distribution fit with the sum of the two gaussian is shown.

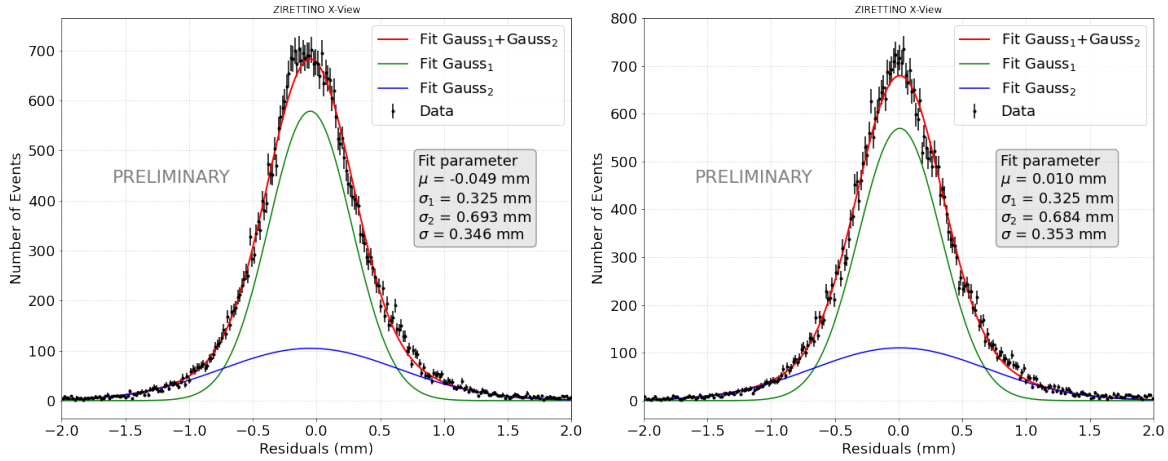

Figure 5.13: Residual distributions for the Zirettino tracker module after two iteration of the alignment procedure. In left panels is shown the distributions for the X-view plane, in right panel the Y-view plane. The distributions are fitted with the sum of two gaussian to determine the spatial resolution for each plane.

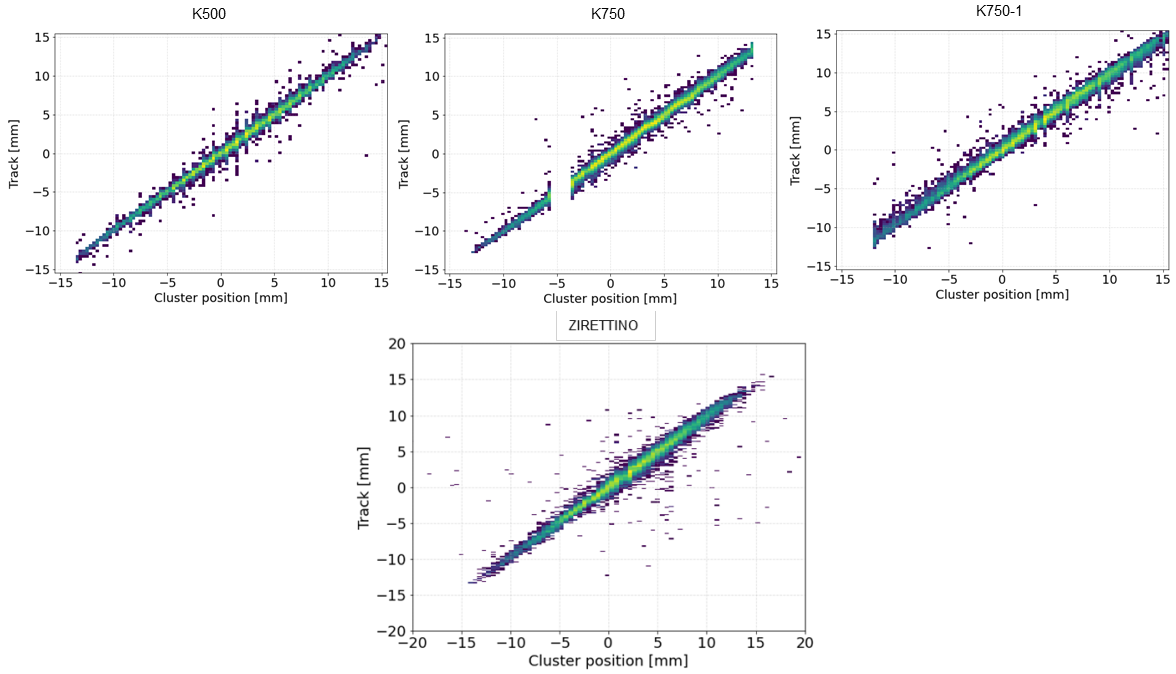

Figure 5.14: Comparison between the reconstructed positions and the cluster positions evaluated as the charge centroid. Top panels refers to the X-view planes of the external tracker modules. The bottom panel refer to the X-view plane of the Zirettino tracker module.

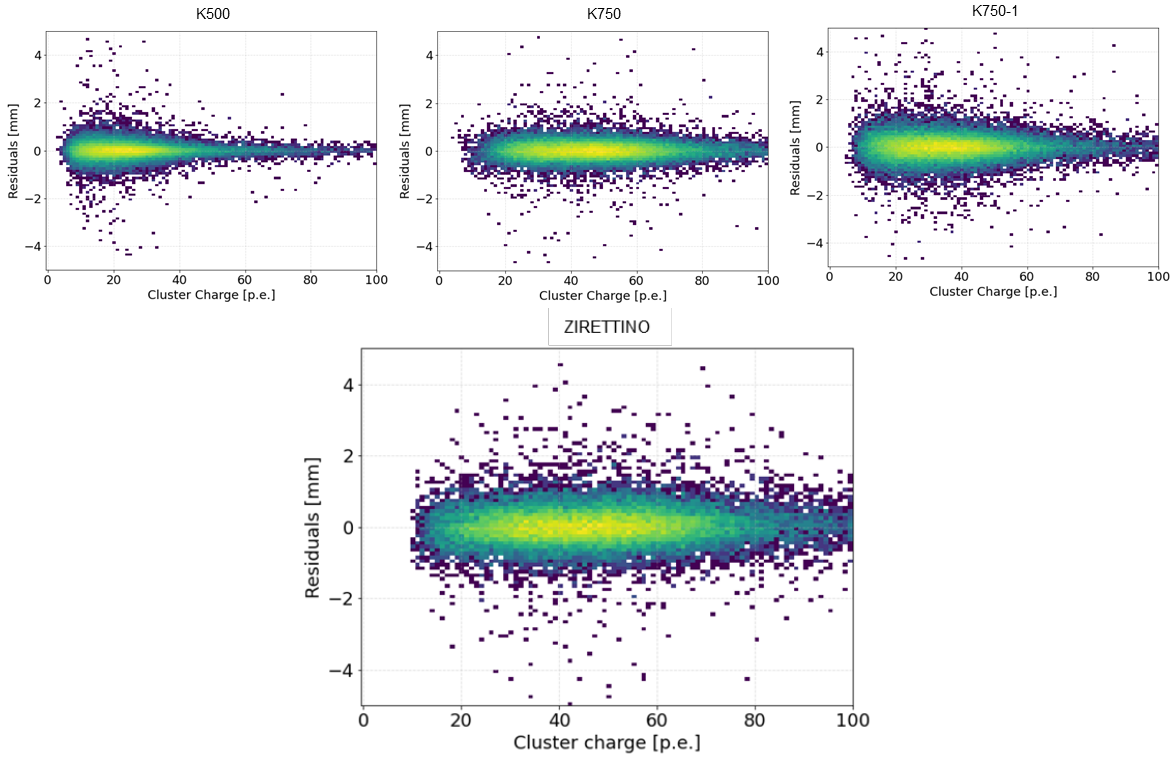

Figure 5.15: Correlation between the residuals and the charge in the clusters. Top panels refers to the X-view planes of the external tracker modules. The bottom panel refer to the X-view plane of the Zirettino tracker module.

5.3.3 Trigger efficiency

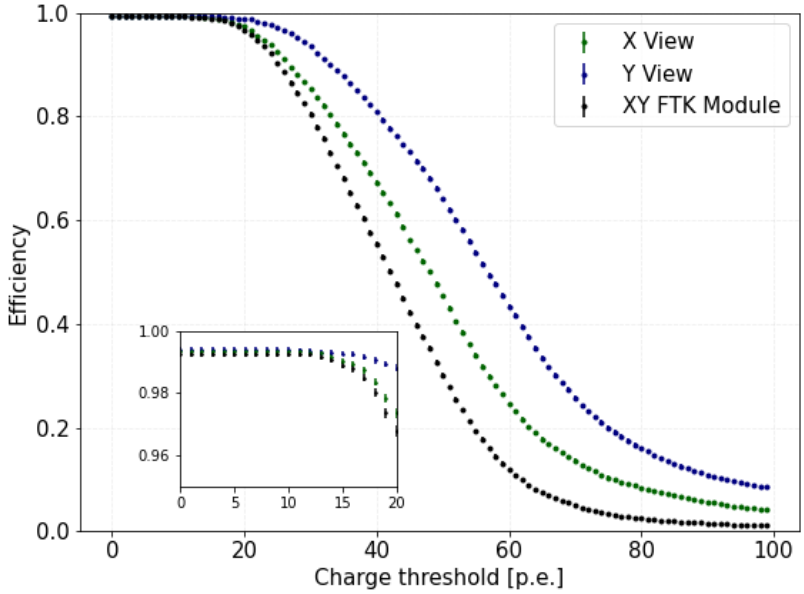

Figure 5.16: Trigger efficiencies of the Zirettino tracker module as a function of the threshold of p.e. per strip.

The main task of the FTK is to reconstruct the tracks of the incoming particles. Additionally, the detector is expected to provide a fast trigger to all other subsystems of Zirè. Therefore, it is essential for the detector to demonstrate a high trigger efficiency. Since the trigger logic requires detection in at least one module in both the X and Y views, the trigger efficiency was evaluated by imposing the condition that at least one strip is activated, with a charge above a certain threshold, in both planes:

$$\epsilon(q_{th}) = \epsilon_X(q_{th}) \cdot \epsilon(q_{th}) \tag{5.4}$$

with

$$\epsilon_i(q_{th}) = P(q_i > q_{th}|\text{i-view hit}) = \frac{N_{q>q_{th}}}{N_{tot}} \tag{5.5}$$

where q_{th} is the charge threshold, q_i is the charge in the i-th view, $N_{q>q_{th}}$ is the number of events in the i-th view with a charge above the threshold in at least one strip, and N_{tot} is the total number of events.

The statistical error can be extimated as

$$\sigma_\epsilon = \sqrt{\frac{\epsilon(1-\epsilon)}{N_{tot}}} \tag{5.6}$$

This efficiency is clearly dependent on the chosen threshold and increases as the

threshold decreases, since more strips are likely to have a charge above the threshold. At the same time, a higher threshold reduces signal contamination from noise, so a threshold high enough to reject noise while still ensuring a high efficiency must be chosen. Figure 5.16 shows the efficiency of the Zirettino module, calculated as the product of the efficiency of the X-view plane and the efficiency of the Y-view plane, which are also shownin the plot as functions of the threshold in photoelectrons units. A plateau corresponding to an efficiency greater than 99% is found, extending up to approximately 15 photoelectrons.

Chapter 6

Space validation

Space-based experiments operate in the harsh environment of space. Sizes, weight and costs of the mission are strongly influenced by the space environment. During its operational life, the satellite must withstand to thermal stresses due to large differences in temperature, systems have to work in vacuum conditions with the risk of outgassing for materials not specifically made for space applications or with the risk of structural deformations caused by the imperfect balance of pressures on the different surfaces. Moreover during the launch phase the satellite is subject to significant mechanical stress due to intense accelerations and vibrations.

In the design and testing of instrumentation for satellite applications, it is essential to consider both the stresses imposed by the space environment and the impossibility of accessing various components for repairs after deployment. For this reason, the Type Test Theory is employed. This theory is based on the principle that the development process must adhere to precise and accurate engineering data, which provide a comprehensive set of specifications and procedures for component fabrication. These specifications are crucial for meticulously controlling the production phases, ensuring that all components are equivalent. Consequently, the results obtained from qualification tests on a single item (the type test article) can serve as validation for all other products, thus qualifying the design.

To verify that items have been manufactured according to specifications, less rigorous acceptance tests (quality control) are sufficient. Quality assurance aims to ensure that manufacturing adheres to the specifications outlined in the engineering data and that parts supplied by vendors meet the required standards. Furthermore, all components and the entire satellite must undergo a qualification program designed to certify the performance of the instrumentation through functional testing and its ability to withstand the space environment. The full space qualification sequence include Thermal, Mechanical and Thermo-Vacuum tests to simulate launch conditions.

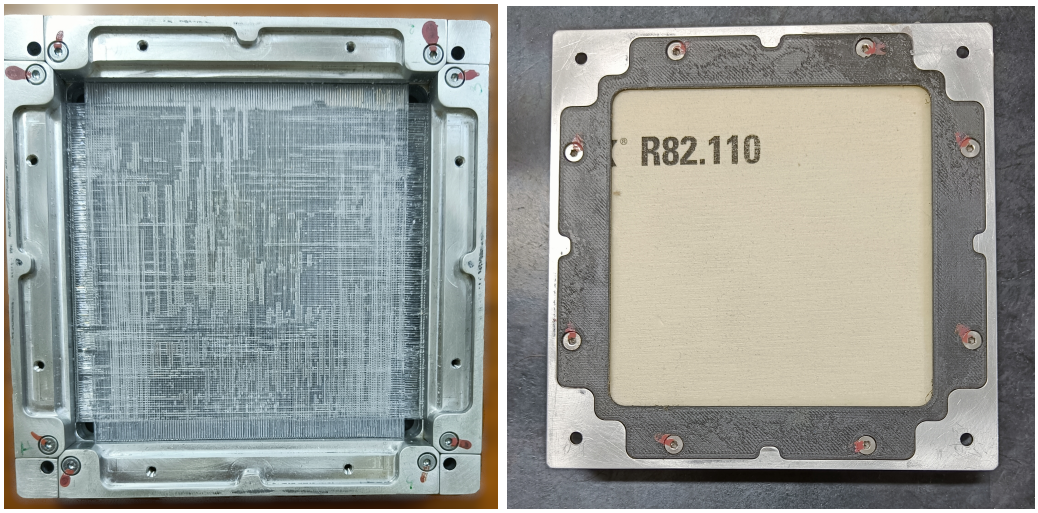

Figure 6.1: The two FTK module assembled for the structural model of Ziré. In the left panel the module with epoxy glue on all the fiber length. In the right panel the module equipped with two AIREX mat.

Vibrational tests must be preceded and followed by functional tests, while functional tests for thermal vacuum scenarios are typically conducted simultaneously.

Before the launch, an environmental verification for Ziré and all its subsystem is required to minimize risks. Tests have to be performed in accordance with the ECSS (European Cooperation for Space Standardization) standards issued by the ESA (European Space Agency).

6.1 Mechanical structure variations

To meet the requirements of space instrumentation, payloads must be robust enough to withstand the launch phase without deterioration. At the same time, the materials chosen must be lightweight to stay within the material budget. For this reason, at the beginning of 2024, when the construction phase of the structural model of Ziré began, two different modules for the FTK were developed in order to compare their performance and test their robustness during dynamic testing.

The main concern is to keep the fibers in position even after the stresses experienced during the launch phase of the satellite preserve the planarity of each tracker layers. To achieve this while maintaining a low material budget, two approaches were used.

The first, more conservative approach, does not significantly impact the standard module design but involves applying the epoxy glue, used to fix the fibers to the support, across the whole surface of the module. This creates a single, continuous mat of fibers bonded together over the entire surface of the module. The left panel of Figure

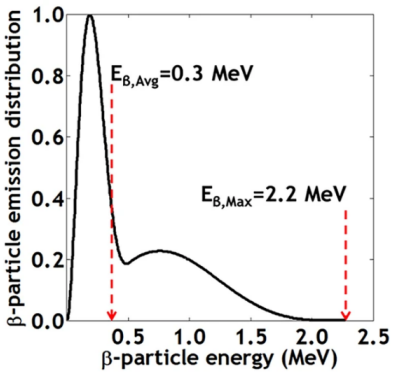

Figure 6.2: Energy distribution of electrons emitted in the Sr-90 beta decay chain. (From: `https://www.nature.com/articles/srep38182`)

6.1 shows a photo of this new module. It can be compared to the photo of the standard FTK in figure 5.6. We see that the fibers are held in position not only at the ends by the endcap of the jig, but also along their entire length by the layer of glue.

The second option involves supporting the fibers and thus ensuring the flatness of the module by using a support structure. To keep the material budget of the module low and avoid altering the performance of the tracker, a material that is both strong and of very low density is required. A mat of AIREX R2[1] was used for this purpose. AIREX is a material widely employed in aerospace applications due to its high mechanical strength combined with low density (the mat used have a density of 110 kg/m^3). It is a rigid foam made of polyvinyl chloride (PVC) characterized by a high resistance to mechanical stresses and by the capability of absorbing vibrations, thus protecting the components it supports. Its good thermal insulation properties further enhance its suitability for this application. The module built with two AIREX supporting mats is shown in the right panel of Figure 6.1.

To verify that the use of glue across the whole fiber surface and the implementation of AIREX mat did not affect the performance of the FTK, I performed laboratory tests using a Sr-90 radioactive source.

Sr-90 is a radioactive isotope of Strontium with a half-life of 28.8 years. It undergoes beta decay into Yttrium-90, with a decay energy of 0.546 MeV distributed among an anti-neutrino, an electron and the Y-90 isotope which decays into stable Zirconium-90. The maximum energy of the electron emitted in the beta decay is of 2.279 MeV. The energy distribution of the electrons emitted in the two beta decays is shown in figure 6.2.

[1] `https://www.3accorematerials.com/en/markets-and-products/airex-foam/airex-r82-resistant-dielectric-foam`

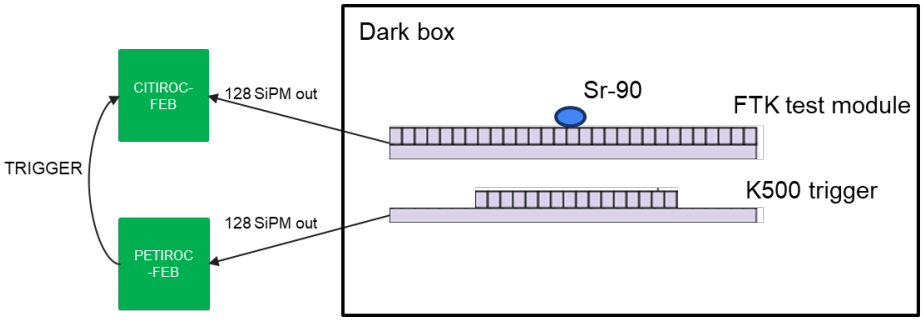

Figure 6.3: Sketch of the set up for tests performed on the three FTK module in laboratory with the Sr-90 radioactive source.

Setup

The setup is illustrated in figure 6.3. A K500 module placed at the base of the system in a dark box was readout on all four sides in OR4 configuration by a PETIROC-FEB, in such a way as to implement the AND_XY trigger logic which, as previously mentioned, requires the coincidence of the signals on the same strip from the left and right sides of the each view, and then requires a coincidence of both views. The K500 module has an active area of 3×3 cm^2. The FTK module to be tested was then placed above this module, ensuring that the central region of the plane, which has a surface of about 10×10 cm^2, was aligned with the tracker underneath. The radioactive source was placed at the center of the quadrant of the tested module in a metallic cylinder with a cavity to host the source. The cylinder has a hole of 2 mm diameter at its bottom that was used both as collimator and to shielding for the rest of the detector from the lateral emission of the source. The weight of the collimator cylinder is such that it can be placed directly on the fiber plane without causing any damage. In this way, the K500 module was used to provide a trigger signal for the events in which an electron emitted by the radioactive source passed through the module under examination. The standard FTK module, the FTK with the epoxy glue and the FTK with AIREX were tested one at a time. The central quadrant of the tested module was read on all four sides by a DAQ-unit of a CITIROC-FEB. For each module, both a pedestal run and a dark run were performed for calibration purposes. To enable comparison, 15-minute runs were recorded for each setup.

Results

Figure 6.4 shows the distributions of the charge in strips (left panel) and of the positions of hit strips (right panel) for the three modules. The fiber yield is nearly identical across the three distributions. The reconstruction of the active strips is also

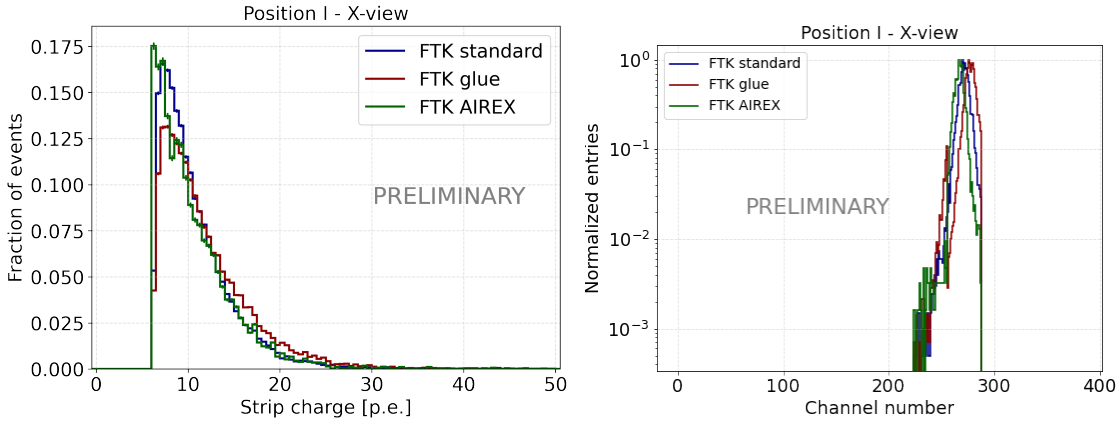

Figure 6.4: Left panel: distributio of charges in strips for the three FTK modules. Right panel: distribution of fired strips. In blue the results for the standard FTK module assembled for Zirettino prototype in red data for the module with epoxy glue along all fibers in red, and results for the module equipped with two Airex mats in green. No substantial differences are observed.

consistent, with minor variations due to the possibility that the source positioning on the plane may not be exactly the same in all three runs.

Figure 6.5 compares the results after the clustering procedure. From the the top panels we see that, on average, a single cluster of about two strips is formed in each module. The bottom left panel shows the distribution of photoelectrons in clusters, we see that the three distributions. The bottom right panel reports the distribution of cluster positions. As with the distribution of the activated strip positions, no significant shift is observed between the three modules, despite the imperfect positioning of the source on the plane. However, in all three cases, the position is accurately reconstructed at the center of the module.

It can be concluded that there are no significant inefficiencies in the performance of the three modules. Therefore, the use of epoxy glue or AIREX to provide rigidity and support to the fibers does not negatively impact on the tracker performance. For the construction of the flight model, the configuration deemed most effective in terms of structural robustness can be adopted.

6.2 FTK dynamic tests

6.2.1 Dynamic tests

During the lift-off phase of the rocket, intense vibrations are generated due to engine ignition, which are transmitted to the satellite structure. These are random vibrations

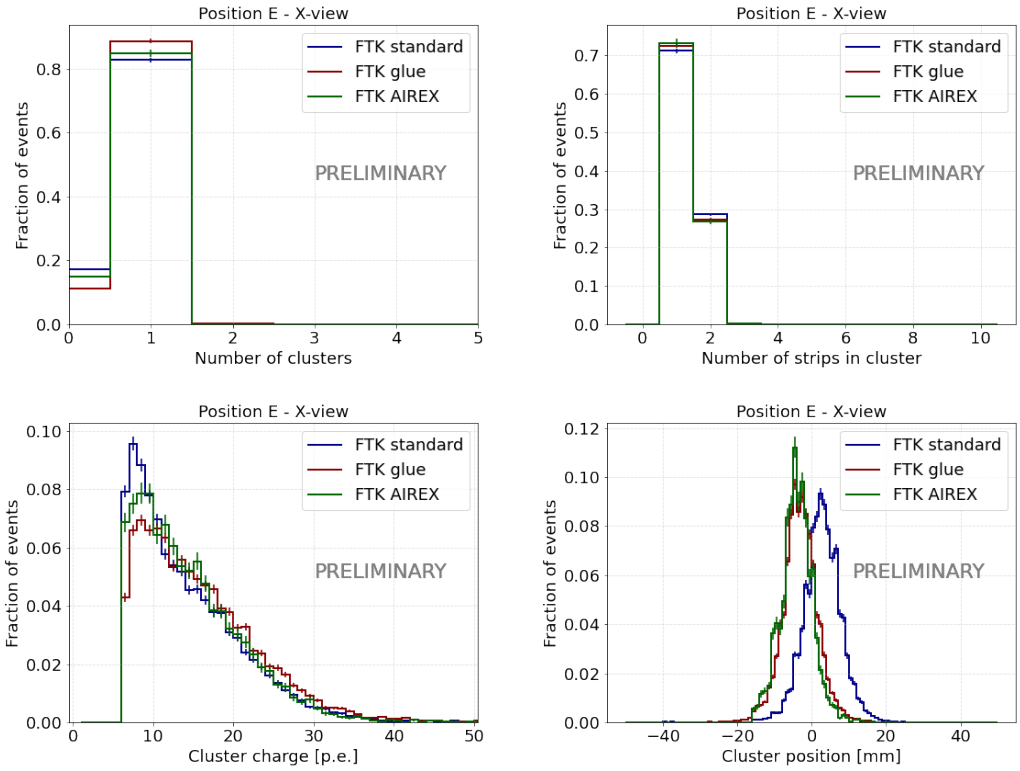

Figure 6.5: Test results for the comparison of the three tracker modules. Results for the standard module are shown in blue, results for the module with adhesive along all fibers in red, and results for the module equipped with two Airex mats in green. Top left panel: distribution of the number of clusters. Top right panel: distribution of cluster sizes. Bottom left panel: distribution of the number of photoelectrons in clusters. Bottom right: Distribution of the cluster position evaluated from the charge centroid. Similar results are obtained for the three modules. A slight difference in position is due to the imperfect alignment of the source across the three runs.

with frequencies in the range [20-2000] Hz, that need to be simulated in order to study the response of the satellite to the stress generated by these loads.

Dynamic tests include both random vibrations and sine vibrations. Sine vibrations are described by a sine function with a fixed frequency. These do not correspond to real vibrations experienced by the satellite, but are used to excite the structure at specific frequencies to evaluate its mechanical response and detect potential weaknesses. A sweep of low-level sine vibration (sine survey) is necessary to measure the fundamental frequency of the object before performing the random vibration tests, in order to correct design imperfections that could cause the random test failure.

Vibrations are generated using an electrodynamic shaker and their effects are measured through piezoelectric accelerometers placed at various positions on the object being tested. These accelerometers measure the acceleration experienced by the body along three directions and produce an electrical output signal that can be recorded and analyzed.

The dynamic tests for the NUSES satellite were carried out at Thales Alenia Space - Italy (TAS-I)[2] on the structural model (SM) assembled at the beginning of 2024 by the Sophia High Tech[3] and shown in figure 6.6. The SM is completely equivalent to the flight model (FM) from the structural point. It consists of all of the final subsystems but the photodetectors and electronics modules are non-functional.

The structural model of the Ziré payload is reported in figure 6.7. It is equipped with all the sub detectors. The FTK was assembled with only two modules, one with the glue along all the fibers planes and the other with the AIREX supports. The central module consists only of the mechanical structure. The module with the AIREX supports is mounted in such a way that it is the innermost one (i.e., closest to the PST). The dummy module is at the center and the module with glue is the most external one. A detail is shown in figure 6.8.

The vibration tests performed consist of a random vibration test and a sine vibration test preceded and followed by a sine sweep. Variations in mode frequency or amplitude in the sine sweep before and after the random vibration tests were used to identify possible structural damages. I also carried out a functional test on the two FTK modules, both before and after the dynamic test sequence.

Several accelerometers have been glued at different locations on the various subsystems. Figure 6.9 shows their positions on the FTK and on the tray, which has been used as a reference for comparing vibrational modes.

The low-level signature sweep was performed in the frequency range $[5-2000]$ Hz at

[2] https://www.thalesaleniaspace.com/it

[3] https://www.sophiahightech.com/zire-satellite/

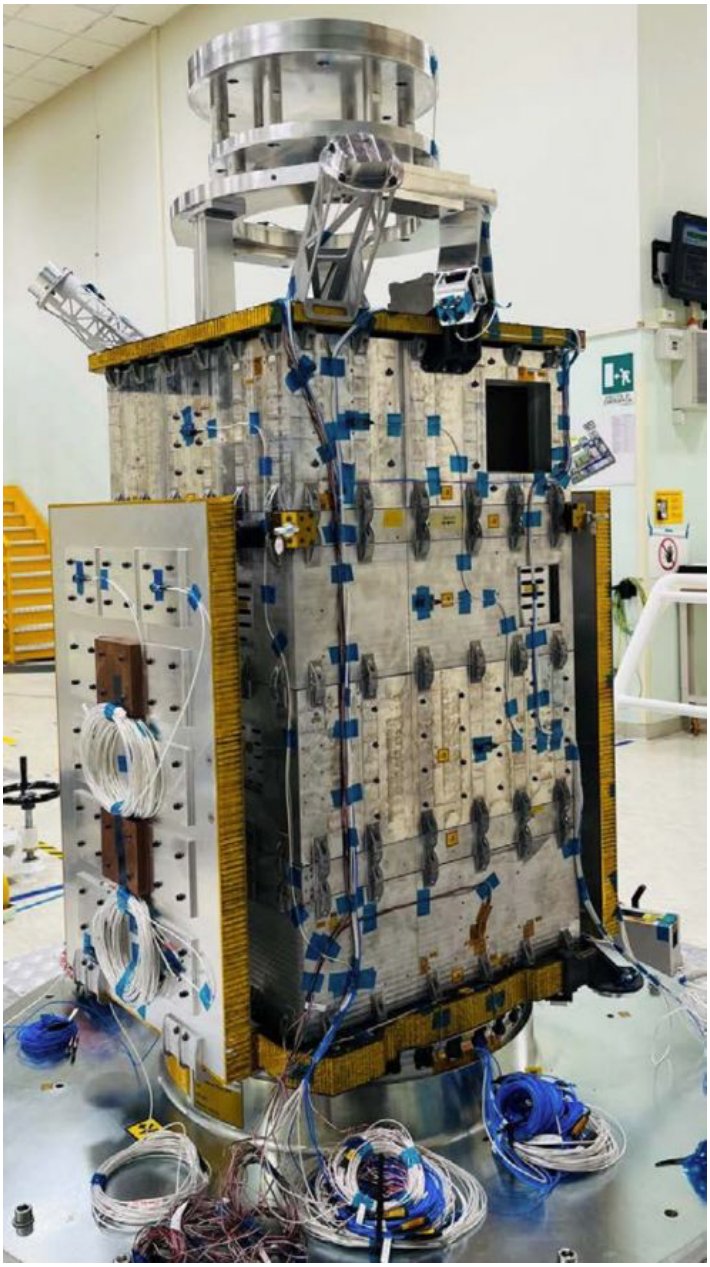

Figure 6.6: NUSES structural model for vibration tests.

Figure 6.7: Ziré structural model for vibration tests.

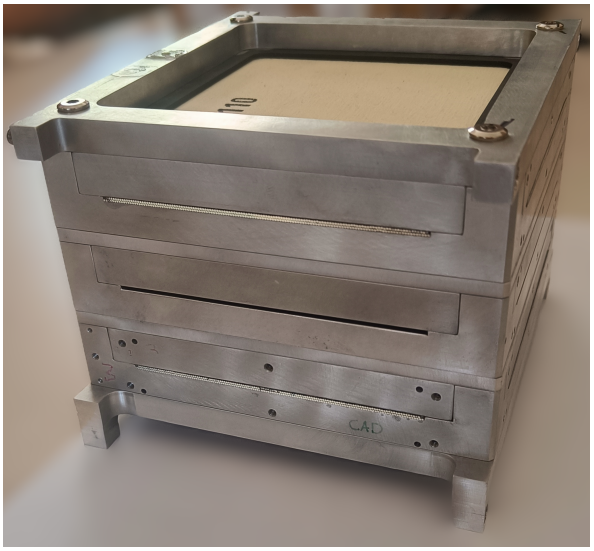

Figure 6.8: Structural model of the Ziré FTK for the dynamic tests.

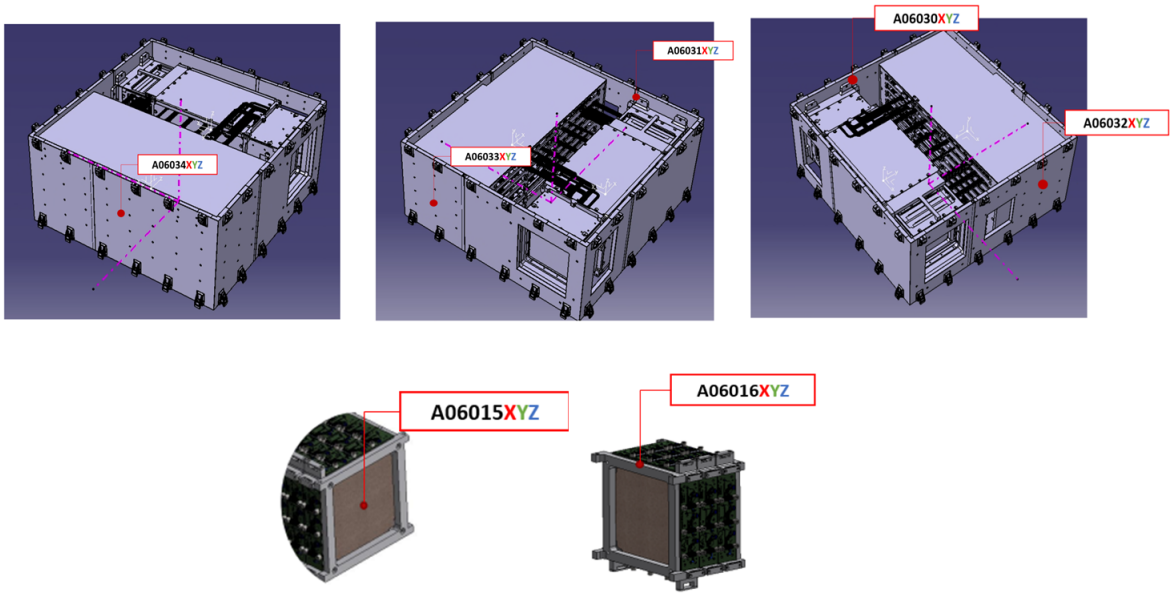

Figure 6.9: Accelerometer location on the tray containing the Ziré payload and on the FTK.

a constant intensity 0.2 g in the lateral directions X and Y and 0.05 g in the Z direction. Its main goal is to study the normal modes before and after the test in order to detect possible shift in the first mode frequency that could be due to a damage of the object. In figures 6.10 and 6.11 are shown the results of the pre and post-sweep tests in the X-direction (left panel) and in the Z-direction (right panel) for the two accelerometers on the FTK. Figure 6.12 reports the displacement of the first mode frequencies, along the Z- and Y-axis before and after the execution of a complete vibration test sequence. A mode at about 40 Hz is observed along the X-axis and a mode at about 140 Hz along the Z-axis. There are no evident shifts in the first mode frequency between the pre and post sweep test results.

In order to compare the vibration on the FTK with the input, an average of all the power spectral density (PSD) from the accelerometer on tray is considered. Figures 6.13 and 6.14 show respectively the comparison with the accelerometer A06015 at the center of the tracker plane and the accelerometer A06016 on the FTK side. Sinusoidal vibrations are performed in the low-frequency range [5-125] Hz. The mode frequencies of the FTK are the same as the tray.

Usually random vibrations are analyzed by means of the power spectral density (PSD) of the acceleration measured by the accelerometer. It is the acceleration mean square per unit bandwidth.

Figures 6.15 and 6.16 show the result of the random in the Y (top panels) and Z (bottom panels) directions for the FTK (solid line) and for the tray (dashed line). The

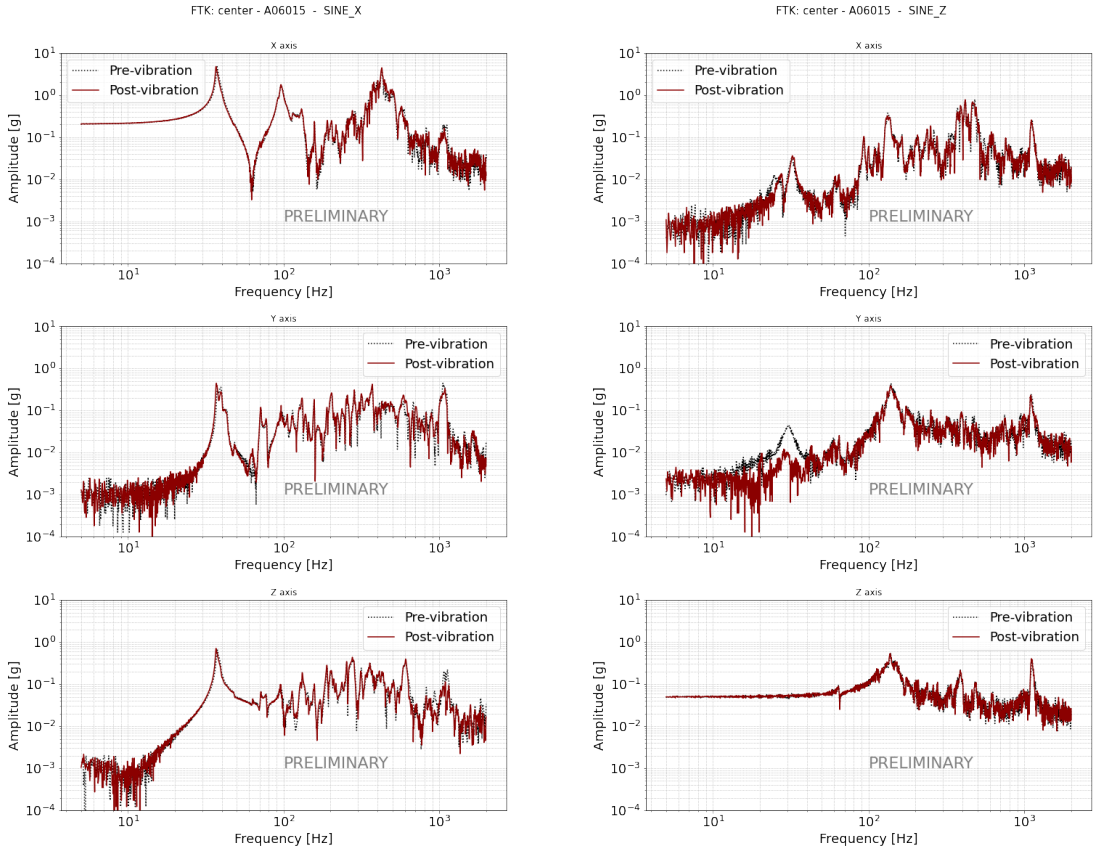

Figure 6.10: Low-level signature sweep results form accelerometer at the center of the fiber tracker module A06015. In black results of the sine sweep test before the random vibration, in red the result after. The three panel on the left report the results for the X, Y and Z direction for the sine vibration along the X direction (axial stress).The panels on the right report the seme plots for vibration in the Z direction.

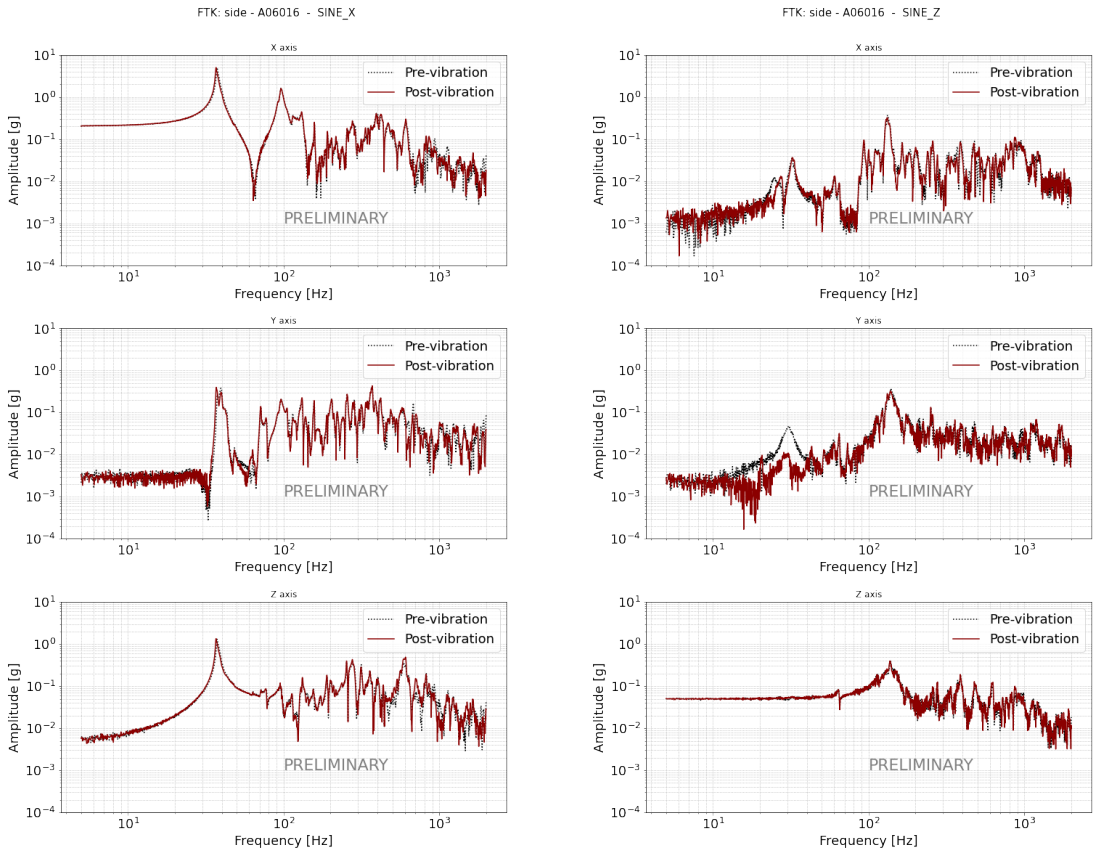

Figure 6.11: Low-level signature sweep results form accelerometer on the side of the fiber tracker module A06016. In black results of the sine sweep test before the random vibration, in red the result after. The three panel on the left report the results for the X, Y and Z direction for the sine vibration along the X direction (axial stress).The panels on the right report the seme plots for vibration in the Z direction.

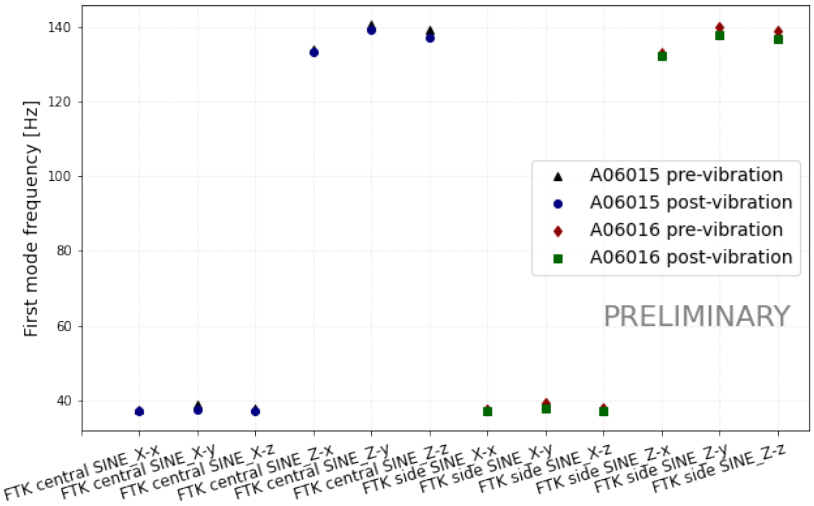

Figure 6.12: Summary of the first mode frequency for vibration along each axis for the two accelerometer before and after the random vibration test. No frequency shift was observed.

		g_{RMS} [mm]		
		A06015	A06016	Tray
Random Y	x	30.20	5.39	4.15
	y	10.08	8.29	7.81
	z	6.56	5.10	5.00
Random Z	x	53.2	9.24	9.30
	y	11.63	8.31	12.53
	z	16.08	13.43	12.90

Table 6.1: Summary of the g_{RMS} values for the random tests.

area under the PSD curve is the mean square of the signal, g^2. Its square root, the g_{RMS}, defines the overall energy of the random vibration. It has been evaluated for all the PSDs of both the FTK and the tray. Results are summarized in table 6.1. It can be observed that a significant amount of energy is recorded by the accelerometer positioned at the center of the tracker along the x-axis, which, in the chosen reference frame, corresponds to the direction transverse to the plane. This occurs both for the random vibrations along the Y-axis and the Z-axis. When compared to the g_{RMS} values in other directions, these readings are considerably higher, especially when compared to those of the tray. The amplified vibrations in this direction could be due to *drum* effect.

Starting from the PSD of acceleration, $PSD_a(f)$, it is possible to evaluate the $PSD_d(f)$ (of displacement) in order to determine how much a component moves in

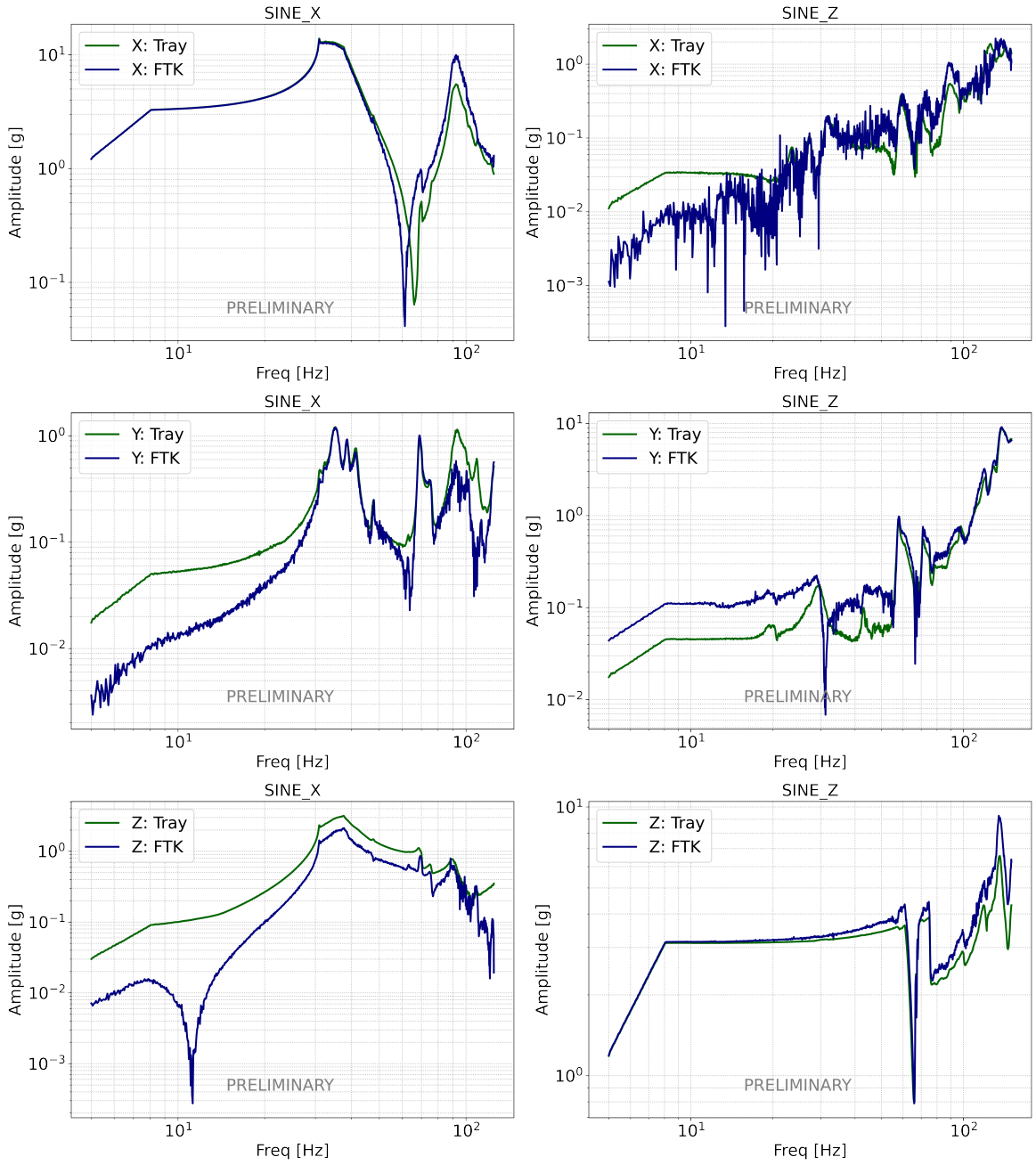

Figure 6.13: Results of the sinusoidal vibration tests from the accelerometer at the center of the fiber tracker module A06015 (blue line) and from the mean of the signals on the three accelerometer on the tray considered as a reference (green line). The three plots on the left show the results in the three direction (from top to bottom x, y, z) for the solicitation in the X direction, the plots on the right refers to the vibration along the Z direction.

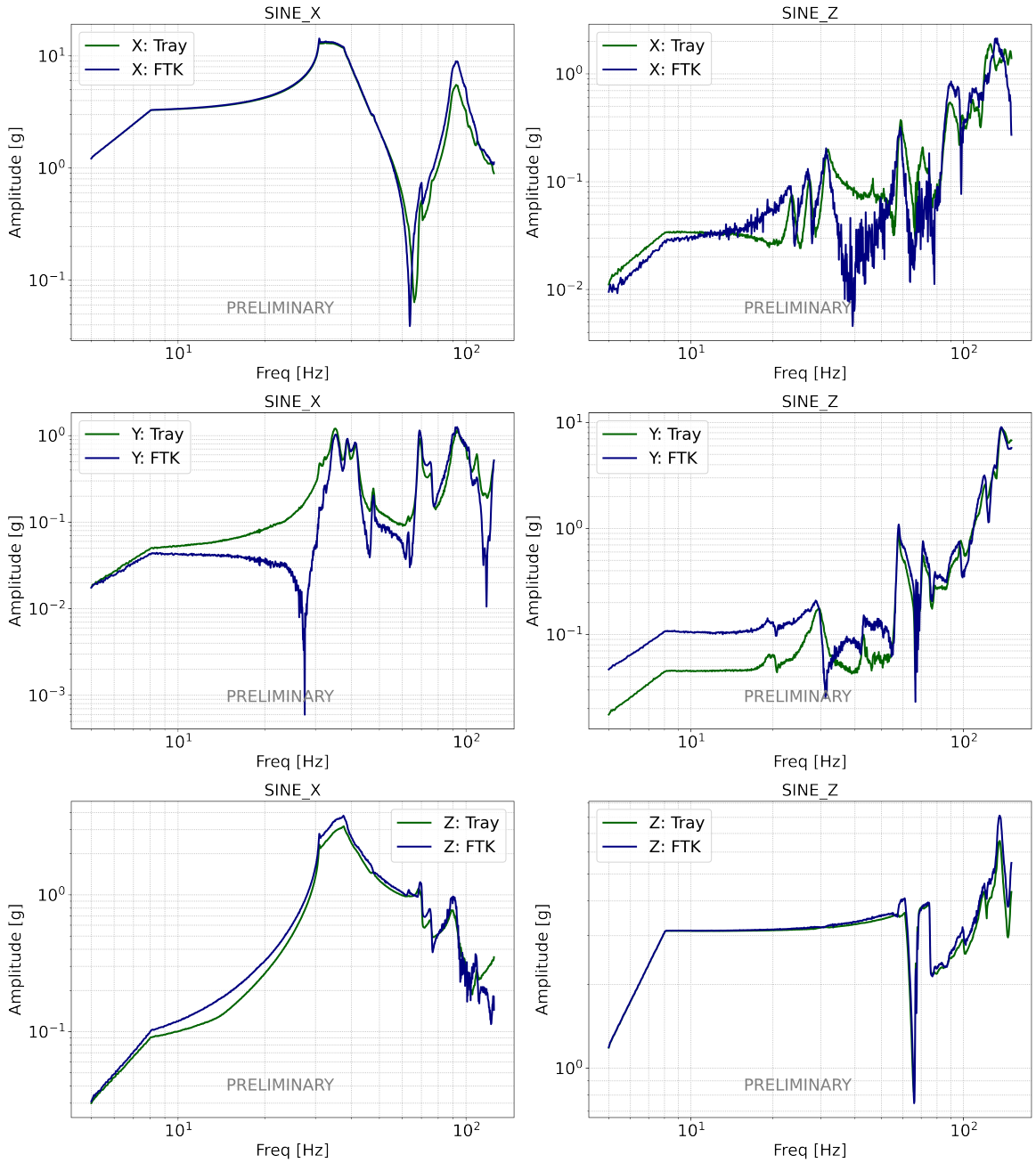

Figure 6.14: Results of the sinusoidal vibration tests from the accelerometer on the side of the fiber tracker module A06016 (blue line) and from the mean of the signals on the three accelerometer on the tray considered as a reference (green line). The three plots on the left show the results in the three direction (from top to bottom x, y, z) for the solicitation in the X direction, the plots on the right refers to the vibration along the Z direction.

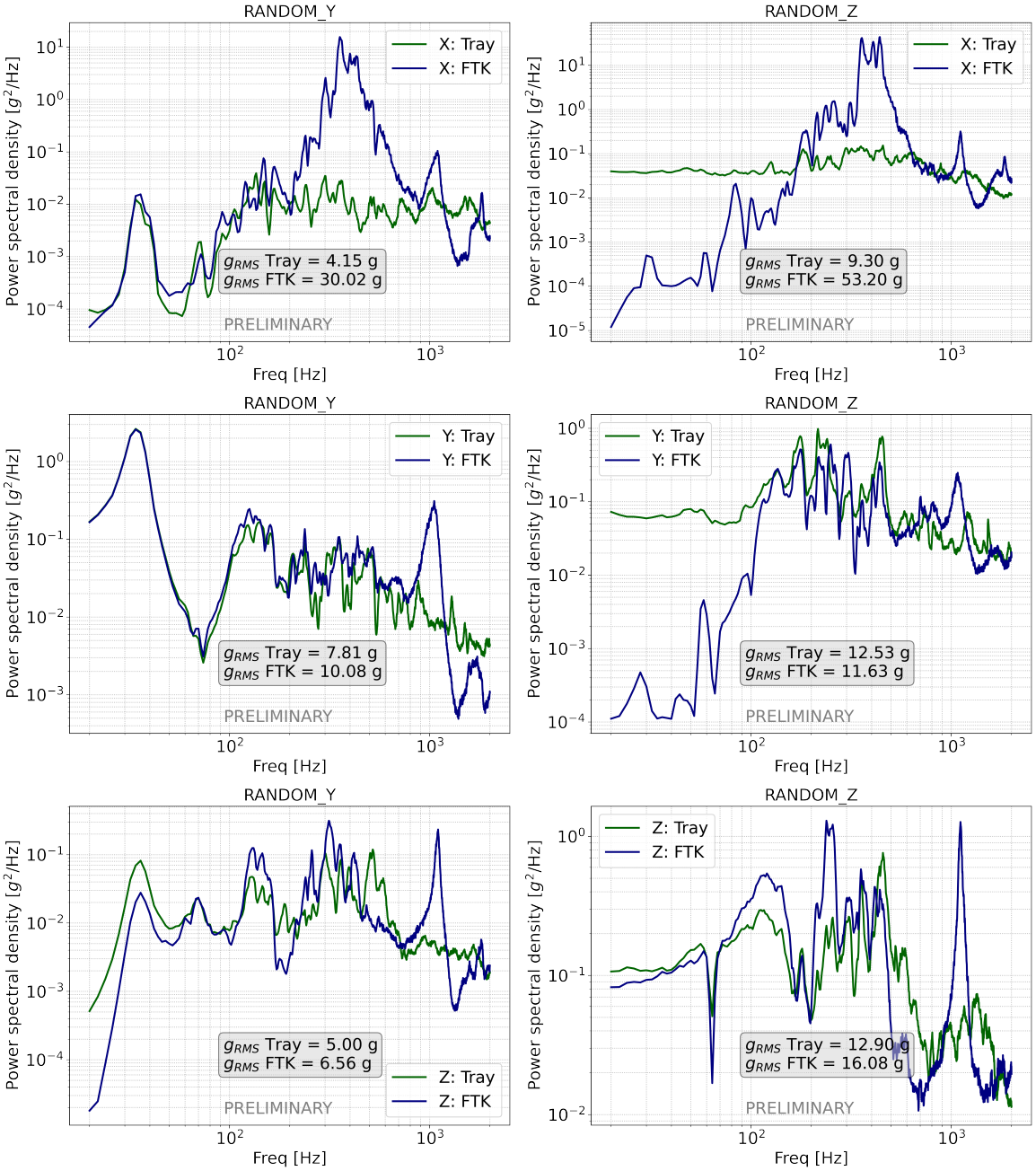

Figure 6.15: Results of the random vibration test from the accelerometer on the center of the fiber tracker module A06015 (blue line) and from the mean of the signals on the three accelerometer on the tray considered as a reference (green line). The three plots in the left panels show the results in the three direction (from top to bottom x, y, z) for the solicitation in the X direction, the plots in the right panels refers to the vibration along the Z direction. In each plot the g_{RMS} value is reported.

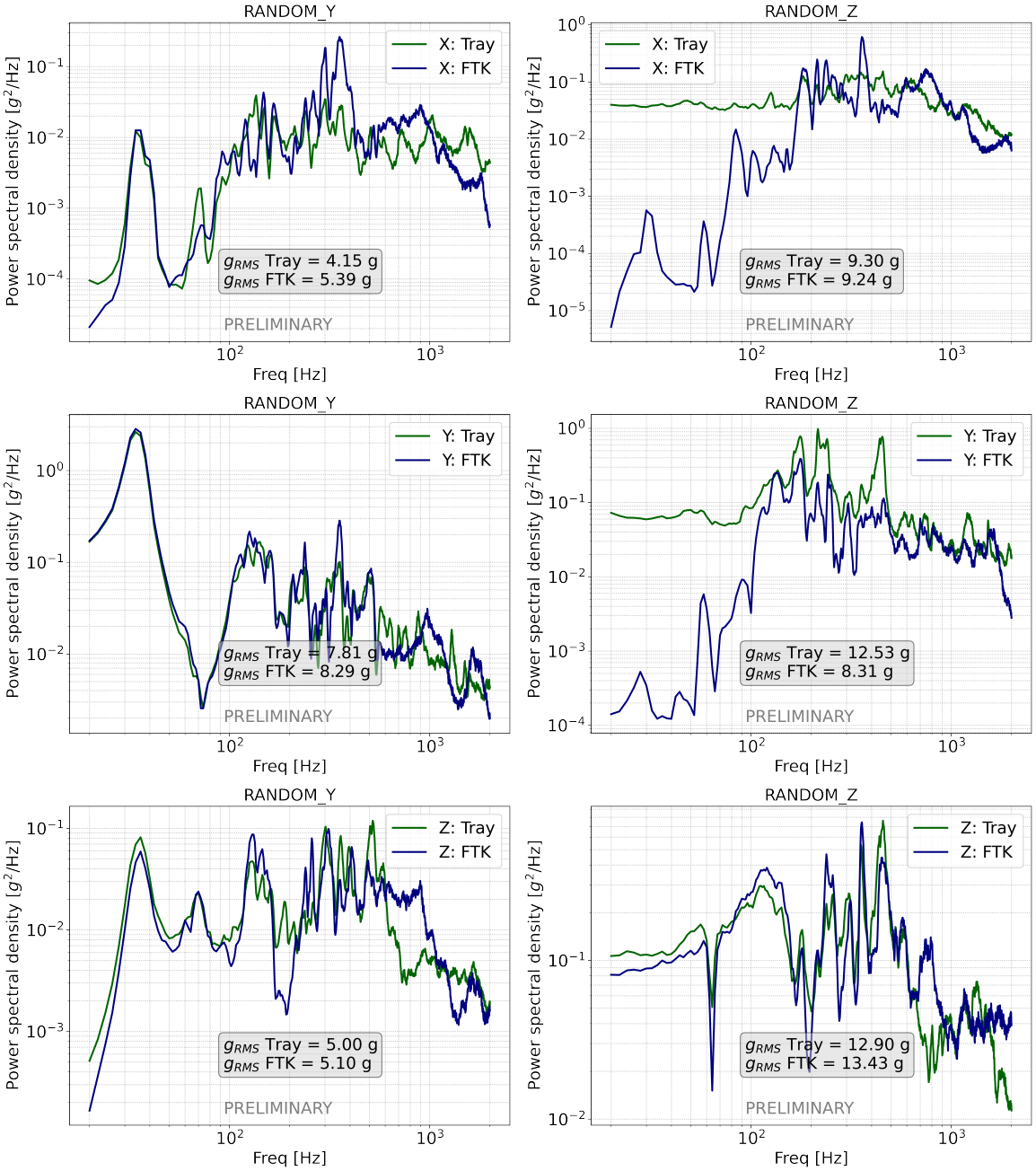

Figure 6.16: Results of the random vibration test from the accelerometer on the side of the fiber tracker module A06016 (blue line) and from the mean of the signals on the three accelerometer on the tray considered as a reference (green line). The three plots in the left panels show the results in the three direction (from top to bottom x, y, z) for the solicitation in the X direction, the plots in the right panels refers to the vibration along the Z direction. In each plot the g_{RMS} value is reported.

response to vibrational excitation. This is crucial for assessing potential collisions between different parts of the system. In the case of the FTK, it helps identify possible collisions between the planes. Displacement can be calculated from acceleration using the following relationship between the $PSD_a(f)$ and the $PSD_d(f)$ deriving from mathematical transformations in the frequency domain of the equations of motion:

$$x(t) = A \ \sin(\omega t + \phi) \tag{6.1}$$

$$\ddot{x}(t) = -\omega^2 x(t) \Rightarrow x(t) = -\frac{\ddot{x}(t)}{\omega^2} = -\frac{\ddot{x}(t)}{(2\pi f)^2} \tag{6.2}$$

Hence considering the Fourier transforms:

$$\hat{x}(f) = -\frac{\hat{a}(f)}{(2\pi f)^2} \tag{6.3}$$

Since the PSD is defined as the square modulus of the Fourier transform of the signal normalized for the amplitude the same relation stands for the PSDs:

$$PSD_d(f) = \frac{PSD_a(f)}{(2\pi f)^4} \tag{6.4}$$

The PSDs of the displacement are reported in figures 6.17 and 6.18 respectively for the center of the plane and for the side of the module. The PSD of displacement can be integrated over the frequency range to estimate the d_{RMS}. Results are summarized in table 6.2. The displacement of the fiber tracker with respect to the displacement of the whole tray are of the order of a few tens of microns and consistent with expectations. Because of the term f^4 to the denominator in the eq. 6.2.1 the contribution of high frequencies to the displacement is drastically reduced while that of low frequencies is amplified. For this reason low-frequency motions dominate the overall displacement. Hence the contribution of high-frequency resonances that significantly influences the g_{RMS} does not contribute to the d_{RMS}. In fact, it can be noted that even in the x-direction the displacement recorded by the accelerometer placed at the center of the FTK plane is contained. In no case is the movement such as to cause collisions between the planes of the tracker or compromise its planarity.

After the dynamic tests, the FTK modules were carefully inspected to visually check for any potential damage caused by the vibrations. Before the tests, we marked the position of the screws with permanent markers to ensure that no movement had occurred during the tests. From this inspection, no damage was detected and all the structure component kept the correct position. In figure 6.19 some details of the visual

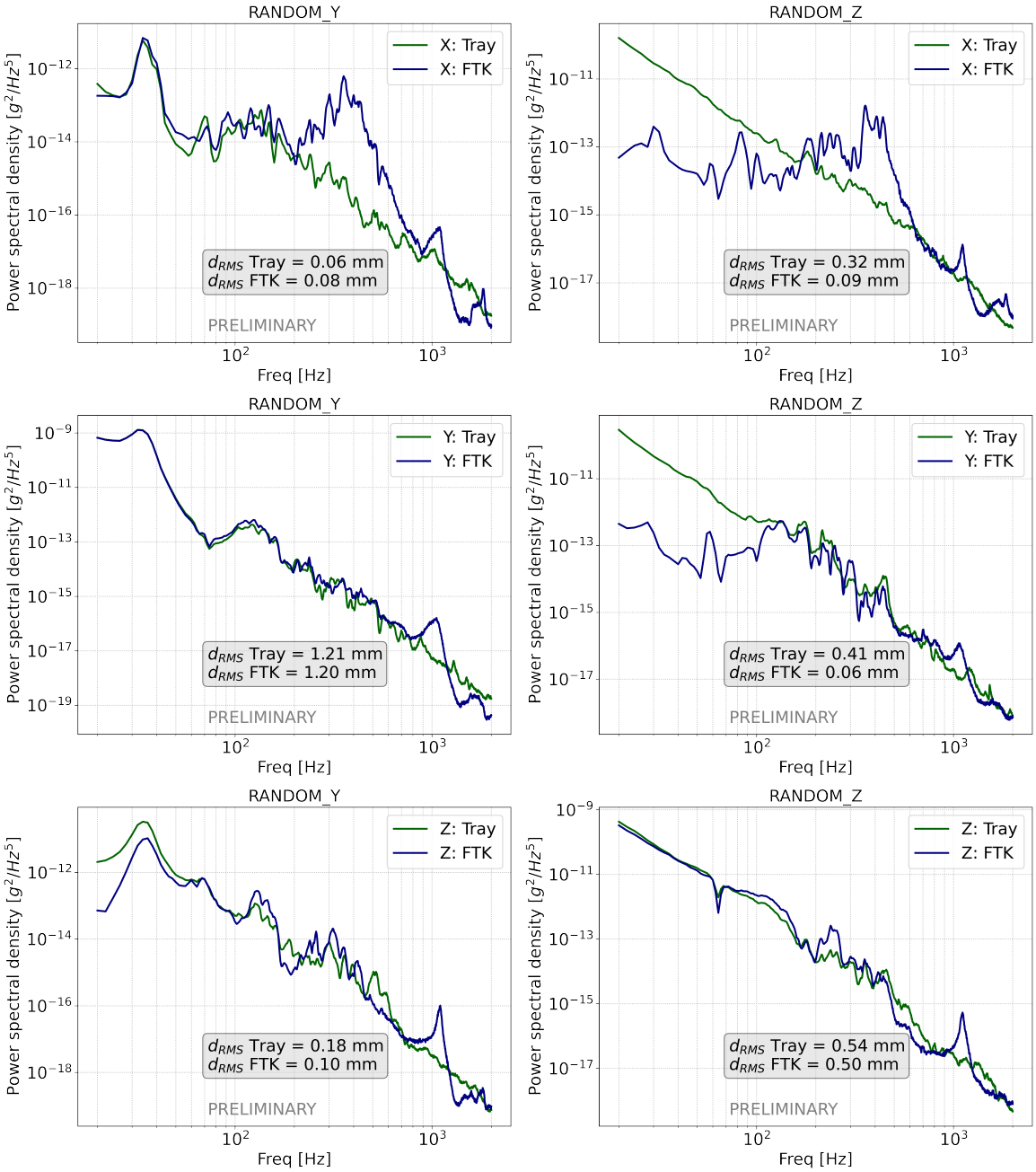

Figure 6.17: Displacement calculated from the acceleration PSD of the random vibration test from the accelerometer on the center of the fiber tracker module A06015 (blue line) and from the mean of the signals on the three accelerometer on the tray considered as a reference (green line). The three plots in the left panels show the results in the three direction (from top to bottom x, y, z) for the solicitation in the X direction, the plots in the right panels refers to the vibration along the Z direction. In each plot the d_{RMS} value is reported.

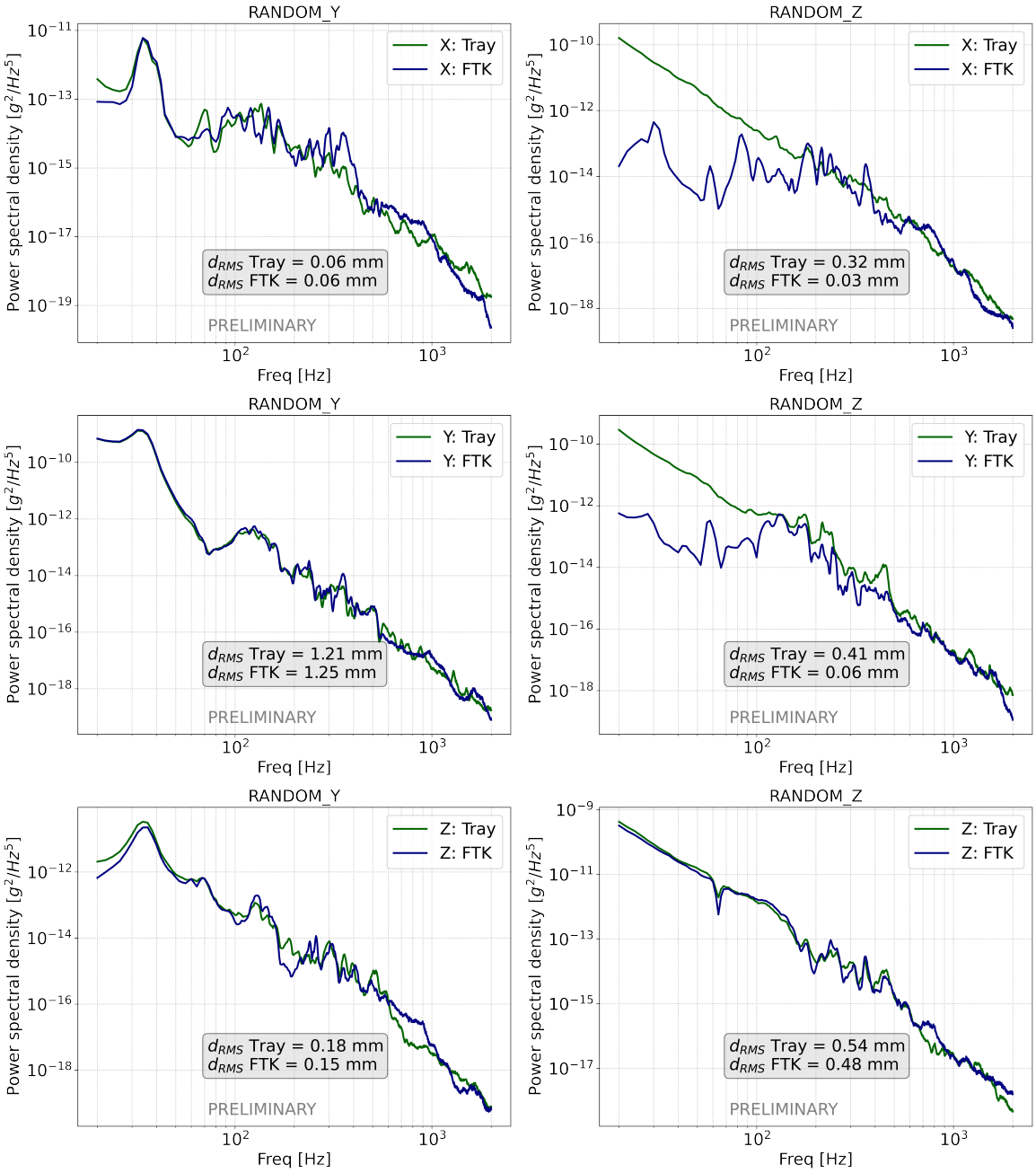

Figure 6.18: Displacement calculated from the acceleration PSD of the random vibration test from the accelerometer on the side of the fiber tracker module A06016 (blue line) and from the mean of the signals on the three accelerometer on the tray considered as a reference (green line). The three plots in the left panels show the results in the three direction (from top to bottom x, y, z) for the solicitation in the X direction, the plots in the right panels refers to the vibration along the Z direction. In each plot the d_{RMS} value is reported.

		d_{RMS} [mm]		
		A06015	A06016	Tray
Random Y	x	0.08	0.06	0.06
	y	1.21	1.25	1.21
	z	0.10	0.15	0.18
Random Z	x	0.09	0.03	0.32
	y	0.06	0.06	0.41
	z	0.50	0.48	0.54

Table 6.2: Summary of the d_{RMS} values for the random tests.

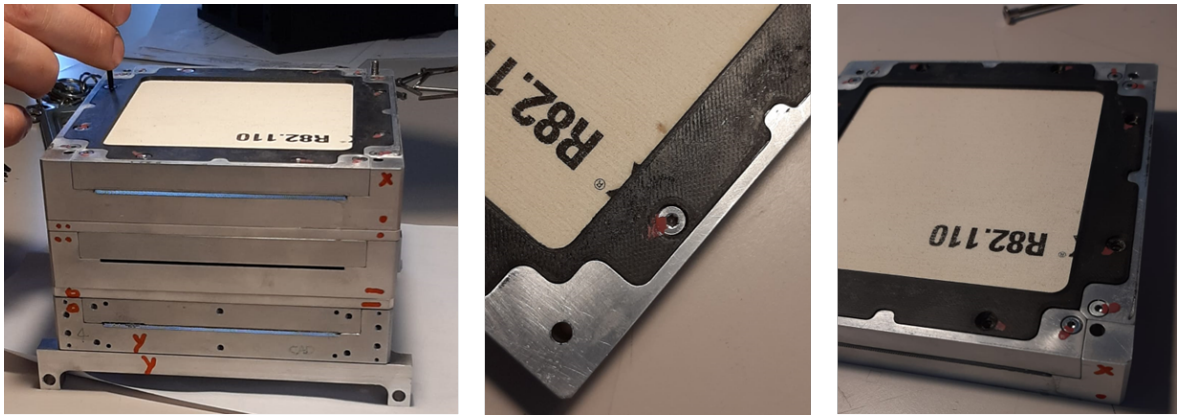

Figure 6.19: Photos of the visual inspection of the FTK SM after the vibration tests. Central and left panels show a detail of the reference on the screw.

inspection are reported.

6.2.2 Functionality check

To confirm the validation of the structural model, the dynamic tests are complemented by functionality tests, performed both before and after the vibrational tests. The two FTK modules of the SM were properly inspected prior to testing, using the setup described in section 6.1. This test has the goal of identifying any defects in the module and, consequently, potential inefficiencies associated with specific regions of the module, such as improper fiber positioning or damage to the fibers resulting from the assembly process.

Pre-vibration tests

To achieve this, all nine quadrants of the tracker module, labeled according to the scheme in figure 6.20, were tested with the radioactive source as previously described. To perform measurements in the various regions of the plane, the module was positioned

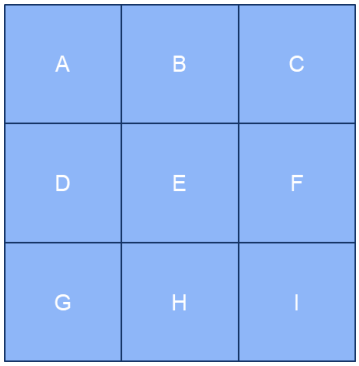

Figure 6.20: Scheme of the nine quadrant tested before and after the vibration tests for the two FTK modules.

above the K500 prototype, used as a trigger source, ensuring that the quadrant under examination was aligned with the active region of the trigger module.

In figures 6.21 and 6.22, the charge distributions across the strips for the three modules in the X and Y views respectively are shown. No significant differences are observed in the measured charge between the three modules. However, when examining the distribution of active strips in Figure 6.23, a defect is noticeable in the Y-view plane corresponding to quadrants A and B in the module with glue. This issue is caused by a misalignment of the fibers at the end of the endcap of the mechanical structure, a defect that was already identified during visual inspection after the assembly. Figure 6.24 shows a photo of the module where the defect is indicated with a red arrow. It is a region of the plane where some fibers were glued in an incorrect position and hence they do not have a perfect linearity.

Post-vibration tests

After the dynamic tests, functional check were performed again to verify the proper operation of the two SM modules. These tests were performed by positioning the radioactive source on different quadrants of the tested module. However, instead of operating in external trigger mode, the internal trigger mode was used, requiring signal coincidence at both ends of the same fiber and on both planes in the quadrants under test. The test was conducted both on the non-vibrated standard Zirettino FTK module and on the two modules that had been subjected to vibration testing.

Figure 6.25 and 6.26 shows the the comparison of charge distributions in strips and clusters respectively between the vibrated and not vibrated modules for all the positions.

The charge distributions are significantly different compared to those obtained with the previous setup in external trigger. This is because, without imposing the

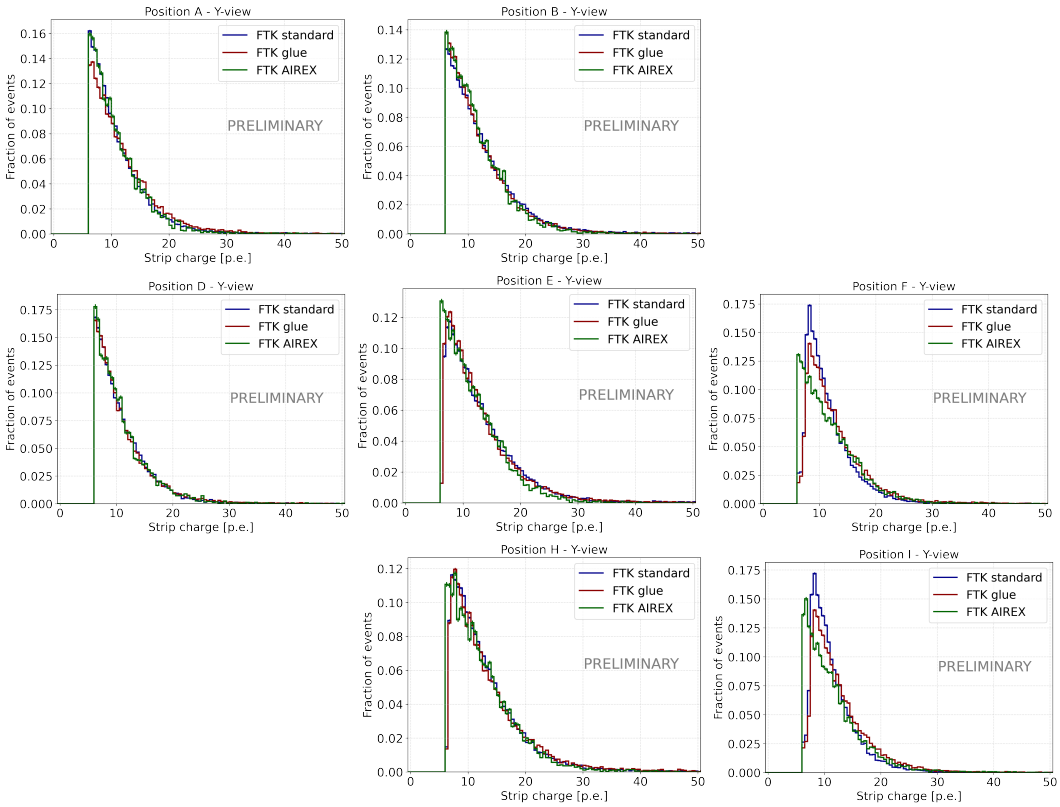

Figure 6.21: Distribution of charge in the strips for the position tested. In blue data for the standard module, in red results for tests on the module with the epoxy along the whole fiber length, in green results for the module with the AIREX supports. Data for the Y-view plane.

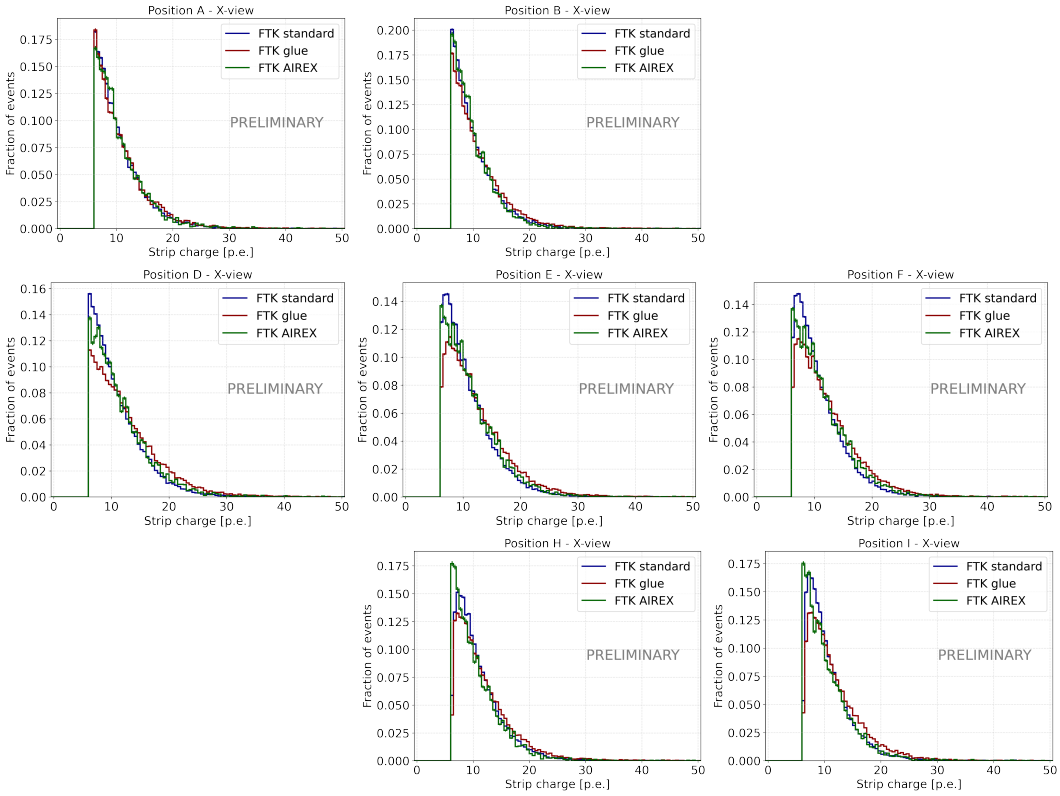

Figure 6.22: Distribution of charge in the strips for the position tested before the vibration tests. In blue data for the standard module, in red results for tests on the module with the epoxy along the whole fiber length, in green results for the module with the AIREX supports. Data for the X-view plane.

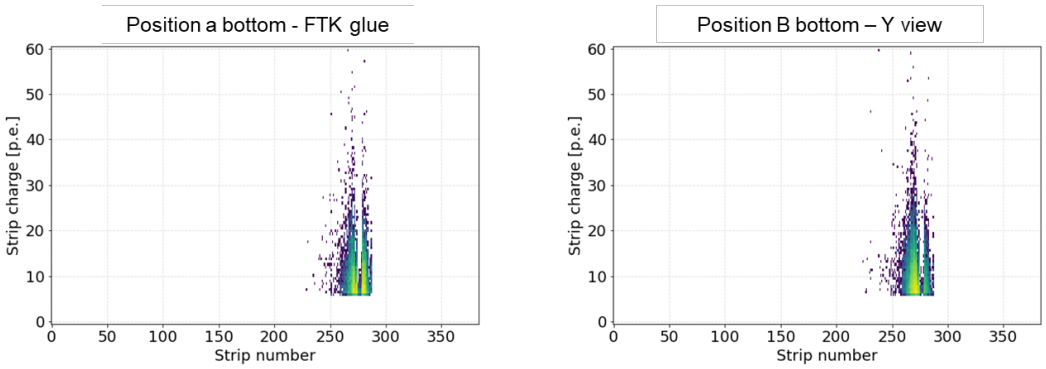

Figure 6.23: Distributions of the strip charges as a function of the strip ID for the two quadrant in which is present a structural defect on the FTK module with epoxy glue along the whole fibers length. Results of tests before the vibration tests.

Figure 6.24: Photo of one side of the Y-view plane of the FTK module with the glue on the whole fiber length. The red arrow indicates the defect in the fiber positioning.

requirement for the electron to pass through the module below, but only through the one being tested, lower-energy electron events are also selected. These electrons are not energetic enough to reach the trigger module, but they deposit more energy or are even absorbed in the fibers.

An additional validation was conducted by testing the three modules on a particle beam during a test beam campaign held at the T10 line of the PS facility at the CERN in late September 2024. Each of the three modules was placed in the beam one at a time, with the quadrant under test positioned to ensure that the beam struck the central region. Data acquisition was controlled by an internal trigger generated by requiring coincidences on both the right and left sides in both views for the specific module section under investigation. An external tracking system provided a validation signal to discard events in which the signal was not generated by a beam particle.

A comparison of the three modules results at the central position (E) and at position F with a beam of π^- with a momentum of 10GeV/p is reported. Figure 6.27 shows the distribution of the number of clusters detected in each event. Left panels refer to the horizontal fiber corresponding to the Y-view and the right panels refer to the X-view. The top panels show the result for the position E while the bottom panel report the results for the F position. It can be observed that the standard module (not vibrated) shows the same distribution that the two vibrated modules. In figure 6.28 are reported the distribution of the number of strip in each cluster. Figure 6.29 and figure 6.30 show respectively the distributions of photoelectrons in clusters and the distribution of the position reconstructed as the charge centroid of the cluster. The position distributions

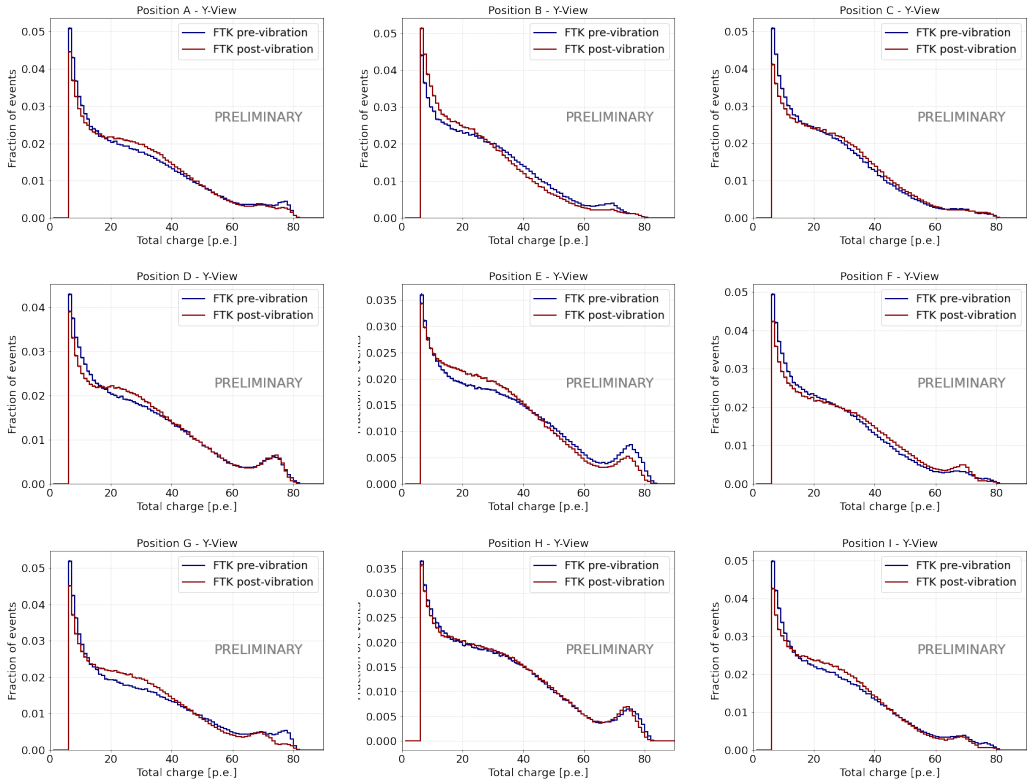

Figure 6.25: Distribution of charge in the strips for the position tested after the vibration tests. Dashed line: data for the standard module, that did not experienced the vibration test, taken as reference. Solid line: data for the vibrated module with glue. Data for the X-view plane.

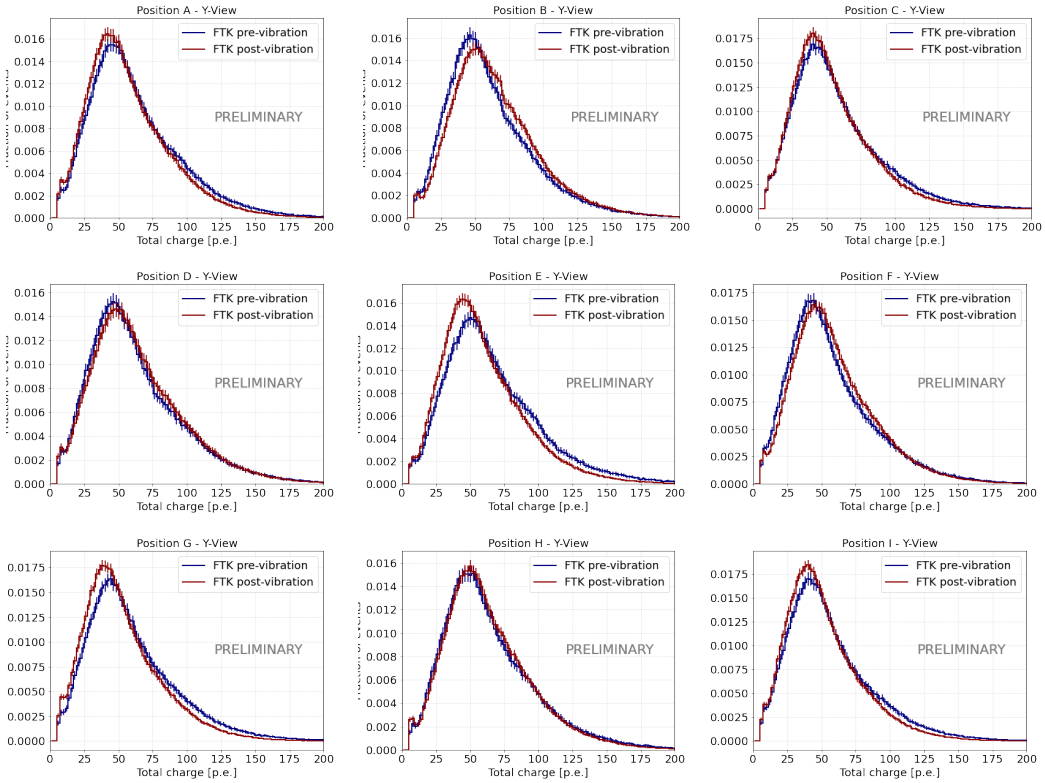

Figure 6.26: Distribution of charge in clusters for the quadrant tested after the vibration tests. Dashed line: data for the standard module, that did not experienced the vibration test, taken as reference. Solid line: data for the vibrated module with glue. Data for the X-view plane.

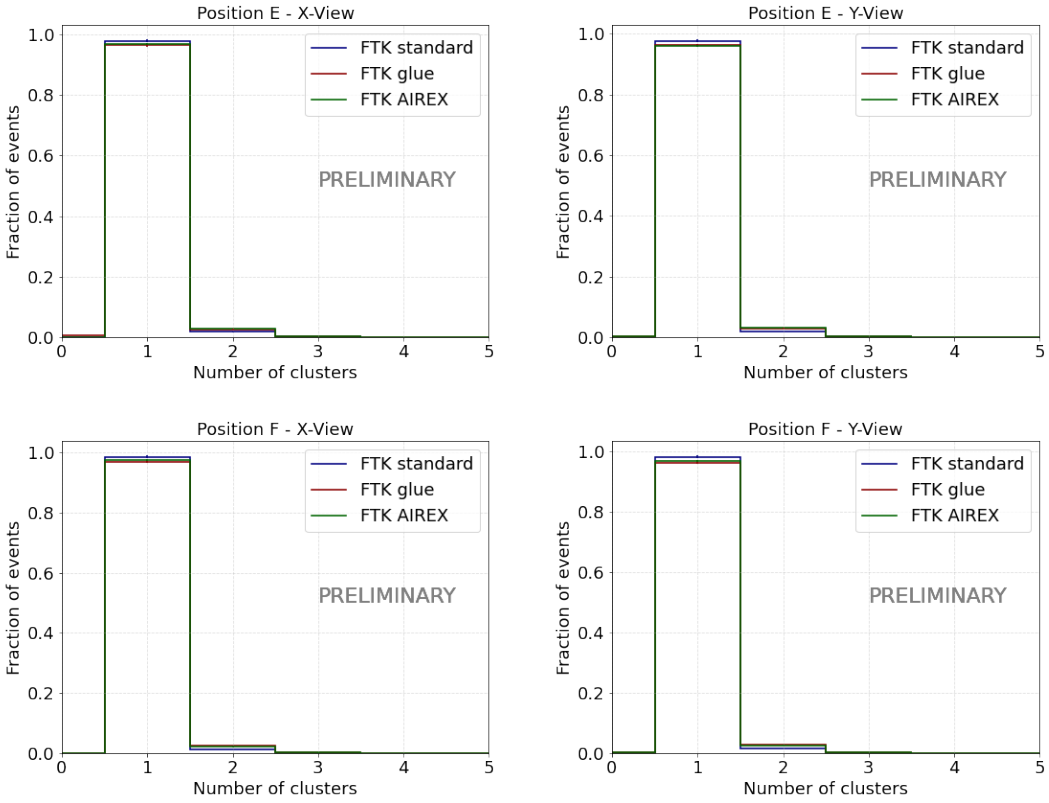

Figure 6.27: Distribution of the number of clusters for for two of the nine quadrants tested in the beam test after the vibration tests. In blue data for the standard module, in red results for tests on the module with the epoxy along the whole fiber length, in green results for the module with the AIREX supports. Top left panel: distributions for the X-view plane of position E. Bottom left panel: distributions for the X-view plane of position F. Top right panel: distributions for the Y-view plane of position E. Bottom right panel: distributions for the Y-view plane of position F.

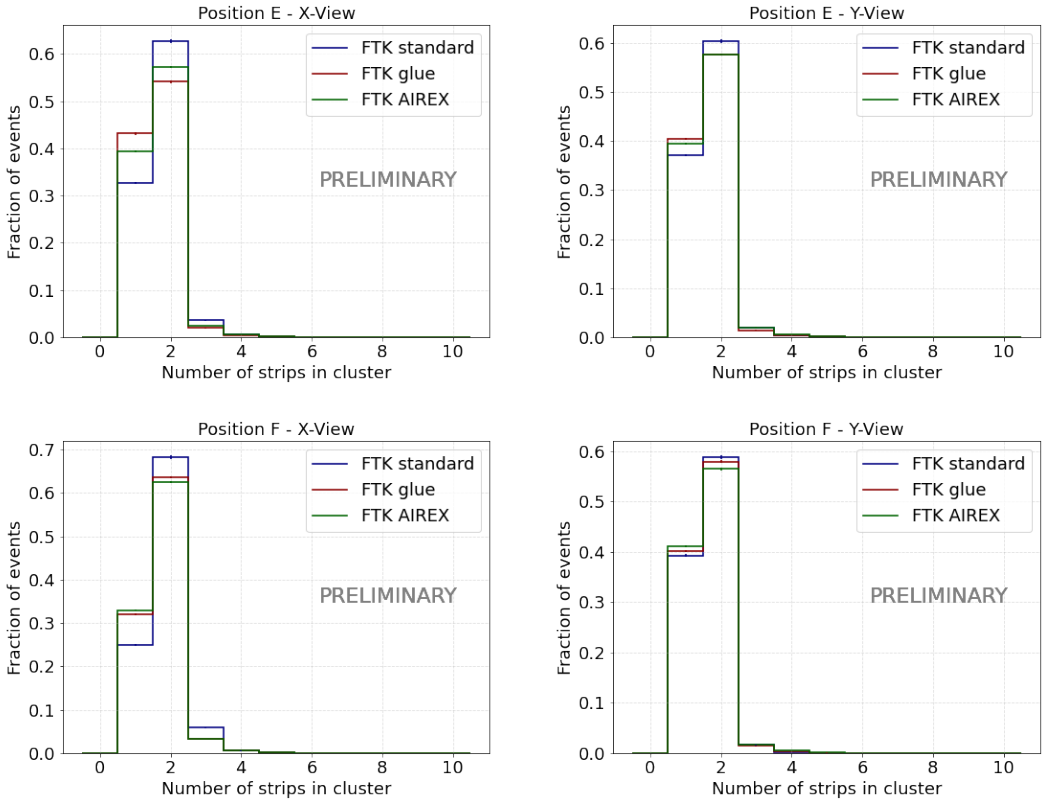

Figure 6.28: Distribution of the number of strips in clusters for two of the nine quadrants tested in the beam test after the vibration tests. In blue data for the standard module, in red results for tests on the module with the epoxy along the whole fiber length, in green results for the module with the AIREX supports. Top left panel: distributions for the X-view plane of position E. Bottom left panel: distributions for the X-view plane of position F. Top right panel: distributions for the Y-view plane of position E. Bottom right panel: distributions for the Y-view plane of position F.

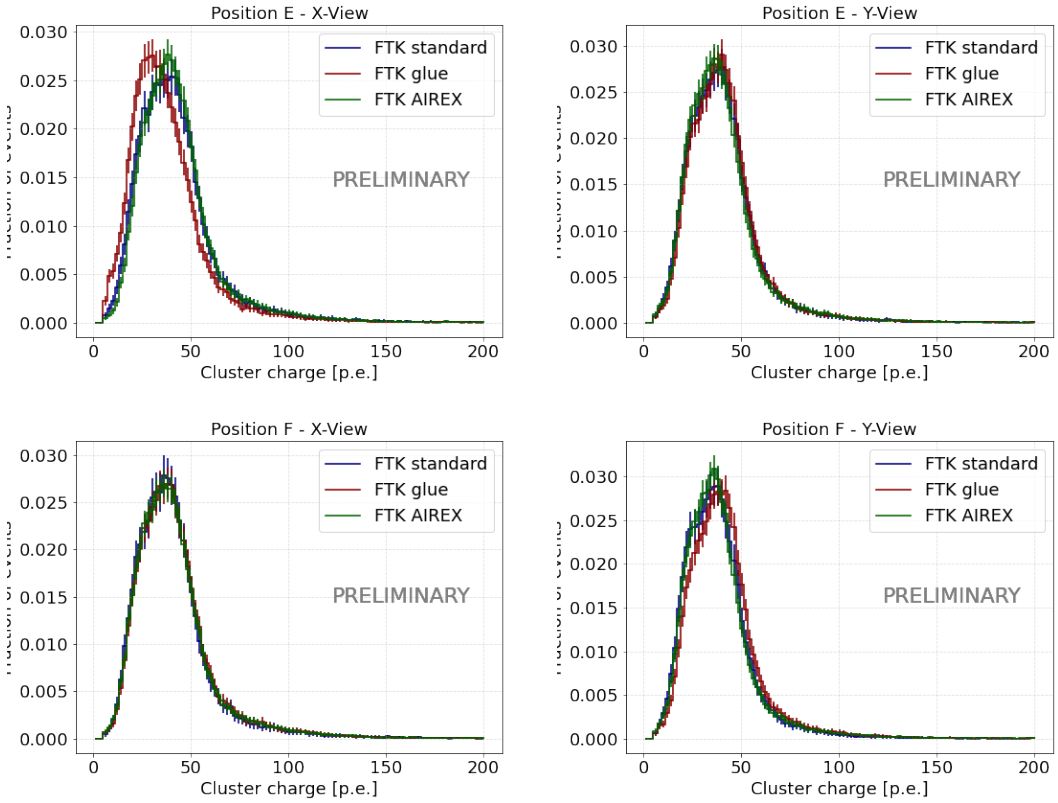

Figure 6.29: Distribution of the number of photoelectrons in clusters for two of the nine quadrants tested in the beam test after the vibration tests. In blue data for the standard module, in red results for tests on the module with the epoxy along the whole fiber length, in green results for the module with the AIREX supports. Top left panel: distributions for the X-view plane of position E. Bottom left panel: distributions for the X-view plane of position F. Top right panel: distributions for the Y-view plane of position E. Bottom right panel: distributions for the Y-view plane of position F.

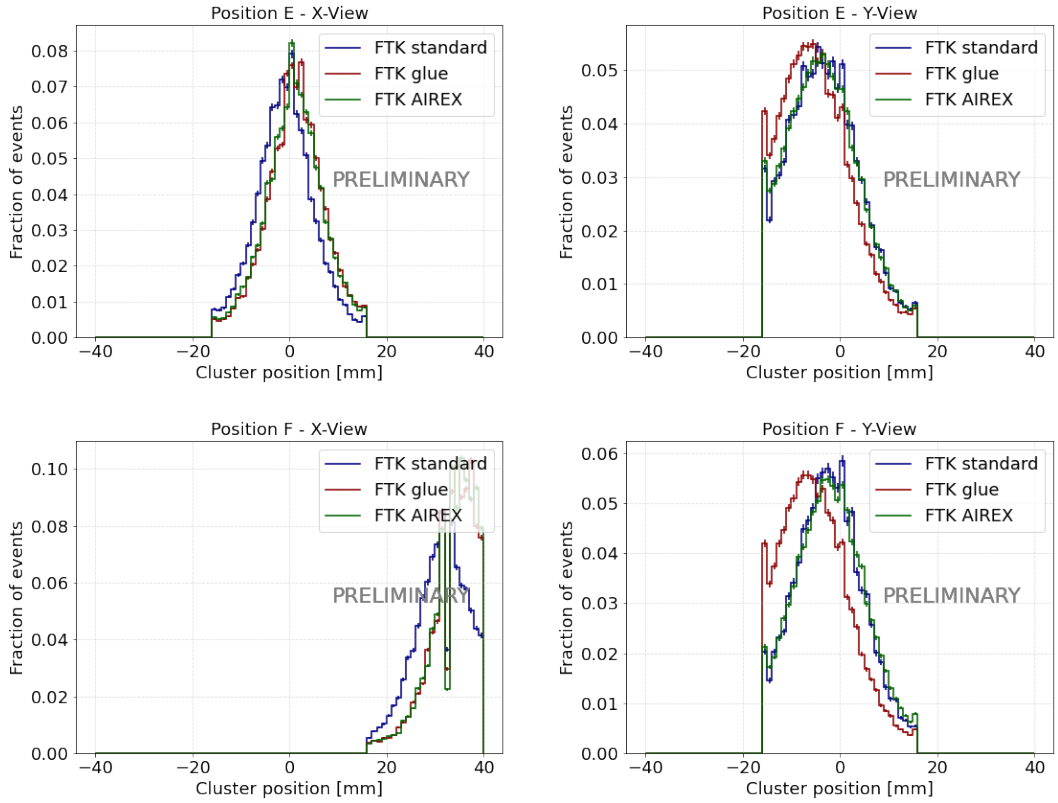

Figure 6.30: Distribution of the cluster positions for two of the nine quadrants tested in the beam test after the vibration tests. In blue data for the standard module, in red results for tests on the module with the epoxy along the whole fiber length, in green results for the module with the AIREX supports. Top left panel: distributions for the X-view plane of position E. Bottom left panel: distributions for the X-view plane of position F. Top right panel: distributions for the Y-view plane of position E. Bottom right panel: distributions for the Y-view plane of position F.

in the Y-view is truncated because only the quadrant under examination was read at a time. It can be observed that no differences were found between the module that was not subjected to vibration tests and the other two modules that underwent these tests.

It can be concluded that these tests did not reveal any inefficiencies compared to the performance of the standard module. Therefore, the FTK was not affected by any damage caused by vibration tests.

Conclusions

Cosmic radiation produced by extremely energetic phenomena in the Universe represents a unique probe for understanding the physics behind them. The past and present generation of space-borne experiments have significantly advanced our understanding of many astrophysical sources and have opened up new opportunities to probe the Universe.

The development of detectors for space-borne experiments is technically challenging because they have to meet the constraints required for space flown instrumentation. In particular, important limitations come from the maximum allowed weight for the payload and the maximum allowed power consumption. In addition, the detectors must be robust enough to withstand the intense vibrations during launch and the extreme conditions of the space environment.

NUSES is a future space mission for the study of low-energy cosmic rays that will also serve as a pathfinder for developing and testing new technologies for space applications. In this work I developed a plastic scintillator fiber tracker with SiPM readout for the Ziré experiment onboard NUSES. The tracker consists of multiple modules, each composed by two planes of fibers, oriented along the X and Y directions respectively. The fiber planes are readout by linear arrays of SiPMs. Tracker detectors based on scintillating fibers are a consolidated technology for ground-based experiments, but the latest development of SiPM linear arrays have made them a valuable option also for the next generation of space-borne cosmic-ray detectors. The use of a scintillating fiber tracker rather than a standard silicon tracker offers a number of advantages, due to the low material budget and the possibility of instrumenting large volume detectors while keeping a reduced number of electronic channels.

The aim of this thesis was to evaluate the performance of the designed tracker. For this purpose, a Geant4 simulation framework was initially developed to verify the tracker performance in detecting low-energy electrons and protons ($<$300 MeV), aiming to determine the detector sensitivity in the energy range of interest for the Zirè experiment. These studies demonstrated that the tracker can detect electrons with energies above a few MeV and protons with energies above a few tens of MeV

with efficiency larger than 90%. The simulations were also used to compare detector configurations with different fiber radii and SiPM array pitches, with the goal of finding the optimal compromise between spatial resolution, detection efficiency, and number of readout channels.

During my PhD, several prototype tracker modules were built. The first module was initially assembled with 500µm diameter fibers from Saint Gobain Crystals. However, preliminary tests showed that the light yield of these fibers was lower than the nominal value. Therefore, three additional modules were built using Kuraray fibers with diameters of 500µm and 750µm. As module readout, Hamamatsu MPPC S13552 linear SiPM arrays were used, with 128 channels and a strip pitch of 250µm. To study the module performance with different strip pitches, dedicated PWBs were designed to group (OR) adjacent channels in groups of 2 strips (OR2) and 4 strips (OR4), allowing for effective pitches of 500µm and 1 mm, respectively. The readout system was based on the use of a custom front-end board based on four PETIROC 2A ASICs by Omega Microelectronics and Weeroc.

The modules were tested in various configurations with a 15 GeV/c negative pion beam at the CERN PS T9 line. Results indicated that the configuration with 750µm diameter fibers exhibits a higher light yield, ensuring a better detection efficiency while significantly reducing the number of electronic channels.

Based on these results, the tracker plane for the first prototype of the Ziré experiment, named "Zirettino", was assembled. Zirettino is a prototype, including all the Ziré subsystems on a smaller scale, developed to test the instrument acquisition chain and performance.

Zirettino was tested with a 10 GeV/c negative pion beam at CERN PS line T10, with the previous tracker prototypes positioned along the beamline to serve as an ancillary external tracker to determine the impact point of the particles on the Zirettino tracking plane. These tests enabled spatial resolution measurements for each tracking plane.

The spatial resolution on the tracker of Zirettino was measured based on the tracks estimated with external trackers, resulting in a value of 143 µm, consistent with the expected value.

Before the launch, an environmental verification test campaign for Ziré and all its subsystem is required to minimize risks.

At the end of 2023, the structural model of Ziré was assembled to perform initial environmental testing. In spring 2024, the structural model underwent dynamic testing. In this work the results of vibration tests on the fiber tracker modules are presented. Results of sine sweep vibration tests revealed no significant shifts in the primary modes

of the tracker after the random vibrations. Analysis of random vibration tests indicated displacements on the order of tens of microns, which do not suggest any risk of collisions between the tracker planes.

To complete the validation, functional tests on the fiber tracker units of the structural model were carried out, before and after vibration tests. These checks showed no deterioration in the detector performance.

Further tests, including thermal vacuum and shock tests, are scheduled in early 2025 to finalize the Ziré validation. Following this, work will begin on the flight models of Ziré and NUSES, with a planned launch in 2026.

The successful operation of the Ziré fiber tracker would demonstrate the feasibility of this technology for future space missions.

Bibliography

[Aab et al., 2020] Aab, A. et al. (2020). Measurement of the cosmic-ray energy spectrum above 2.5 $\times$ $10^1$8 ev using the pierre auger observatory. *Physical Review D*, 102(6).

[Abbasi et al., 2008] Abbasi, R. U. et al. (2008). First Observation of the Greisen-Zatsepin-Kuzmin Suppression. *Physical Review Letters*, 100(10):101101.

[Abbott et al., 2016] Abbott, B. P. et al. (2016). Observation of gravitational waves from a binary black hole merger. *Physical Review Letters*, 116(6).

[Abdo et al., 2009] Abdo, A. A. et al. (2009). Fermilat observation of diffuse gamma rays produced through interactions between local interstellar matter and high-energy cosmic rays. *The Astrophysical Journal*, 703(2):1249–1256.

[Abdo et al., 2010] Abdo, A. A. et al. (2010). Fermi Large Area Telescope First Source Catalog. *Astrophysical Journal, Supplement*, 188(2):405–436.

[Abdollahi et al., 2020] Abdollahi, S. et al. (2020). Fermi large area telescope fourth source catalog. *The Astrophysical Journal Supplement Series*, 247(1):33.

[Abdollahi et al., 2022] Abdollahi, S. et al. (2022). Incremental fermi large area telescope fourth source catalog. *The Astrophysical Journal Supplement Series*, 260(2):53.

[Acerbi and Gundacker, 2019] Acerbi, F. and Gundacker, S. (2019). Understanding and simulating sipms. *Nuclear Instruments and Methods in Physics Research Section A: Accelerators, Spectrometers, Detectors and Associated Equipment*, 926:16–35. Silicon Photomultipliers: Technology, Characterisation and Applications.

[Acero et al., 2016] Acero, F. et al. (2016). The first fermi lat supernova remnant catalog. *The Astrophysical Journal Supplement Series*, 224(1):8.

[Ackermann et al., 2013] Ackermann, M. et al. (2013). Detection of the characteristic pion-decay signature in supernova remnants. *Science*, 339(6121):807–811.

[Ackermann et al., 2015] Ackermann, M. et al. (2015). The spectrum of isotropic diffuse gamma-ray emission between 100 mev and 820 gev. *The Astrophysical Journal*, 799(1):86.

[Agostinelli et al., 2003] Agostinelli, S. et al. (2003). Geant4—a simulation toolkit. *Nuclear Instruments and Methods in Physics Research Section A: Accelerators, Spectrometers, Detectors and Associated Equipment*, 506(3):250–303.

[Ajello et al., 2022] Ajello, M. et al. (2022). The fourth catalog of active galactic nuclei detected by the fermi large area telescope: Data release 3. *The Astrophysical Journal Supplement Series*, 263(2):24.

[Aloisio et al., 2023a] Aloisio, R. et al. (2023a). The Terzina instrument on board the NUSES space mission. *PoS*, ICRC2023:391.

[Aloisio et al., 2023b] Aloisio, R. et al. (2023b). The Zire experiment on board the NUSES space mission. *PoS*, ICRC2023:139.

[Antonucci, 1993] Antonucci, R. (1993). Unified models for active galactic nuclei and quasars. *Annual Review of Astronomy and Astrophysics*, 31(Volume 31, 1993):473–521.

[Atwood et al., 2009] Atwood, W. et al. (2009). The Large Area Telescope on the Fermi Gamma-Ray Space Telescope Mission. *Astrophysical Journal, Supplement*, 697(2):1071–1102.

[Baldini et al., 2005] Baldini, L. et al. (2005). The gamma-ray large area space telescope: an astro-particle mission to explore the high energy sky. volume 1, pages 191 – 195.

[Ballet et al., 2024] Ballet, J., Bruel, P., Burnett, T. H., Lott, B., and collaboration, T. F.-L. (2024). Fermi large area telescope fourth source catalog data release 4 (4fgl-dr4).

[Ballet et al., 2020] Ballet, J., Burnett, T. H., Digel, S. W., and Lott, B. (2020). Fermi large area telescope fourth source catalog data release 2.

[Bartocci et al., 2020] Bartocci, S. et al. (2020). Galactic cosmic-ray hydrogen spectra in the 40–250 mev range measured by the high-energy particle detector (hepd)

on board the cses-01 satellite between 2018 and 2020. *The Astrophysical Journal*, 901(1):8.

[Beckmann and Shrader, 2012] Beckmann, V. and Shrader, C. (2012). *Active Galactic Nuclei*.

[Beckmann and Shrader, 2013] Beckmann, V. and Shrader, C. R. (2013). The agn phenomenon: open issues.

[Bell, 1978] Bell, A. R. (1978). The acceleration of cosmic rays in shock fronts - I. *Monthly Notices of the RAS*, 182:147–156.

[Birks, 1964] Birks, J. (1964). Chapter 4 - the scintillation process in inorganic crystals—i. In Birks, J., editor, *The Theory and Practice of Scintillation Counting*, International Series of Monographs in Electronics and Instrumentation, pages 68–95. Pergamon.

[Birks, 1951] Birks, J. B. (1951). Scintillations from organic crystals: Specific fluorescence and relative response to different radiations. *Proceedings of the Physical Society. Section A*, 64(10):874.

[Bissaldi et al., 2009] Bissaldi, E. et al. (2009). Ground-based calibration and characterization of the fermi gamma-ray burst monitor detectors. *Experimental Astronomy*, 24:47–88.

[Boella et al., 1997] Boella, G., Butler, R. C., Perola, G. C., Piro, L., Scarsi, L., and Bleeker, J. A. M. (1997). BeppoSAX, the wide band mission for X-ray astronomy. *Astronomy and Astrophysics, Supplement*, 122:299–307.

[Bonnardeau, 1977] Bonnardeau, M., editor (1977). *Observation of cosmic gamma rays with the COS-B satellite*.

[Bourquin, 2005] Bourquin, M. (2005). The ams tracking detector for cosmic-ray physics in space. *Nuclear Instruments and Methods in Physics Research Section A: Accelerators, Spectrometers, Detectors and Associated Equipment*, 541(1):110–116. Development and Application of Semiconductor Tracking Detectors.

[Bravar et al., 2020] Bravar, A., Briggl, K., Corrodi, S., Damyanova, A., Gerritzen, L., Grab, C., Hildebrandt, M., Papa, A., and Rutar, G. (2020). The mu3e scintillating fiber timing detector. *Nuclear Instruments and Methods in Physics Research Section A: Accelerators, Spectrometers, Detectors and Associated Equipment*, 958:162564. Proceedings of the Vienna Conference on Instrumentation 2019.

[Briggs et al., 1996] Briggs, M. S. et al. (1996). BATSE Observations of the Large-Scale Isotropy of Gamma-Ray Bursts. *Astrophysical Journal*, 459:40.

[Caraveo, 2010] Caraveo, P. A. (2010). Fermi pulsar revolution.

[Corti et al., 2016] Corti, C., Bindi, V., Consolandi, C., and Whitman, K. (2016). Solar modulation of the local interstellar spectrum with voyager 1, ams-02, pamela, and bess. *The Astrophysical Journal*, 829(1):8.

[Costa et al., 1997] Costa, E. et al. (1997). Discovery of an x-ray afterglow associated with the γ-ray burst of 28 february 1997. *Nature*, 387(6635):783–785.

[De Angelis and Pimenta, 2018] De Angelis, A. and Pimenta, M. (2018). *Introduction to Particle and Astroparticle Physics: Multimessenger Astronomy and its Particle Physics Foundations*. Undergraduate Lecture Notes in Physics. Springer Nature, Heidelberg.

[De Mitri and Fernandez Alonso, 2023] De Mitri, I. and Fernandez Alonso, M. (2023). The Zire experiment on board the NUSES space mission. *PoS*, ICRC2023:139.

[De Robertis et al., 2018] De Robertis, G., Fanizzi, G., Loddo, F., Manzari, V., and Rizzi, M. (2018). A modular system for acquisition, interface and control (mosaic) of detectors and their related electronics for high energy physics experiment. *EPJ Web of Conferences*, 174:07002.

[Di Bernardo et al., 2015] Di Bernardo, G., Grasso, D., Evoli, C., and Gaggero, D. (2015). Diffuse synchrotron emission from galactic cosmic ray electrons. *ASTRA Proceedings*, 2:21–26.

[Fermi, 1949] Fermi, E. (1949). On the origin of the cosmic radiation. *Physical Review*, 75:1169–1174.

[Fichtel et al., 1977] Fichtel, C. E., Hartman, R. C., Kniffen, D. A., Thompson, D. J., Ogelman, H. B., Ozel, M. E., and Tumer, T. (1977). SAS-2 observations of the diffuse gamma radiation in the galactic latitude interval from 10 to 90 deg in both hemispheres. *Astrophysical Journal*, 217:L9–L13.

[Fishman and Meegan, 1995] Fishman, G. J. and Meegan, C. A. (1995). Gamma-Ray Bursts. *Annual Review of Astron and Astrophys*, 33:415–458.

[Galama et al., 1998] Galama, T. J. et al. (1998). An unusual supernova in the error box of the γ-ray burst of 25 april 1998. *Nature*, 395(6703):670–672.

[Goldhaber and Teller, 1948] Goldhaber, M. and Teller, E. (1948). On nuclear dipole vibrations. *Phys. Rev.*, 74:1046–1049.

[Goldreich and Julian, 1969] Goldreich, P. and Julian, W. H. (1969). Pulsar Electrodynamics. *Astrophysical Journal*, 157:869.

[Goldstein et al., 2017] Goldstein, A. et al. (2017). An ordinary short gamma-ray burst with extraordinary implications: Fermi-gbm detection of grb 170817a. *The Astrophysical Journal Letters*, 848(2):L14.

[Group et al., 2020] Group, P. D., Zyla, P. A., et al. (2020). Review of Particle Physics. *Progress of Theoretical and Experimental Physics*, 2020(8):083C01.

[Gruber, 2020] Gruber, L. (2020). Lhcb scifi — upgrading lhcb with a scintillating fibre tracker. *Nuclear Instruments and Methods in Physics Research Section A: Accelerators, Spectrometers, Detectors and Associated Equipment*, 958:162025. Proceedings of the Vienna Conference on Instrumentation 2019.

[Gundacker and Heering, 2020] Gundacker, S. and Heering, A. (2020). The silicon photomultiplier: Fundamentals and applications of a modern solid-state photon detector. *Physics in Medicine and Biology*, 65.

[Hillas, 1984] Hillas, A. M. (1984). The Origin of Ultra-High-Energy Cosmic Rays. *Annual Review of Astronomy and Astrophysics*, 22:425–444.

[Ivanov, 2019] Ivanov, D. (2019). Energy Spectrum Measured by the Telescope Array. *PoS*, ICRC2019:298.

[Johnson et al., 1993] Johnson, W. N. et al. (1993). The Oriented Scintillation Spectrometer Experiment: Instrument Description. *Astrophysical Journal, Supplement*, 86:693.

[Joram et al., 2015] Joram, C., Haefeli, G., and Leverington, B. (2015). Scintillating fibre tracking at high luminosity colliders. *Journal of Instrumentation*, 10(08):C08005.

[Kharzheev, 2019] Kharzheev, Y. (2019). Radiation hardness of scintillation detectors based on organic plastic scintillators and optical fibers. *Physics of Particles and Nuclei*, 50:42–76.

[Klebesadel et al., 1973] Klebesadel, R. W., Strong, I. B., and Olson, R. A. (1973). Observations of Gamma-Ray Bursts of Cosmic Origin. *Astrophysical Journal, Letters*, 182:L85.

[Klein and Nishina, 1929] Klein, O. and Nishina, T. (1929). Über die Streuung von Strahlung durch freie Elektronen nach der neuen relativistischen Quantendynamik von Dirac. *Zeitschrift fur Physik*, 52(11-12):853–868.

[Kniffen et al., 1991] Kniffen, D. A., Gehrels, N., and Ormes, J. F. (1991). The compton gamma ray observatory. pages 24–31. IEEE.

[Knoll, 2010] Knoll, G. (2010). *Radiation Detection and Measurement (4th ed.)*. John Wiley, Hoboken, NJ.

[Kolanoski and Wermes, 2020] Kolanoski, H. and Wermes, N. (2020). *Particle Detectors: Fundamentals and Applications*. Oxford University Press.

[Kouveliotou et al., 1993] Kouveliotou, C. et al. (1993). Identification of Two Classes of Gamma-Ray Bursts. *Astrophysical Journal, Letters*, 413:L101.

[Kraushaar et al., 1965] Kraushaar, W., Clark, G. W., Garmire, G., Helmken, H., Higbie, P., and Agogino, M. (1965). Explorer XI Experiment on Cosmic Gamma Rays. *Astrophysical Journal*, 141:845.

[Kraushaar et al., 1972] Kraushaar, W. L., Clark, G. W., Garmire, G. P., Borken, R., Higbie, P., Leong, V., and Thorsos, T. (1972). High-Energy Cosmic Gamma-Ray Observations from the OSO-3 Satellite. *Astrophysical Journal*, 177:341.

[Landau, 1944] Landau, L. D. (1944). On the energy loss of fast particles by ionization. *J. Phys.*, 8(4):201–205.

[Lecoq, 2020] Lecoq, P. (2020). *Scintillation Detectors for Charged Particles and Photons*, pages 45–89. Springer International Publishing, Cham.

[Longair, 2011] Longair, M. S. (2011). *High Energy Astrophysics*. Cambridge University Press.

[Lorimer and Kramer, 2004] Lorimer, D. and Kramer, M. (2004). Handbook of pulsar astronomy. *Handbook of pulsar astronomy, by D.R. Lorimer and M. Kramer. Cambridge observing handbooks for research astronomers, Vol. 4. Cambridge, UK: Cambridge University Press, 2004*, -1.

[Manchester and Taylor, 1977] Manchester, R. N. and Taylor, J. H. (1977). Pulsars.

[Mazziotta et al., 2022] Mazziotta, M. et al. (2022). A light tracker based on scintillating fibers with sipm readout. *Nuclear Instruments and Methods in*

Physics Research Section A: Accelerators, Spectrometers, Detectors and Associated Equipment, 1039:167040.

[Mazziotta and Pillera, 2023] Mazziotta, M. N. and Pillera, R. (2023). The light tracker based on scintillating fibers with SiPM readout of the Zire instrument on board the NUSES space mission. *PoS*, ICRC2023:083.

[Mitchell and Gelfand, 2022] Mitchell, A. M. W. and Gelfand, J. (2022). *Pulsar Wind Nebulae*, page 1–52. Springer Nature Singapore.

[Navas et al., 2024] Navas, S. et al. (2024). Review of particle physics. *Phys. Rev. D*, 110(3):030001.

[Nicolaidis et al., 2023] Nicolaidis, R., Nozzoli, F., Pepponi, G., and on behalf of the NUSES Collaboration (2023). A compact particle detector for space-based applications: Development of a low-energy module (lem) for the nuses space mission. *Instruments*, 7(4).

[Otte, 2016] Otte, A. (2016). Sipm's a very brief review. page 001.

[Padovani et al., 2017] Padovani, P., Alexander, D. M., Assef, R. J., De Marco, B., Giommi, P., Hickox, R. C., Richards, G. T., Smolčić, V., Hatziminaoglou, E., Mainieri, V., and Salvato, M. (2017). Active galactic nuclei: what's in a name? *The Astronomy and Astrophysics Review*, 25(1).

[Panzarini et al., 2024] Panzarini, G., Barbato, F., De Mitri, I., Di Giovanni, A., Mazziotta, M., Nicolaidis, R., Nozzoli, F., Pillera, R., and Savina, P. (2024). The ziré instrument onboard the nuses space mission. *Nuclear Instruments and Methods in Physics Research Section A: Accelerators, Spectrometers, Detectors and Associated Equipment*, 1068:169794.

[Piersanti et al., 2020] Piersanti, M. et al. (2020). Magneto-spheric–ionospheric–lithospheric coupling model. 1: Observations during the 5 august 2018 bayan earthquake. *Remote Sensing*, 12(20).

[Pillera et al., 2023] Pillera, R., Altomare, C., Bissaldi, E., De Gaetano, S., De Robertis, G., Dipinto, P., Di Venere, L., Franco, M., Fusco, P., Gargano, F., Giordano, F., Lacalamita, N., Licciulli, F., Loparco, F., Loporchio, S., Lorusso, L., Maiorano, F., Martiradonna, S., Mazziotta, M., Mongelli, M., Pantaleo, F., Panzarini, G., Papagni, M., Pastore, C., Rizzi, M., Serini, D., and Triggiani, R. (2023). A compact, light scintillating fiber tracker with sipm readout.

Nuclear Instruments and Methods in Physics Research Section A: Accelerators, Spectrometers, Detectors and Associated Equipment, 1048:167962.

[Piran, 1999] Piran, T. (1999). Gamma-ray bursts and the fireball model. *Physics Reports*, 314(6):575–667.

[Ptitsyna and Troitsky, 2010] Ptitsyna, K. V. and Troitsky, S. V. (2010). Physical conditions in potential accelerators of ultra-high-energy cosmic rays: updated hillas plot and radiation-loss constraints. *Physics-Uspekhi*, 53(7):691–701.

[Rees and Meszaros, 1992] Rees, M. J. and Meszaros, P. (1992). Relativistic fireballs - Energy conversion and time-scales. *Monthly Notices of the RAS*, 258:41.

[Ressell and Turner, 1990] Ressell, M. T. and Turner, M. S. (1990). The Grand Unified Photon Spectrum: A Coherent View of the Diffuse Extragalactic Background Radiation. *Comments Astrophys.*, 14:323.

[Ruderman and Sutherland, 1975] Ruderman, M. A. and Sutherland, P. G. (1975). Theory of pulsars: polar gaps, sparks, and coherent microwave radiation. *Astrophysical Journal*, 196:51–72.

[Schoenfelder et al., 1993] Schoenfelder, V. et al. (1993). Instrument Description and Performance of the Imaging Gamma-Ray Telescope COMPTEL aboard the Compton Gamma-Ray Observatory. *Astrophysical Journal, Supplement*, 86:657.

[Sgrigna et al., 2005] Sgrigna, V. et al. (2005). Correlations between earthquakes and anomalous particle bursts from sampex/pet satellite observations. *Journal of Atmospheric and Solar-Terrestrial Physics*, 67(15):1448–1462.

[Shaviv and Dar, 1995] Shaviv, N. J. and Dar, A. (1995). Gamma-ray bursts from minijets. *The Astrophysical Journal*, 447:863.

[Smith et al., 2023] Smith, D. A. et al. (2023). The third fermi large area telescope catalog of gamma-ray pulsars. *The Astrophysical Journal*, 958(2):191.

[Tauris and van den Heuvel, 2003] Tauris, T. M. and van den Heuvel, E. (2003). Formation and evolution of compact stellar x-ray sources.

[Terrell et al., 1982] Terrell, J., Fenimore, E. E., Klebesadel, R. W., and Desai, U. D. (1982). Observation of two gamma-ray bursts by VELA X-ray detectors. *Astrophysical Journal*, 254:279–286.

[Thompson, 2008] Thompson, D. J. (2008). Gamma ray astrophysics: the egret results. *Reports on Progress in Physics*, 71(11):116901.

[Thompson and Wilson-Hodge, 2022] Thompson, D. J. and Wilson-Hodge, C. A. (2022). *Fermi Gamma-Ray Space Telescope*, page 1–31. Springer Nature Singapore.

[van Paradijs et al., 1997] van Paradijs, J. et al. (1997). Transient optical emission from the error box of the gamma-ray burst of 28 February 1997. *Nature*, 386:686–689.

[Zatsepin and Kuzmin, 1966] Zatsepin, G. T. and Kuzmin, V. A. (1966). Upper limit of the spectrum of cosmic rays. *JETP Lett.*, 4:78–80.

[Zheng et al., 2022] Zheng, X. et al. (2022). In-orbit radiation damage characterization of sipms in the grid-02 cubesat detector. *Nuclear Instruments and Methods in Physics Research Section A: Accelerators, Spectrometers, Detectors and Associated Equipment*, 1044:167510.

Acknowledgements

I am deeply grateful to all who have contributed to the successful completion of this work.

First and foremost, I would like to express my gratitude to my supervisor, Dr. Nicola Mazziotta, for his invaluable guidance and unwavering support throughout this project. His mentorship, profound knowledge and expertise have been instrumental in shaping this research. The knowledge and skills imparted to me are truly priceless. I am especially thankful for his insightful suggestions, which guided me through every phase of my work, significantly enhancing its quality and depth.

I extend my sincere thanks to my co-supervisor, Prof. Silvia Rainò, for the crucial support she provided throughout this project. Her support during the writing of the thesis has been extremely important.

I am also profoundly grateful to Prof. Francesco Loparco for his constructive feedback and guidance, which have been essential in refining this work.

My thanks go to the technicians and the electronics and mechanical engineers of the INFN Bari mechanical workshop and electronics department for their exceptional work in designing and manufacturing the instrumentation I used in my research. Their expertise and dedication were fundamental to the success of this project.

Finally, I would like to express my thanks to all the members of the Bari Gamma group for their essential contributions, serving as a concrete and invaluable source of support throughout the development of this work. In particular Dr. Leonardo Di Venere, Dr. Davide Serini and Dr Roberta Pillera for their unwavering availability to provide clarifications and advice, offering invaluable guidance. A special acknowledgment goes to Dr. Nadia Lorusso for her invaluable assistance in the laboratory as well as for her unwavering encouragement throughout these years. I am profoundly grateful for all her support.